Contributors

Numbers in parentheses indicate the pages on which the authors' contributions begin.

Hirohiko Adachi (1, 69, 85, 97, 139, 163), Department of Materials Science and Engineering, Kyoto University, Yoshidahonmachi, Sakyo-ku 606-8501, Japan

Turgut Bastug (325, 353), Department of Materials Science, Japan Atomic Energy Research Institute, Tokai-mura, Naka-gun, Ibaraki 319-1195, Japan

Myung Chul Chang (179), Department of Materials Science and Engineering, Kunsan National University, Kunsan 573-701, Korea

Hyunju Chang (291), Advanced Materials Division, Korea Research Institute of Chemical Technology, Taejon 305-600, Korea

D. E. Ellis (271), Department of Chemistry and Materials Research Center, Northwestern University, Evanston, Illinois 60208

Sakir Erkoc (353), Department of Physics, Middle East Technical University, 06531, Turkey

Burkhard Fricke (353), Fachbereich Physik Universität Kassel, 34109–Kassel, Germany

Yasunori Fujimoto (229), Department of Materials Science and Engineering, Waseda University, 3-4-1 Ohkubo, Shinjuku-ku, Tokyo 169-8555, Japan

Kimichika Fukushima (255), Power and Industrial Systems R&D Center, Toshiba Corporation, 4-1 Ukishima-cho, Kawasaki-ku, Kawasaki 210, Japan

Masaru Hirata (325, 335, 353), Department of Materials Science, Japan Atomic Energy Research Institute, Tokai-mura, Naka-gun, Ibaraki 319-1195, Japan

Hidenori Ida (69), Department of Materials Science and Engineering, Kyoto University, Sakyo-ku Kyoto 606-8501, Japan

Shigero Ikeda (127), Ritsumeikan University, Kusatsu, Shiga 525-8577, Japan

Takugo Ishii (69, 85, 97), Department of Materials Science and Engineering, Kyoto University, Sakyo-ku Kyoto 606-8501, Japan

Yukiko Ito (85, 97), Department of Energy Science and Technology, Kyoto University, Sakyo-ku Kyoto 606-8501, Japan

Shinji Kawasaki (301), Faculty of Textile Science and Technology, Shinshu University, 3-15-1 Tokida, Ueda 386-8567, Japan

Tadayoshi Kikko (163), Department of Materials Science and Engineering, Himeji Institute of Technology, 2167 Shosha Himeji 671-2201, Japan

Yoshiyuki Kowada (271), Hyogo University of Teacher Education, Yashirocho, Hyogo 673-14, Japan

Koichiro Koyama (163), Department of Materials Science and Engineering, Faculty of Engineering, Himeji Institute of Technology, 2167 Shosha, Himeji 671-2201, Japan

Tsutomu Kurisaki (57), Department of Chemistry, Faculty of Science, Fukuoka University, 8-19-1 Nanakuma, Jonan-ku, Fukuoka 814-0180, Japan

Jae Do Lee (291), Advanced Materials Division, Korea Research Institute of Chemical Technology, Taejon 305-600, Korea

Ning Liu (301), Epson Kowa Corp., 1077-5 Shimonogo, Ueda 386-1214, Japan

Shuji Matsuoa (153), Department of Chemistry, Faculty of Science, Fukuoka University, Nanakuma, Jonan-ku, Fukuoka 814-0180, Japan

Masahiko Morinaga (163, 193), Department of Materials Science and Engineering, Nagoya University, Furocho, Chigusa-Ku, Nagoya 464-0814, Japan

Masao Morishita (163), Department of Materials Science and Engineering, Faculty of Engineering, Himeji Institute of Technology, 2167 Shosha, Himeji 671-2201, Japan

Takeshi Mukoyama (111, 127, 139, 353), Institute for Chemical Research, Kyoto University, Uji, Kyoto 611-0011, Japan

Katsumi Nakagawa (365), Canon Ecology R&D Center, 4-1-1 Kizugawadai, Kizu-cho Souraku-gun, Kyoto, Japan

Toyohisa Nakajima (301), Epson Kowa Corp., 1077-5 Shimonogo, Ueda 386-1214, Japan

Hirohide Nakamatsu (111, 127, 237, 325, 335, 375), Institute for Chemical Research, Kyoto University, Uji, Kyoto 611-0011, Japan

Kazuyoshi Ogasawara (69, 85, 97), Department of Materials Science and Engineering, Kyoto University, Sakyo-ku, Kyoto 606-8501, Japan

Kazuchika Ohta (57), Department of Functional Polymer Science, Faculty of Textile Science and Technology, Shinshu University, Ueda 386-8567, Japan

Yoshio Oka-Inagaki (57), Department of Functional Polymer Science, Faculty of Textile Science and Technology, Shinshu University, Ueda 386-8567, Japan

Fujio Okino (301), Faculty of Textile Science and Technology, Shinshu University, 3-15-1 Tokida, Ueda 386-8567, Japan

Jun Onoe (237, 311, 325, 335, 375), The Institute of Physical and Chemical Research (RIKEN), 2-1 Hirosawa, Wako, Saitama 351-0198, Japan

Rika Sekine (237, 325, 335, 375), Department of Chemistry, Faculty of Science, Shizuoka University, 836 Ohya, Shizuoka 422-8529, Japan

Akio Shigemi (127), Institute for Chemical Research, Kyoto University, Uji, Kyoto 611-0011, Japan

Shoichi Tachimori (325, 335), Department of Materials Science, Japan Atomic Energy Research Institute, Tokai-mura, Naka-gun, Ibaraki 319-1195, Japan

Kazuo Takeuchi (237), The Institute of Physical and Chemical Research (RIKEN), 2-1 Hirosawa, Wako, Saitama 351-0198, Japan

Isao Tanaka (69, 85, 97, 213), Department of Energy Science and Technology, Kyoto University, Sakyo-ku, Kyoto 606-8501, Japan

Kumiko Tanaka (237, 375), Department of Chemistry, Faculty of Science, Shizuoka University, 836 Ohya, Shizuoka 422-8529, Japan

Kazuo Taniguchi (139), Department of Solid State Electronics, Osaka Electro-Communication University, Neyagawa, Osaka 572-8530, Japan

Hidekazu Touhara (301), Faculty of Textile Science and Technology, Shinshu University, 3-15-1 Tokida, Ueda 386-8567, Japan

Masayuki Uda (31, 229), Department of Materials Science and Engineering, Waseda University, 3-4-1 Ohkubo, Shinjuku-ku, Tokyo 169-8555, Japan

Sven Varga (353), Fachbereich Physik, Universität Kassel, 34109-Kassel, Germany

Hisanobu Wakita (57, 153), Department of Chemistry, Faculty of Science, Fukuoka University, 8-19-1 Nanakuma, Jonan-ku, Fukuoka 814-0180, Japan

Toshio Yamaguchi (57, 153), Department of Chemistry, Faculty of Science, Fukuoka University, 8-19-1 Nanakuma, Jonan-ku, Fukuoka 814-0180, Japan

Masateru Yamamoto (69), Department of Materials Science and Engineering, Kyoto University, Sakyo-ku, Kyoto 606-8501, Japan

Mitsutoshi Yokomizo (57), Department of Chemistry, Faculty of Science, Fukuoka University, 8-19-1 Nanakuma, Jonan-ku, Fukuoka 814-0180, Japan

Soo-Chang Yu (179), Department of Chemistry, Kunsan National University, Kunsan 573-701, Korea

Hiroshi Yukawa (193), Department of Materials Science and Engineering, Nagoya University, Furocho, Chigusa-Ku, Nagoya 464-0814, Japan

Preface

Electronic state calculation is an enormous topic in the physics and chemistry of matter, and with recent progress in the computer and computational techniques, the field is rapidly growing. The discrete variational (DV) Xα molecular orbital method has proved to be a very powerful tool for calculation of the electronic states of various kinds of materials. The field of application of the DV-Xα method is exceedingly wide, including basic problems of inorganic chemistry and solid-state physics, X-ray and electronic spectroscopy, and materials science, where the interfacial science of metals and ceramics has become one of the more interesting topics. The first volume on DV-Xα research was published in 1997 by Academic Press as *Advances in Quantum Chemistry,* Vol. 29, containing edited papers presented at the First International Workshop on the DV-Xα Method (DV-Xα '96) held in Debrecen, Hungary, in 1996.

This volume includes the papers presented at the first Japanese–Korean DV-Xα Joint Symposium (DV-Xα '98). The 11th annual meeting of the Society for Discrete Variational Xα (Japan) was held at the Hoam Convention Center of Seoul University, Seoul, Korea, August 2–4, 1998. The symposium was organized by the Society for Discrete Variational Xα, Seoul National University, and Kunsan National Unversity. More than 80 scientists participated and discussed topics. The scientific program contained more than 50 papers, including three keynote lectures and five invited lectures, on the topics of theoretical research, especially research on materials science and X-ray and electron spectroscopies.

During the meeting, various applications of and perspectives on the DV-Xα method were discussed in detail. Among them, the usefulness of theoretical analysis using DV-Xα calculation for X-ray and electron spectroscopy such as XPS, XES (X-ray emission spectroscopy), XANES, ELNES, and AES was presented and discussed. A new universal computational method for the many-electron-state, DV-ME (DV-multielectron) method was introduced by demonstrating its advantages and possibilities for application to the calculation of the multiplet structure of the d–d transition in various transition metal oxides. Another topic was the application of the DV-Xα method to materials science. The study of

electronic states and chemical bonding in hydrogen storage alloys and advanced ceramics such as transparent metal oxide conductors was discussed from the viewpoint of the design of practical materials. Various materials such as metals, alloys, metal oxides, ceramics, and fullerenes have attracted attention. Relativistic effects on electronic states and chemical bonding were shown to be important, especially in materials containing heavy elements.

For supporting the symposium and the publication of this volume, we acknowledge our great debt to the Korean Society of Promotion of Science (KSPS), Seoul National University, Kunsan National University, the Japanese Society for Promotion of Science (JSPS), and the Society for Discrete Variational Xα (Japan). Special thanks is also expressed for the financial support of Sony Co., Kawasaki Steel Co., Taiyo Yuden Co., Kobe Steel, and other companies including Nippon Steel, Cobelco Research Institute, Fuji Research Institute Co., and Sumitomo Metals.

H. Adachi, M. Uda, and R. Sekine
Guest Editors
December 1999

Theoretical Analysis of X-Ray and Electron Spectra by DV-Xα Method

Hirohiko Adachi

Department of Materials Science and Engineering, Kyoto University, Yoshidahonmachi, Sakyoku, Kyoto 606-8501, Japan

(Received September 13, 1999)

The electronic state calculation by discrete variational (DV) Xα molecular orbital method is introduced to demonstrate the usefulness for theoretical analysis of electron and x-ray spectroscopies, as well as electron energy loss spectroscopy. For the evaluation of peak energy, Slater's transition state calculation is very efficient to include the orbital relaxation effect. The effects of spin polarization and of relativity are argued and are shown to be important in some cases. For the estimation of peak intensity, the first-principles calculation of dipole transition probability can easily be performed by the use of DV numerical integration scheme, to provide very good correspondence with experiment. The total density of states (DOS) or partial DOS is also useful for a rough estimation of the peak intensity. In addition, it is necessary to use the realistic model cluster for the quantitative analysis. The applications of DV-Xα method to the electron and x-ray spectroscopies for various kinds of materials are presented.

KEYWORDS: x-ray spectroscopy, electron spectroscopy, theoretical analysis, DV-Xα cluster method

e-mail: adachi@dvxa4.mtl.kyoto-u.ac.jp

ADVANCES IN QUANTUM CHEMISTRY, VOLUME 37

0065-3276/01 $35.00

1. Introduction

X-ray and electron spectroscopies are very useful techniques to study the electronic state and chemical bonding of various kinds of functional materials, such as ceramics and alloys. Since the leading achievement by Siegbahn et al.[1], x-ray photoelectron spectroscopy (XPS) is known to be very efficient for chemical state analysis of matters. They provide information not only on chemical components but also that on the valence electronic state and the chemical bonding of atoms constructing the materials. The direct information on the density of state (DOS) for solid state material can be obtained from XPS of the valence state region. Figure 1 schematically illustrates the relationship between the electronic state of matter and photoelectron spectrum as well as x-ray emission and absorption spectroscopies, and also the characteristics of these spectroscopies.

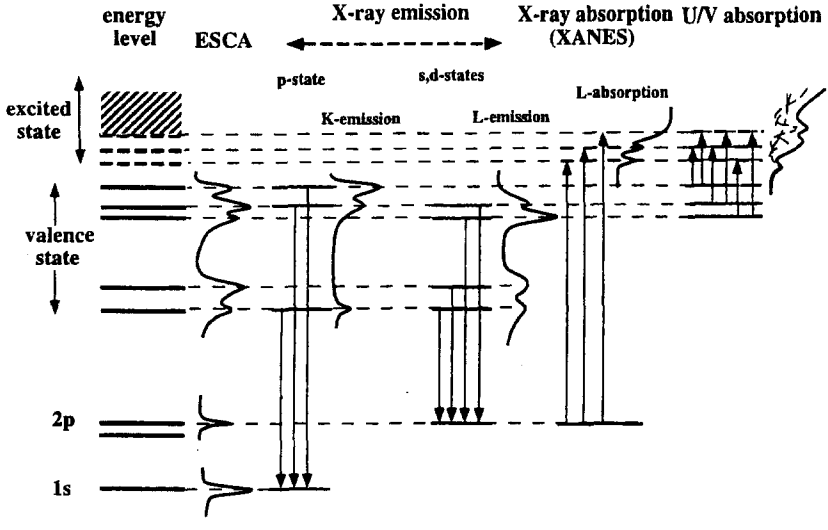

Fig.1 Schematic illustration of relationship between electronic state and photoelectron and x-ray spectroscopies.

X-ray fluorescence or emission spectroscopy (XES)[2] has also been used for the elementary analysis of the material, and it enable us to obtain a knowledge of the valence state as well. For the valence electronic state, XES gives the partial density of state (PDOS) due to the dipole selection rule, in contrast with XPS which provides total DOS(see Fig.1). Extended x-ray absorption fine structure (EXAFS) presents important information on the local structure around the atom which absorbs x-ray. However, x-ray absorption near edge structure(XANES or NEXAFS) involves much more information about the excited electronic structure which is very sensitive to the local structure[3]. Recent developments of photon technologies, especially those with synchrotron facility have attracted increasing attention. A speedy and precise measurement of x-ray emission , absorption or photoelectron spectrum is feasible by the use of the synchrotron radiation source. The highly resolved spectrum even in the valence state region can easily be obtained. Recently, apart from x-ray spectroscopy, electron energy loss spectroscopy (EELS) combined with a high resolution electron microscope (HREM) is considered to be very useful for local structural analysis[4] at very narrow region like a grain boundary. It is known that the core loss spectrum called as energy loss near edge structure (ELNES) gives a very similar spectrum to XANES.

In order to make a correct analysis of such an experimental spectrum, an appropriate theoretical calculation is indispensable. For this purpose, some of calculational methods based on the molecular orbital theory and band structure theory have been applied. Usually, the calculation is performed for the ground electronic state. However, such calculation sometimes leads to an incorrect result, because the spectrum corresponds to a transition process among the electronic states, and inevitably involves the effects due to the electronic excitation and creation of electronic hole at the core or/and valence levels. Discrete variational(DV) Xα molecular orbital (MO) method[5] which utilizes flexible numerical atomic orbitals for the basis functions has several advantages to simulate the electronic transition processes. In the present paper, some details of the computational procedure of the self-consistent-field (SCF) DV-Xα method is firstly described. Applications of the DV-Xα method to the theoretical analysises of XPS, XES, XANES and ELNES spectra are

presented[6]. We discuss about the effects of the orbital relaxation, spin polarization and relativity on these spectra.

2. Computational procedure

The molecular potential in the present method is composed of a coulomb potential and Slater's exchange potential of the density functional theory and is given by

$$V_{eff} = V_c + V_{xc} \quad . \tag{1}$$

Here we use the self-consistent-charge (SCC) approximation[5] to construct the coulomb potential Vc. The effective atomic charges are estimated by Mulliken population analysis and are spherically averaged around each nucleus. Then, they are superimposed to construct the molecular coulomb potential. For the exchange potential, Slater's approximation[7]

$$V_{xc\uparrow} = -3\alpha\left(\frac{3}{4\pi}\rho_{\uparrow}\right)^{1/3} \quad , \tag{2}$$

is employed for up-spin electron, where $\rho_{\uparrow}$ is the density of up-spin electron, and α is the scaling parameter which is fixed to be 0.7 in the present work. The similar form is also used for down-spin.

The MO wave function is expressed by an LCAO (linear combination of atomic orbitals) scheme as usual MO method, and written by

$$\phi_\ell = \sum_i C_{i\ell}\chi_i \quad . \tag{3}$$

In the present DV-Xα method, the numerical atomic orbitals are utilized to construct the basis set, different from the other MO methods. The wave function is obtained by numerically solving Schrödinger equation for " atom in molecule". The effective charge of the atom in molecule varies every SCF iteration until it converges at the SCF. Then, the atomic orbitals are computed at each iteration in order to supply the optimal basis functions for the molecular

calculation. This procedure is very important to efficiently include the orbital relaxation effects in the calculation, especially for an excitation process where the atomic potential is drastically changed, compared with that in the ground state (GS). For the theoretical evaluation of the peak energy in the x-ray and photoelectron spectra, we use Slater's transition state (STS)[8]. The concept of STS is schematically illustrated in Fig.2. By STS calculation with SCF procedure, the orbital relaxation effects

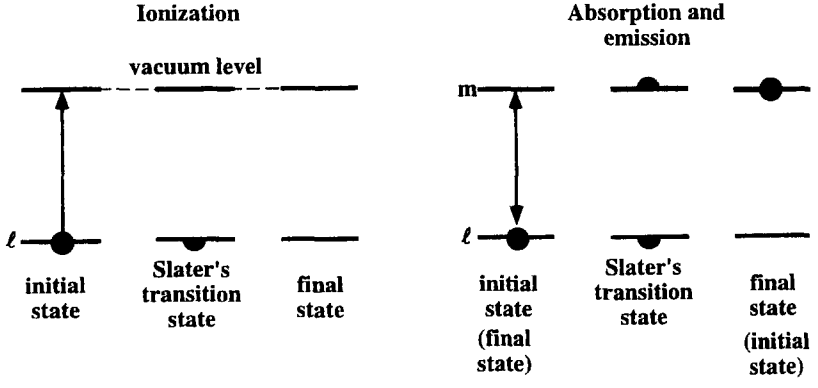

Fig.2 Concept of Slater's transition state for ionization and electronic transitions

caused by the electronic transition can essentially be taken into account. For the photoelectron spectrum, the MO eigenvalue for level i in STS, $\varepsilon_i^{(STS)}$ can be a good approximation to the ionization energy or the electron binding energy, $(BE)_i$,

$$\left(BE\right)_i = -\varepsilon_i^{(STS)} \quad . \tag{4}$$

For the x-ray emission and absorption spectrum, a peak energy (PE) corresponds to transition energy of an electron is evaluated as the energy separation between a core level i and valence or excited level j in STS, namely

$$\left(PE\right)_{i-j} = \varepsilon_j^{(STS)} - \varepsilon_i^{(STS)} \ . \qquad (5)$$

In evaluating the spectral peak energy, we practically use non-spin-polarized model for a non-magnetic material at the ground state, namely, the exchange potential for non-spin-polarized system,

$$V_{xc} = -3\alpha\left(\frac{3}{8\pi}\rho\right)^{1/3} , \qquad (6)$$

is used instead of eq.(2). However, it is not correct, because a spin polarization[9] takes place in any electronic transition process as demonstrated in Fig.3. Thus, it is

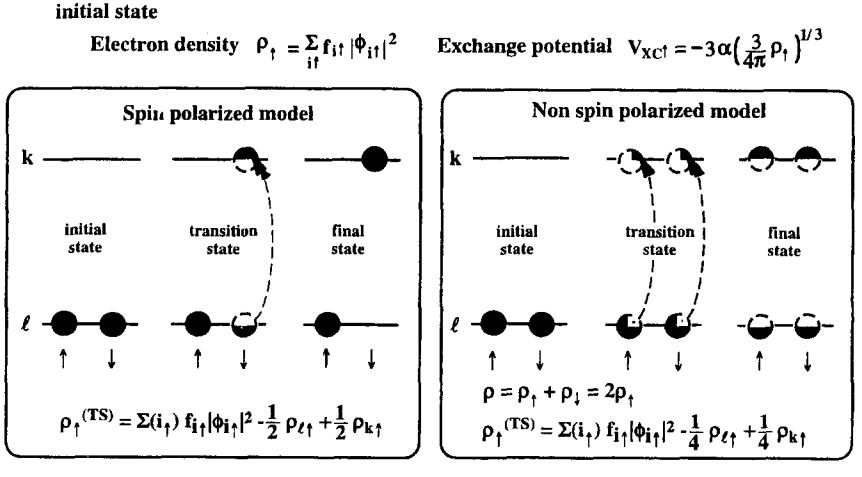

Fig.3 Spin polarization effects in electronic excitation process

neccessary to examine the deviation from the correct model using eq.(2), though it is sometimes not very large.

For a system which contains elements with a large atomic number, the error due to the non-relativistic approximation become very serious in the electronic state calculation. Besides, a large energy shift of core level takes place even for rather light elements. Thus, relativistic Dirac equation should be

solved instead of non relativistic Schrödinger equation for the correct evaluation of the peak energy. Within the framework of DV-Xα method, DV-Dirac Slater (DS) model calculation[10] is available for such purpose. By the DV-DS calculation, we can reasonably include the so-called relativistic effects of the level shifts such as mass-velocity and Darwin terms and the level splitting by spin-orbit coupling.

There are following steps to get a correct estimation of the spectral peak energy within the one-electron model,

(1) ground state MO calculation

(2) calculation of Slater's transition state(STS)

(3) spin-polarized model calculation

(4) relativistic DV-DS calculation.

For further accurate calculation, the many-electron effects like the multiplet structure should be taken into account. Although this type of calculation is feasible with the first-principles DV multi-electron method[11], any details will not be described here.

Although the electron binding energy of the core level is inherent to the element, the level energy is somewhat affected by the chemical environment. Thus the energy shift is detected as the chemical shift and is used for the chemical state analysis. In general, higher oxidation state of the element gives larger electron binding energy, because the electron-electron repulsion potential is reduced.

In addition to the calculation of peak energy, an accurate estimation of peak intensity is neccessary for a quantitative analysis of the spectrum. For the photoelectron spectrum, the peak intensity can generally be assumed as the sum of the atomic orbital contributions[12] and is written by

$$I_\ell = \sum_i Q_i^\ell \sigma_i \ , \qquad (7)$$

where Qi^ℓ is the orbital population of the i th atomic orbital in the ℓ th molecular orbital. This can be calculated by the Mulliken population analysis, and σ_i is photoionization cross section for an electron of the atomic orbital i. The value is estimated using the dipole approximation and is given by

$$\sigma_i = \frac{8\pi^2\alpha_0}{3}(\varepsilon_f - \varepsilon_i)\left|<\chi_i|\,\mathbf{r}\,|\chi_f>\right|^2 , \qquad (8)$$

where α_0 is the fine structure constant and i and f mean the initial and final states of the photoionization process. Thus the energy separation ε_f - ε_i corresponds to the photon energy hν. The wave function χ_i and χ_f are the solutions of Schrödinger equation for the atomic potential, then the χ_i is the wave function for the atomic orbital i, and χ_f is that for a continuum state f with ε_f>0. The theoretical evaluation of σ_i has been reported by several workers[13]. However, the computer code, where we calculate it for the atomic orbital used as the basis function of the MO calculation, is available. The details of the computational procedure has been described elsewhere[14].

For the x-ray absorption process, the transition probability can also be estimated by the approximation of the dipole transition. In the x-ray process, the oscillator strength is evaluated from the dipole matrix element $<\mathbf{r}>_{c\ell}$ between a core state c and a unoccupied molecular state ℓ and is given by

$$f_{c\ell} = \frac{2}{3}(\varepsilon_\ell - \varepsilon_c) \times <\mathbf{r}>_{c\ell}^2 . \qquad (9)$$

The dipole-matrix element is calculated by

$$<\mathbf{r}>_{c\ell} = \int \chi_c\,\mathbf{r}\,\phi_\ell dv = \sum_i C_{i\ell} \cdot <\chi_c|\,\mathbf{r}\,|\chi_i> . \qquad (10)$$

The first-principles calculation of the multi-center integral for the dipole-matrix element above is feasible by the use of DV numerical integration procedure[15].

For the x-ray emission process, the transition probability[16] is also calculated from the dipole matrix similar to the case of the x-ray absorption, but the molecular state ℓ in eq.(10) is of occupied in this case. The transition probability corresponds to the spontaneous emission rate, then is given by Einstein formula as

$$A_{\ell c} = \frac{4\alpha_0^3}{3}(\varepsilon_\ell - e_c)^3 <\mathbf{r}>_{\ell c}^2 . \qquad (11)$$

For the dipole transition, Laporte selection rule ($\Delta\ell = \pm 1$) for the emitting or absorbing atom is valid, when the probability of interatomic transition is very small. In such a case, the atomic orbital component (or partial density of states) obtained from Mulliken population analysis is useful for a rough estimation of

peak intensity.

3. X-ray photoelectron spectroscopy(XPS)

The calculation of ionization energy (or electron binding energy), namely peak energy in XPS spectrum can be examined by the several procedures (1) - (4), as above mentioned. Figure 4, 5 and 6 plot the orbital energies both of valence and

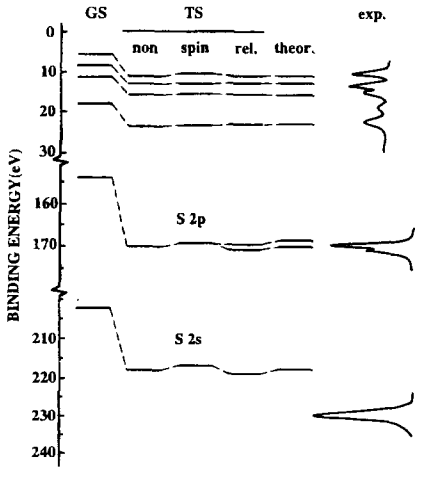

Fig.4 MO energies at GS and STS and XPS spectra for H_2S

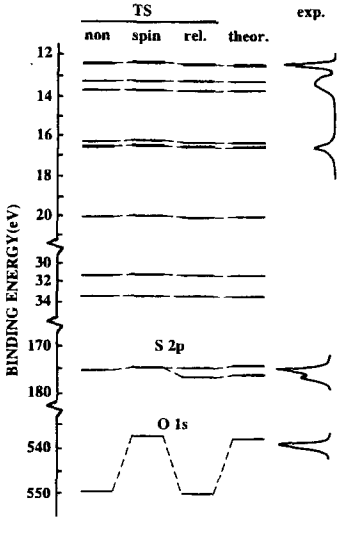

Fig.5 MO energies at STS and XPS spectra for SO_2

core levels for H_2S, SO_2 and SF_6 molecules, respectively, obtained by these four types of calculations and compare them with experimental ionization energies measured by XPS[1]. Here, GS denotes the MO energy obtained for the ground state(neutral molecule), TS means that by Slater's transition

state(STS). Among them, we examine three types of calculations, namely non-spin-polarized calculation using eq.(6) labeled as "non", spin-polarized one "spin" by eq.(2) and relativistic DS calculation "rel" within the non-spin-polarization scheme. Finally, we determined the most proper value of the theoretical ionization energy "theor." as the relativistic value, but taken account of the spin polarization effect. We compare these theoretical ionization energies with the experimental values of XPS in the figure. By STS calculation, the orbital energies are almost uniformly shifted downward compared with GS values. The amounts of the level shift are 4-5 eV for valence levels and about 15 eV for 2s and 2p core levels. This is because of the reduction of electron-electron repulsive potential by the removal of a half electron in STS. It is seen that the TS values agree well the experimental ionization energies. The non-spin-polarized calculation, however does not includes the spin polarization effects during the ionization process as shown in Fig.3, and overestimates the spin density and then the exchange potential(see eq.(2)). With the spin polarization, the levels are

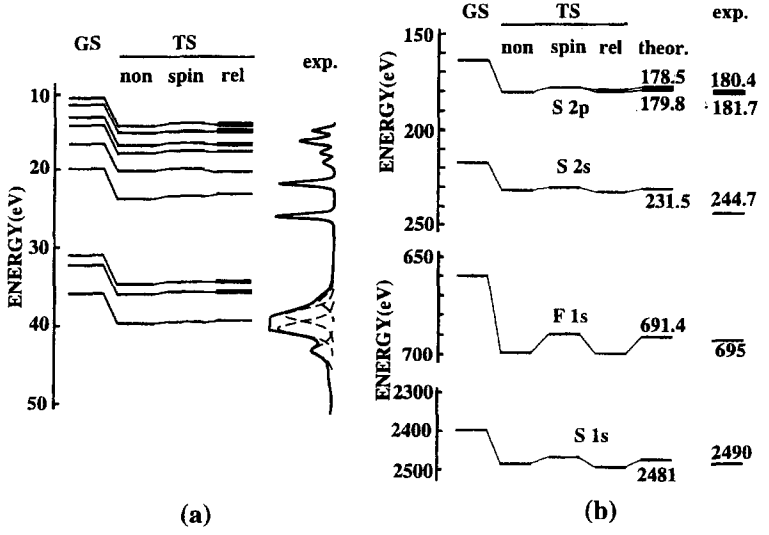

Fig.6 MO energies at GS and STS of (a) valence and (b) core levels and XPS for SF_6

somewhat lifted by the correct estimation of spin density. By this calculation, the agreement with experiment generally becomes better. The level shifts for deep core levels are considerably large. It counts more than ten eV, for example, in the case of O 1s (see Fig.5). In general, we perform non-relativistic calculations, since the relativistic Dirac equation is much more complicated and the actual calculation is very tedious. However, it sometimes causes serious error in the electronic state. The notable effects due to the relativity appear in the level shift and level splitting. The levels with smaller azimuthal quantum number ℓ are shifted much more downward, and contrary those with lager ℓ are relatively shifted upward. The level splitting is caused by the spin-orbit coupling and takes place except for s orbitals. These effects are not very large and are appreciable only in core levels for light elements, though it extends to valence levels for heavy elements[17]. In the experimental spectra, the level splittings are seen in S 2p level, and the relativistic calculation well reproduces the experiment. It can be mentioned from these calculations that STS calculation of non-spin-polarized model already reproduce very well the experimental XPS peak position for valence state of non-magnetic molecules, and the consideration of spin polarization and relativistic effects substantially improves peak energies for core levels as well. The deviation from the experiment is less than 1% in absolute energy except S 2s level. However, the calculation systematically gives smaller binding energy for S 2s level compared with experiment. The deviation is more than ten eV. The reason is not clear, but may be ascribed to some error in Xα potential.

The valence state XPS of solid state material is useful for discussion of its chemical bonding. The valence state XPS spectrum is considered to roughly reflect the density of states (DOS). For theoretical spectrum, we calculate for a cluster model which represents the solid state material, to obtain the MO levels. Then the discrete levels are substituted and broadened by Gaussian or Loretzian to display the valence electronic structure as DOS. The electron binding energy is referred to Fermi level in usual measurement for a solid state sample. Therefore, DOS obtained by an electronic structure calculation for ground state is often used as a theoretical XPS spectrum. However, we must be more careful when we treat a material with strong covalency, because its valence state

is constructed by admixture of various atomic orbitals with different ionization cross sections. A quantitative analysis from the electronic state calculation should be made by using eq.(7), where the spectral intensity is evaluated by a sum of PDOS(corresponds to atomic orbital component), but multiplied by each atomic ionization cross section. Figure 7 shows comparison between the experimental and theoretical XPS spectra for $SrTiO_3$[18]. It is seen that the total DOS does not reproduce well the measured spectrum. From the electronic state calculation, it is found that rather strong covalent interaction between Ti 3d and O 2p atomic orbitals exists. Then, these orbitals are mixed up to construct the valence band. The cross section of the photoionization process for these

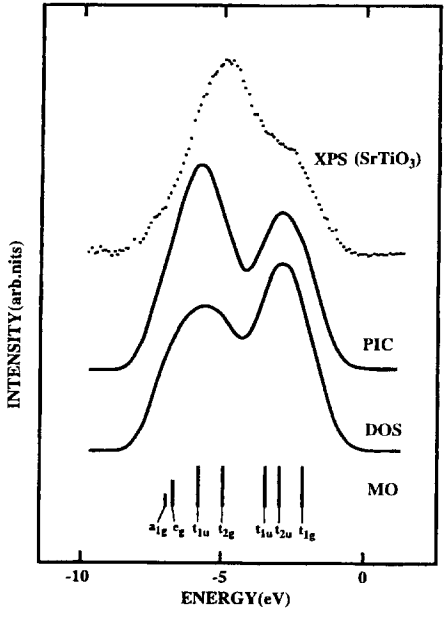

Fig.7 Comparison between theoretical and experimental XPS for $SrTiO_3$. PIC means theoretical spectrum with photoionization cross section

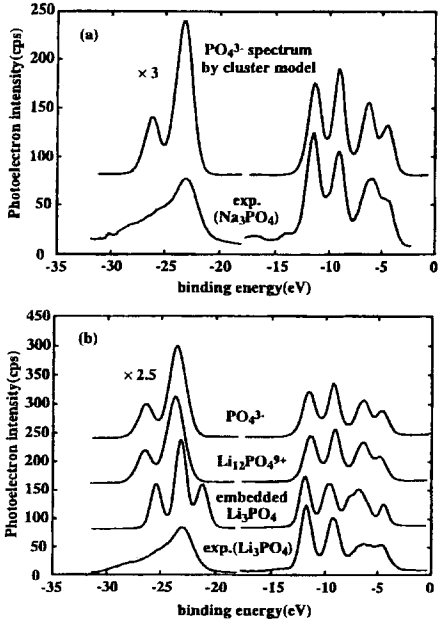

Fig.8 Comparison of theoretical spectrum with realistic cluster model (a) and those of various cluster models(b) with experiment

atomic orbitals are considerably different, reflecting their spatial expansion. In contrast to DOS, the theoretical spectrum with taking account of the atomic ionization cross section well reproduces the experiment.

The recent electron spectrometer provides highly resolved spectrum for valence state XPS, which supplies us with very useful information for discussion on chemical bonding, when combined with an appropriate theoretical analysis as mentioned above. Therefore, an accurate calculation of electronic state is required for such a purpose. The DOS calculated by DV-Xα method has been demonstrated to reproduce well the valence state XPS for some oxyanions[19], compared with other theoretical calculations. The calculation was made using a simple model cluster XO_4^{n-} with T_d symmetry, thus the theoretical analysis was insufficient for the valence structure in details. This has significantly been improved by a careful analysis with more realistic model clusters[20], which are determined from crystallographic data for those oxyanions. The comparison of the theoretical and experimental spectra for PO_4^{3-} ions is shown in Fig.8. The agreement is very good even for the fine structure in the valence band.

The electronic state and chemical bonding of metal cluster complexes attract increasing attention in inorganic chemistry. The valence state is determined by covalent interaction between metal cluster orbitals and those of the ligands, which strongly affects the valence band structure. Thus the valence state XPS is very powerful tool for such a study. The electronic state calculations for cubane-type molybdenum cluster complexes like $(Mo_3X_4(H_2O)_9)^{4+}$, where X = O and S, have been done by DV-Xα method, to provide the theoretical XPS spectra, which are in very good agreement with the experiment[21].

Although the valence state XPS conveys more information on the electronic state and chemical bonding, the chemical shift observed in the core level is more often used in general. The core level of the atom with a higher oxidation state usually possesses a higher binding energy. The chemical shift of core level gives knowledge of the oxidation state of the element. The element sulfur has many oxidation state, namely from -2 to +6. The chemical shifts of 2s and 2p levels for sulfur compounds shown in Fig.4, 5 and 6 are plotted in

Fig.9. In the figure, two types of calculated values for the ground state(GS) and Slater's transition state(TS) are indicated and compared with the experimental values. These values are referred to that of H_2S. As previously mentioned, the absolute energy of S 2s level calculated systematically deviates from the measurement. However, the chemical shifts, namely the relative changes of the level energy both for GS and TS show good agreement with the experiment.

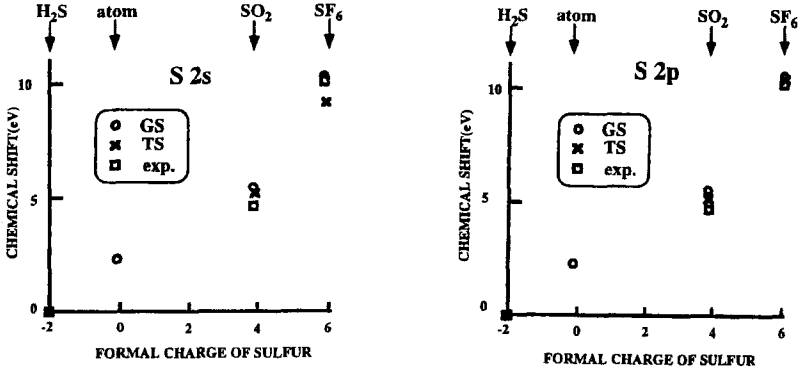

Fig.9 Theoretical and experimental values of the chemical shifts for S 2s and 2p levels

4. X-ray emission spectroscopy(XES)

For chemical state analysis, X-ray emission spectroscopy(XES) for the valence state is very useful. The valence state XPS gives total DOS of the material, while XES reflects the partial DOS, because the dipole transition is predominant in the x-ray emission process. Thus a core hole in an s level, for

example, leads to an electronic transition from p states, followed by a K x-ray emission(see Fig.1). For the theoretical analysis of XES, the peak energy is evaluated by STS calculation. The theoretical peak intensity can accurately be obtained by the calculation of dipole transition probability using eq.(11), though PDOS is often used as an approximation of the transition probability. Figure 10 demonstrates the comparison between measured and calculated X $L_{2,3}$ emission spectra for Li_nXO_4[16]. The calculation has

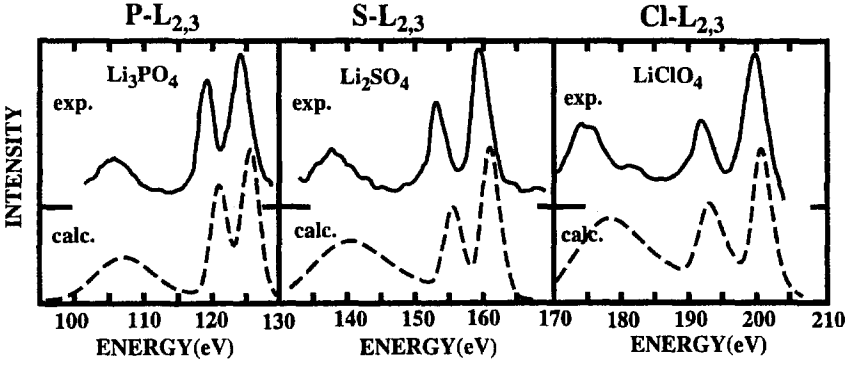

Fig.10 Theoretical and experimental X-$L_{2,3}$ spectra of Li_nXO_4

been made for a very simple cluster model of XO_4^{n-}. Because the x-ray process reflects local electronic property within the region of core state orbital, even this small cluster provides a very accurate theoretical spectrum both for the absolute energy and the intensity.

The chemical effects on atomic x-ray spectrum has widely been investigated by DV-Xα calculations, where the contribution of interatomic transition, in other word, the cross-over transition to x-ray emission rate can essentially be estimated by eq.(11). The abnormality in atomic Kβ/Kα emission ratio for some 3d transition metal compounds has been observed.

Figure 11 displays the experimental and theoretical Kβ x-ray emission spectra of Cr and Mn in metal oxides[22], interpreting the detailed mechanism of Kβ emission, that is the contribution of t_2-type molecular orbitals.

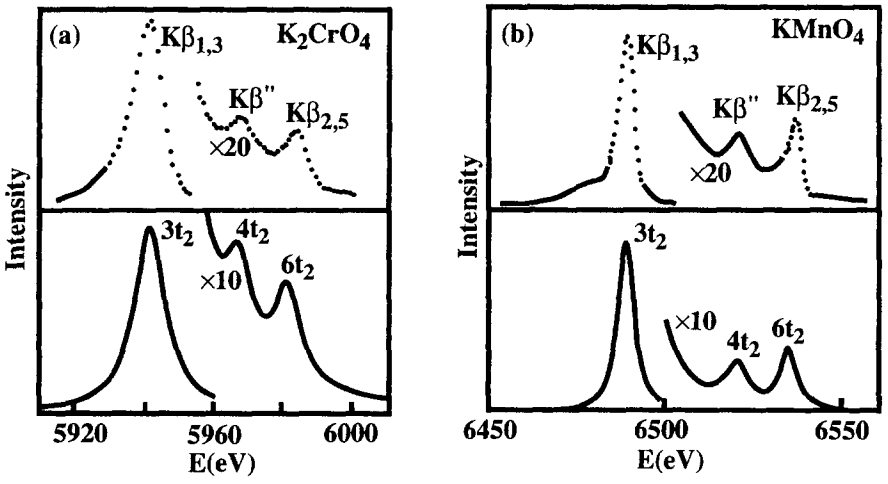

Fig.11 Experimental and theoretical Kβ x-ray emission of Cr in KCr_2O_4(a) and Mn in $KMnO_4$(b)

Resonance x-ray emission observed above threshold is useful to detect a dangling bond state. In boron Kα x-ray fluorescence spectra of mechanically milled boron nitride with hexagonal structure, h-BN, a satellite peak above threshold has been observed as seen in Fig.12(a). In order to clarify the origin of the high energy satellite peak, DV-Xα calculations for model cluster sown in Fig.12(b)[23] has been performed. The peak has been assigned to the resonance x-ray scattering which corresponds to unoccupied n* orbitals, namely dangling bond states of h-BN cluster(see Fig.13).

XES has been shown to be a powerful technique to determine the local structure in the material, when combined with DV-Xα cluster calculation. The atomic arrangement around oxygen atom in boron oxide $B_{12}O_2$ was not well-

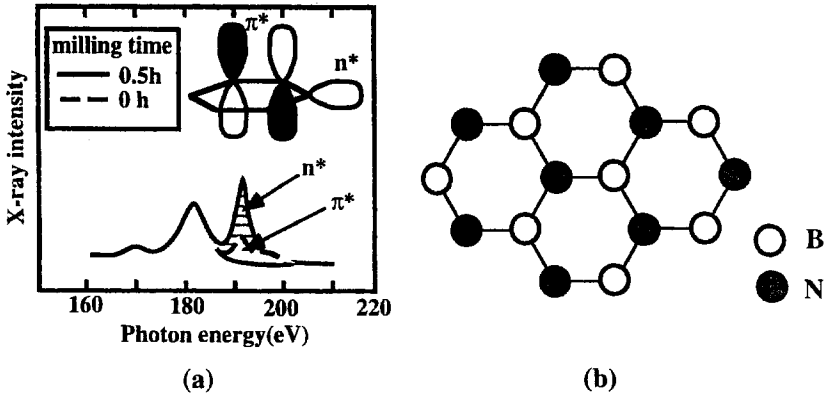

Fig.12 Boron Kα and resonance scattering spectra of milled h-BN(a) and cluster model used for DV-Xα calculations(b)

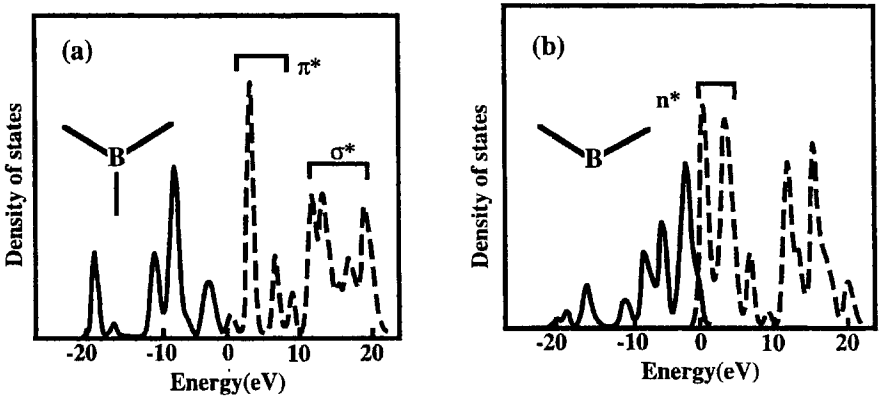

Fig.13 Calculated boron 2p PDOS of (a) three- and (b) two-fold coordination borons. Solid line denotes occupied and dashed line unoccupied.

known. Then, the theoretical spectra obtained by DV-Xα model cluster calculations[24] for $B_{12}O_2$ were examined to find an appropriate model which reproduced well the measured XES. The local atomic arrangement thus

expected has been confirmed by the x-ray diffraction analysis[25]. The usefulness of the theoretical analysis has also been reported for Si Kβ x-ray fluorescence spectra of SiO_2-Na_2O binary slag[26].

5. X-ray absorption near edge structure(XANES)

X-ray spectrum near absorption edge contains a direct information on unoccupied excited electronic states. The excited electronic states observed as XANES spectrum are generally classified into the valence state, molecular Rydberg state, shape-resonance state and free-electron state. DV-Xα calculations has been made to clarify the relationship between the electronic state and XANES spectrum for some molecules such as H_2S[6] and SF_6[27]. The valence state and molecular Rydberg state provide spectral peaks at lower energies than ionization potential. The shape resonance state appears at higher energy region than the threshold and shows an intensive peak. It has been found that these electronic states could thoroughly been represented by the molecular orbital states. Figure 14 illustrates the calculated[6] and measured[28] S-K XANES of H_2S molecule. The measured peaks, which

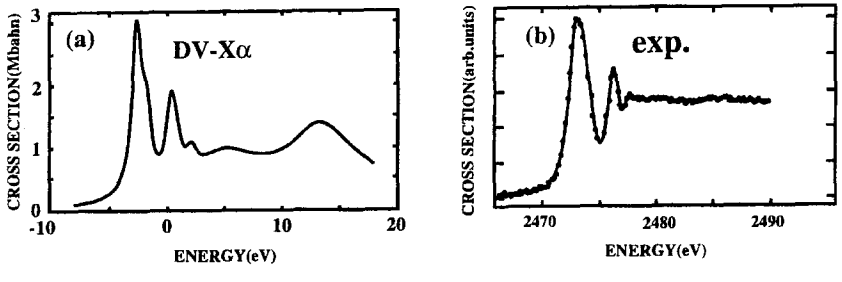

Fig.14 Calculated (a) and experimental (b) sulfur K x-ray absorption spectra for H_2S

were previously assigned to the molecular Rydberg states, have well been reproduced by the DV-Xα molecular orbital calculation and can be attributed to electronic transitions to the excited molecular orbital states.

For an interpretation of so-called shape-resonance state, an assumption of potential barrier surrounding the molecule was introduced. However, the origin of the potential barrier has not been clarified yet. DV-Xα calculation has also been applied to solve this problem. The theoretical and measured S $L_{2,3}$ and F K XANES spectra of SF_6 molecule are compared in Fig.15 and 16. In both cases, the agreements between theory and experiment are quite good. From the calculation, it is found that any potential barrier is not created and the excited MO states corresponding to the shape-resonance peaks are naturally generated by the molecular potential.

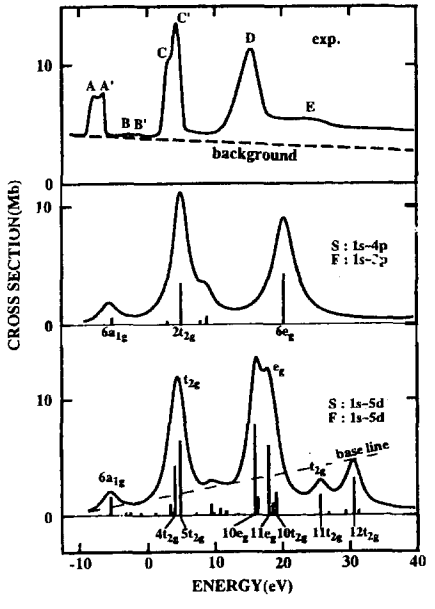

Fig.15 S-$L_{2,3}$ XANES for SF_6. Two theoretical spectra with different basis sets are compared with experiment

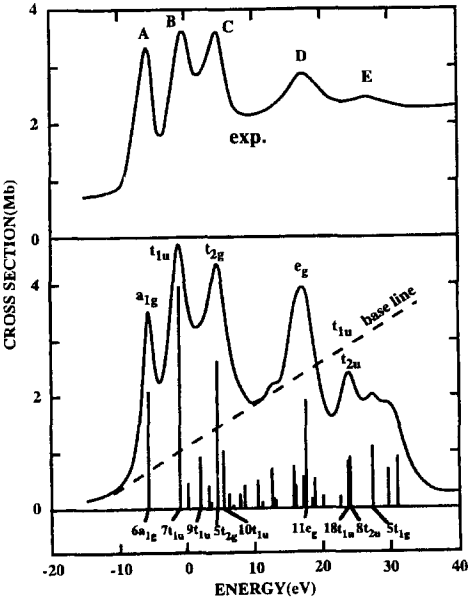

Fig.16 Experimental and theoretical F-K XANES spectra for SF_6

For the structure at higher energies, the agreement becomes better when the basis set is extended[29]. The molecular orbital approximation has been proved to be efficient even for generation of continuum wave function of free-electron state[30] when the extension of the basis set is sufficient.

The theoretical analysis of XANES by DV-Xα method has also been reported to be very useful for the structural investigation as well as study of chemical state and chemical bonding for the square-planar tetraaza and diazadioxa macrocyclic copper(II) complexes[31].

6. Energy loss near edge structure(ELNES)

The core loss structure in electron energy loss spectroscopy (EELS) is known to be very similar to XANES, because the core loss spectrum is caused by physically the same process as that of x-ray absorption, corresponding to the electronic transition from core level to unoccupied excited states. Therefore, the theoretical analysis for ELNES can be carried out by almost the same procedure used for that of XANES. For the chemical state analysis of oxide ceramics, ELNES has also been proved to be very efficient with theoretical analysis by DV-Xα cluster calculation[32]-[35]. The cluster calculation indicates that the core-hole effect due to the electronic transition is sometimes very important[34] and the ground state calculation gives a serious errors in excited electronic state.

Recent development of transmission electron microscope enables us to make microscopic observation with sub-nanometer spatial resolution, because the electron beam can be focused within 1 nm diameter. The advantage of the use of EELS technique is that an investigation of electronic state at very small local space of sub-nanometer scale is feasible when it is combined with the high resolution electron microscopic(HREM) technique. A schematic illustration of the combination of HREM and ELNES is indicated in Fig.17.

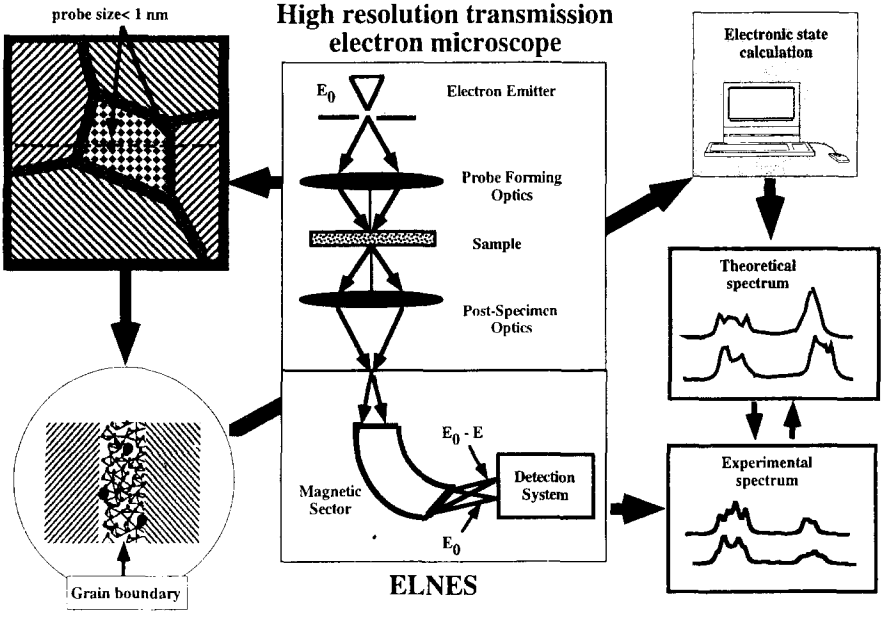

Fig.17 Schematic illustration for combination of HREM and EELS. In addition to observation of lattice image by HREM, chemical analysis by EELS can separately be made with focused probe on grain and grain boundary. Theoretical analysis by model cluster for grain boundary is feasible by comparison with experimental spectra.

From the high resolution electron microscopic observation of a sinterred ceramic material for high purity silicon nitride Si_3N_4[36], it has been found that a glassy film with 1 nm thickness exists at the grain boundary. By the use of experimental technique above mentioned, the grain boundary of silicon nitride ceramics has been reported to demonstrate Si-L ELNES spectra[37] both for the grain boundary and inside of the grain. These two spectra are shown in Fig.18. It can be pointed out that the main differences of the spectrum at grain boundary from that of grain are the energy shift to higher energy by about 1 eV and broadening of the onset peak. From the EELS measurement, the chemical compositions[38] have also been obtained semi-quantitatively. It is found the the glassy film at the grain boundary, which was once considered to be

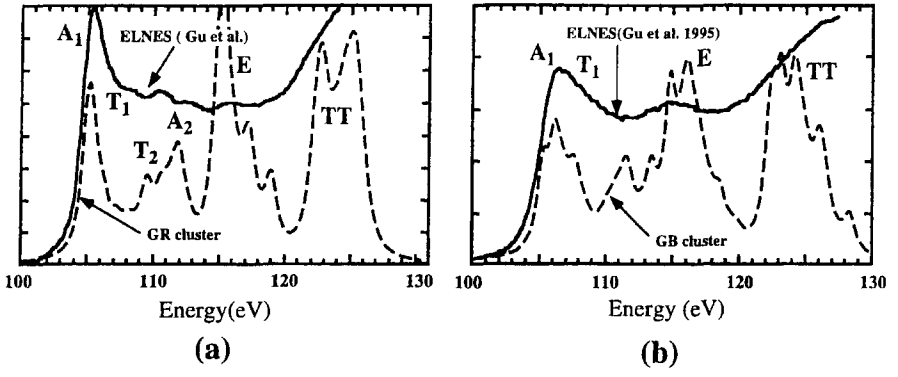

Fig.18 Experimental and theoretical Si-L ELNES for Si_3N_4 grain (a) and grain boundary (b).Model clusters calculated are $Si_9N_{25}^{39-}$ for grain and $Si_7N_{13}O_7^{25-}$ for grain boundary

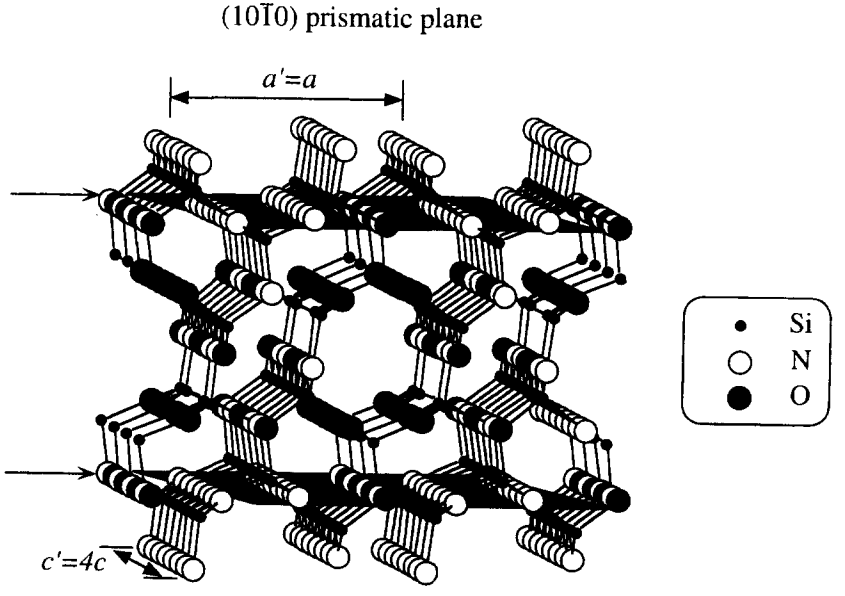

Fig.19 Grain boundary model of glassy film in Si_3N_4 ceramics

composed of silicon dioxide, contains about 30% nitrogen. Based on the information obtained by experiments, DV-Xα cluster calculations[39] have been carried out to investigate the microstructure and property of the grain boundary. Several cluster models were examined to find an suitable atomic arrangement which reproduce well the ELNES spectrum for the grain boundary. The grain boundary model thus determined is demonstrated in Fig.19. For the calculation of theoretical ELNES, the cluster $Si_7N_{13}O_7^{25-}$ taken from the grain boundary model has been used. The theoretical spectra for the grain and grain boundary are depicted in Fig.18. The spectral changes of the level shift and the broadening are ascribed to reorganization of chemical bonding of mixed coordination of oxygen and nitrogen to silicon. The stability of the grain boundary model has been confirmed by a static lattice simulation with a pair-wise potential[39].

There are three polytypes of boron nitride (BN), namely those with cubic(c-BN), wurtzite-type(w-BN) and hexagonal(h-BN) structures. Because the ELNES spectrum reflects the difference of the local structure, ELNES for h-BN, which has a graphite-type layered structure, shows considerably different spectrum from the other polytypes[40],[41] as shown in Fig.20. Among these polytypes, the near edge structures for c- and w-BN resemble each other, because of the similarity of their structures. As mentioned above,

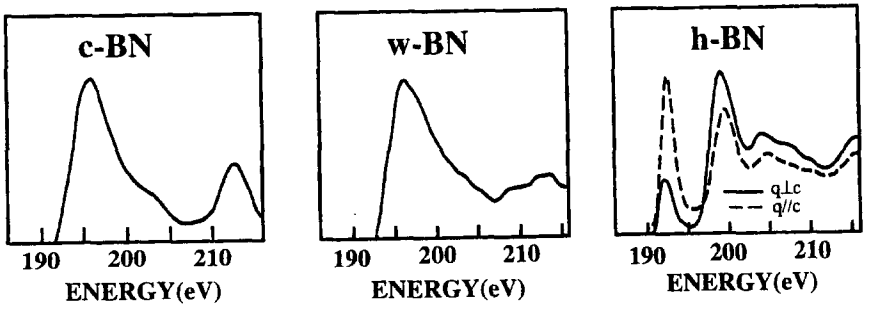

Fig.20 Experimental B-K ELNES spectra for BN polytypes[40]

the similar structures can be expected in x-ray absorption spectra. The XANES spectra[42] for these polytypes have also been reported. The electronic states and chemical bonding for these BN polytypes have thoroughly been studied by DV-Xα cluster model calculations[43]. It has been pointed out that ELNES and XANES are sensitive to their local structures and the core-hole effects are considerably important in these spectra, because the wave functions of excited states significantly localize near the core hole.

For h-BN, both spectra of ELNES and XANES have previously been reported[40]-[42]. These spectra show very similar structures. Figure 21

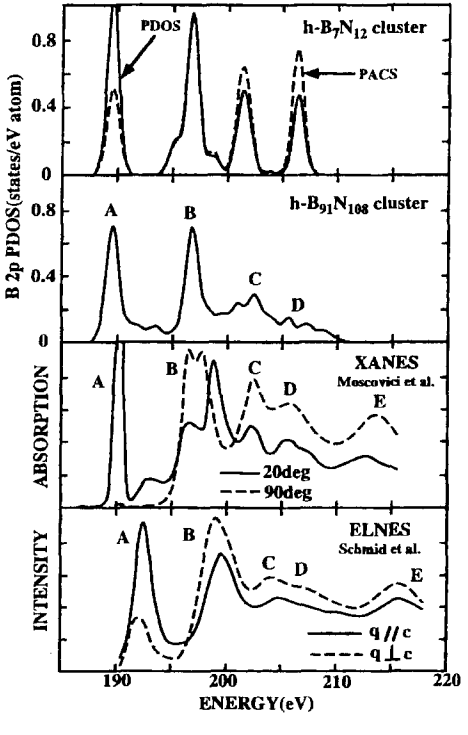

Fig.21 Theoretical and experimental B-K XANES and ELNES for h-BN

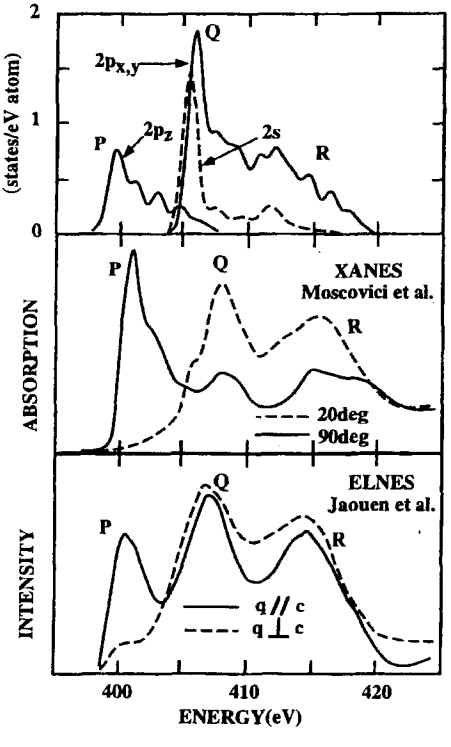

Fig.22 Theoretical and experimental N-K XANES and ELNES for h-BN

displays theoretical and experimental B-K near edge structures. The spectra of N-K near edge are indicated in Fig.22. The experimental B-K spectra resemble C-K spectrum of graphite, because the main component of the excited state is B 2s and 2p orbitals. Two types of measurements for ELNES have been made, namely those under conditions where momentum-transfer vector q is perpendicular (q⊥c) and parallel (q//c) to c axis. Similarly, two types of XANES spectra have also been measured corresponding to these two conditions. DV-Xα cluster calculations for small and large cluster models(B_7N_{12} and $B_{91}N_{108}$) have been carried out. The theoretical results reproduce very well the experiments. The agreement of the peak energies is quite good and the deviation is within 1eV in absolute energy. The result of the larger cluster reproduce very well the experimental spectra even for the structure at higher energies. For small cluster model, two theoretical spectra, namely photoabsorption cross section (PACS) evaluated by eq.(9) and PDOS of B 2p are depicted. The approximation by PDOS is fairly good. Thus, only B 2p PDOS is shown for the large cluster model in the figure. In the spectra, the first peak(labeled as A in the figure) at about 190 eV has been assigned to π^* state and the second peak(B) at about 198 eV to σ^* state. In the ELNES spectrum, however, the peak A seems to have σ^* component, in other word, the peak A remains in the spectrum even under q⊥c condition. From DV-Xα calculations, it is found that this peak does not have any σ^* component. This has been confirmed by the XANES measurements shown in Figs.21 and 22 and also by recent x-ray Raman-scattering spectroscopy[44]. The cluster calculation suggests that π^* component also exists in the peak B, corresponding to the measured spectra under q//c condition. The theoretical and experimental spectra for c- and w-BN are indicated in Fig.23. The difference between the measured spectra of two polytypes is not very clear. The theoretical spectra, however, suggest that it is likely possible to identify these polytypes by ELNES or XANES spectrum with a higher resolution.

The DV-Xα cluster calculation has also been applied to investigations of local chemical bondings at dopant-modified grain boundary in $SrTiO_3$[45] and around Si impurity in MgO[46], through the theoretical analysis of ELNES spectra.

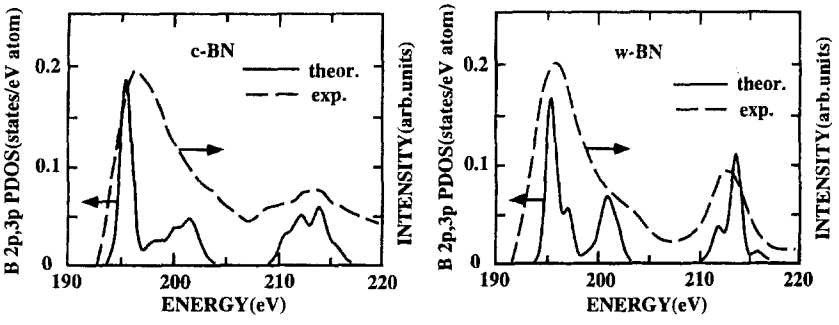

Fig.23 Theoretical and experimental[40] B-K ELNES for c- and w-BN

7. Conclusion

DV-Xα molecular orbital calculation is demonstrated to be very efficient for theoretical analysis of the photoelectron and x-ray spectroscopies. For photoelectron spectroscopy, Slater's transition state calculation is very effective to give an accurate peak energy, taking account of the orbital relaxation effect. The more careful analysis including the spin-polarized and the relativistic effects substantially improves the theoretical results for the core level spectrum. By consideration of the photoionization cross section, better theoretical spectrum can be obtained for the valence band structure than the ordinary DOS spectrum. The realistic model cluster reproduce very well the valence state spectrum in details.

For x-ray emission spectroscopy(XES), the accurate peak intensity can be evaluated by the calculation of dipole transition matrix, though the partial DOS usually give a good approximation. The theoretical analysis by the cluster model calculation is exhibited to be very useful for the investigations of the

chemical effects on atomic x-ray spectrum, the local structure in boron oxide, and the origin of the satellite peak from boron nitride.

X-ray absorption near edge structure(XANES) and electron energy loss near edge structure(ELNES) show similar spectra, thus almost the same theoretical analysis is valid both for these spectroscopies. The careful analysis including higher excited atomic orbitals in the basis set reproduce very well the spectral structure even in details. The core-hole effects are sometimes very important in the excited state electronic state. The theoretical analysis by the cluster model calculation provides very useful information on the local electronic property and the micro structure.

Acknowledgement

The present work was supported by a Grant-in-Aid for Science Research from the Ministry of Education, Sports, Science and Culture of Japan.

References

(1) K.Siegbahn, C.Nording, G.Johaansson, J.Hedman, K.Hamrin, U.Gelius, T.Bergmark, L.O.Werme, R.Mann, Y.Baer,"ESCA Applied to Free Molecules",North-Holland, 1969
(2) A.Meisel, G.Leonhardt, R.Szargen, "Rontgenspektren and Chemische Bindung", Geist & Portig, Leipzig, 1977.
(3) J.Stohr, "NEXAFS Spectroscopy", Springer-Verlag, 1992
(4) N.D.Browning, M.F.Chisholm, and S,J,Pennycook, Nature **366**(1993), 143
(5) H.Adachi, M.Tsukada and C.Satoko, J.Phys.Soc.Jpn. **45**(1978) 875
(6) H.Adachi, T.Mukoyama and H.Nakamatsu, Advance in X-Ray Analysis **23** (1992) 19

(7) J.C.Slater, Phys.Rev. **81**(1951) 385
(8) J.C.Slater,"Quantum Theory of Molecules and Solids", vol.4, McGraw-Hill,1974
(9) H.Adachi, S.Shiokawa, M.Tsukada, C.Satoko and S.Sugano, J. Phys. Soc. Jpn. **47**(1979) 1528
(10) A.Rosen and D.E.Ellis, J.Chem.Phys. **62**(1975) 3039
(11) K.Ogasawara, T.Ishii, Y.Ito, H.Ida, I.Tanaka and H.Adachi, Jpn. J. Appl. Phys. **37**(1998) 4590
(12) U.Gelius, "Electron Spectroscopy", ed. by D.A.Shirley, North-Holland, 1972, p.311
(13) J.H.Scofield, J.Electr. Spectr.Relat.Phenom. **8**(1976) 129. J.J.Yeh and I.Lindau, Atomic Data and Nuclear Data Table **32**(1985) 1
(14) H.Adachi, Advance in Quantum Chemistry **29**(1997) 179
(15) D.E.Ellis and G.S.Painter, Phys.Rev. **B2**(1970) 2887
(16) H.Adachi and K.Taniguchi, J.Phys.Soc.Jpn. **49**(1980) 1944
(17) H.Adachi, A.Rosen and D.E.Ellis, Molecular Phys. **33**(1977) 199. J.Onoe, K.Takeuchi, H.Nakamatsu, T.Mukoyama, R.Sekine and H.Adachi, J.Electr.Spectr. **60**(1992),29
(18) H.Nakamatsu, H.Adachi and S.Ikeda, J.Electr.Spectr. **24**(1981) 149
(19) T.Sasaki and H.Adachi, J.Electr.Spectr. **19**(1980) 261
(20) I.Cserny, L.Kover, H.Adachi, I.Tanaka, R.Sanjines, C.Coluzza and G.Margaritondo, Surface and Interface Analyysis **23**(1995) 477
(21) G.Sakane, T.Shibahara and H.Adachi, J.Cluster Science **6**(1995) 503
(22) T.Mukoyama, K.Taniguchi and H.Adachi, Phys.Rev. **B34**(1986) 3710. T.Mukoyama, K.Taniguchi and H.Adachi, Phys.Rev. **B41**(1990) 8118
(23) J.Kawai, S.Tadokoro,Y.Myramatsu, S.Kashiwagi, H.Kohzuki, M.Motoyama, H.Kato and H.Adachi, Physca B **208&209**(1995) 251. Y.Muramatsu, M.Oshima, J.Kawai, S.Tadokoro, H.Adachi, A.Agui, S.Shin, H.Kato, H.Kohzuki and M.Motoyama, Phys. Rev. Letters, **76** (1996) 3846
(24) J.Kawai, K.Maeda, I.Higashi, M.Takami, Y.Hayashi and M.Uda, Rhys. Rev. **B42**(1990) 5693
(25) M.Kobayashi, I.Higashi, G.Brodhag and F.Thevenot, J.Mater.Sci. **28**(1993) 2129
(26) M.Morishita, K.Koyama, M.Morinaga and H.Adachi, Mater. Trans. JIM **38**(1997) 724
(27) H.Nakamatsu, T.Mukoyama and H.Adachi, Chem.Phys. **143**(1990) 221
(28) S.Bodeur and J.M.Esteva, Chem.Phys. **100**(1985) 415
(29) H.Nakamatsu, T.Mukoyama and H.Adachi, Jpn. J.Appl. Phys., **32** (1993), 23
(30) H.Nakamatsu, H.Adachi and T.Mukoyama, Bull. Institute for Chem. Resear. Kyoto Univ. **72**(1994), 45

(31) S.Yamashita, M.Fujikawa, Y.Kato, T.Yamaguchi, H.Wakita and H.Adachi, Advance in Quantum Chemistry **29**(1997) 357
(32) I.Tanaka, J.Kawai and H.Adachi, Phys.Rev. **B52**(1995) 11733
(33) I.Tanaka and H.Adachi, J.Phys. D:Appl.Phys.**29**(1996) 1725
(34) I.Tanaka and H.Adachi, Phys.Rev. **B54**(1996) 4604
(35) H.Kanda, M.Yoshiya, F.Oba, K.Ogasawara, H.Adachi and I.Tanaka, Phys.Rev. **B58**(1998) 9693
(36) H.-J.Kleebe, M.K.Cinibulk, I.Tanaka, J.Bruley, J.S.Vetrano and M.Ruhle, " Tailoring of Mechanical Properties of Si_3N_4 Ceramics" , Academic Publishers,1994,p.259. I.Tanaka, H.- J.Kleebe, M. K. Cinibulk, J.Bruley, D.R.Clarke and M.Ruhle, J.Amer.Ceram.Soc. 77(1994) 911
(37) H.Gu, M.Geh, S.Stemmer, H.Mullejans and M.Ruhle, Ultramicroscopy **59**(1995) 215
(38) H.Gu, R.M.Cannon and M.Ruhle, J. Mater. Res. **13**(1998) 376
(39) M.Yoshiya, I.Tanaka and H.Adachi, J.Am.Ceram.Soc. **82**(1999) 3231. M.Yoshiya, I.Tanaka and H.Adachi, Key Eng. Mater. **175-176** (1999) 107
(40) H.K.Schmid, Microsc. Microanal. Microstruc., **6**(1995) 99
(41) M.Jaouen, G.Hug, V.Gonnet, G.Demazeau and G.Tourillon, Microsc. Microanal. Microstruc. **6**(1995) 127
(42) J.Moscovici, G.Loupias, Ph.Parent and G.Tourillon, J. Phys. Chem. Solids **57**(1996) 1159
(43) I.Tanaka, H.Araki, M.Yoshiya, T.Mizoguchi, K.Ogasawara and H.Adachi, Phys.Rev. **B60** (1999) 4944
(44) N.Watanabe, H.Hayashi, Y.Udagawa, T.Takeshita and H.Kawata, Appl.Phys.Letters **69** (1996) 1370
(45) I.Tanaka, T.Nakajima, J.Kawai, H.Adachi, H.Gu and M.Ruhle,Phil. Mag. Letters **75**(1997) 21
(46) T.Mizoguchi, I.Tanaka, M.Yoshiya, F.Oba and H.Adachi, J. Phys.: Condens. Matter **11**(1999) 5661

Extended Analysis of Satellite Structures in Particle Induced X-ray Emission Spectra Using Molecular Orbital Calculations

M. Uda [a, b]

[a] *Department of Materials Science and Engineering, Waseda University 3-4-1 Ohkubo, Shinjuku-ku, Tokyo 169-8555, Japan*
[b] *Laboratory for Materials Science and Technology, Waseda University 2-8-26 Nishiwaseda, Shinjuku-ku, Tokyo 169-0051, Japan*

(Received September27, 1999)

Methods for estimating intensity distributions of X-ray satellite spectra induced by accelerated ions with energies of a few MeV/amu are reviewed, where the orbitals responsible for X-ray emission are written in the molecular frame, not in the atomic frame.

The ionization cross section is written here in the frame of the direct Coulomb interaction and the shake process. The following two factors are taken into account: (1) changes in the number of orbital electrons due to molecular orbital formation and (2) deviation of the number of electric charges on the projectile ion from the nuclear charge Z. Here the semi-classical approximation (SCA) has been used to calculate the Coulomb interaction between the projectile ion and the orbital electrons. In order to estimate the intensity of X-rays emitted from multiply ionized states changes in the fluorescence yield from the yield of isolated atoms caused by resonant orbital rearrangement (ROR), were also taken into account. Furthermore the energy loss of the projectile ions and absorption of emitted X-rays in the material were taken into account. The agreement between the calculated and the observed X-ray satellite intensities is satisfactory when we use all the correction terms mentioned above.

KEY WORDS : PIXE, X-ray satellite, Electronic structure, Molecular orbital calculation, DV-Xα, Resonant orbital rearrangement

e-mail : muda@mn.waseda.ac.jp

ADVANCES IN QUANTUM CHEMISTRY, VOLUME 37

0065-3276/01 $35.00

1.Introduction

Particle induced X-ray emission (PIXE) was first developed by Johansson et al. in 1970 as a multi-element-analytical method with high sensitivity[1]. The advantages of this method, over similar kinds of analytical methods, i.e. X-ray photoelectron spectroscopy(XPS), X-ray fluorescence(XRF), electron probe micro-analysis(EPMA) and Auger electron spectroscopy(AES), lie in its high signal-to-background ratio, its practicable performance both in vacuum and arbitrary gas atmospheres, including air and inert gases, the short time for analysis, the small amounts of the samples that are needed, and in the fact that it has almost the same sensitivity to all the elements detected [2].

In the case of an ion impacting an atom, the ionization cross section and the X-ray emission yield are almost proportional to the square of the atomic number Z of the projectile ion. Therefore it appears that it is advantageous to use high Z elements rather than low Z ones as projectiles. However, in most PIXE analyses, H and He ions with energies of a few MeV/amu have been used. This is because, in the X-ray spectra, low Z or light ions produce characteristic X-rays composed mainly of the diagram line, but high Z or heavy ions produce intense satellite lines together with the diagram line. Here the diagram lines are X-rays emitted from initial states with the only one vacancy in an inner shell, while the satellite lines are X-rays emitted from initial states with multiple vacancies in inner and outer shells. The diagram lines are used in elemental analysis, but the satellite lines obstruct elemental analysis. Therefore heavy ion impacts lead to difficulty in estimating the X-ray intensity originated from the diagram line alone. Thus light ions such as protons and α particles have widely been used in PIXE analysis.

The electronic structures of atom-aggregates, i.e. molecules, liquids, solids, and so on, have also been analyzed using the energy shifts and changes in intensity distributions of the emitted spectra from atomic spectroscopy methods like XPS, XRF, EPMA and AES. However, PIXE is one of the best methods for emphasizing the differences in the electronic structures of atoms embedded in different chemical environments. This is because of the fact that X-ray satellites are sensitive to change in chemical environment and they are emphasized in heavy ion induced PIXE spectra [3,4]. Such positive utilization of X-ray satellite spectra enhances the value of PIXE analysis considerably. However, except for some papers written by the present author's group [5-8], there have been no reports concerned with the analysis of X-ray satellite structures in the molecular orbital frame. In our previous papers molecular orbital calculations were used to explain a single phenomenon such as ionization,

the splitting of orbitals into components and the rearrangement of orbitals during ionization.

A series of theoretical treatments for combining these phenomena, concerned with how to reproduce the intensity distribution of the X-ray satellites, will be given in this review article. Here we have estimated the ionization cross section using the semi-classical approximation (SCA), which describes the Coulomb interaction acting between a projectile ion and the orbital electrons of the target atom, when an X-ray transition occurs between two inner shells. The shake process, where atomic electrons are excited or ionized due to the sudden creation of an inner-shell vacancy, was also considered in regard to the simultaneous production of multiple vacancies in inner and outer shells. The projectile's energy loss and the self-absorption of emitted X-rays by the target were also taken into account. When the atomic number of the projectile is larger than 6 we replaced the nuclear charge of the projectile with the effective or equilibrium charge, in a given target material, of the projectile. The ionization cross section was rewritten in the molecular orbital frame using the coefficients of the molecular orbitals which were involved in the X-ray transition. The rearrangement of the molecular orbitals during ionization, which occurs when a resonant condition between two initial states is fulfilled, was also taken into account. This effect leads to a change in the fluorescence yield. At present a variety of X-ray satellite structures have been explained systematically in the molecular orbital frame.

2. Satellite Intensity Distributions Written in the Atomic Frame

2-1. Light ion impacts

An isolated atom has a characteristic set of discrete energy levels. Then if one electron is removed from an inner shell of the atom, electronic relaxation occurs due to one of the outer shell electrons filling the electron hole left in the inner shell. This leads to the emission of a characteristic X-ray. In such cases, only one spectral line, originating from the X-ray transition between an inner shell and one of the discrete outer shells, can be observed. However, when multiple ionization occurs during a single excitation process, as in the case of energetic ion impact, a fine structure or finger pattern is necessarily observed in the spectrum. In PIXE,

energetic ions, such as H^+, He^{n+}, C^{n+}, N^{n+}, O^{n+}, and so on with n=1-4 and with energies of a few MeV/amu have been used for electronic excitation. In such cases, the ionization of the target atom is approximately described in the direct Coulomb interaction frame, and is considered to be almost independent of the interaction the orbital electrons during ionization. This enables us to express K X-ray satellite structure as a superposition of characteristic X-rays emitted from K^1L^n initial states, where K^1L^n denotes a state with one K and n L vacancies. If the X-ray energies are limited to the low range K^1L^0- K^1L^n, then the X-ray intensity is proportional to the ionization cross section of the inner shell electron involved. Then the X-ray satellite structure intensity distribution can be written in the form of $P_{K^1L^1}(b)$, using the binomial equation, where $P_{K^1L^n}(b)$ is the probability for simultaneous ionization of one K and n L orbital electrons localized on a single atom,

$$P_{K^1L^n}(b) = \sum_{l,m} \binom{2}{1} [P_{1s}(b)] [1 - P_{1s}(b)]^{2-1} \times \binom{2}{l} [P_{2s}(b)] [1 - P_{2s}(b)]^{2-l} \times \binom{6}{m} [P_{2p}(b)]^m [1 - P_{2p}(b)]^{6-m}. \quad (1)$$

Here the first factor is the ionization probability for the 1s electrons, the second is for the 2s electrons and the third is for the 2p electrons. b is the impact parameter, l and m are the number of vacancies in the 2s and 2p orbitals respectively, with $n = l + m$, and $\binom{e}{c}$ is the binomial coefficient. The ionization probability $P(b)$ is usually written in the semi-classical approximation (SCA) frame for the ion-atom collision as,

$$P(b) = \int_0^\infty \frac{1}{\hbar^2} \left| \int_{-\infty}^{\infty} e^{i\omega t} \quad \langle \chi_f | V | \psi_i \rangle dt \right|^2 dE_f, \quad (2)$$

where $\omega = (E_f - E_i)/\hbar$, E_f and E_i are, respectively, the final and initial state energies of the target electrons, χ_f is the wave function associated with outgoing ionized electron, V is the direct Coulomb interaction between the projectile ion and an orbital electron of the target atom, ψ_i is the wave function associated with the orbital electron of the target in the initial state, and t is the time, respectively. Here the direct Coulomb interaction potential is expressed as

$$V = \left| \frac{Ze^2}{\vec{R}(t) - \vec{r}} \right|, \tag{3}$$

where Z is the atomic number of the projectile, and $\vec{R}(t)$ and $\vec{r}$ are the coordinates of the projectile and the orbital electron of the target atom, respectively.

The ionization cross section can be written, in terms of the projectile energy, as a product of the ionization probability and the area defined by the impact parameter b, as,

$$\sigma(E) = 2\pi \int_0^\infty b db P(b). \tag{4}$$

Then the multiple ionization cross section, responsible for emitting the emission of the K^1L^n satellite line, is given by

$$\sigma_{K^1L^n}(E) = 2\pi \int_0^\infty b db P_{K^1L^n}(b). \tag{5}$$

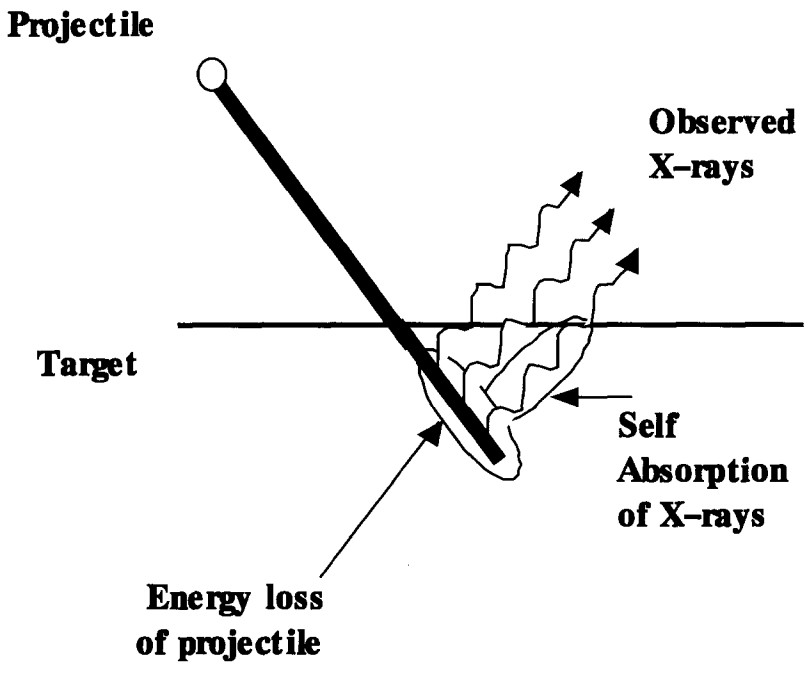

Fig.1. Schematic explanation of the energy loss of projectile ions, and the self-absorption of the emitted X-rays in a target material with medium thickness.

In order to estimate the intensity of the observed X-rays which are emitted from target materials with medium thickness, the energy loss of the projectile ions passing through the target and the self- absorption of the emitted X-rays in the target, as schematically shown in Fig.1, should also be taken into account. The X-ray yield $Y_{K^1L^n}$ for a given K^1L^n satellite line emitted from an element in the target can now be expressed as

$$Y_{K^1L^n} \propto \omega_{K^1L^n} \int_{E_i}^{E_0} \frac{\sigma_{K^1L^n}(E) T_{K^1L^n}(E')}{S(E)} dE, \qquad (6)$$

and

$$T_{K^1L^n}(E') = \exp\left(-\left(\frac{\mu}{\rho}\right)\frac{\cos\alpha}{\sin\theta}\int_{E_i}^{E_0}\frac{1}{S(E)}dE\right),$$

where $\omega_{K^1L^n}$ is the K^1L^n state fluorescence yield, E is the projectile energy, E_i and E_0 are, respectively, the incident and final projectile energies, $T_{K^1L^n}$ is the transmission rate of the K^1L^n X-ray with energy E', $\left(\frac{\mu}{\rho}\right)$ is the mass attenuation coefficient of the X-ray produced by the projectile in the target, α is the angle between the incident projectile and the target surface normal of, θ is the take-off angle of the emitted X-ray, and $S(E)$ is the stopping power of the matrix for the projectile with energy E in the target.

Generally, for light ion impacts, the observed intensity distributions of satellite structures or finger patterns can be reproduced by eq. (6). Shown in Fig. 2 are examples for the impact of H^+ on K and Cr, and the impact of

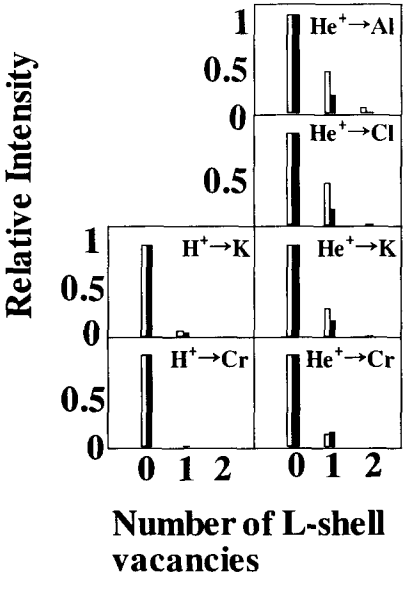

Fig. 2. Schematic K X-ray spectra induced by 1.4 MeV/amu H^+ and He^+ impact. Here white lines indicate observed spectra [9] and black lines spectra calculated in the direct Coulomb interaction frame.

He^{2+} on Al, Cl, K and Cr. The agreement between the observed and calculated satellite intensity distributions is fair but not satisfactory. Therefore in order to reproduce multiply ionized states the shake process must be added to the direct Coulomb process. Now the multiple ionization cross section $\sigma^{s}_{K^1L^n}$ taking into account the shake process can be rewritten as,

$$\sigma^{s}_{K^1L^0} = (1 - P^{0\to1}_{shake})\sigma_{K^1L^0} \tag{7}$$

for the K^1L^0 singly ionized state, and

$$\sigma^{s}_{K^1L^n} = (1 - P^{n\to n+1}_{shake})\sigma_{K^1L^n} + P^{n-1\to n}_{shake}\sigma_{K^1L^{n-1}} \tag{8}$$

for the K^1L^n multiply ionized states. Here $P^{s\to t}_{shake}$ is the shake probability for a change in an L shell vacancy state from s to t. In this section, we assume $P^{s\to t}_{shake}$ can be approximated by $P^{0\to1}_{shake}$, and we refer to the $P^{0\to1}_{shake}$ = 0.1845 value calculated by Mukoyama and Taniguchi[10]. As shown in Fig. 3, if we replace $\sigma_{K^1L^n}$ in eq .(6) by $\sigma^{s}_{K^1L^n}$ defined by

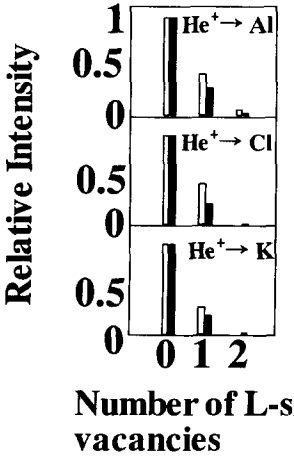

Fig. 3. Schematic K X-ray spectra induced by 1.4 MeV /amu He^+. Here white lines indicate observed spectra [9] and black lines calculated, where the direct Coulomb interaction and the shake process for multiple ionization have been taken into account.

eq.(8), the observed Al, Cl, and K satellite structures, induced by He^+ impact, are reproduced well. This suggests that satellite structures induced by light ion impacts can only be explained well in the atomic frame, when the X-ray transition is concerned only with the inner shells.

2-2. Heavy ion impacts

For heavy ion impacts on targets of medium thickness, the atomic number Z, that is, the nuclear charge of the projectile ions in eq. (3), should be replaced by the effective or equilibrium charge of the projectile ions. This is because the projectile looses or gains some orbital electrons, and reaches its equilibrium charge $\bar{q}$, after passing through a certain thickness of the target material. An empirical formula for the estimation of $\bar{q}$ [11] is given by,

$$\bar{q} / Z_1 = \left[1 - \exp\left(-1.25X + 0.32X^2 - 0.11X^3\right)\right] \times \left[1 - 0.0019\left(Z_2 - 6\right)\sqrt{X} + 0.00001\left(Z_2 - 6\right)^2 X\right] \qquad (9)$$

where Z_1 and Z_2 are the atomic number of the projectile and the target, respectively, X is the reduced ion velocity $\left(X = v / 3.6 \times 10^8 Z_1^{0.45}\right)$, and v is the projectile velocity in cm/sec.

The observed satellite structure intensity distributions for heavy ion $(Z \geq 6)$ impacts such as C^{4+} and O^{4+} on K and Cr are shown in Fig.4. They are shifted to lower numbers of L shell vacancies compared with results calculated from eq. (1). However, as shown in Fig. 5, these distributions can be well explained by modifying eq. (1) by replacing Z in eq. (3) by the appropriate effective charges (E.C.), i.e. +5.5~+5.8 for C ion impact and +6.0~+6.8 for O ion impact on Al, Cl, K and Cr. The effective charges estimated here are almost the same as the equilibrium charges $\bar{q}$ estimated from eq.(9). The intensity distribution of the X-ray satellite spectra emitted from multiply ionized K^1L^n states has been explained in the atomic frame, when the X-ray transition is concerned only two inner shells. We considered here the energy loss of the projectile, the self-absorption of emitted X-rays in the target, and also the change in the effective charge of the projectile in the target.

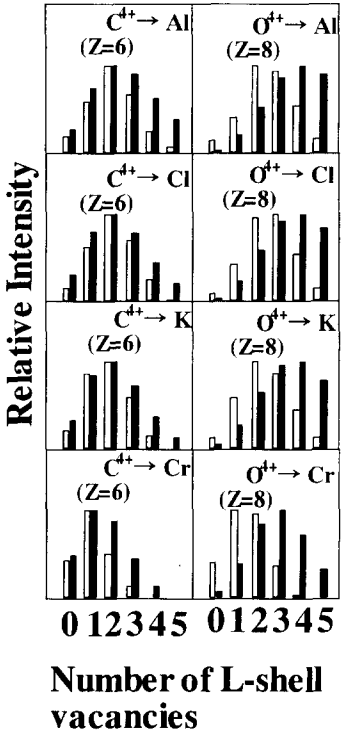

Fig. 4. Schematic spectra for observed (white) [9] and calculated (black) K1Ln X-ray satellites. The incident ions were 1.4 MeV/amu C^{4+} and O^{4+}, and in the X-ray satellite intensity calculations the nuclear charges were assumed to be 6 and 8, respectively.

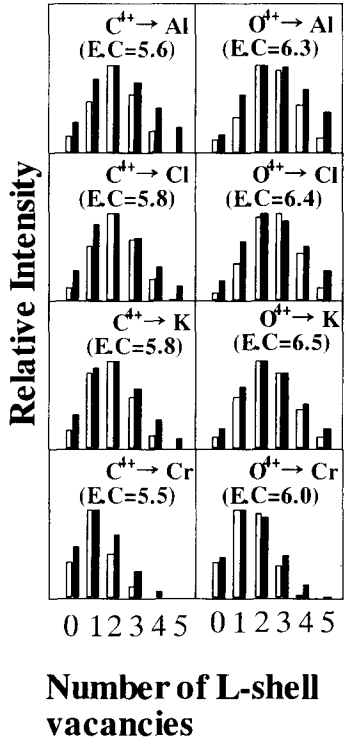

Fig. 5. Comparison between observed X-ray satellite spectra, same as those in Fig. 4, and calculated, where in the calculations the projectile nuclear charges were assumed to be the effective charge (E.C) numbers shown in parentheses.

3. Change in the Ionization Cross Section and Splitting of theK^1L^0 Line due to Molecular Orbital Formation

The ionization cross section can be written in the atomic frame and estimated using SCA, as explained in the previous chapter, for all the X-ray transitions in isolated atoms, and for the X-ray transitions which occur between two inner shells for atoms in atom-aggregates. However, for atom-aggregates, if valence shells are involved in the X-ray transitions then we have to take molecular orbital effects on the ionization cross sections into account. In such cases, ψ_i **in eq. (2) must be replaced by the wave function for a molecule** ψ_i^M **which can be expressed as a linear combination of all the atomic orbitals** ϕ_j **concerned,**

$$\psi_i^M = \sum_j C_j \phi_j , \tag{10}$$

where the C_j **is the partial coefficient. The final state wave function** χ_f **for a molecule involved in an X-ray transition is of the same form as that for an isolated atom. This is because the outgoing ionized electron can be considered as a free electron not an electron bound in a molecular orbital.**

Since the probability to ionize orbital electrons originating from neighboring atoms is negligible on the atom of interest, i.e. a central atom, eq. (10) can be rewritten as,

$$\psi_i^M \approx C_C \phi_C , \tag{11}$$

where C_C **and** ϕ_C **are the coefficient and the wave function for the central atom, respectively. In order to confirm the validity of the above**

calculations written in the molecular orbital frame, we may compare the series of observed F K^1L^n spectra, emitted from MgF_2, FeF_2, CoF_2, NiF_2 and ZnF_2 with a rutile structure shown in Fig. 6, with calculated spectra. For this purpose a DV-X α molecular orbital calculation [13] was performed to estimate C_j in eq. (10). We used a $(FM_3)^{5+}$ cluster with C_{2v} symmetry, and a well potential of depth -3 Hartree and of width 0.67 of the M-F distance. Here M denotes Mg, Fe, Co, Ni and Zn.

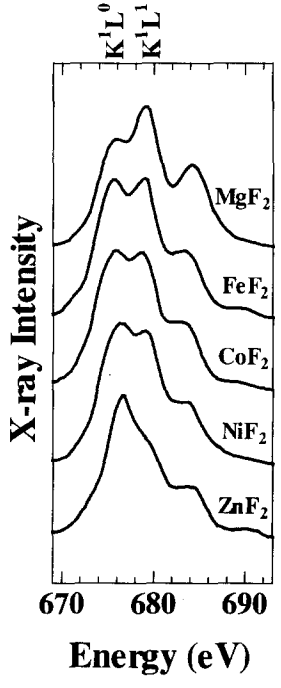

Fig. 6. F Kα satellite spectra induced by 2 MeV H_e^+ [12].

In the ground K^0L^0 state of the above fluorides F 2p orbitals mix with the outer orbitals of the metals to form the valence band. An example is $18a_1$ and $15a_1$ for the NiF_2 A_1 symmetry block shown in Fig. 7(a). Here the

K^0L^0 state is an initial state responsible for emitting a part of the K^1L^0 line. The same kind of orbital mixing is also found in B_1 and B_2 blocks. However, the F 2p in the K^0L^1 ionized state, the F 2p orbital is separated from the metal orbitals. The K^0L^1 ionized state, shown in Fig. 7(b) as $15a_1$, is an initial state responsible for emitting a part of the K^1L^1 line. This is because, when one vacancy is created in the L shell of the F atom, the molecular orbital composed of the F 2p becomes much deeper and gets separated from the orbitals composed of the ligand metal outer orbitals. This means that the molecular orbital composed of the F 2p at the K^0L^1 state behaves as the orbital of the isolated atom. This is also true for the other two blocks. Therefore, in the following discussions, the F K^1L^0 X-ray line will be described in the molecular orbital frame, while the F K^1L^1 X-ray line will written in the atomic frame.

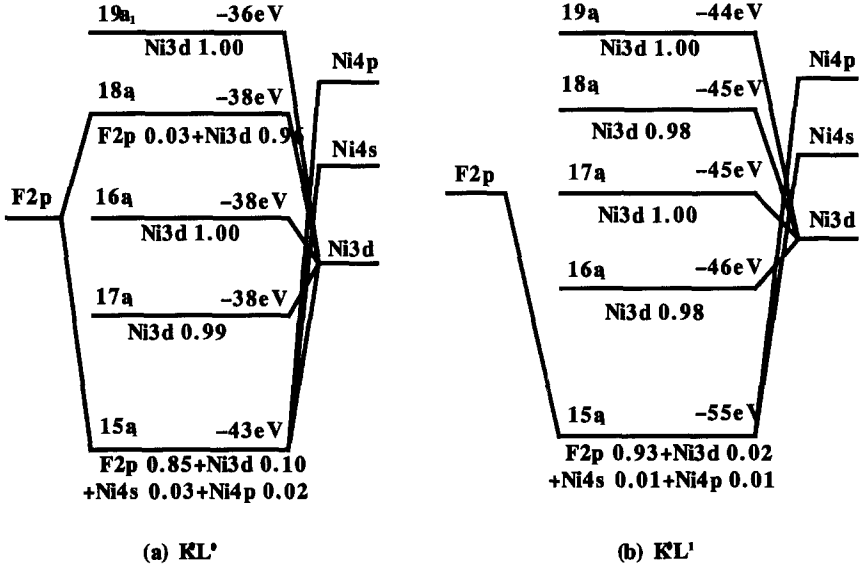

Fig. 7. Molecular orbital diagrams for NiF_2 [14] in the K^0L^0 ground state (a), and the K^0L^1 state (b). K^0L^0 and K^0L^1 are considered to be initial states responsible for emitting the K^1L^0 and K^1L^1 X-rays, respectively. Here the orbital components are expressed as the sum of the squares of the partial expansion coefficients and of the overlap populations for the orbitals.

Table I
The square of the partial coefficients in the ground K^0L^0 state for the outer orbitals composed, at least in part, of F 2p. Also shown in parentheses are the energies (eV), relative to the energies of the highest occupied molecular orbitals (HOMO) for MgF_2, FeF_2, CoF_2, NiF_2 and ZuF_2.

MO	Square of partial coefficient $(C_j^{(k)})^2$				
	MgF_2	FeF_2	CoF_2	NiF_2	ZnF_2
8b2					0.54 (0)
7b2		0.02 (0)	0.04 (0)	0.04 (1)	0.31 (1)
5b2		0.96 (5)	0.93 (4)	0.91 (4)	0.14 (2)
3b2	0.99 (0)				
14b1					0.20 (0)
13b1				0.06 (0)	0.25 (1)
10b1		0.91 (6)	0.88 (5)	0.86 (5)	0.48 (3)
6b1	0.97 (1)				
20a1					0.16 (0)
18a1		0.02 (0)	0.03 (0)	0.03 (1)	0.13 (1)
15a1		0.90 (7)	0.87 (6)	0.85 (6)	0.62 (3)
10a1	0.96 (2)				

The square of the molecular orbital coefficient for the K^0L^0 state is summarized in Table I. Also shown, in parentheses, is the energy (eV) relative to the energy of the highest occupied molecular orbital (HOMO). Here the orbital components are expressed as the sum of the squares of the partial expansion coefficients and of the overlap populations for the orbitals. From Table 1 it is easily seen that the K^1L^0 X-ray line is mainly composed of three components each separated by 1eV. The observed X-ray satellite spectra for MgF_2 and NiF_2 are shown in the solid lines in Figs. 8 and 9. Fig. 8 shows spectra induced by 2 MeV He^+ impact, and Fig. 9 by 84 MeV N^{4+} impact. These excitation conditions produce mostly direct Coulomb ionization, not shake ionization. The observed spectra are now deconvoluted into K^1L^n components. The rather broad K^1L^0 line is further deconvoluted into three molecular orbital components each separated by

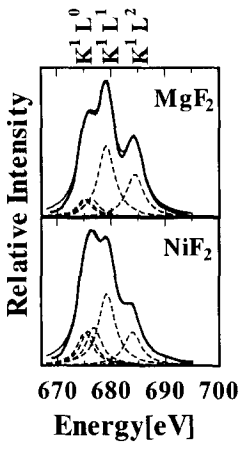

Fig. 8. Observed F Kα satellite spectra (solid line) excited by 2 MeV He^+ [12]. The deconvolution of the spectra is shown in the dashed lines.

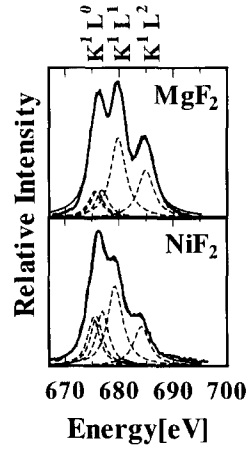

Fig. 9. Observed F Kα satellite spectra (solid line) excited by 84 MeV N^{4+} [4].The deconvolution of the spectra is shown in the dashed lines.

about 1eV each. The agreement between calculated and observed profiles for the K^1L^0 line is satisfactory. This suggests that the use of the partial coefficients for some of the molecular orbital components is indispensable if the valence electrons are involved in the X-ray transition. However, when we estimate the relative intensities K^1L^1/ K^1L^0 using eq.(6), where $\sigma_{K^1L^n}$ is written using eqs.(2), (5) and(11), we get 1.24 and 1.11 for 2MeV He^+ impacts, and 1.01 and 0.93 for 84MeV N^{4+} impacts on MgF_2 and NiF_2, respectively. These relative calculated intensities can be compared with the observed results, which are 1.41, 0.66, 1.03 and 0.59 (in the same order as described above). The agreement between the calculated and observed results is fair but not satisfactory. This suggests that an additional correction must be made, that is - resonant orbital rearrangement (ROR) during ionization.

4. Resonant Orbital Rearrangement during Ionization

Satellite X-ray has been described, for convenience, using a two-step process, i.e. ionization followed by shake. In each step the energy and the momentum are conserved. Here a shake is defined as the excitation of an outer shell electron to an unoccupied and/or the continuum energy level during ionization. We have no difficulty in explaining satellite X-ray intensity and energy, using the two-step process, when the X-rays are emitted through transitions between two inner shells.

Chemical bonding effects are strongly reflected in PIXE X-ray satellite spectra when valence electrons are involved in the transitions. Such spectra have been used for the chemical specification of atom-aggregates [3,4]. Some typical X-ray spectra, which are induced by 5.5MeV He^+[15], are shown in Fig.10. The intensity ratios K^1L^1/ K^1L^0 are very different from one another. These intensity distributions have not yet been explained through the direct Coulomb and shake ionization processes alone, even when written in the molecular frame. The results of calculations based on the above two processes are shown in Fig.11. They are very different from the observed distributions. Therefore we need to introduce two additional factors in order to explain the observed results, they are - resonant orbital rearrangement (ROR), and fluorescence yield, which will be discussed later. In this case, however, the above mentioned conservation rule does not hold. This is because the change in the K^1L^1 intensity can not be explained within the frame of the direct Coulomb and the shake ionization processes. This means that, to be exact, we must describe such a process by the one-step process of ionization accompanied by the orbital rearrangement. However, this one-step process can, fortunately, be replaced by a conventional two-step process, if we assume that each excitation process in the two-step process conserves the energy even if it does not necessarily conserve the momentum.

The present author proposed an the approximation method to explain the deviation of the X-ray satellite spectra intensity distributions from those described by eqs.(2),(5),(8) and (10), which we call "Resonant Orbital Rearrangement (ROR)" [6]. ROR was first used to explain the anomalous intensity distributions in F Kα satellite spectra which are emitted from a series of alkali-fluorides. Here resonance occurs during F 1s ionization between the highest occupied molecular orbital (HOMO) in the K^0L^0 state and HOMO in the (K^1L^1+3s) state corresponding to the lowest unoccupied molecular orbital (LUMO) in the K^0L^0 state. This leads to a reduction in the K^1L^1 X-ray satellite intensity and to an increase in the K^1L^0 X-ray diagram line intensity. Here (K^1L^1+3s) denotes the state with one vacancy in K shell and one vacancy in L shell and one electron in a 3s

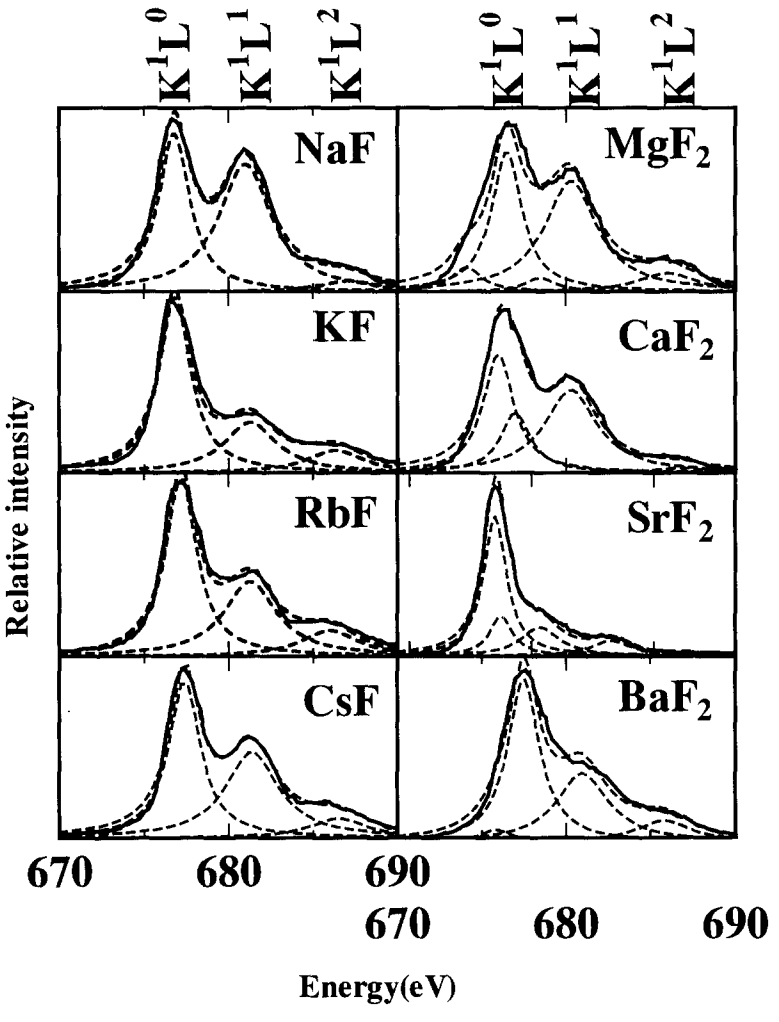

Fig. 10. Observed F Kα spectra (solid lines) excited by 5.5 MeV He^+ [15].The deconvolution of the spectra is shown in the dashed Lines.

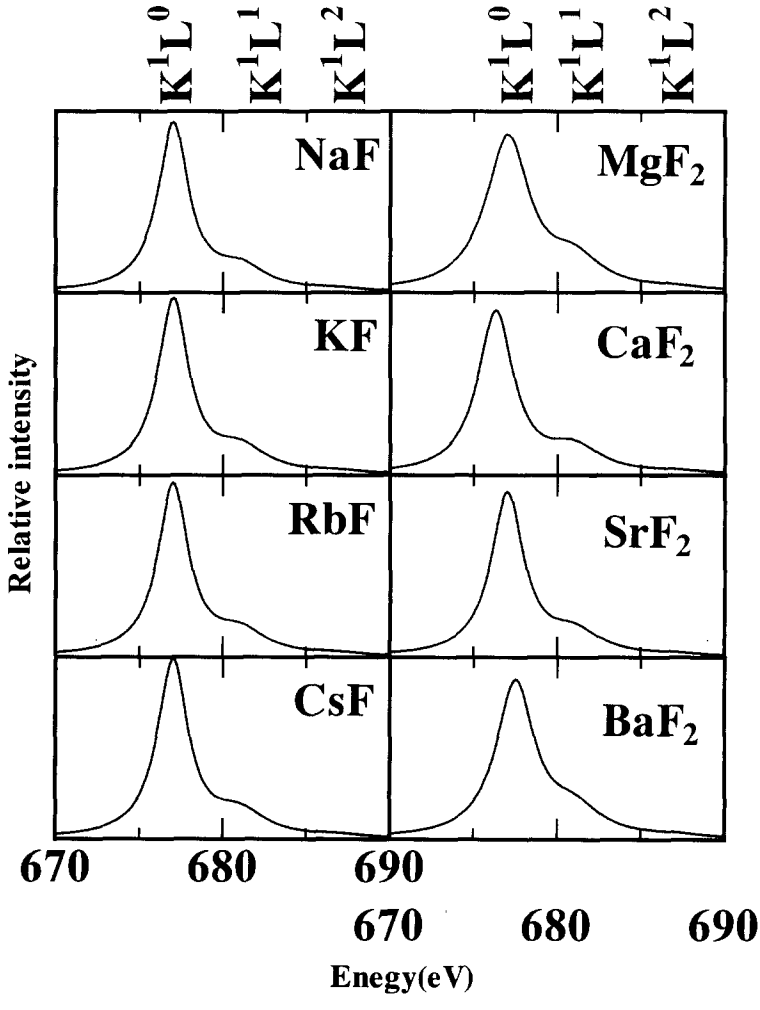

Fig. 11. Calculated F Kα spectra (solid lines) excited by 5.5 MeV He^+ impact, where the direct Coulomb interaction and the shake Prcoesses are taken into account.

level. Furthermore, ROR is not only valid for F 1s ionization but also for shallow inner shell ionization, the schematic drawing of which is shown in Fig.12. The ROR mechanism has been discussed in detail elsewhere[6].

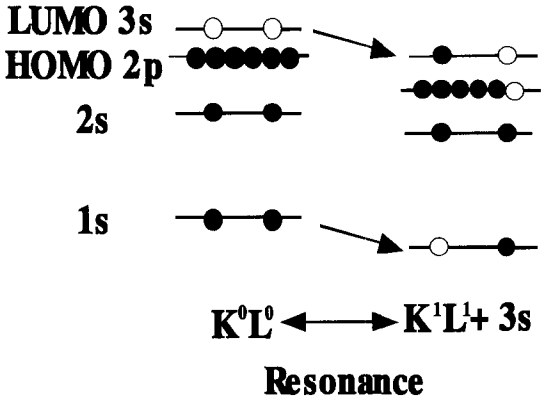

Fig.12. "Resonant Orbital Rearrangement" between the HOMO in the K^0L^0 state and the HOMO in the (K^1L^1+3s) state for an element with Z=9 or less. This is a kind of excitation of an electron from the HOMO to the LUMO during 1s ionization.

Typical photon induced X-ray spectra, emitted from NaF, KF, RbF and CsF, are shown in Fig.13. The intensity distributions of these spectra can be explained by taking only the shake and ROR processes into account, because they are free from the satellite X-rays emitted through the direct Coulomb ionization. Then photon induced satellite spectra can be used, in the following manner, to estimate the ion-induced or particle induced X-ray satellite intensities without any complicated calculations. This is because the excitation process in particle induced X-ray emission (PIXE) can be described by a superposition of the direct Coulomb, the shake and ROR processes. Here the shake and ROR processes are common to both photon- and particle- induced X-ray emission spectra, allowing utilization of the same ROR probability to explain both spectra.

In the case of PIXE for thin target materials, the X-ray intensity emitted from the K^1L^n initial state, $I^{PIXE}_{K^1L^n}$ can be written, from eqs.(7) and (8), with the aid the intensities observed from the photon induced X-ray

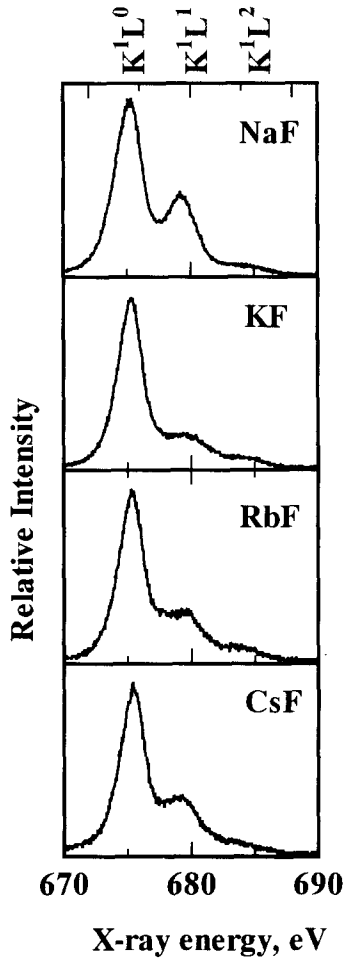

Fig. 13. Observed F Kα spectra induced by photon impact [6].

spectra $I^{XRF}_{K^1L^n}$ **as,**

$$I^{PIXE}_{K^1L^0} \propto \left(1 - \frac{I^{XRF}_{K^1L^1} + I^{XRF}_{K^1L^2} + \cdots}{I^{XRF}_{K^1L^0} + I^{XRF}_{K^1L^1} + I^{XRF}_{K^1L^2} + \cdots}\right)\sigma^{M}_{K^1L^0}$$

$$\propto \left(\frac{I^{XRF}_{K^1L^0}}{I^{XRF}_{K^1L^0} + I^{XRF}_{K^1L^1} + I^{XRF}_{K^1L^2} + \cdots}\right)\sigma^{M}_{K^1L^0} \qquad \textbf{(12)}$$

and

$$I^{PIXE}_{K^1L^1} \propto \frac{I^{XRF}_{K^1L^0}}{I^{XRF}_{K^1L^0} + I^{XRF}_{K^1L^1} + I^{XRF}_{K^1L^2} + \cdots}\sigma^{M}_{K^1L^1} + \frac{I^{XRF}_{K^1L^1} + I^{XRF}_{K^1L^2} + \cdots}{I^{XRF}_{K^1L^0} + I^{XRF}_{K^1L^1} + I^{XRF}_{K^1L^2} + \cdots}\sigma^{M}_{K^1L^0}$$

$$\propto \frac{I^{XRF}_{K^1L^0}}{I^{XRF}_{K^1L^0} + I^{XRF}_{K^1L^1} + I^{XRF}_{K^1L^2} + \cdots}\sigma^{M}_{K^1L^1} + \frac{I^{XRF}_{K^1L^1}}{I^{XRF}_{K^1L^0} + I^{XRF}_{K^1L^1} + I^{XRF}_{K^1L^2} + \cdots}\sigma^{M}_{K^1L^0}$$

(13)

with the condition $I^{PIXE}_{K^1L^1} >> I^{PIXE}_{K^1L^2}$, **where** $\sigma^{M}_{K^1L^0}$ **and** $\sigma^{M}_{K^1L^1}$ **are, respectively, the ionization cross sections for the production of K^1L^0 and K^1L^1 states due to the direct Coulomb interaction for a molecule. Thus for a thin target, the calculated relative intensities** $I^{PIXE}_{K^1L^1} / I^{PIXE}_{K^1L^0}$ **can be expressed as**

$$\frac{I^{PIXE}_{K^1L^1}}{I^{PIXE}_{K^1L^0}} = \frac{\sigma^{M}_{K^1L^1}}{\sigma^{M}_{K^1L^0}} + \frac{I^{XRF}_{K^1L^1}}{I^{XRF}_{K^1L^0}} \qquad \textbf{(14)}$$

If we take into account the changes in fluorescence yields for K^1L^n states with different n, the emitted X-ray intensities too can be expressed, in an alternative way to eqs.(12) and (13), as

$$I_{K^1L^0} = \eta_{K^1L^0}\sigma^M_{K^1L^0}\left(1 - P^{0\to1}_{shake}\right) \qquad (15)$$

$$I_{K^1L^1} = \eta_{K^1L^1}\sigma^M_{K^1L^1}\left(1 - P^{1\to2}_{shake}\right) + \eta_{K^1L^1}\sigma^M_{K^1L^0}P^{0\to1}_{shake} \qquad (16)$$

and

$$I_{K^1L^2} = \eta_{K^1L^0}\sigma^M_{K^1L^2}\left(1 - P^{2\to3}_{shake}\right) + \eta_{K^1L^0}\sigma^M_{K^1L^1}P^{1\to2}_{shake} \qquad (17)$$

where η is the fluorescence yield and $\eta_{K^1L^0} = \eta_{K^1L^2} = 0.013$ for F atoms [16] but $\eta_{K^1L^0} \neq \eta_{K^1L^1}$, because ROR only produces change in $\eta_{K^1L^1}$. If we assume the shake probability P_{shake} to be the same for all $P^{s\to t}_{shake}$ we can determine $\eta_{K^1L^1}$ from observation of the XRF spectra.

This makes it possible to calculate the X-ray intensities for the K^1L^n satellite lines. The relative intensities K^1L^1/K^1L^0 so calculated are shown in Fig.14. Thay compare well with the observed ones shown in Fig.10. Here the partial expansion coefficients C_j appearing in eq.(10) were calculated using the DV-X α molecular orbital (MO) calculation method[13]. They are necessary for the estimation of ψ_i in eq.(2) in the molecular orbital frame. For the MO calculations, we used $(M_6F)^{5+}$ (M denotes the cation) with an NaCl type structure, and a potential well of depth -3.0 Hartree and of width 0.9 atomic distances. We have therefore shown that eqs.(15) and (16), which take into account the direct Coulomb, shake and ROR processes, are suitable for the explanation of a wide variety of K X-ray fine structures due to multiple ionization.

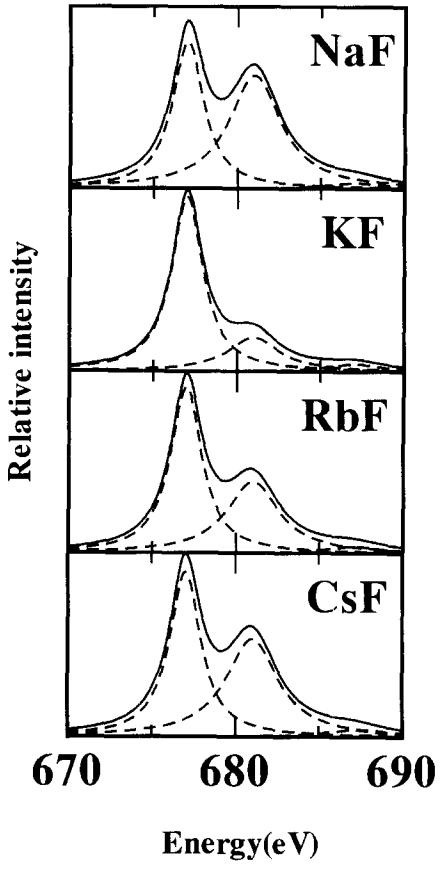

Fig. 14. Calculated F Kα satellite spectra for excitation by 5.5 MeV He^+. Here ROR was taken inti account. They should be compared with the Observed spectra shown in Fig. 10.

Conclusion

The PIXE X-ray satellite intensity distributions which have been described here are in the molecular frame, not in the atomic frame, which are sensitive to changes in the chemical environment of the atom of interest. Together with the direct Coulomb ionization process, the shake and resonant orbital rearrangement (ROR) processes, accompanied by change in the fluorescence yield, were taken into account for the explanation of X-ray satellites originating from multiply ionized states. Furthermore we also considered the effective charge and energy loss of the projectile ions, as well as the absorption of emitted X-rays by the target material, when explaining the X-ray satellite intensity distributions. These corrections are indispensable for the extended analyses of observed X-ray satellite spectra emitted through transitions between inner and valence shells.

Acknowledgement

I am much appreciated to Dr. T. Yamamoto and Prof. T. Mukoyama for their fruitful discussions and some calculations. M. Mochizuki, and T. Takenaga are also acknowledged for their assistance in data preparations.

References

[1] T.B. Johansson, R. Akselsson, S.A.E. Johansson, Nucl. Inst. Meth., 84 (1970) 141
[2] S.A.E. Johansson, J.L. Cambell, PIXE: A Novel Technique for Elemental Analysis, Wiley, N.Y. 1988
[3] M. Uda, H. Endo, K. Maeda, Y. Awaya, M. Kobayashi, Y. Sasa, H. Kumagai, T. Tonuma, Phys. Rev. Lett., 42(1979) 1257
[4] M. Uda, O. Benka, K. Fuwa, K. Maeda, Y. Sasa, Nucl. Instr. Meth., B 22 (1987) 5

[5] M. Mochizuki, T. Yamamoto, S. Nagashima, M. Uda, Nucl. Instr. Meth., 109/110 (1996) 31
[6] M. Uda, T. Yamamoto, T. Takenaga, Adv. Quantum Chem., 29 (1997) 389
[7] M. Uda, T. Yamamoto, Nucl. Instr. Meth., B 150 (1999) 1
[8] M. Uda, T. Yamamoto, T. Takenaga, M. Mochizuki, T. Mukoyama, Nucl. Instr. Meth., B150 (1999) 50
[9] F. Folkmann, Suppl. Z. Phys. D 21S (1991) 262, F. Folkmann, Nucl. Instr. Meth., B 75 (1993) 9
[10] T. Mukoyama, K. Taniguchi, Phys. Rev. A 36 (1987) 693
[11] K. Shima, T. Ishihara, T. Mikumo, Nucl. Instr. Meth., 200 (1982) 605
[12] G. Deconninck, S. Van Den Broek, IEEE Trans. Nucl. Sci. NS 28 (1981) 1404
[13] H. Adachi, M. Tsukada, C. Satoko, J. Phys. Soc. Jpn. 49 (1978) 875
[14] M. Mochizuki, T. Yamamoto, M. Uda, : Application of Accelerators in Research and Intensity, J.L. Duggan, I.L. Morgan (ed) AIP Press, NY (1997) P 245
[15] O. Benka, R.L. Watson, R.A. Kenefick, Phys. Rev. Lett., 47 (1980) 1202
[16] M. Krause, J. Phys. Chem. Ref. Data 8 (1979) 307

XANES spectral changes for discotic liquid crystals of bis[1,2-bis(3,4-dioctyloxyphenyl) ethanedione dioximato]Ni(II)

Mitsutoshi Yokomizo, Tsutomu Kurisaki, Toshio Yamaguchi and Hisanobu Wakita*

Department of Chemistry, Faculty of Science, Fukuoka University, 8-19-1 Nanakuma, Jonan-ku, Fukuoka, 814-0180 Japan.

Yoshio Oka-Inagaki, Kazuchika Ohta

Department of Functional Polymer Science, Faculty of Textile Science and Technology, Shinshu University, Ueda, 386-8567 Japan.

(Received September 22, 1999)

The one-dimensional stacking structures of a liquid crystal Ni complex- [1,2-bis(3,4-dialkoxyphenyl)ethanedione dioximato]Ni(II), [Ni{$(C_8O)_4$dpg}$_2$], which shows thermochromism, (see Fig. 1) have been investigated over a temperature range from room temperature to 220°C by analyzing X-ray absorption near-edge structure (XANES) spectra together with a DV-Xα molecular orbital calculation. The thermochromic character of the complex is discussed through the structural change with temperature in Ni-Ni and Ni to ligand atom interactions.

KEYWORDS: liquid crystal, thermochromism, nickel complex, structure analysis

*Corresponding author, e-mail: wakita@sunsp1.sc.fukuoka-u.ac.jp

ADVANCES IN QUANTUM CHEMISTRY, VOLUME 37

0065-3276/01 $35.00

1. INTRODUCTION

One-dimensional d^8 metal complexes with various kinds of 1,2-dionedioximes show interesting electrical and optical properties at high temperatures (1,2). Recently, Shirotani et al. have investigated the piezochromism of bis(glyoximato)metal(II) complexes (3), and pointed out their possible application as a pressure indicator. In order to obtain discotic liquid crystals of bis(glyoximato)metal(II) complexes exhibiting such a unique chromism, some of us has introduced long-alkyl-substituents into the glyoximato ligands, and successfully synthesized bis(octaalkoxy-substituted diphenylglyoxymato)Ni(II) complexes, bis[1,2-bis(3,4-dialkoxyphenyl)ethane dione dioximato]Ni(II), abbreviated as

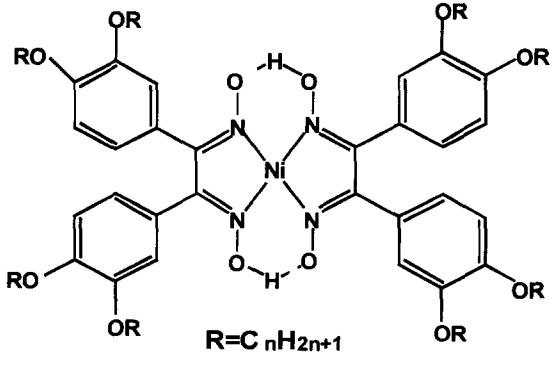

Fig. 1 Molecular structure of $[Ni\{(C_nO)_4dpg\}_2]$.

$[Ni\{(C_nO)_4dpg\}_2]$ with n=4, 8, 12 (Fig. 1) (4-6). It has been found that the $[Ni\{(C_nO)_4dpg\}_2]$ complexes have discotic hexagonal disordered columnar (D_{hd}) mesophases, and that the complexes indicate typical thermochromism and solvatochromism. These particular characteristics are apparently caused by the introduction of long alkoxy chains. Figure 2 shows the molecular stacking structure of the $[Ni\{(C_8O)_4dpg\}_2]$ complex as revealed from X-ray powder analysis (2). It seems interesting to investigate the effect of temperature on the stacking structure of the complex to understand the mechanism of thermochromism for this complex.

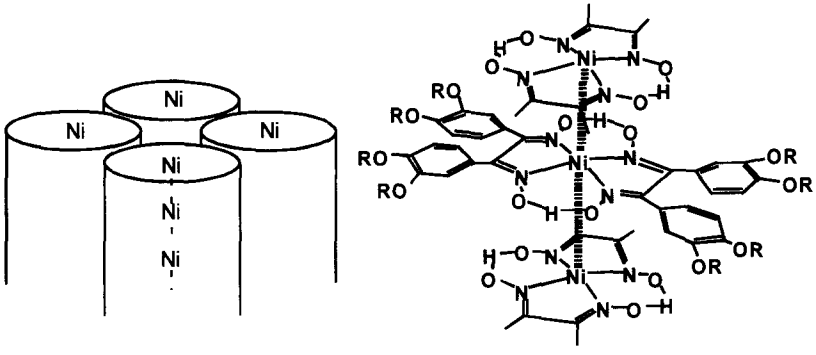

(a) Model of stacking structure

(b) Molecular model of a part of stacking structure

Fig. 2 One-dimensional stacking structure for $[Ni\{(C_8O)_4dpg\}_2]$.

In the present work, the structure of the $[Ni\{(C_8O)_4dpg\}_2]$ complex at various temperatures, from room temperature (r.t.) to 220°C, is investigated by Ni-*K* XANES spectra measurements and by DV-Xα molecular orbital calculations.

2. EXPERIMENTAL

2.1. Sample preparations

The procedure for synthesizing the $[Ni\{(C_8O)_4dpg\}_2]$ complex has been described in previous papers (1-4).

The sample was identified the same way as used in previous papers.

2.2. Collection of XAFS data

The Ni *K*-edge spectra of the sample were collected using the unfocused bending magnet beamline 10B at the Photon Factory, KEK, Tsukuba, operated at 2.5GeV and 250mA. Monochromatic radiation was obtained using a Si(311) channel-cut monochromator. Two ion-chambers with flowing gas mixtures, N_2 and 50% N_2 + 50% Ar, for I_0 and I, were used to measure the incident and transmitted X-ray intensities, respectively. The energy scale was calibrated using of an external calibration method where the first inflection point of the Cu *K*-edge of Cu metal foil was assigned to 8980 eV.

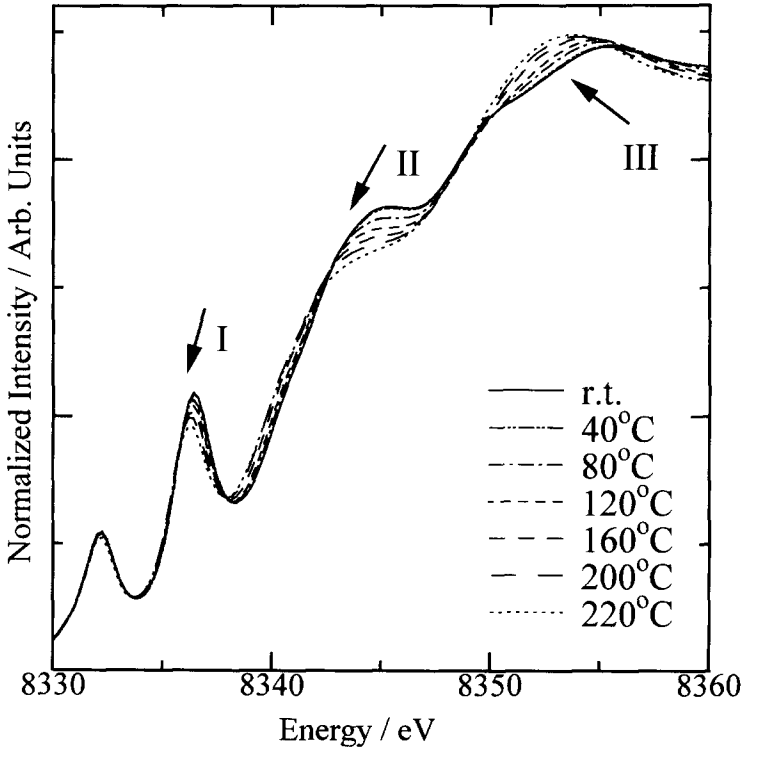

Fig. 3 Experimental Ni *K*-XANES spectra of $[Ni\{(C_8O)_4dpg\}_2]$ at various temperatures. Arrows indicate prominent spectral changes with temperature.

The sample was pulverized using an agate mortar and placed in a cell. The thickness of the sample was adjusted to obtain $1 \leq \mu t \leq 1.5$. At each temperature the spectrum was measured by heating the sample with an electrically controlled furnace. The temperatures at which measurements were performed were r.t., 40, 80, 120, 160, 200 and 220°C. The spectra obtained are shown in Fig. 3.

3. DV-Xα CALCULATIONS

The computational details of the DV-Xα method have previously been described (7-11). The Slater exchange value α used was 0.7. The stacking model for the [Ni{$(C_8O)_4$dpg}$_2$] complex at room temperature was built up from the crystal structure of bis(2,3-ethanedione dioximato)Ni(II) (12). The XANES spectrum of the [Ni{$(C_8O)_4$dpg}$_2$] complex at room temperature presents a very similar profile to that of bis(2,3- ethanedione dioximato)Ni(II). Thus, the results of single crystal analysis of bis(2,3- ethanedione dioximato)Ni(II) were referred to in order to build the model structure of the present complex. In the molecular structure of bis(2,3- ethanedione dioximato)Ni(II) a central Ni atom and four coordinated N atoms form a square planar structure with Ni-Ni axis stands vertically on the NiN4 plane. The core and the stacking structures of the complex thereby built up are shown in Fig. 4(a) and 4(b). The N-Ni-N angles in the Ni-N4 plane are shown as α (^{a}N-Ni-^{b}N) and β (^{a}N-Ni-^{a}N), the Ni-Ni distance as $r_{Ni\text{-}Ni}$ and the Ni-N distance as $r_{Ni\text{-}N}$ in Fig. 4(c).

As shown in Fig. 3, the XANES spectra are similar as a whole, but clearly different from each other at individual temperatures and shift as shown by the directed arrows with increasing temperature. Two different stacking models, T and M, of the complex molecules depending on the temperature, are shown in Fig. 4(c). The bond distances and angles of the model at room temperature are shown in Table I.

When the temperature was raised, in model T, Ni-Ni distances ($r_{Ni\text{-}Ni}$) varied as given in Table II, whereas in model M, each molecule slid along on the stacking plane with the tilt angle from the Ni axis (γ varying as given in Table III.

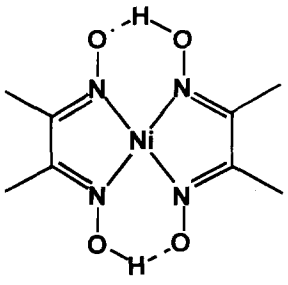

(a) Core structure model of the complex

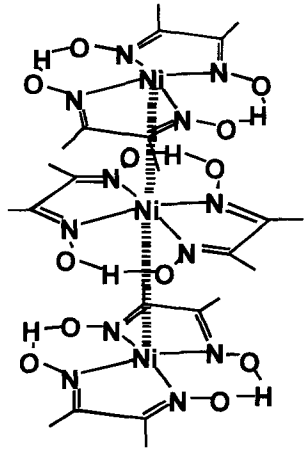

(b) Stacking structure model of the complex

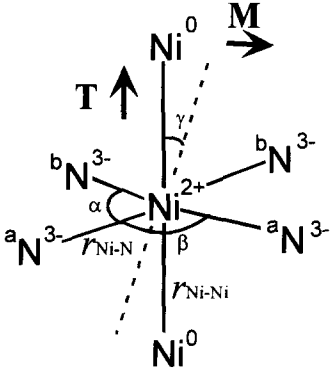

(c) Movements of T and M considered for spectral changes

Fig. 4 Models of $[Ni\{(C_8O)_4dpg\}_2]$ used for DV calculations. (a) Core structure around Ni atom in the complex molecule. (b) The stacking structure of $[Ni\{(C_8O)_4dpg\}_2]$ complex. (c) The core model of the complex. Bond lengths and bond angles suggested are given in Table I. Two kinds of model structures (T and M) have bond lengths and angles given in Tables II and III.

Table I. Bond distances and angles between the bonds for the core and stacking models (Fig. 4(c)) of $[Ni\{(C_8O)_4dpg\}_2]$ at room temperature.

Interaction	r / Å	angle	θ/°
$r_{Ni\text{-}N}$	1.88	α	80
$r_{Ni\text{-}Ni}$	3.33	β	100
		γ	0

The basis functions used were the 1s to 5p atomic orbitals for Ni, and 1s to 3p for N. A grid of 12000 sample points was used in the numerical integration. Self-consistency to within 0.001 electrons was obtained for the orbital populations.

Table II. Ni-Ni distances used in Model T for $[Ni\{(C_8O)_4dpg\}_2]$.

Model	$r_{Ni\text{-}Ni}$ / Å
T1	3.40
T2	3.60
T3	3.80

Table III. Angles γ used in Model M for $[Ni\{(C_8O)_4dpg\}_2]$.

Model	γ /°
M1	5
M2	10
M3	15

4. RESULTS AND DISCUSSIONS

First, EXAFS analyses were performed on the observed X-ray absorption spectra, in the usual manner using program FEFF (13-15), and the structure parameters obtained are summarized in Table IV. In Table IV, the Ni-Ni distances obtained with the EXAFS analysis do not change significantly with temperature. This suggests that the change in the structure parameters over the temperature range used is not detectable by EXAFS analysis.

The observed XANES spectra over the temperature range from r.t. to 220°C are shown in Fig. 3. Despite the EXAFS result, the XANES spectra do show a systematic shift with temperature as directed by the arrows.

In our previous work (7), the XANES spectrum of the $[Ni\{(C_8O)_4dpg\}_2]$ complex at room temperature combined with DV-Xα calculations indicated a blind type structure in which the complex molecules are stacked on top of each other in the Ni-Ni axial direction (16).

Table IV. Structure parameters obtained from EXAFS analysis of $[Ni\{(C_8O)_4dpg\}_2]$ at different temperatures. (*) means the atoms of neighboring stacking molecules.

T /°C	Ni-N		Ni-C		Ni-O		Ni-Ni*	
	r / Å	$10^2\sigma^2$ /Å	R / Å	$10^2\sigma^2$ /Å	r / Å	$10^2\sigma^2$ /Å	r / Å	$10^2\sigma^2$ /Å
r.t.	1.88	0.13	2.82	0.74	2.78	0.62	3.32	1.09
40	1.88	0.14	2.74	-0.16	2.84	-0.06	3.33	0.89
80	1.88	0.15	2.74	-0.12	2.84	-0.03	3.33	0.95
120	1.88	0.16	2.78	0.51	2.81	0.59	3.33	1.17
160	1.88	0.17	2.77	0.55	2.81	0.60	3.33	1.22
200	1.88	0.19	2.77	0.54	2.81	0.68	3.32	1.27
220	1.88	0.19	2.73	-0.15	2.84	-0.01	3.34	1.10

T /°C	Ni-N*		Ni-C*		Ni-O*			
	R / Å	$10^2\sigma^2$ /Å	r / Å	$10^2\sigma^2$ /Å	r / Å	$10^2\sigma^2$ /Å	ΔE_0 / eV	R_f
r.t.	3.86	1.44	4.40	10.18	4.27	0.92	13.31	0.012
40	3.88	1.23	4.44	4.85	4.27	1.00	10.18	0.009
80	3.89	1.03	4.43	4.06	4.27	1.28	10.30	0.009
120	3.90	1.19	4.44	10.07	4.28	1.30	13.23	0.011
160	3.90	1.14	4.42	9.94	4.27	1.41	13.17	0.012
200	3.91	1.26	4.41	10.25	4.27	1.42	13.08	0.011
220	3.93	0.94	4.52	0.73	4.22	0.91	10.10	0.007

σ : Debye-Waller factor

ΔE_0 : correction of photoelectron energy

R_f : reliability factor =

$$\left[\sum k^6\{\chi_{obs}(k)-\chi_{calc}(k)\}^2 / \sum k^6 \chi_{obs}{}^2(k)\right]^{\frac{1}{2}}$$

k range used : 2.00 - 11.50 Å^{-1}

r range used : 1.00 - 4.50 Å^{-1}

Starting from this blind type of structure in the present analysis, the core structure of the complex was changed step by step as in models T and M with rising temperature. To analyze the shape and shift of the spectra quantitatively, we calculated the spectra for models T and M by DV-Xα calculations and compared these with the observed spectra.

Figure 5 shows the results for model T. The calculated spectra were obtained from Gaussian convolution applied to the election transition probabilities from the Ni 1s orbital with a full-width at half-height (FWHH) of 1.0 eV. The energy scale for the calculated spectra was calibrated by assigning the calculated 1s → 3d transition to the energy of the pre-edge peak in the each recorded XANES spectra. The calculated spectra have three peaks, which however, have a poor fit to the observed one at the positions arrowed, especially, the point II.

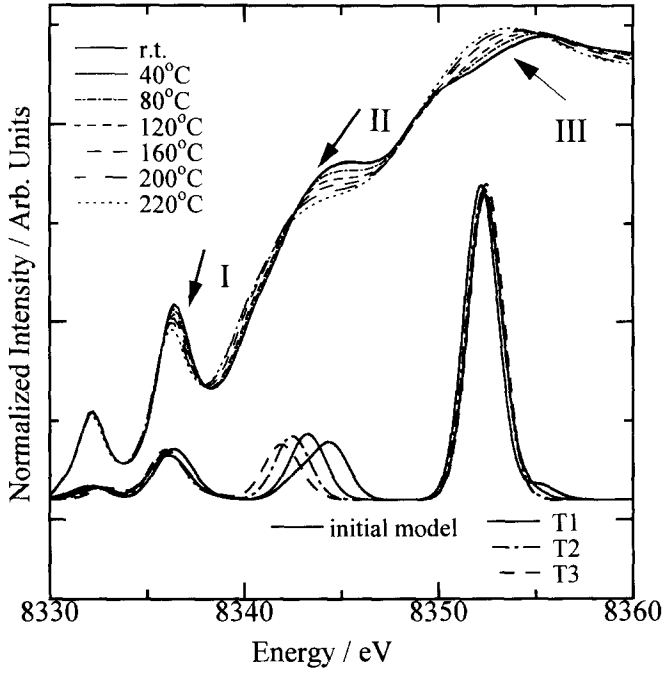

Fig. 5 Calculated Ni *K*-XANES spectra (Models T, shown below) and experimental Ni *K*-XANES spectra of [Ni{$(C_8O)_4$dpg}$_2$] at various temperatures. Calculated spectra are gaussian convoluted for the oscillator strengths.

The results for model M are shown in Fig. 6, where the calculated curves were obtained in the same way as in Fig. 5. In Fig. 6, the calculated spectra have three peaks and show the same tendencies as seen in the corresponding experimental spectra at all three points arrowed as the temperature rises. Thus, model M corresponds to the structural changes of the [Ni{$(C_8O)_4$dpg}$_2$] complex with high temperature.

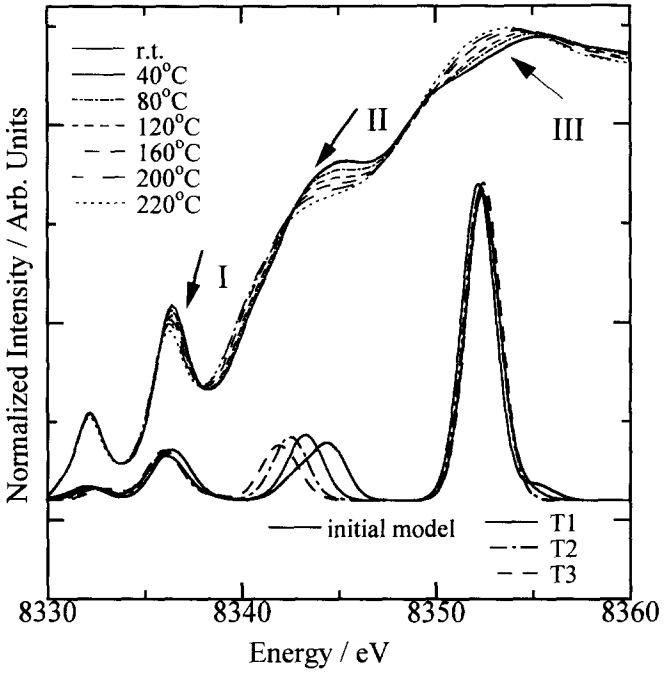

Fig. 6 Calculated Ni *K*-XANES spectra (Model M, shown below) and experimental Ni *K*-XANES spectra of [Ni{$(C_8O)_4$dpg}$_2$] at various temperatures. Calculated spectra are Gaussian convoluted for the oscillator strengths.

The assignments of the individual peaks in the observed XANES spectra were also made from the calculation results. The peak at ~ 8334 eV was ascribed to the 1s → 3d (mainly) and 1s → 4p transitions, the peaks at ~ 8337 eV and 8344 eV to the 1s → 4s and 1s → 4p transitions, and the peak at ~ 8353 eV to the 1s → 4p transition. The changes in the peaks as the temperature rises come from the changes in electron transition probabilities (13).

Molecular vibration might be taken into account to explain the spectral change with temperature. With increasing temperature, the one-dimensional stacking structure of the Ni complex may vibrate at high temperatures in the molecular plane; however, both the Ni-Ni and Ni-N interactions between the molecules are strong enough to preserve the stacking structure, as seen in the almost constant distance between the molecular planes at the higher temperatures investigated.

5. CONCLUSION

A discotic Ni complex, $[Ni\{(C_8O)_4dpg\}_2]$, has a one-dimensional stacking structure and show typical thermochromism. When the temperature is raised, the molecular structure does not change and the intermolecular interactions are so strong that the main stacking structure keeps the same conformation as it has at room temperature, even at temperatures as high as 220°C. However, XANES analysis combined with DV-Xα calculations suggested that the structural change of the complex with temperature occurs a sliding movement of the complex along the molecular plane.

6. ACKNOWLEDGEMENT

The present work was performed with the approval of the Photon Factory Advisory Committee (Proposal No. 95G190). This work has been partially supported by Grant-in-Aids (c) (No. 11640618 and No. 09640660) from the Japanese Ministry of Education, Science, Sports and Culture.

REFERENCES

(1) Ohta, K.; Hasebe, H.; Moriya, M.; Fujimoto, T.; Yamamoto, I. *J. Mater. Chem.* **1991**, *1*, 831.
(2) Ohta, K.; Hasebe, H.; Moriya, M.; Fujimoto, T.; Yamamoto, I. *Mol. Cryst. Liq. Cryst.* **1991**, *208*, 43.
(3) Shirotani, I.; Suzuki, K.; Suzuki, T.; Yagi, T.; Tanaka, M. *Bull. Chem. Soc. Jpn.* **1992**, *65*, 1078.
(4) Ohta, K.; Hasebe, H.; Moriya, M.; Ikejima, M.; Fujimoto, T.; Yamamoto, I. *Bull. Chem. Soc. Jpn.* **1993**, *66*, 3559.
(5) Ohta, K.; Ikejima, M.; Moriya, M.; Hasebe, H.; Yamamoto, I. *J. Mater. Chem.* **1998**, *8*, 1971.
(6) Ohta, K.; Higashi, R.; Ikejima, M.; Yamamoto, I.; Kobayashi, N. *J. Mater. Chem.* **1998**, *8*, 1979.
(7) Yamashita, S.; Fujiwara, M.; Kato, Y.; Yamaguchi, T.; Wakita, H. *Adv. in Quantum Chem.* **1997**, *29*, 357.
(8) Valli, M.; Matsuo, S.; Wakita, H.; Yamaguchi, T.; Nomura, M. *Inorg. Chem.* **1996**, *35*, 5462.
(9) Adachi, H.; Tsukada, M.; Satoko, C. *J. Phys. Soc. Jpn.* **1978**, *45*, 875.
(10) Satoko, C.; Tsukada, M.; Adachi, H. *J. Phys. Soc. Jpn.* **1978**, *45*, 1333.
(11) Adachi, H.; Shiokawa, S.; Tsukada, M. *J. Phys. Soc. Jpn.* **1979**, *47*, 1528.
(12) Yamashita, S.; Yanase, Y.; Yamaguchi, T.; Wakita, H. *Bull. Chem. Soc. Jpn.* **1989**, *62*, 2902.
(13) Mustre de Leon, J.; Rehr, J. J.; Zabinsky, S. I.; Albers, R. C. *Phys. Rev. B* **1991**, *44*, 4146.
(14) Rehr, J. J.; Albers, R. C.; Zabinsky, S. I. *Phys Rev. Lett.* **1992**, *69*, 3397.
(15) Rehr, J. J.; Mustre de Leon, J.; Zabinsky, S. I.; Albers, R. C.; *J. Am. Chem. Soc.* **1991**, *113*, 5135.
(16) The detailed data are available from H. Wakita.

Separation of the effects of charge transfer, covalency and electron correlations on the multiplet structure of ruby based on first-principles cluster calculations

Kazuyoshi Ogasawara*, Masateru Yamamoto, Takugo Ishii, Hidenori Ida[1] and Hirohiko Adachi

Department of Materials Science and Engineering
Kyoto University, Sakyo-ku, Kyoto 606-8501 JAPAN

Isao Tanaka

Department of Energy Science and Technology
Kyoto University, Sakyo-ku, Kyoto 606-8501 JAPAN

(Received May 24, 1999)

First-principles calculations of the multiplet structure of ruby have been carried out using two different methods. One is a hybrid method of the DV-Xα method and the ligand field theory (DV-LFT method), in which the parameters of the electron-electron repulsion are calculated using the pure atomic orbitals of the impurity chromium ion. The DV-LFT calculations were carried out for a chromium ion embedded only in the point charges and for a chromium ion in a cluster consisting of 63 atoms. The other is a more direct method, in which the matrix elements of the electron-electron repulsion are calculated numerically using the molecular orbitals obtained by the DV-Xα cluster calculations (DV-ME method). The DV-ME calculations were carried out with and without correction to the electron correlation effects. By comparing the results, the effects of charge transfer, covalency and electron correlations were evaluated quantitatively from first principles.

KEYWORDS: multiplet, electron correlation, first-principles calculation

* Corresponding Author, e-mail: ogasa@dvxa4.mtl.kyoto-u.ac.jp

---

[1] Present address: Manufacturing Engineering Center, Mitsubishi Electronic Corporation, 8-1-1 Tsukaguchi-honmachi, Amagasaki, Hyogo 661-8661, Japan.

0065-3276/01 $35.00

1. INTRODUCTION

A crystal of white sapphire (Al_2O_3 or alumina) containing trivalent chromium ions as impurities exhibits a beautiful red color and widely known as a precious gemstone, "ruby". The origin of the red color of ruby is the absorption of light in the region of the complementary color (blue green) due to the excitation of the impurity chromium ions. In an isolated trivalent chromium ion, three eletrons occupy ten degenerate $3d$ orbitals (d^3 configuration). In such an open shell system, the total Coulomb repulsion energy of the outer-shell electrons strongly depends on the choice of the occupied orbitals even though the orbitals are all degenerate. In this case, a direct calculation of the energy levels of the total electrons is indispensable. The quantum states of the total electrons in an open shell system are generally called "multiplets". When a trivalent chromium ion is placed within an alumina crystal, the situation becomes more complicated due to two factors. First, the pure chromium $3d$ orbitals are no longer stable, and impurity orbitals mainly consisting of the chromium $3d$ orbitals are formed within the band gap of the host alumina crystal. Although, these impurity orbitals are slightly delocalized compared to the pure $3d$ orbitals due to the covalent interaction between the chromium ion and the host crystal, the three outershell electrons still occupy the ten impurity orbitals. Therefore, we also denote this configuration as d^3, borrowing the atomic notation for simplicity. Secondly, the energies of the multiplets are significantly modified due to the presence of the crystal field. In the case of ruby, a chromium ion substitutes for an aluminum ion. Although the true site symmetry at an aluminum ion in alumina is C_3, it is surrounded by six oxygen ions and the crystal field is mostly dominated by the octahedral contribution.

The multiplet energies of transition-metal (TM) ions in the octahedral (or tetrahedral) crystal field are generally analyzed by a parameter fitting method based on the ligand field theory (LFT) developed by Sugano *et al.* (1). Although the optical spectrum of ruby has been successfully interpreted by the ligand field theory (1), the meanings of the parameters are somewhat ambiguous because of the several critical approximations. One is the cubic approximation, where the low-symmetry crystal fields such as the trigonal field in ruby are neglected. The other is the neglect of the differential delocalization. In the octahedral crystal field, the impurity states can be classified into two states, t_{2g} and e_g, according to their symmetry properties. In general, the degree of delocalization of the impurity states due to the covalent interaction is more or less different between the t_{2g} and e_g states. However, in the ligand field theory, the difference in delocalization between these states is completely neglected. Moreover, since the parame-

ters are determined by fitting to the experimental data, the various effects such as charge transfer, covalency and electron correlations are "hidden" in the empirical parameters and no longer separable. For the quantitative analysis of these effects, first-principles calculations are indispensable.

In order to clarify the effect of covalency, we have recently developed a general method to calculate multiplet structures from first principles (2) based on the discrete variational-Xα (DV-Xα) method. This method can be applied not only to the calculation of multiplet structures, but also to the calculation of electronic states of general many-electron systems. Considering such generality, we call it the discrete variational-multielectron (DV-ME) method. The most remarkable feature of this method is the applicability to the systems with arbitrary symmetry. Taking advantage of this method, we applied it to the calculation of the multiplet structure of ruby (2). Although the first-principles calculation of the electronic structure of ruby has been already attempted by several researchers, these works were based on the one-electron approximation and the multiplet energies were evaluated only for two states (R line and U band) (3,4). Therefore, our previous report was the first theoretical calculation of the "entire" multiplet structure of ruby without referring to any experimental data. Moreover, the effects of covalency and distortion of the impurity-state orbitals were clarified for the first time.

In our previous report, however, the calculated multiplet energies tend to be overestimated especially for the doublets. This is due to the underestimation of the effect of electron correlations. Recently, we have developed a simple method to take into account the remaining effect of electron correlations. In this method, the electron-electron repulsion integrals are multiplied by a certain reduction factor (correlation correction factor) , c, and the value of c is determined by the consistency between the spin-unrestricted one-electron calculations and the multiplet calculations. The details of this method will be described in another paper (5). In the present paper, the effect of electron correlations on the multiplet structure of ruby is investigated by the comparison between the results with and without the correlation corrections.

Although the ligand field theory is based on the several critical approximations, a first-principles calculation based on the ligand field theory can also provide a useful information when the results are compared to those of the DV-ME calculations. For example, a comparison between the calculations based on the LFT using the pure atomic orbitals (AOs) and the DV-ME calculations using the molecular orbitals (MOs) provide a clear separation of the effect of covalency. Therefore, in the present work, we also carried out the calculation of the multiplet structure of ruby based on the LFT. In this approach, the parameters representing the electron-electron repulsion are calculated using the pure $3d$ atomic orbitals of the

chromium ion used in the DV-Xα calculation. Since this is a hybrid method of the DV-Xα and the LFT, we call it the DV-LFT method. In our DV-Xα computation code, the numerical atomic orbitals are generated to be consistent with the Mulliken charges (6), and flexible to the chemical environment. Therefore, the effect of the charge transfer is also reflected in the spatial extension of the pure atomic orbitals. Thus the atomic orbitals of the trivalent chromium ion in the cluster (cluster model) is more delocalized than those of the trivalent chromium ion surrounded only by the point charges (point charge model) due to the decrease of the effective charge. In this paper, the effect of charge transfer is also evaluated by comparing the results between these two models.

Since all of charge transfer, covalency and electron correlations work to decrease the electron-electron repulsion energy, these effects are evaluated quantitatively in terms of the reduction of the Coulomb integrals.

2. COMPUTATIONAL METHOD

2.1. One-electron calculation

One-electron calculations were carried out self-consistently based on the local density functional approach using the Slater's Xα potential (7). In the present calculation, α was fixed at 0.7, which was found to be the most appropriate value in many cases (8). The molecular orbitals were constructed as linear combination of the atomic orbitals (LCAO). The most remarkable feature of our program is that the atomic orbitals are created numerically in each iteration and flexible to the chemical environment. The details of this program have been described by Adachi *et al.* (9).

2.2. DV-LFT method

In the ligand field theory, the matrix elements of the many-electron Hamiltonian for the TM ions in the octahedral (or tetrahedral) symmetry (Tanabe-Sugano matrices) are expressed in terms of the effective crystal-field splitting, and the Racah parameters, B and C (1). Here the effective crystal-field splitting means the energy separation between adjacent electronic configurations designated by the occupation numbers of the t_{2g} and e_g states. For example, in the case of d^3 configuration, four different electronic configurations $(t_{2g})^3$, $(t_{2g})^2(e_g)^1$, $(t_{2g})^1(e_g)^2$, $(e_g)^3$ are possible.

The energy separation of the above configurations can be evaluated by the one-electron energy difference, $\varepsilon_{eg} - \varepsilon_{t2g}$, calculated in the Slater's transition state, $(t_{2g})^{2.5}(e_g)^{0.5}$, $(t_{2g})^{1.5}(e_g)^{1.5}$ and $(t_{2g})^{0.5}(e_g)^{2.5}$, respectively (7). However, as we have already pointed out, the value of $\varepsilon_{eg} - \varepsilon_{t2g}$ is quite insensitive to the electronic configuration (2). Therefore, in the present paper, we approximated all of these effective crystal-field splittings by the value of $\varepsilon_{eg} - \varepsilon_{t2g}$ calculated in the ground state. On the other hand, the Racah parameters represent the electron-electron repulsion interaction and can be calculated by the radial part of the pure $3d$ atomic orbitals of the impurity chromium ion (1). After evaluating the value of these parameters, the multiplet structure of ruby can be obtained by diagonalizing the Tanabe-Sugano matrices.

2.3. DV-ME method

In the DV-ME method, only the electrons occupying the impurity states are considered directly. After the one-electron calculation based on the DV-Xα cluster calculations, the Slater determinants for all the possible choice of the impurity-state orbitals are constructed and are used as basis functions for diagonalization of the effective many-electron Hamiltonian. For the calculation of the matrix elements, we adopt the approach proposed by Fazzio *et al.* (10). First we classify all the Slater determinants into several electronic configurations. Then the diagonal matrix element of the i-th Slater determinant belonging to the n-th electronic configuration is expressed as,

$$E(n;i) = \hat{E}(n) + \Delta E(n;i) \tag{1}$$

where $\hat{E}(n)$ is the average energy of all the Slater determinants belonging to the n-th electronic configuration and $\Delta E(n;i)$ is the deviation of $E(n;i)$ from $\hat{E}(n)$. The value of $\hat{E}(n)$ relative to another configuration corresponds to the total energy difference between these configurations. In ruby, the impurity states can be roughly classified into the states with approximately t_{2g} and e_g symmetry. Since the further splits due to the trigonal crystal field is quite small, all the Slater determinants are classified into the four electronic configurations, $(t_{2g})^3$, $(t_{2g})^2(e_g)^1$, $(t_{2g})^1(e_g)^2$, $(e_g)^3$ in the present work. In this case, the energy separations of these configurations are the same as the effective crystal-field splitting defined in the previous section. Thus we also evaluated them by the one-electron energy difference, $\varepsilon_{eg}-\varepsilon_{t2g}$, in the ground state.

Since the off-diagonal elements and the remaining part of the diagonal elements, $\Delta E(n;i)$, represent the electron-electron interaction, it can be

expressed in terms of electron-electron repulsion integrals such as,

$$\langle ij \mid\mid kl \rangle = \int\int \phi_i^*(\mathbf{r}_1)\phi_j^*(\mathbf{r}_2)\frac{1}{r_{12}}\phi_k(\mathbf{r}_1)\phi_l(\mathbf{r}_2)d\mathbf{r}_1 d\mathbf{r}_2, \tag{2}$$

where ϕ's are the impurity-state orbitals. In the present work, above integrals are calculated as the weighted sum of integrands at sampling points (11) using the equation,

$$\langle ij \mid\mid kl \rangle = \sum_{\alpha} \omega(\mathbf{r}_\alpha)\phi_i^*(\mathbf{r}_\alpha)[\sum_{\beta(\neq\alpha)} \omega(\mathbf{r}_\beta)\phi_j^*(\mathbf{r}_\beta)\frac{1}{r_{\alpha\beta}}\phi_l(\mathbf{r}_\beta)]\phi_k(\mathbf{r}_\alpha), \tag{3}$$

where ω is a weight function proportional to the inverse of the sampling point density. One can therefore avoid computational difficulty associated with the multicenter integration. When all the matrix elements are obtained, the multiplet energy levels are calculated easily by diagonalization. The details of this method have been described in Ref. (2):

2.4. Correlation correction factor

The effect of electron correlations is generally taken into account through the configuration interaction (interaction among the Slater determinants) (12). However, in the present calculations, the number of the Slater determinants used for the diagonalization of the Hamiltonian is not enough to describe the effect of electron correlations accurately. Since the electron-electron repulsion integrals are somewhat reduced due to the remaining electron correlation effects, we multiplied all the electron-electron repulsion integrals by a certain reduction factor (correlation correction factor), c, for the calculation of the matrix elements of the many-electron Hamiltonian. Although the multiplet energies depend on the value of c, we have recently developed a simple method to evaluate the value of c from first-principles using the consistency between the spin-unrestricted one-electron calculations and the multiplet calculation. For example, in the case of ruby, the transition energy of spin-flip within the $(t_{2g})^3$ configuration was can be calculated by the one-electron energy difference, $\varepsilon_{t2g\downarrow} - \varepsilon_{t2g\uparrow}$ in the Slater's transition state, $(t_{2g}\uparrow)^{2.5}(t_{2g}\downarrow)^{0.5}$. The same spin-flip transition energy should coincide with the average energy of the multiplet states within the $(t_{2g}\uparrow)^2(t_{2g}\downarrow)^1$ configuration, $E^E(c)$, relative to the energy of the $(t_{2g}\uparrow)^3$ configuration (ground state), $E^G(c)$. In the case of ruby, the ground state corresponds to $^4A_2$ while the spin-flip excited state, $(t_{2g}\uparrow)^2(t_{2g}\downarrow)^1$, corresponds to four different states, $^2T_2$, $^2T_1$, ^2E, and $^4A_2$ ($S_z = 1/2$), where S_z is the z-component of the total spin. Therefore, in the actual calculation,

the gravity center of these four states was taken as $E^E(c)$. Then the value of c can be determined by the following equation,

$$E^E(c) - E^G(c) = \varepsilon_{t2g\downarrow} - \varepsilon_{t2g\uparrow}. \tag{4}$$

The details of the theoretical evaluation of c will be explained elsewhere (5).

2.5. Computational Models

In the present work, the multiplet structure of ruby was calculated using a $(CrAl_{14}O_{48})^{51-}$ cluster shown in Fig. 1 (cluster model). This cluster consists of 63 atoms and is larger than the one consisting of 41 atoms adopted in our previous report (2). The results of the Mulliken population analysis (6) showed that the compositions of the impurity-state orbitals calculated for the present cluster are slightly different from those for the previous cluster. Although the difference is quite small (1.4 $\sim$ 1.6 % for the Cr $3d$ composition in the t_{2g} states), this time we adopted the larger one for better accuracy.

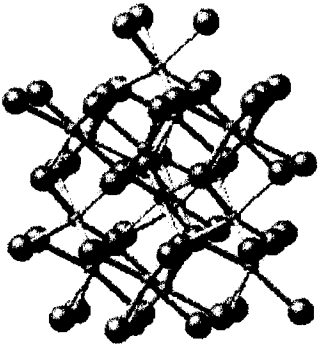

Fig 1. The cluster model adopted for the first-principles calculation of the multiplet structure of ruby. The small black sphere at the center of the cluster represents the impurity chromium ion. Small gray spheres and large gray spheres represent aluminum ions and oxygen ions, respectively.

In order to estimate the effect of charge transfer, a DV-LFT calculation using a trivalent chromium ion surrounded only by the point charges (point charge model) was also carried out. In order to compare the pure effect of

the spatial extension of the atomic orbitals, the value of the crystal-field splitting was set equal to the one calculated for the cluster model even for the calculation of the point charge model. The basis functions used in the calculations were 1*s*-4*p* for chromium, 1*s*-2*p* for oxygen and 1*s*-3*d* for aluminum. The number of sampling points was 20000 for the point charge model and 40000 for the cluster model.

3. RESULTS AND DISCUSSIONS

3.1. One-electron energy level of ruby

The one-electron energy level structure calculated for the $(CrAl_{14}O_{48})^{51-}$ cluster is shown in Fig. 2, which is essentially the same with our previous result using the smaller cluster (2). The valence band mainly consists of the O 2*p* orbitals and the conduction band mainly consists of the Al 3*s*, 3*p*, 3*d* orbitals. There are impurity states of approximately t_{2g} and e_g symmetry mainly consisting of the Cr 3*d* orbitals.

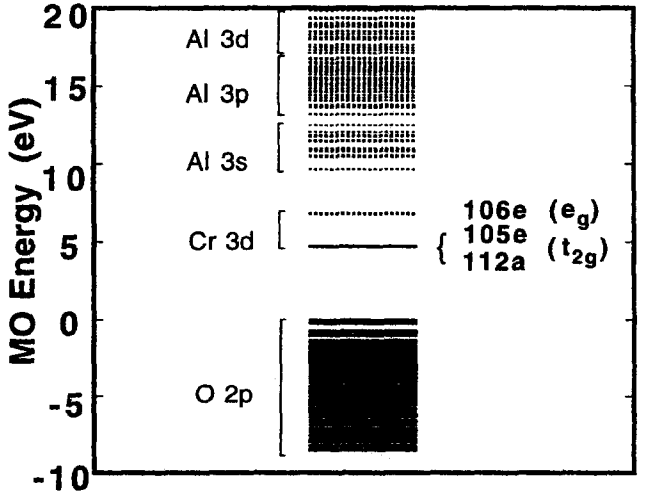

Fig 2. The calculated molecular orbital (MO) energy levels using the $(CrAl_{14}O_{48})^{51-}$ cluster. The energy of the top of the valence band is set at zero. Solid lines denote the occupied states and dotted lines the unoccupied states.

Due to the presence of the trigonal field, the t_{2g} state further splits into the 112a and 105e states. However, since this split is less than 0.04 eV, we still use the notation of t_{2g} and e_g for simplicity and evaluated the energy of t_{2g} state by the gravity center of the energies of the 112a and 105e states. The calculated value of the crystal-field splitting is 2.11 eV.

3.2. Multiplet Structure of ruby

The multiplet structures of ruby calculated by the DV-LFT method using the point charge model and the cluster model are shown in Fig. 3. For comparison, the peak positions of the experimental absorption spectra of ruby obtained by Fairbank *et al.* (13) are shown together. Here each state is labeled according to the notation in the octahedral symmetry for simplicity.

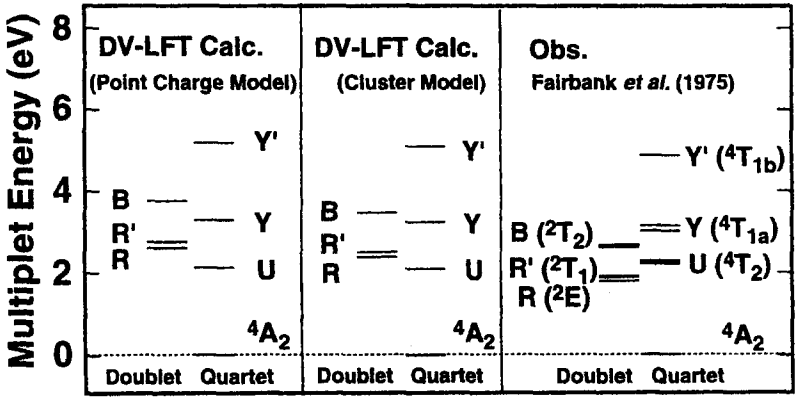

Fig 3. The multiplet structures of ruby calculated by the DV-LFT method using the point charge model and the cluster model, together with the peak positions in the absorption spectra of ruby reported by Fairbank *et al.* (13). In each result, the doublets are shown at left and quartets are at right.

Since the ground state is a quartet ($^4A_2$), transitions to the quartets, $^4T_2$, $^4T_{1a}$ and $^4T_{1b}$ are allowed by the spin-selection rule and observed as strong

and broad bands. Although transitions to the doublets, ^2E, $^2T_1$ and $^2T_2$ are forbidden by the spin-selection rule, they are slightly allowed due to the presence of the spin-orbit interaction and observed as weak and sharp lines. Each peak slightly splits due to the trigonal crystal field (quartets) or due to the spin-orbit interaction (doublets). Since the DV-LFT calculations are based on the cubic approximation and the spin-orbit interactions are not taken into account, these fine structures are not reproduced in the calculated results. Therefore, in the present work, we discuss only the average energy of each state for simplicity.

In the results of the DV-LFT calculations, the positions of the quartets are relatively well reproduced while the positions of the doublets are significantly overestimated. As a result, the relative positions of the doublets to the quartets are qualitatively inconsistent with the experimental results. This discrepancy is mainly due to the neglect of the effects of covalency. By comparing the results of the cluster model with those of the point charge model, the energy positions of the doublets slightly decreased. This can be interpreted as the effect of the charge transfer between the cations and the anions. In the point charge model, the atomic orbitals of the chromium ion are calculated under the potential produced by the formal charge of the trivalent chromium ion (+3 in the unit of the charge of an electron). However, in the cluster calculation, the charge transfer between the cation and the anion occurs, and the effective charge of the trivalent chromium ion is reduced compared to the formal charge. The calculated effective charge of the chromium ion in the $(CrAl_{14}O_{48})^{51-}$ cluster is +2.19. Due to the smaller effective charge, the atomic orbitals slightly delocalize, resulting in the reduction of the electron-electron repulsion energy. In the multiplet energy level of ruby, the states $^4A_2$, ^2E, $^2T_1$, $^2T_2$, all mainly consist of the $(t_{2g})^3$ electronic configuration (1). Therefore, the splits of these states are dominated by the electron-electron repulsion energy. On the other hand, the states $^4T_2$, $^4T_{1a}$, $^4T_{1b}$ mainly consist of $(t_{2g})^2(e_g)^1$, $(t_{2g})^2(e_g)^1$, $(t_{2g})^1(e_g)^2$ electronic configurations, respectively (1). Therefore, the energies of these states are mainly dominated by the effective crystal-field splitting. As a result, the energies of the doublets are more sensitive to the change of the electron-electron repulsion energy than those of the quartets.

The multiplet structures of ruby calculated by the DV-ME method with and without the correlation correction are shown in Fig. 4. The experimental values are also shown together. In this case, the multiplet structures are calculated directly using the molecular orbitals of the impurity states obtained by the cluster calculation. In the calculated results, each level is broadened by the presence of the trigonal crystal field. Although the split of each peak seems to be somewhat overestimated due to the computational errors, it can be improved by increasing the number of sampling points (2).

Therefore, we also discuss only the average energy of each state in this case. Comparing the results of the DV-ME calculation without the correlation correction with those of the DV-LFT calculation, the energies of the doublets decrease significantly due to the covalency between the chromium ion and the host alumina crystal. In this case, the relative positions of the doublets to the quartets are qualitatively reproduced. On the other hand, the energies of the quartets are not significantly changed and also well reproduced. When the correlation correction is taken into account, the energies of the doublets decrease further and the calculated values agree with the experimental ones excellently. The value of c determined by eq. (4) is 0.844 indicating that the electron-electron repulsion integrals are reduced to 84.4 (%) on the average due to the effect of electron correlation.

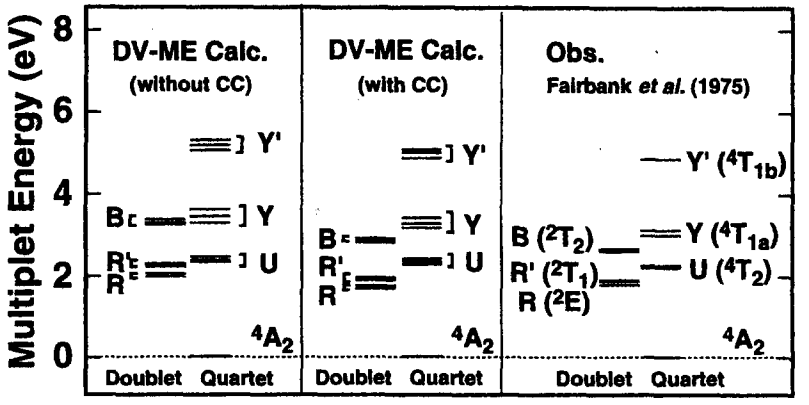

Fig 4. The multiplet structures of ruby calculated by the DV-ME method using the $(CrAl_{14}O_{48})^{51-}$ cluster, together with the peak positions in the absorption spectra of ruby reported by Fairbank *et al.* (13). In each result, the doublets are shown at left and quartets are at right.

According to the observed spectra, the peak position of the R line (^2E) is 1.79 eV, while that of the U band ($^4T_2$) is 2.23 eV and 2.28 eV for the σ ($E \perp C_3$) and π ($E \parallel C_3$) spectra, respectively. Theoretical calculation of these energies has been attempted by Ohnishi and Sugano (2), and Xia *et al.* (3) within the one-electron approximation. The R line and U band energies calculated by Ohnishi and Sugano are 1.63 eV and 2.27 eV, respectively, while those by Xia *et al.* are 2.29 eV and 2.70 eV, respectively. In

the present work, the R line and U band energies are calculated as 1.73 eV and 2.35 eV, respectively. Therefore, our calculation reproduced the R line energy better than the calculation of Ohnishi and Sugano, while their calculation reproduced the U band energy slightly better than ours. However, considering the fact that they adopted a simple model cluster consisting of seven atoms, in which the ligand oxygen ions are located at regular cubic positions, the good reproduction of the U band energy in their calculation is probably due to the cancellation of the various approximations. On the other hand, in the present work, we calculate the entire multiplet structure of ruby from first principles using a larger model cluster with C_3 symmetry. Therefore, the present calculation is more appropriate for the interpretation of the electronic structure of ruby. One of the possible reasons for the overestimation of the U band energy in the present calculation is the effect of lattice relaxation around the chromium ions. According to the analysis of the extended X-ray absorption fine structures (EXAFS) reported by Kizler *et al.*, the Cr-O bond lengths in ruby is slightly longer than Al-O bond lengths in alumina (14). The longer Cr-O bond lengths would cause a decrease of the effective crystal-field splitting, resulting in the decrease of the U-band energy. Therefore, if the lattice relaxation is taken into account, the agreement with the experimental value will be improved.

2.3. Coulomb integrals

Since all of the effects of charge transfer, covalency and electron correlation work to decrease the electron-electron repulsion energy, they can be quantitatively evaluated by the reduction of the Coulomb integrals. For example, in the ligand field theory, the Coulomb integral between the e_g states, $J(ee)$, and the Coulomb integral between the t_{2g} states, $J(tt)$, are the same and expressed in terms of the Racah parameters as, $A+4B+3C$. The Racah parameters can be easily calculated by the pure AOs of the impurity chromium ion. In the point charge model, the calculated values of the Racah parameters are $A = 22.15$ eV, $B = 0.14$ eV and $C = 0.53$ eV, and the Coulomb integrals are calculated as $J(ee) = J(tt) = A + 4B + 3C = 24.3$ eV. On the other hand, in the cluster model, the calculated values of the Racah parameters are $A = 20.75$ eV, $B = 0.13$ eV and $C = 0.49$ eV, and the Coulomb integrals are calculated as $J(ee) = J(tt) = A + 4B + 3C = 22.7$ eV. Therefore, the Coulomb integrals decrease by 1.6 eV due to the effect of charge transfer. Next we calculate the Coulomb integrals using the MOs of the impurity states. The calculated values are $J(ee) = 18.9$ eV, $J(t_{(a)}t_{(a)}) = 20.1$ eV and $J(t_{(e)}t_{(e)}) = 20.5$ eV, where $t_{(a)}$ and $t_{(e)}$ denote the a and e states corresponding to the t_{2g} states in the octahedral symmetry. Therefore, the decrease of the above Coulomb integrals due to the effect of

covalency are 3.8 eV, 2.6 eV and 2.2 eV, respectively. When the correlation correction (CC) is taken into account, the coulomb integrals are multiplied by c, and become $J(ee) = 16.0$ eV, $J(t_{(a)}t_{(a)}) = 17.0$ eV and $J(t_{(e)}t_{(e)}) = 17.3$ eV, respectively. Therefore, they further decrease by 2.9 eV, 3.1 eV and 3.2 eV, respectively. The calculated Coulomb integrals are listed in **Table 1**. Compared to the original values calculated by the AOs in the point charge model, these Coulomb integrals reduced to 65.8 (%), 70.0 (%), 71.2 (%), respectively. As shown in the calculated multiplet energies, the doublet energies are significantly influenced by the reduction of the Coulomb integrals. Therefore, the inclusion of the effect of charge transfer, covalency and electron correlations is quite important for the quantitative evaluation of the doublet energies.

Table I. The calculated Coulomb integrals (eV). AO(p), AO(c), MO, MO(CC) denote the values calculated by the Cr-3d AOs in the point charge model (p), by the Cr-3d AOs in the cluster model (c), by the MOs of the impurity states and by the MOs of the impurity states with the correlation correction (CC), respectively. e and t represent the e_g and t_{2g} states in the octahedral notation, while (a) and (e) specify the states split by the trigonal crystal field.

	AO(p)	AO(c)	MO	MO(CC)
$J(ee)$	24.3	22.7	18.9	16.0
$J(t_{(a)}t_{(a)})$	24.3	22.7	20.1	17.0
$J(t_{(e)}t_{(e)})$	24.3	22.7	20.5	17.3

4. SUMMARY

The multiplet structure of ruby has been calculated with two different approaches. One is a hybrid method of the DV-Xα method and the ligand field theory, where the parameters of the electron-electron repulsion are calculated using the numerical atomic orbitals of the impurity chromium ion (DV-LFT method). In order to evaluate the effect of charge transfer between the chromium ion and the oxygen ions, the DV-LFT calculations were carried out for the chromium ion surrounded only by the point charges (point charge model) and for the chromium ion in the cluster consisting of 63 atoms (cluster model). Although the results of the DV-LFT calculations

reproduced the quartet energies satisfactorily, the doublet energies are significantly overestimated due to the overestimation of the electron-electron repulsion energy. The doublet energies calculated for the cluster model are slightly improved compared to those calculated for the point charge model, due to the effect of charge transfer however, the relative positions of the doublets to the quartets are still inconsistent with the experimental values. Therefore, the effect of covalency is quite important for the evaluation of the doublet energies.

In order to take into account the effect of covalency, we also carried out calculations based on a more general method, in which the matrix elements of the electron-electron repulsion are calculated numerically using the molecular orbitals obtained by the DV-Xα cluster calculations (DV-ME method). The effect of covalency was investigated by comparing the results of the DV-ME calculations with those of the DV-LFT calculations. In the results of the DV-ME calculations, the doublet energy significantly decreased compared to those of the DV-LFT calculations. As a result, the relative positions of the doublets to the quartets are qualitatively reproduced. Although the doublet energies are still slightly overestimated, this small discrepancy can be also improved by taking into account the effect of electron correlations appropriately.

In the DV-ME method, we have recently developed a simple method to take into account the correction to the effect of electron correlation efficiently. Thus the effect of electron correlation was also evaluated quantitatively by comparing the DV-ME calculations with and without the correlation correction (CC). In the results of the DV-ME calculation with CC, the doublet energies decreased further and quantitatively reproduced the experimental values.

Since the effects of charge transfer, covalency and electron correlation all reduce the Coulomb integrals, they are evaluated quantitatively in terms of the reduction of Coulomb integrals. Contrary to the doublets, the quartet energies are quite insensitive to the change of the Coulomb integrals and relatively well reproduced by all calculations. This is due to the fact that the quartet energies are mainly dominated by the effective crystal-field splitting while the doublet energies are mainly dominated by the magnitude of the Coulomb integrals.

As we have demonstrated in the present work, a combination of the DV-LFT calculations and the DV-ME calculations is a quite effective tool for quantitative analysis of various effects such as charge transfer, covalency and electron correlation on the multiplet structure of the transition metal ions in crystals.

ACKNOWLEDGMENT

This work was supported by a Grant-in-Aid for Scientific Research from the Ministry of Education, Science, Sports and Culture of Japan.

REFERENCES

(1) Sugano, S.; Tanabe, Y.; Kamimura, H. "Multiplets of Transition-Metal Ions in Crystals" ; Academic Press: New York, 1970.
(2) Ogasawara, K.; Ishii, T.; Ito, Y.; Ida, H.; Tanaka, I.; Adachi, H. *Jpn. J. Appl. Phys.* **1998**, *37*, 4590.
(3) Ohnishi, S; Sugano, S. *Jpn. J. Appl. Phys.* **1982**, *21*, L309.
(4) Xia, S.; Guo. C.; Lin. L.; Ellis, D. E. *Phys. Rev.* **1987**, *B35*, 7671.
(5) Ogasawara, K.; Ishii, T.; Tanaka, I.; Adachi, H. *Phys. Rev.* **2000**, *B61*, 143.
(6) Mulliken, R. S.; *J. Chem. Phys.* **1955**, *23*, 1833.
(7) Slater, J. C. "Quantum Theory of Molecules and Solids"; McGraw-Hill: New York, 1974; Vol. IV.
(8) Satoko, C.; Tsukada, M.; Adachi, H. *J. Phys. Soc. Jpn.* **1978**, *45*, 1333.
(9) Adachi, H.; Tsukada, M.; Satoko, C. *J. Phys. Soc. Jpn.* **1978**, *45*, 875.
(10) Fazzio, A.; Caldas, M.; Zunger, A. *Phys. Rev.* **1984**, *B29*, 5999.
(11) Adachi, H.; Taniguchi, K. *J. Phys. Soc. Jpn.* **1980**, *49*, 1944.
(12) Szabo, A.; Ostlund, N. S. "Modern Quantum Chemistry"; Macmillan Publishing Co.; New York: 1982.
(13) Fairbank, W. M., Jr ; Klauminzer, G. K.; Schawlow, A. L. *Phys. Rev.* **1975**, *B11*, 60.
(14) Kizler, P.; He, J.; Clarke, D. R.; Kenway, P. R. *J. Am. Ceram. Soc.* **1996**, *79*, 3.

First-principles calculation for multiplet structure of emerald

Takugo Ishii* and Kazuyoshi Ogasawara

Department of Materials Science and Engineering, Kyoto University, Sakyo-ku, Kyoto 606-8501, Japan

Yukiko Ito and Isao Tanaka

Department of Energy Science and Technology, Kyoto University, Sakyo-ku, Kyoto 606-8501, Japan

Hirohiko Adachi

Department of Materials Science and Engineering, Kyoto University, Sakyo-ku, Kyoto 606-8501, Japan

(Recieved November 24, 1998)

We report on the first-principles calculations for multiplet structure of emerald (Cr^{3+}:$Be_3Al_2(SiO_3)_6$, chromium-doped beryllium aluminium silicate, or beryl) obtained by using small $[CrO6]^{9-}$ and larger $[CrBe_3Al_3Si_6O_{42}]^{42-}$ model clusters, both of which have trigonal distorted symmetry from cubic. We revealed that the result of $[CrO6]^{9-}$ model cluster qualitatively reproduced the peak positions of experimental absorption spectrum. Also the energy splittings of each peak due to the trigonal symmetry were obtained. The result of larger model cluster showed better agreement with experiment, and the effect of atomic orbitals of additional host cations were evaluated.

KEYWORDS: first-principles calculation, multiplet structure

* Corresponding author, e-mail: *tack@dvxa4.mtl.kyoto-u.ac.jp*

ADVANCES IN QUANTUM CHEMISTRY, VOLUME 37

0065-3276/01 $35.00

1. INTRODUCTION

Emerald (Cr^{3+}:$Be_3Al_2(SiO_3)_6$, chromium-doped beryllium aluminium silicate or beryl) is a well known gem, and its beautiful green color has been attracted people for a long time. Nowadays, emerald crystal is also known as a tunable solid-state laser material, and its optical properties have been studied (1-10).

To understand the mechanism of interaction between light and electrons from a view of quantum chemistry, it is necessary to calculate the electronic structures including many-electron interaction, which has been, however, a great problem in physics due to the difficulty on computational procedure. Most of the general methods for electronic-state calculation are carried out in the one-electron approximation, which could not be applied to the direct calculations in many-electron system, such as multiplet structure in optical spectrum.

Avoiding to directly calculate the electronic structure in many-electron system, many studies about analysis of optical spectra for solid-state laser materials have been successfully done by a parameter-fitting method based on ligand field theory developed by Sugano *et al.* (11), and the empirical method have been widely applied also to emerald (1,4). The empirical method has brought us many pictures of how to understand the overall multiplet structure, and has enabled us to assign the peaks in observed spectrum to the corresponding electronic states. Although the method is very useful for the materials whose experimental spectrum is already known, it is difficult, however, to apply it to the development of new materials, since the method analytically parametrizes all the integrals of electron-electron repulsive interaction and determines the values of parameters by fitting into the experimental data. Moreover, several critical approximations are introduced into it for simplification, for example; the radial parts of all wave functions are assumed to be the same, and all the distortions intrinsic to crystal structure are neglected. Therefore this empirical method has little power for "materials design", which requires predictions on the electronic structures based on the first-principles calculations.

As we know, a few first-principles calculations for multiplet structure have been tried by several researchers. Ohnishi and Sugano calculated the energy positions of the ^2E (R line) and $^4T_2$ (U band) states in ruby, under one-electron approximation (12). Xia *et al.* carried out similar calculations using more realistic model cluster (13). They could, however, only consider the energies of lower-lying two states in multiplet structure. Watanabe and Kamimura combined one-electron calculations with ligand field theory, and carried out first-principles calculation for the "full" multiplet structure of several transition metal impurities

in semi-conductors under Td (or Oh) symmetry. They showed that the empirical method sometimes results in a crucial fault on the interpretation of optical spectra due to its approximations for simplification (14-16).

We recently developed a general method, to directly calculate the electronic structure in many-electron system; DV-ME (Discrete Variational MultiElectron) method. The first application of this method has been reported by Ogasawara *et al.* in ruby crystal (17). They clarified the effects of covalency and trigonal distortion of impurity-state wave functions on the multiplet structure.

In the present paper, we applied the newly developed DV-ME method to the calculations of the multiplet structure in emerald, in which dilutely doped Cr^{3+} ions substitutes for aluminium ions and work as a color active center.

2. COMPUTATIONAL PROCEDURE

2.1. DV-ME method

The computational procedure for calculation of multiplet energy in the DV-ME method has two steps; in the fist step, one-electron molecular orbitals (MOs) and MO energies of the impurity states are calculated by the DV-Xα molecular orbital method (18); in the second step, the many-electron Hamiltonian, in which the interactions between two electrons are exactly described, is diagonalized within a subspace spanned by Slater determinants made up of the obtained one-electron MOs.

In the first step, the DV-Xα molecular orbital method is carried out self-consistently, in which the exchange and correlation energies are taken into account by the use of Xα potential given by Slater (19). In the present calculations, the coefficient α is fixed at 0.7, which was found to be an appropriate value (20). The MOs are expressed as linear combinations of atomic orbitals (LCAOs). These atomic orbitals are numerically adjustable to the chemical environment in each iteration. The details of the DV-Xα method have been described by Adachi *et al.* (18).

In the second step which is a core part of the DV-ME method, the many-electron wave functions are described as linear combinations of Slater determinants, and all the matrix elements of the many-electron Hamiltonian are calculated, then finally diagonalized to obtain the multiplet energies and many-electron wave functions.

The many-electron wave function corresponding to the l-th state in multiplet is expressed as,

$$\Psi_l = \sum_{j=1}^{n} W_{jl} \Phi_j \tag{1}$$

where Φ_j is the Slater determinants of j-th micro state, n is the total number of the Slater determinants, and W are the coefficients of the linear combinations. The Slater determinants are made up by the obtained one-electron MOs of impurity state φ, such as,

$$\Phi_m = \frac{1}{\sqrt{n!}} \begin{vmatrix} \varphi_1(\boldsymbol{r}_1) & \varphi_1(\boldsymbol{r}_2) & \cdots & \varphi_1(\boldsymbol{r}_n) \\ \varphi_2(\boldsymbol{r}_1) & \varphi_2(\boldsymbol{r}_2) & \cdots & \varphi_2(\boldsymbol{r}_n) \\ \vdots & & & \vdots \\ \varphi_n(\boldsymbol{r}_1) & \varphi_n(\boldsymbol{r}_2) & \cdots & \varphi_n(\boldsymbol{r}_n) \end{vmatrix} \tag{2}$$

In the present version of the DV-ME method, we adopt an approach proposed by Fazzio *et al.* (21) for the calculation of the effective many-electron Hamiltonian. In that method, the many-electron Hamiltonian is divided into two parts; one is the effective one-electron Hamiltonian and the other is the electron-electron repulsive interaction. The energy levels in multiplet are classified into several electron configurations. In the case of d^3 configuration under cubic symmetry, the possible electron configurations are $(t_{2g})^m(e_g)^n$, (m,n) = (3,0), (2,1), (1,2), (0,3). The gravity centers of energy in each electron configuration are determined by the one-electron MO energies obtained in the first step, which are added to the diagonal parts of the matrix of many-electron Hamiltonian.

The time-consuming calculation is that of the electron-electron repulsion parts in matrix elements of the many-electron Hamiltonian. This calculation is reduced to that of the two-electron integrals, which is expressed in atomic unit as,

$$\iint \varphi_i^*(\boldsymbol{r}_1)\, \varphi_j^*(\boldsymbol{r}_2)\, \frac{1}{|\boldsymbol{r}_1 - \boldsymbol{r}_2|}\, \varphi_k(\boldsymbol{r}_1)\, \varphi_l(\boldsymbol{r}_2)\, d\boldsymbol{r}_1\, d\boldsymbol{r}_2 \tag{3}$$

In the present work, above integrals are calculated as weighted sum of integrands

at DV sample points (22), such as,

$$\sum_{\alpha}\sum_{\beta\neq\alpha}\varphi_i(r_\alpha)\,\varphi_j(r_\beta)\,\frac{1}{|r_\alpha - r_\beta|}\,\varphi_k(r_\alpha)\,\varphi_l(r_\beta)\,\omega(r_\alpha)\,\omega(r_\beta) \tag{4}$$

where ω are the weight functions proportional to the inverse of density of DV sample points. This numerical method makes us possible to overcome the computational difficulty in multicenter integration.

When all the matrix elements are obtained, the multiplet structure can be easily obtained by diagonalization the matrix. The details of the DV-ME method have been described by Ogasawara *et al.* (17).

In the present work, the effect of electron correlation was additionally considered by a convenient method. The electron correlation energy derives from underestimation of the interaction between two electrons mainly with opposite spins, when the Slater determinants are used. Within the limited subspace, therefore, the effective electron repulsion energy should be somewhat reduced. In order to take into account of this effect, we multiplied an averaged factor C (C<1) in the expression (4), such as,

$$C\sum_{\alpha}\sum_{\beta\neq\alpha}\varphi_i(r_\alpha)\,\varphi_j(r_\beta)\,\frac{1}{|r_\alpha - r_\beta|}\,\varphi_k(r_\alpha)\,\varphi_l(r_\beta)\,\omega(r_\alpha)\,\omega(r_\beta) \tag{5}$$

The correlation factor C can be determined from first principles so that the averaged energy difference associated with one-electron spin flip transition in multiplet structure corresponds to the transition energy obtained by one-electron calculation in the Slater's transition state. The details on the correlation factor C will be described by Ogasawara *et al.* (23). The calculated theoretical value through the results in the present study ranged from 0.86 to 0.91 slightly depending on the model clusters.

2.2. Model clusters

Emerald is an oxide in which chromium ions are dilutely doped and work as color active centers. The host crystal is beryllium aluminium silicate, or simply

called beryl, which contains Be^{2+}, Al^{3+}, Si^{4+}, and O^{2-} ions. The Cr^{3+} ions substitute for Al^{3+} ions which are sixfold coordinated by O^{2-} ions. This octahedron has intrinsic distortion from cubic symmetry, D_3 symmetry on the center Cr^{3+} site, and the octahedron is a key structure when we consider the multiplet structure. The structural details are described in (2,10,25).

For the calculation of the multiplet structure of emerald, we used three types of model clusters, shown in Fig. 1; (1) $[CrO_6]^{9-}$ in hypothetical O_h symmetry, (2) $[CrO_6]^{9-}$ in D_3 symmetry, and (3) $[CrBe_3Al_3Si_6O_{42}]^{42-}$ including cations making up of the host lattice. The model (1) is a model where the trigonal distortion is removed to have a cubic symmetry for a comparison with the model (2) in D_3 symmetry, to confirm that the local symmetry is to be considered in the DV-ME calculation. In the model (2), the atomic locations are taken from a real structure of the host lattice whose symmetry is D_3 on the Al^{3+} site. The model (3) is extended from the model (2) to have additional ions which make up of host lattice, and the point charges are placed at the external atomic sites so as to reproduce the effective Madelung potential.

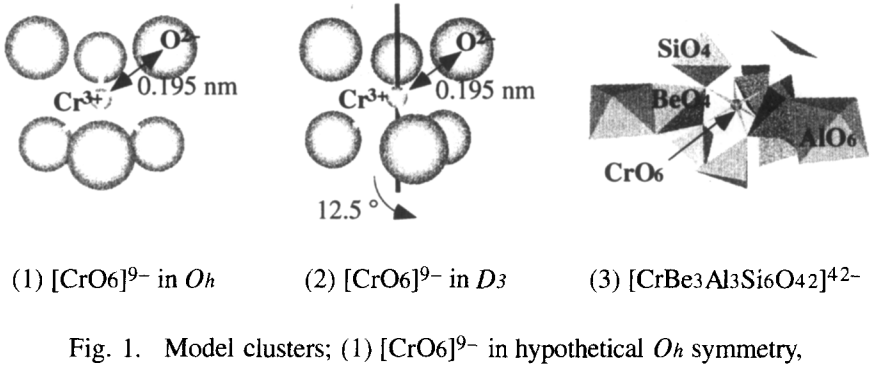

(1) $[CrO_6]^{9-}$ in O_h (2) $[CrO_6]^{9-}$ in D_3 (3) $[CrBe_3Al_3Si_6O_{42}]^{42-}$

Fig. 1. Model clusters; (1) $[CrO_6]^{9-}$ in hypothetical O_h symmetry, (2) $[CrO_6]^{9-}$ in D_3 symmetry, and (3) $[CrBe_3Al_3Si_6O_{42}]^{42-}$ including the host cations.

The number of DV sample points used are 90000 for models (1) and (2), and 96000 for model (3). Espescially for the small models (1) and (2), the number is well enough to express the effect of the difference in local symmetries.

The basis functions used are $1s$-$2p$ for beryllium and oxygen, $1s$-$3d$ for aluminium and sillicon, and $1s$-$4p$ for chromium.

3. RESULTS AND DISCUSSION

3.1. One-electron MO energies

The calculated one-electron MO energies in ground state are shown in Fig. 2, where the energies of the highest occupied MOs are set at zero. The valence band consists mainly of O-2*p* orbitals. In the model (3), the band structure appears, and the conduction band is described mainly by Be-2*sp*, Al-3*spd*, and Si-3*spd* orbitals. In all the results, the levels mainly occupied by Cr-3*d* orbitals appear well above the O-2*p* valence. These levels are taken as the impurity levels to form the Slater determinants.

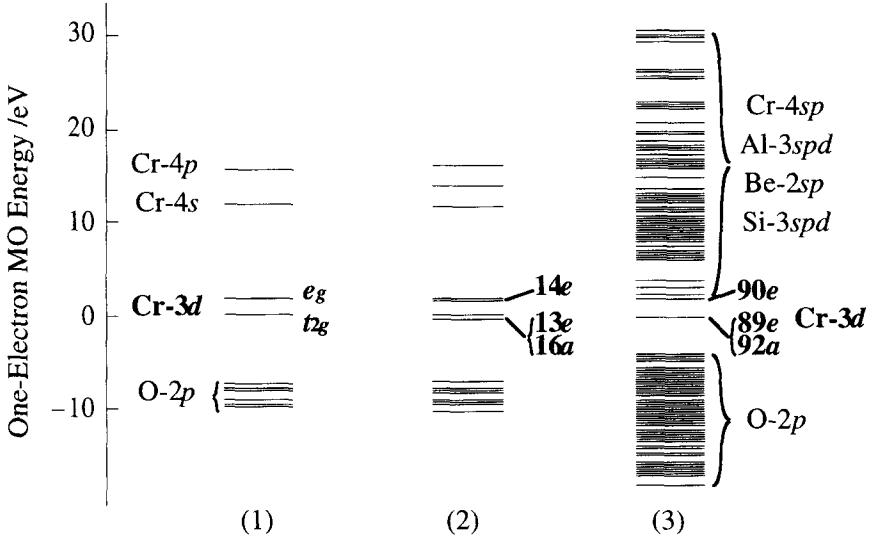

Fig. 2. Calculated one-electron MO energies for each model cluster, (1), (2), and (3).

In the result of the hypothetical model (1) with O_h symmetry, the impurity MO levels split into the levels with t_{2g} and e_g symmetry. The magnitude of this splitting is generally called a crystal field splitting, and is given a symbol Δ_{eff}. The calculated value of Δ_{eff} is 1.88eV. In the results of models (2) and (3) with

D_3 symmetry, the t_{2g} state splits further into a and e states affected by the trigonal distortion in the local structure. Since the calculated value of the trigonal splitting is relatively smaller than that of Δ_{eff}, we still use the notations of t_{2g} and e_g in O_h symmetry for simplicity, and evaluated the energy of the t_{2g} state by averaging the energy of corresponding a and e states. By this simplification, we can estimate the values of Δ_{eff} also for models (2) and (3), and they are 1.85eV and 1.88eV, respectively.

3.2. Multiplet structures

The calculated multiplet structures are shown in Fig. 3. The obtained energies actually ranged up to 10 eV, but the results here are shown only within the energy region of visible light for the comparison with an experimental absorption spectrum obtained by Fairbank *et al.* (1). The referential spectrum has trigonal anisotropy, which shows different spectra depending on whether the direction of the vector of the electric field of incident light is perpendicular ($\boldsymbol{E}\perp c$) or horizontal ($\boldsymbol{E}//c$) to the crystallographic c-axis. All the peak positions are plotted with the corresponding assignments.

In each multiplet structure, the data are separated according to the spin degeneracy; spin quartet state on the right hand and spin doublet state on the left. The electron configuration of the Cr^{3+} ion is usually expressed as d^3 under atomic notation, and the quartet and doublet state correspond to the high spin state and low spin state, respectively. Since the ground state $^4A_2$ is a quartet state, the transitions to the quartet states are the spin-allowed transitions which have large intensities and broad bands in the absorption spectra, on the other hand, the transitions to the doublet states are the spin-restricted transitions which have more than one order smaller intensities and narrow line peaks which are not obvious in the experimental spectra in Fig. 3.

First, we compare the results of models (1) and (2), whose differrence is only in their local symmetries. In the result of model (1) in hypothetical O_h symmetry, all the labeled levels show exact twofold or threefold degeneracy affected by the spatial symmetry, that is E state or T state respectively, except the ground state $^4A_2$. This indicates that the result of DV-ME calculation well reflects the local structure of model cluster with appropriate degeneracies in energy. On the other hand in the result of model (2) which is in the D_3 symmetry, all the threefold degenerate levels split into A and E states affected by the trigonal distortion of the symmetry of the model cluster. This splittings correspond to the spectral

anisotropy in the experimental spectrum. In general, this effect of the trigonal distortion is considered only by empirical way, but here we calculated the energy splittings without introducing any approximations in wave functions nor referring any experimental data. In the previous report on multiplet structure in ruby by Ogasawara *et al.* (17), the calculated results didn't show excellent degeneracies, and they assumed that it is due to the small number of DV sample points which they used are 20000 points for the equivalent model clusters to ours. In the present paper, we used much more DV sample points, 90000 points, to improve the accuracy of integration.

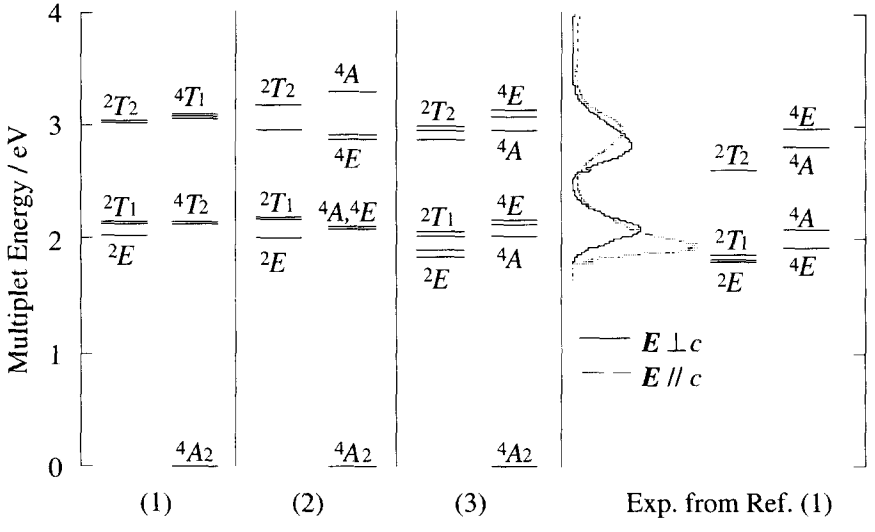

Fig. 3. Calculated multiplet structures for model cluster (1), (2), and (3). The experimental absorption spectrum is drawn in the right column for comparison. The levels are classified into quartet and doublet state, respectively right and left columns in each datum.

Next, we compare the result of model (3) with that of model (2). The result of the larger model (3) shows better agreement with experimental absorption spectrum in overall peak positions espescially in doublet states, and also in the trigonal splittings.

All the states in doublet state within the region of visible light in Fig. 3, plus the ground state $^4A_2$ in quartet state, belong to $(t_{2g})^3$ electron configuration

under the notation in O_h symmetry, and the difference in energy between them derives only from the difference in electron-electron repulsive interactions. Since their average energy lies in the gap between the lowest ^2E and $^4A_2$ states, the peak position of ^2E state can be regarded as an indication for the magnitude of the Coulomb repulsive energy. The reason why the doublet state in the result of model (3) shifted down to be relatively better than that of model (2), is mainly ascribed to the presence of the cations constituting the host lattice. When the overlap of atomic orbitals between ligand oxygens and the host cations is considered, the ligand oxygen's orbitals will vary to mix more with impurity-state MOs, and also the cations' orbitals will directly mix with them. As a result, the impurity-state MOs with t_{2g} and e_g symmetries will be spatially extended in some degree, and the associated Coulomb repulsion energies decrease.

In fact, this is confirmed by analysing the propotion of the atomic orbitals in the impurity-state MOs by Mulliken's method (25). The results for the models (2) and (3) are shown in Table I. We can see from the result that the MOs in the model (2) are more Cr-3*d* like ones, and the O-2*p* component is smaller than that of the model (3). This indicates that the impurity-state orbitals in the model (2) are relatively localized on the chromium ion, therefore, the electron-electron repulsive interaction in the model (2) is much larger than that of the model (3). In the model (3), we can expect that the additional contribution of Si-3*spd* orbitals causes further extensions of MOs, resulting in the reduction of the Coulomb repulsion energy.

From the Table I, moreover, we can see that the contributions of Cr-3*d* orbital are significantly different between the MOs with t_{2g} and e_g symmetry. This result indicates that the difference of interaction between the impurity and the ligand orbitals according to the direction of spatial extension of the orbitals is very important for the calculation of multiplet structure. Why the empirical method has been seemed to be successfully explained the multiplet structure, nevertheless it approximates the radial parts of wave functions to be the same one, is supposed that it "hides" and "rounds off" the errors by adjusting the parameters arbitrarily to the experimental data.

The energy splittings of each peaks in the model (3) seem to be better in agreement with experimental data than that in model (2). The old empirical methods have been restricted the discussions only about the circumstance within the first-nearest neighbor, but our results imply that the existence of host cations outside of the ligand oxygens is not negligible. Although there seem to be some discrepancies in the trigonal energy splittings in each peak between the calculated result and the experimental one, they may be ascribed to the still small size of the model cluster.

Table I. The propotion of the atomic orbitals in the impurity-state MOs [%] for the models (2) and (3) by Mulliken's method.

Model (2)		t_{2g} 16*a*	t_{2g} 13*e*	e_g 14*e*
Cr	3*d*	95.8	95.7	87.1
	4*sp*	0.3	0.1	0.1
	total	96.1	95.8	87.2
O	2*s*	0.0	0.0	1.9
	2*p*	3.9	4.1	11.0
	total	3.9	4.1	12.9

Model (3)		t_{2g} 92*a*	t_{2g} 89*e*	e_g 90*e*
Cr	3*d*	93.9	92.9	83.2
	4*sp*	0.0	0.1	0.0
	total	93.9	93.0	83.2
O	2*s*	0.1	0.2	2.1
	2*p*	4.9	4.8	11.6
	total	5.0	5.0	13.7
Al	3*spd*	0.0	0.0	0.0
Be	2*sp*	0.2	0.1	0.2
Si	3*s*	0.3	0.6	0.5
	3*p*	0.4	0.7	1.2
	3*d*	0.3	0.4	1.1
	total	1.0	1.7	2.8

4. SUMMARY

The multiplet structure of emerald was calculated form first principles with three types of model clusters. The calculated results revealed that the overall multiplet structure was qualitatively reproduced without referring any empirical data. Moreover, the energy splittings due to the trigonal distortion was obtained from first principles. Enlarging the size of model cluster, we considered the effect of atomic orbitals of the host cations by quantitative Mulliken's population analysis, and revealed that not only the ligand oxygen orbitals but also Si-3*spd* orbitals should be included on the description of the multiplet structure.

ACKNOWLEDGMENT

This work was supported by a Grant-in-Aid for Scientific Research from the Ministry of Education, Sports, and Culture. The calculations were partly carried out by the application server Silicon Graphics Inc. POWER CHALLENGE

10000 XL (MIPS R10000, 8 CPU) in *Data Processing Center, Kyoto University, Japan.*

REFERENCES

(1) Fairbank, W. M. Jr.; Klauminzer, G. K.; Schawlow, A. L. *Phys. Rev.* **1975**, *B 11*, 60.
(2) Quarles, G. J.; Suchocki, A.; Powell, R. C. *Phys. Rev.* **1988**, *B 38*, 9996.
(3) Kisliuk, P; Moore, C. A. *Phys. Rev.* **1967**, *160*, 307.
(4) Wood, D. L; *J. Chem. Phys.* **1965**, *42*, 3404.
(5) Burns, G; Geiss, E. A.; Jenkins, B. A.; Nathan, M. I. *Phys. Rev.* **1965**, *139*, A1687.
(6) Buchert, J.; Katz, A.; Alfano, R. R. *IEEE J. Quantum Electron.* **1983**, *QE-19*, 1477.
(7) Halperin, B.; Nicollin, D.; Koningstein, J. A. *Chem. Phys.* **1979**, *42*, 277.
(8) Veremeichik, T. F.; *Phys. Status Solidi* **1984**, *B 124*, 719.
(9) Hasan, Z.; Keany, S. T.; Manson, N. B. *J. Phys.* **1986**, *C 19*, 6381.
(10) Edgar, A.; Hutton, D. R. *J. Phys.* **1978**, *C 11*, 5051.
(11) Sugano, S.; Tanabe, Y; Kamimura, H. *Multiplets of Transition-Metal Ions in Crystals*; Academic Press, New York, 1970.
(12) Ohnishi, S.; Sugano, S. *Jpn. J. Appl. Phys.* **1982**, *21*, L309.
(13) Xia, S.; Lin, C. G. L.; Ellis D. E. *Phys. Rev.* **1987**, *B 35*, 7671.
(14) Watanabe, S.; Kamimura, H. *J. Phys. Soc. Jpn.* **1987**, *56*, 1078.
(15) Watanabe, S.; Kamimura, H. *J. Phys.* **1987**, *C 20*, 4145.
(16) Watanabe, S.; Kamimura, H. *Mater. Sci. and Eng.* **1989**, *B 3*, 313.
(17) Ogasawara, K.; Ishii, T.; Ito, Y; Ida, H.; Tanaka, I.; Adachi, H. *Jpn. J. Appl. Phys.* **1998**, *37*, 4590.
(18) Adachi, H.; Tsukada, M.; Satoko, C.; *J. Phys. Soc. Jpn.* **1978**, *45*, 875.
(19) Slater, J. C. *Quantum Theory of Molecules and Solids Vol. 4*; McGraw-Hill, New York, 1974.
(20) Satoko, C.; Tsukada, M.; Adachi, H. *J. Phys. Soc. Jpn.* **1978**, *45*, 1333.
(21) Fazzio, A.; Caldas, M. J.; Zunger, A. *Phys. Rev.* **1984**, *B 30*, 3430.
(22) Adachi, H.; Taniguchi, K.; *J. Phys. Soc. Jpn.* **1980**, *49*, 1944.
(23) Ogasawara, K.; Ishii, T.; Tanaka, I.; Adachi, H.; in this proceedings.
(24) Bragg, W. L.; West, J. *Proc. R. Soc. London* **1926**, *Ser. A 111*, 691.
(25) Mulliken, R. S. *J. Chem. Phys.* **1955**, *23*, 1833.

The effect of intrinsic trigonal distortion on the multiplet structures of ruby and emerald

Yukiko Ito* and Isao Tanaka

Department of Energy Science and Technology
Kyoto University, Sakyo-ku, Kyoto 606-8501 Japan

Takugo Ishii, Kazuyoshi Ogasawara and Hirohiko Adachi

Department of Materials Science and Engineering
Kyoto University, Sakyo-ku, Kyoto 606-8501 Japan

(Recieved November 24, 1998)

In most of the practical solid-state laser materials, the local structure around the impurity ion is more or less distorted from cubic symmetry. For example in ruby and emerald, each chromium ion is surrounded by six oxygen ions but these oxygen octahedrons are trigonally distorted in different ways. In the traditional analysis based on the ligand-field theory, such distortions are ignored. So in order to clarify the effect of low symmetry on multiplet structures of ruby and emerald, we gradually changed the cluster symmetry from that of the real crystal to cubic, and calculated the multiplet structures for all of these clusters, using the recently developed discrete variational-multielectron (DV-ME) method. The calculated results indicate that the dominant factor of the low symmetry effect is quite different between ruby and emerald.

KEYWORDS: multiplet structure, laser materials, low symmetry

*Corresponding author: e-mail yukiko@dvxa4.mtl.kyoto-u.ac.jp

ADVANCES IN QUANTUM CHEMISTRY, VOLUME 37

0065-3276/01 $35.00

1. INTRODUCTION

In solid-state laser materials, such as ruby (chromium doped alumina, $Al_2O_3:Cr^{3+}$) (1) and emerald (chromium doped beryl, $Be_3Al_2(SiO_3)_6:Cr^{3+}$) (2), transitions between multiplets of impurity states are utilized. These states mainly consist of $3d$ orbitals of the impurity chromium ions. For the analysis of these multiplet structures, the semi-empirical ligand-field theory (LFT) has been frequently used (3). However, this theory can be applied only to the high symmetry systems such as O_h (or T_d). Therefore, the effect of low symmetry is always ignored in the analysis based on the LFT, although most of the practical solid-state laser materials actually possess more or less distorted local structures. For example, in ruby and emerald, the impurity chromium ions are substituted for the aluminum ions in the host crystals and the site symmetry of the aluminum ions are C_3 in alumina and D_3 in beryl. Therefore, it is important to clarify the effect of low symmetry on the multiplet structure, in order to understand the electronic structure of ruby and emerald.

Recently, we have developed a general method to calculate multiplet structures from first principles, which we call discrete variational-multielectron (DV-ME) method (4). In this method, multiplet structures of distorted molecular orbitals can be calculated since the distortion of the molecular orbitals are directly taken into account by the numerical calculation of matrix elements of electron-electron repulsion. Taking advantage of this method, we applied it to the investigation of the low-symmetry effects on the multiplet structures of ruby and emerald. By calculating the multiplet structure using various CrO_6 clusters, in which the cluster symmetry is gradually changed from that of the real crystal to cubic, the dominant factors of the low-symmetry effect in ruby and emerald are clarified for the first time.

2. COMPUTATIONAL METHOD

In the DV-ME method, multiplet structures are calculated with two steps. First the molecular orbitals (MOs) and orbital energies are obtained by one-electron cluster calculations and second, the many-electron Hamiltonian is diagonalized within the subspace spanned by the Slater determinants constructed from the obtained MOs.

One-electron cluster calculations are carried out based on the local density functional approach using the DV-Xα computation code developed by Adachi *et al.* (5). The exchange-correlation energy is taken into account using the Slater's Xα potential (6). In the present work, α is set at 0.7, which is found to be the most appropriate value in many cases (7). The MOs are obtained as linear combinations of atomic orbitals (LCAO). The most remarkable feature of our program is that the atomic orbitals (AOs) are numerically calculated in each iteration and optimized for the chemical environment. The details of this program have been discribed in ref. (5)

After the one-electron calculation, the Slater determinants corresponding to all the possible selections of impurity-state orbitals are constructed as,

$$\Psi = \frac{1}{\sqrt{n!}} \begin{vmatrix} \phi_1(\mathbf{r}_1) & \phi_2(\mathbf{r}_1) & \cdots & \phi_n(\mathbf{r}_1) \\ \phi_1(\mathbf{r}_2) & \phi_2(\mathbf{r}_2) & \cdots & \phi_n(\mathbf{r}_2) \\ \vdots & & \ddots & \vdots \\ \phi_1(\mathbf{r}_n) & \phi_2(\mathbf{r}_n) & \cdots & \phi_n(\mathbf{r}_n) \end{vmatrix}, \tag{1}$$

where ϕ_n are the MOs obtained by the DV-Xα calculation. These detarminants are used as basis-functions to describe the many-electron system. The Hamiltonian of the many-electron system can be expressed as,

$$H = \sum_k \{-\frac{1}{2}\nabla_k^2 - \sum_\gamma \frac{Z_\gamma}{r_{k\gamma}}\} + \sum_i \sum_{j<i} \frac{1}{r_{ij}}, \tag{2}$$

where Z_γ is nuclear charge of the γ -th atom.

The first term is the kinetic energy and the second term is the Coulomb potential of the nuclei and the third term is the Coulomb repulsion energy

between electrons. Multiplet structures are obtained by diagonalizing this many-electron Hamiltonian. For the actual calculation of the multiplet structures of ruby and emerald, however, only the electrons in the impurity states are treated directly. In this approximation, it is necessary to evaluate the average potential of the remaining electrons, which is not a simple problem. Instead of calculating the explicit form of the potential, Fazzio *et al.* proposed a simple method to calculate the matrix elements of the many-electron Hamiltonian (8). In this method, the Slater determinants are classified into several electronic configurations and the average energies of each configuration are evaluated by one-electron calculations. In the present work, we adopt this approach and the Slater determinants are classified into the electronic configurations in the form of $(t_{2g})^m(e_g)^n$ and the energy separation of these configurations are evaluated using the orbital energies calculated in the ground state as we did in our previous work (4). For the evaluation of the third term in Eq.(2) associated with the electrons in the impurity states, we have to calculate electron-electron repulsion integrals in the form of

$$\langle ij \,\|\, kl \rangle = \iint \phi_i^*(\mathbf{r}_1)\phi_j^*(\mathbf{r}_2)\frac{1}{r_{12}}\phi_k(\mathbf{r}_1)\phi_l(\mathbf{r}_2)\,d\mathbf{r}_1 d\mathbf{r}_2 \qquad (3)$$

In the DV-ME method, these integrals are calculated as the weighted sum of integrands at sampling points (9) using the equation,

$$\langle ij \,\|\, kl \rangle = \sum_{\alpha} \omega(\mathbf{r}_\alpha)\phi_j^*(\mathbf{r}_\alpha)\left[\sum \omega(\mathbf{r}_\beta)\phi_j^*(\mathbf{r}_\beta)\frac{1}{r_{\alpha\beta}}\phi_l(\mathbf{r}_\beta)\right]\phi_k(\mathbf{r}_\alpha). \qquad (4)$$

where ω is the sampling point density. One can therefore avoid the computational difficulty associated with the multicenter integration. Moreover, the effect of distortion of the MOs can be taken into account through the numerical integration of Eq. (4). The details of the DV-ME method have been described in ref. (4) In the present work, the electron correlation effects are also taken into account making use of the spin-polarized DV-Xα method (9).

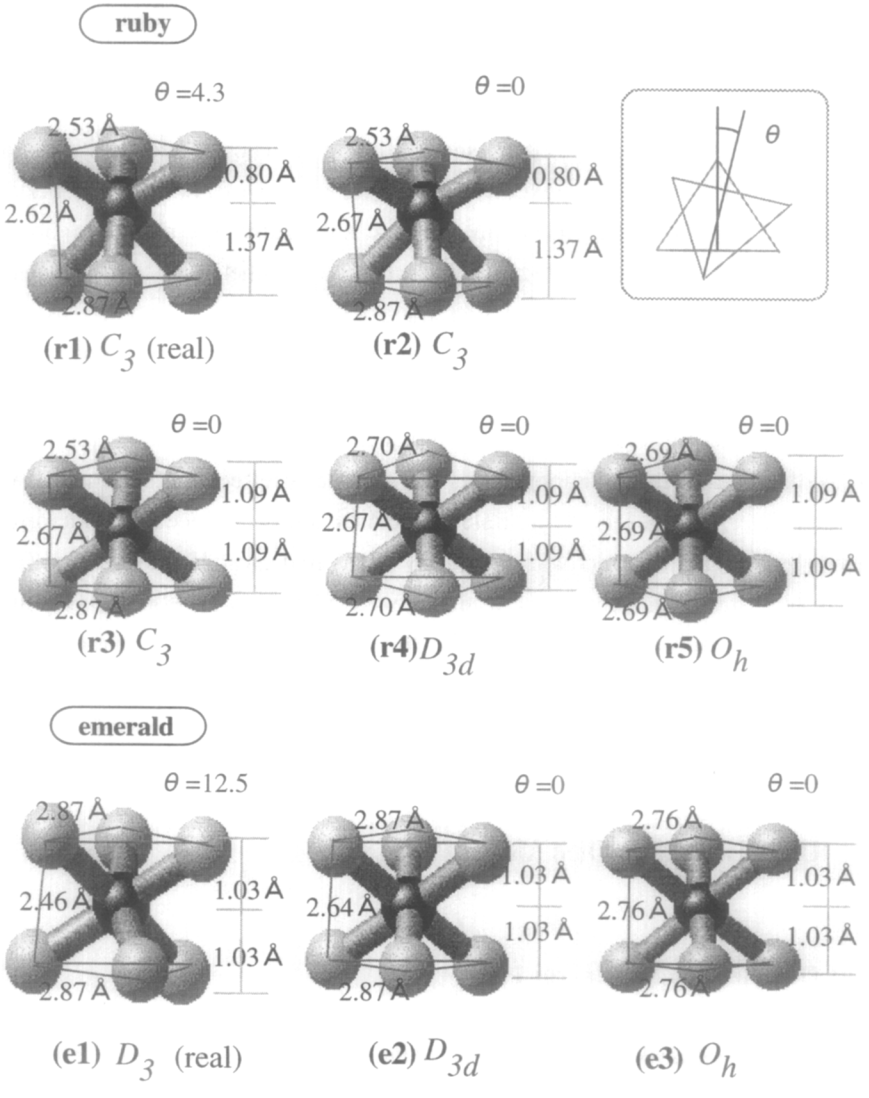

Fig 1. Model clusters used for the calculation of the multiplet structures of ruby and emerald ;
In each cluster, the chromium ion at the center is surrounded by six oxygen ions located at the positions described in the figure.

3. Cluster Models

In order to clarify the low-symmetry effects in ruby and emerald, various CrO_6 clusters are constructed as shown in Fig 1. The atomic positions of clusters (**r1**) and (**e1**) are taken from the real crystal of alumina and beryl, respectively, where the chromium ions are substituted for aluminum ions. Other clusters are constructed by changing the symmetry of these clusters gradually toward cubic symmetry (**r5** and **e3**). Although it is better to use larger clusters for the reproduction of the observed multiplet structures, the clusters with gradually changed symmetry cannot be constructed uniquely, if the cations of the host materials are included. Therefore, we adopt the CrO_6 clusters for the investigation of the low-symmetry effect for simplicity. As shown later, the observed multiplet structures are reproduced satisfactorily even by the CrO_6 clusters with symmetry of the real crystals (**r1** and **e1**). The multiplet structures of these clusters are calculated using 90000 sampling points for each cluster. The basis functions used in the one-electron calculations are 1*s*-2*p* for oxygen and 1*s*-4*p* for chromium.

4. RESULTS AND DISCUSSIONS

4.1 One-electron MO energy levels

The one-electron MO energy levels calculated for the various model clusters of ruby and emerald are shown in Fig 2. The valence band mainly consists of O-2*s*,2*p* orbitals. The width of the valence band decrease as the symmetry of the cluster approaches to cubic. The decrease of the valence band width is more significant in ruby than in emerald. The conduction band is not reproduced in these calculations, because the cations of the host crystals are not included in the present clusters. There are impurity states with

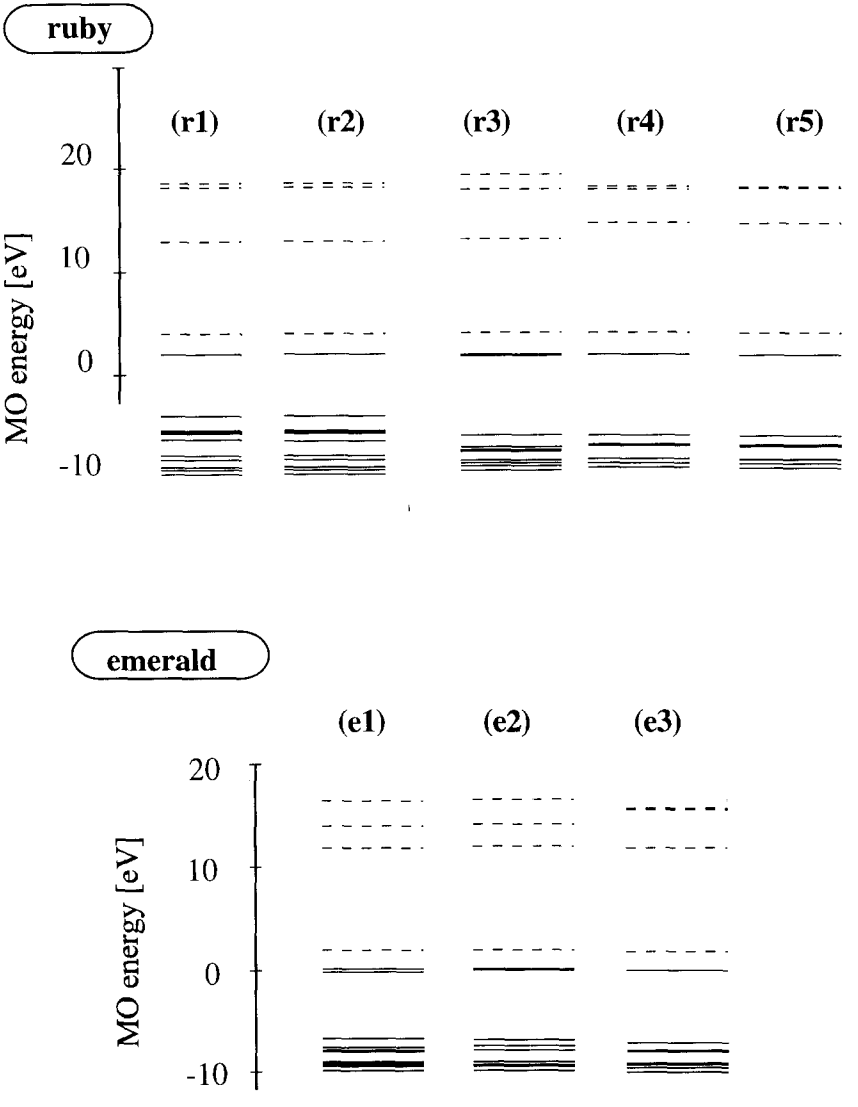

Fig 2. Calculated one-electron MO energies for the clusters shown in Fig 1;
The highest occupied molecular orbital (HOMO) levels are set at zero.

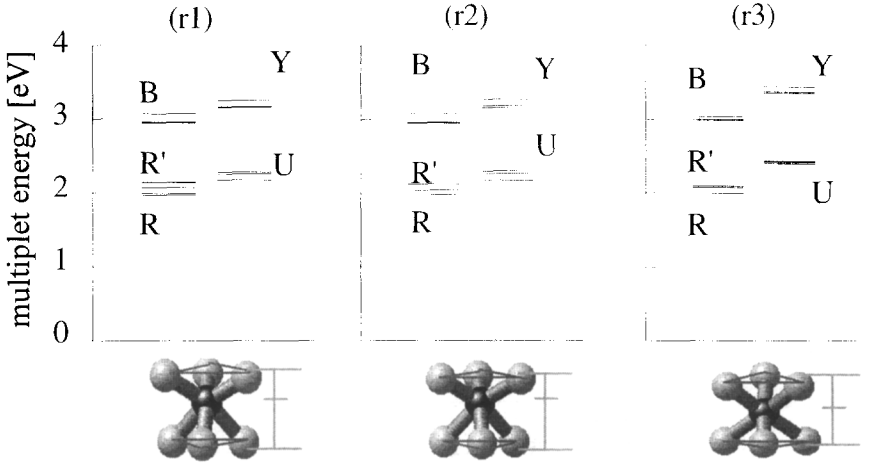

Fig 3. Calculated multiplet energies for the various model clusters of ruby shown in Fig 1;

approximately t_{2g} and e_g symmetry mainly consisting of Cr-3*d* orbitals. Except the cluster with cubic approximation (**r5** and **e3**), the t_{2g} state further splits into *a* and *e* states. However, because these splits are quite small, we still use the notation of t_{2g} and e_g for simplicity and evaluate the energy of t_{2g} as the average energy of correspondig *a* and *e* states. In this way, the matrix elements of the many-electron Hamiltonian are calculated by the Fazzio's method. The energy separation between t_{2g} and e_g orbitals is almost independent of the clusters. However, the symmetry of the impurity orbitals changes gradually according to the symmetry of the clusters. In the DV-ME method, multiplet structures of distorted MOs can be calculated directly using the numerically obtained MOs. As shown in the subsequent sections, the effect of distortion of the MOs are demonstrated in the multiplet energy levels.

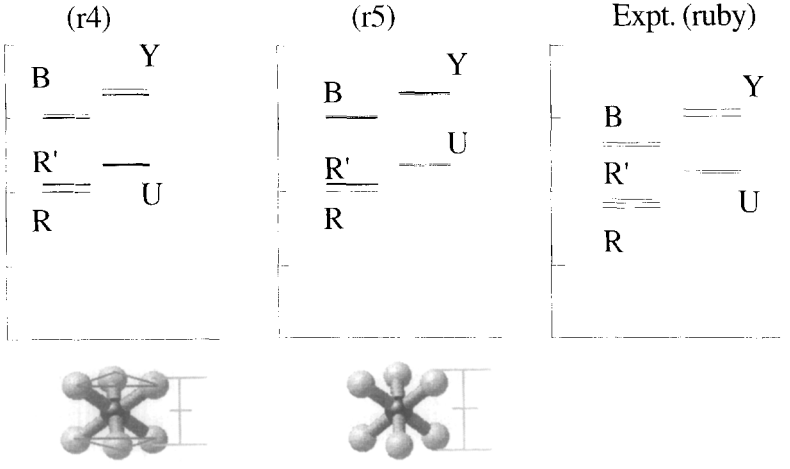

In the results for each cluster, doublets are shown on the left and quartets are on the right. The peak positions of the observed absorption spectra of ruby (10) are shown on the far right.

4.2 Effect of low symmetry in ruby

The calculated multiplet structures for the various model clusters of ruby are shown in Fig 3. The peak positions in the observed optical spectra are also shown on the right (10). In the results of each cluster, the doublets are shown on the left and quartets are on the right. Since the ground state is a quartet, the transitions to quartet states are allowed by the spin-selection rule and observed as strong and broad bands (U and Y).

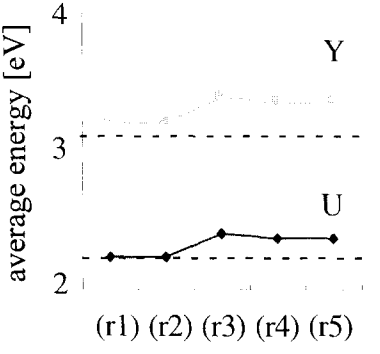

Fig 4. The calculated average energy of the U band (solid rhombus) and that of the Y band (solid square) for each model cluster of ruby;
Dotted lines are the average energy of the U band and that of the Y band in the observed absorption spectra.

On the other hand, the transitions to doublet states are forbidden by the spin-selection rule. However, the spin-selection rule is slightly released by the presence of the spin-orbit interaction and these transitions are observed as weak and sharp lines (R, R' and B). For the calculated results of the cluster with symmetry of the real crystal (**r1**), the experimental peak positions are well reproduced as shown in Fig 3. In our previous result using the same cluster (4), the energy of R' line is slightly greater than U band. This discrepancy can be ascribed to the effect of electron correlation, since the energy separation between R line and R' line is due to the electron-electron repulsion. In the present work, the electron-electron repulsion energy is reduced due to the electron correlation and thus the energy of R' line decreased. Moreover, in the present work, the number of sampling points is 90000, which is much greater than that in our previous calculation (20000). Therefore, the present calculation is more accurate. As a result, the degeneracy of each level is improved and trigonal splits of each state are demonstrated clearly.

Although we have pointed out that the effect of the aluminum ions is important for the quantitative analysis of the multiplet structure of ruby (2), the result of the cluster (**r1**) reproduces the experimental values quite satisfactorily due to the correction of electron correlation and larger number of sampling points. Therefore, in the present work, we investigated the low-symmetry effect on the multiplet structure of ruby using the CrO_6 clusters for simplicity. Comparing the calculated results of each cluster, the average energies of each doublet state (R, R' and B) are almost unchanged, indicating that the electron-electron repulsion energy is almost unaffected by the intrinsic trigonal distortion in ruby. On the other hand, the average energies of each quartet state change significantly depending on the clusters, indicating that the energy of quartet states are rather sensitive to the same trigonal distortion.

An abrupt change occurs between the cluster (**r2**) and the cluster (**r3**) as shown in Fig 4. Therefore, the dominant factor of the low-symmetry effect is the asymmetric position of the chromium ion along C_3-axis as shown in Fig 1. For the cluster with cubic approximation (**r5**), the energies of U and Y are considerably overestimated. In the traditional analysis based on the ligand-

field theory, however, the trigonal distortion is ignored and this discrepancy is absorbed in the empirical parameters during the fitting process. As a result, the empirical crystal-field splitting is estimated to be smaller. Therefore, the physical meaning of the parameters in the LFT is quite ambiguous because they include various effects such as covalency, distortion of the molecular orbitals or electron correlation, and quantitative analysis of these effects is no longer possible. On the other hand, these effects can be evaluated quantitatively by the first-principles calculation based on the DV-ME method. In the present work, for example, we calculated the multiplet structures of distorted molecular orbitals from first-principles and the dominant factor of the low-symmetry effect in ruby is clarified for the first time.

4.3 Effect of low symmetry in emerald

The calculated multiplet structures for the various model clusters of emerald are shown in Fig 5. The peak positions in the observed optical spectra are also shown on the right (10). The overall multiplet structure is very similar to that of ruby, although the energies of quartet states are slightly smaller in emerald than those in ruby. In the results of the cluster with symmetry of the real crystal (**e1**), the peak positions of the observed absorption spectra are reproduced well. Although the split of each state due to the trigonal distortion is larger than the observed ones, they can be improved by enlarging the size of the cluster.

The average energies of each doublet state (R, R' and B) are almost independent of the cluster, while the average energies of each quartet state are sensitive to the cluster symmetry as shown in Fig 6. The most significant change occurs between the cluster (**e1**) and the cluster (**e2**), indicating that the twist of the oxygen octahedron is the dominant factor. In the case of ruby, the asymmetric position of chromium ion along C_3-axis is the dominant factor of the low-symmetry effect on the multiplet structure. On the other hand, in emerald, the chromium ions are originally located at symmetric position along C_3-axis and the most dominant factor is the twist of the oxygen octahedron.

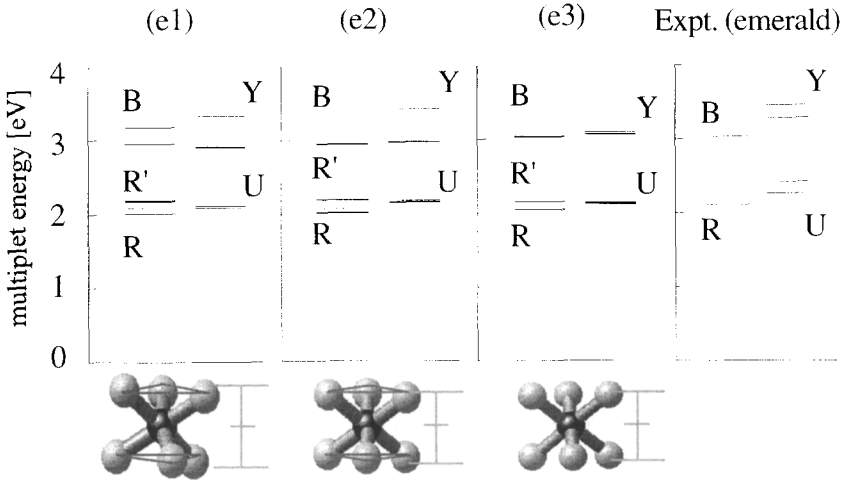

Fig 5. Calculated multiplet energies for the various model clusters of emerald shown in Fig 1;
In the results of each cluster, doublets are shown on the left and quartets are on the right. The peak positions of the observed absorption spectra of emerald (10) are shown on the far right.

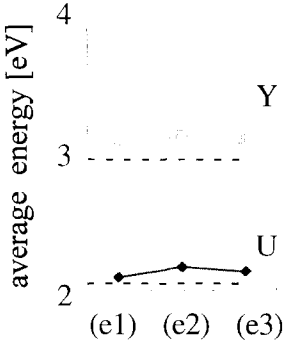

Fig 6. The calculated average energy of the U band (solid rhombus) and that of the Y band (solid square) for each model cluster of emerald;
Dotted lines are the average energy of the U band and that of the Y band in the observed absorption spectra.

This is a reasonable result considering that the twist angle of the oxygen octahedron is 12.5° in beryl, which is much greater than that in alumina (4.3°).

5. SUMMARY

In order to clarify the low-symmetry effects on the multiplet structures of ruby and emerald, we calculated the multiplet structures using various clusters with gradually changed symmetry. Surprisingly, the energies of doublet states are almost independent of the cluster, indicating that the electron-electron repulsion energies are almost unaffected by the intrinsic trigonal distortions in these materials. On the other hand, the energies of quartet states are significantly affected by the same trigonal distortions. The calculated results indicate that the dominant factor of the low-symmetry effect is quite different between ruby and emerald. In the case of ruby, the asymmetric position of the chromium ion along C_3-axis influences the multiplet structure significantly. On the other hand, in the case of emerald, the chromium ion is originally located at the symmetric position along C_3-axis. Instead, the twist of the oxygen octahedron influences the multiplet structure significantly. Although the cause of the low-symmetry effect is quite different between ruby and emerald, the energies of the quartets decrease due to the presence of trigonal distortions. In the traditional analysis based on the ligand-field theory, these effects are absorbed in the empirical parameters. This difference between ruby and emerald is clarified for the first time by the first-principles calculations based on the DV-ME method. The DV-ME method is an effective tool for quantitative analysis of the effects of covalency, distortion of molecular orbitals and electron correlation on multiplet structures, which is essential for the fundamental understanding of electronic structure of various solid-state laser materials.

ACKNOWLEDGEMENT

This work was supported by a Grant-in-Aid for Scientific Research from Ministry of Education, Science, Sports and Culture of Japan.

REFERENCES

(1) Maiman, T. H.; *Nature* **1960,** *187*, 493.

(2) Buchest, J.; Alfano, R. R. *Laser Focus*, **1983,** *Sep*, 117.

(3) Sugano, S.; Tanabe, Y.; Kamimura, H. *Multiplet of Transition-Metal Ions in Crystals* ; Academic Press: New York, 1970.

(4) Ogasawara, K.; Ishii, T.; Ito, Y.; Ida, H.; Tanaka, I; adachi, H. *Jpn. J. Appl. Phys.* **1998,** *37*, 4590.

(5) Adachi, H.; Tsukada, M.; Satoko, C. *J. Phys. Soc. Jpn.* **1978,** *45*, 875.

(6) Slater, J. C. *Quantum Theory of Molecules and Solids* ; McGraw-Hill: New York, 1974; Vol. 4.

(7) Satoko, C.; Tsukada, M.; Adachi, H. *J. Phys. Soc. Jpn.* **1978,** *45* ,1333.

(8) Fazzio, A.; Caldas, M.; Zunger, A. *Phys. Rev.* **1984,** *B29*, 5999.

(9) Ogasawara, K.; Ishii, T.; Tanaka, I.; Adachi,H. (in this proceedings).

(10) Fairbank, W. M. Jr.; Klauminzer, G. K.; Schawlow, A. L. *Phys. Rev.* **1975,** *B11*, 60.

Assignment of Ce XANES spectra for CeO_2 and $CeO_{1.75}$ and effect of oxygen vacancy

Hirohide Nakamatsu* and Takeshi Mukoyama

Institute for Chemical Research, Kyoto University, Uji, Kyoto 611-0011, Japan

(Received May 14, 1999)

Theoretical XANES spectra for CeO_2 and vacancy-including $CeO_{1.75}$ are obtained in the framework of the L^2 method with the first-principles molecular orbital method. Peaks in the Ce L_3 X-ray absorption spectra are assigned to quasi-bound states which are generated by the cage effect due to the eight oxygen cube surrounding the Ce atom, and have quasi-standing waves dominated with the Ce *d* components. These states are split into e_g and t_{2g} orbitals depending on their directions with respect to the oxygen atoms. A low peak close to the Ce *4f* band is attributed to quasi-bound states among the oxygen atoms with slight involvement of Ce *d*. A spectral change originating from the oxygen vacancy is analyzed with the theoretical spectra. It is found that valence fluctuation of Ce, possibly caused by the vacancy formation, is undistinguishable in the theoretical spectra. The local atomic arrangement substantially determines the XANES spectra for CeO_2 and $CeO_{1.75}$.

KEYWORDS: cerium oxide, oxygen vacancy, local structure, X-ray absorption spectra, L^2 method

*Corresponding author, e-mail: nakamatsu@elec.kuicr.kyoto-u.ac.jp

ADVANCES IN QUANTUM CHEMISTRY, VOLUME 37

0065-3276/01 $35.00

1. INTRODUCTION

XANES (X-ray Absorption Near-Edge Structure) is X-ray absorption spectroscopy for the lower energy region than EXAFS (Extended X-ray Absorption Fine Structure). It is sensitive to the local atomic arrangement around the absorbing atom and to the chemical states because the low energy electrons emitted through the photoabsorption are affected by details of the molecular potential (1).

XANES is one of powerful tools for the study of chemical states of lanthanoid compounds. Most of the conclusions drawn from the XANES for the lanthanoid compounds have been concerned with the chemical states or characteristics of the electronic structures. In particular, valences of lanthanoids have been studied using such spectra (2). They were obtained by assigning some of the peaks in the spectra to different valences. By using the Anderson impurity model, the valences were derived from intensities of shake-up peaks (3).

Some theoretical XANES spectra for CeO_2 have been reported(3-6). Most of them were based on electronic structure models with adjustable parameters and devoted to the analyses of the peaks attributed to different numbers of *4f* electrons caused in the X-ray absorption process. Soldatov et al. obtained the Ce L_3 XANES using the multiple-scattering method with an assemble of atomic charge densities derived with the help of the Dirac–Slater method (6). They convoluted the multiple-scattering spectra for different electron configurations and provided theoretical spectra in good agreement with the experimental one. At the present, there are variety of interpretations and assignments for the peaks, but they depend on the electronic structure models used for the analyses. Moreover, the other fundamental factor, the local atomic arrangement, was not taken into consideration in the previous works. Exceptionally Soldatov et al. (6) concluded that the peaks arose from multiple scattering of the excited photoelectron within a large cluster inside the crystal. The relation between the structure and the multiple scattering was not well clarified though they discussed the symmetric features of the wavefunctions.

Theoretical X-ray absorption spectra have been obtained with molecular orbital methods as well as multi-scattering methods (7). At the beginning, the physical basis for describing the continua concerning the X-ray absorption within the framework of the molecular orbital method was not clear, but later Langhoff et al. clarified it by introducing the so called L^2 method which utilizes a square-integrable basis set (8). Then the molecular orbitals

extended in this scheme represent all the one-electron states in XANES: vacant valence states (or conduction bands in crystals), Rydbergs and quasi-bound states in the continua.

The discrete variational (DV) Xα molecular orbital method with the L^2 extension has been successfully applied to calculations of the theoretical XANES spectra for various free molecules and solids (1, 9-13). The advantages of applying the DV-Xα method to XANES consist in the more realistic potential for electrons than the muffin-tin type and the use of efficient basis sets obtained from direct numerical solutions for atomic-like potentials. Relativistic Dirac-Fock-Slater calculations using the DV method were successfully applied to reveal the ionic and covalent bonds in CeO_2 (14).

In the present work, the theoretical XANES spectrum for CeO_2 is calculated with the DV-Xα method and the peaks therein are assigned to states which are analyzed with wavefunctions, emphasizing the local structural effects. As an application of the present method and the peak assignment, it is clarified how oxygen vacancy affects the spectra for cerium oxides.

2. COMPUTATIONAL

The first-principles calculations for theoretical XANES spectra consist of three procedures, that is obtaining the self-consistent charge density, the discretized continua and the X-ray absorption spectra. The self-consistent charge densities for the chemical species were calculated with software called SCAT which implemented the DV-Xα molecular orbital method (15). For calculations of the continua and X-ray absorption spectra, the method was extended within the framework of square-integrable (L^2) discretized wavefunction method (9-11).

The CeO_8^{-12} cluster was adopted for representing the local electron charge density of the CeO_2 crystal. This consisted of a central Ce surrounded by a O_8 cube and had O_h symmetry with the O-O interatomic distance of 2.7055Å (16). To represent $CeO_{1.75}$ which has an eighth of the oxygen atoms less, we took the $CeO_7^{-10.5}$ cluster which is a CeO_8^{-12} cluster where one oxygen atom was removed and which has additional 0.5 electrons, corresponding to the reduction of the eighth of two oxygen(–II) atoms. The Slater exchange parameter was set at 0.7 for all the present calculations.

A number of basis functions were generated and utilized for two steps of the continuum calculations. First, an extended basis set with continuum wavefunctions of limited spatial extent and the minimal set of atomic orbitals corresponding to the states filled with electrons were used to obtain self-consistent charge density. Then a further extended basis set was used to represent the states in the continuum through the orthogonalization to the wavefunctions for the electron charge density. To reduce the number of matrix elements, the basis functions were transformed to the symmetry-adapted orbitals before the orthogonalization.

When the basis set was enlarged, almost linearly dependent basis functions appeared. They were akin to some orbitals generated on different atoms in the molecule because the linear combination of many basis functions at multi-centers spanned the space repeatedly. The linear dependence among the symmetry-adapted orbitals was removed before the orthogonalization.

A linear combination of the bound and L^2 continuum atomic wavefunction was used to approximate the continua (10). Wavefunctions in the spherical potential were separated into the spherical harmonics and the radial wavefunctions. The spherical harmonics are expressed in terms of the associated Legendre functions. The differential equation for the radial wavefunction R at position r is

$$\frac{\mathrm{d}}{\mathrm{d}r}\left(r^2\frac{\mathrm{d}R}{\mathrm{d}r}\right)+\left|-l(l+1)+r^2(\varepsilon-V)\right|R=0, \qquad (1)$$

where l, ε and V are the angular momentum quantum number, the energy of the electron and the atomic potential, respectively. Equation (1) was solved numerically with the Hamming method. The numerical solutions for the bound states were derived with a standard computer code similar to a nonrelativistic version of the HEX code of Liberman et al. (17). For the continuum states, the outward integration was numerically performed from the origin out to a finite distance. In the present work, the integration of Eq. (1) was performed up till r = 7 au and then a third order polynomial decreasing function was smoothly connected to it.

The basis sets used for the spectra of the CeO_2 and $CeO_{1.75}$ clusters consisted of orbitals from 1*s* to 9*p* for Ce and 1*s* to 4*f* for O, including *f* wavefunctions and the atomic continua from 0 Hr to +1.6 Hr with a step of 0.2 Hr, containing *s*, *p*, *d* and *f* wavefunctions. The present basis sets produced ~11 discretized states per eV for the continua.

The effect of the hole formation on the X-ray absorption spectra was explicitly included in the procedure to obtain self-consistent charge density. This hole effect was connected to the subsequent procedure for getting the

spectra, using the following relation. The X-ray absorption energy ΔE is expressed as:

$$\Delta E = E[\,\mathrm{K}(-1)\,] - E[\,\mathrm{K}(0)\,], \tag{2}$$

where $E[\,\mathrm{K}(0)\,]$ and $E[\,\mathrm{K}(-1)\,]$ are the total energies in the ground state and in the state with a hole at level K. In the present work, the effect of the electron excited into the continuum was taken to be negligible because the electron was spread over infinite space. In the Xα method, it is convenient to calculate the differential energy by the transition-state method, i.e. a half electron is removed from the orbital concerned. By this method, ΔE is evaluated using the orbital energy ε_{K} of the level K (18):

$$\Delta E = \varepsilon_{\mathrm{K}}[\,\mathrm{K}(-0.5)\,]. \tag{3}$$

The oscillator strength f_{ij} for a transition from state i to state j was calculated in the dipole approximation:

$$f_{ij} = \frac{2}{3}\omega \left| \left\langle f \left| \boldsymbol{r} \right| i \right\rangle \right|^2, \tag{4}$$

where ω was the energy difference between the state i and j. Numerical integrations for the dipole matrix elements were performed in the same way as that in Ref. 19, 20. To improve the integration precision by one digit, the sampling points were scattered appropriately according to the spatial distribution of the core wavefunction in question. The photoabsorption cross section for a molecule is given by

$$\sigma_{ij} = 2\pi^2 \alpha a_0^2 f_{ij} \delta(\omega - \omega_p), \tag{5}$$

where α is the fine-structure constant, a_0 is the Bohr radius and ω_p is the photon energy. The function δ expresses the line shape including the instrumental resolution and lifetime contribution of the excited state.

The L^2 states are connected with the continua through the sum rule of the oscillator strengths:

$$\sum_j \left\langle \chi_j \left| \boldsymbol{r} \right| i \right\rangle = \int \mathrm{d}E \left\langle \phi(E) \left| \boldsymbol{r} \right| i \right\rangle, \tag{6}$$

where $\psi(E)$ is the continuum wavefunction and χ_j is the j th discretized one. From the viewpoint of numerical integrations which are expressed as summations of discrete values, a weight ω_j links these wavefunctions at the energy E_j together (21):

$$\chi_j = \omega_j \psi(E_j). \tag{7}$$

In the L^2 method, the differential equation for the continua is resolved in the same way as for the molecular orbital method. Sufficient basis sets represent the continuum wavefunctions in the molecular region and then ω_j depends only on the density of the discretized states. Therefore, the density curves derived from smoothing the oscillator strengths of the L^2 states correspond to the photoabsorption spectra (10, 21). In the present work, the Lorentzian curve with the peak width (FWHM) of 3.0eV was used as a combined function of δ and the smoothing. Though the discretized states depend on the choice of basis set, the spectrum obtained is practically independent of this. This was confirmed by using different sizes of the basis sets.

3. RESULTS AND DISCUSSION

3.1. CeO_2 spectrum

Figure 1 shows the Ce L_3 X-ray absorption spectrum of the CeO_8 cluster which is an approximation to the CeO_2 crystal together with an experimental spectrum (22). The theoretical spectrum is shifted so as to fit with the experimental one. The better agreement in energy, without needing this shift would be expected if relativistic calculations suitable for evaluating the high binding energy of the L_3 electrons were performed. Though only the obtained spectrum is meaningful, the discretized L^2 states are also shown for checking the density of the generated states effective to the cross sections .

The experimental spectrum has four characteristic features which are indicated by A-D in the figure. The results of the present calculations give assignments for the peaks A-C. The details of this assignment will be described with the wavefunctions later. The peak A appears 1eV or more higher than the Ce 4*f* band. Resonances due to the molecular potential for the oxygen atoms take place and Ce *d* components which are slightly involved in these appear as the peak A. The second and third peaks B and C are assigned to quasi-bound states where wavefunctions mainly with Ce 5*d* components are trapped in the cage of the eight oxygen atoms surrounding the Ce atom. These states are split into e_g and t_{2g} depending on their directions to the

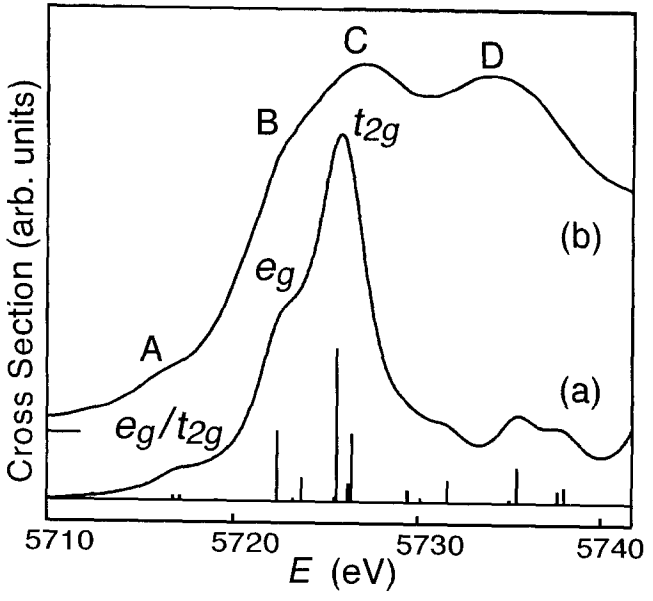

Fig 1. Ce L_3 X-ray absorption spectra for CeO_2: (a) theoretical spectrum and L^2 states, and (b) experimental (22). Vertical bar for each L^2 state is proportional to the oscillator strength.

oxygen atoms in the cube. It is noticeable that the theoretical spectrum obtained for the small CeO_8 cluster with the large basis set in the present work is quite similar to those derived for large clusters of more than 51 constituent atoms by the multiple-scattering method (6).

The characters of the peaks in the XANES are analyzed with the wavefunctions shown in Fig 2. An e_g wavefunction for the peak A is shown in Fig 2(a). Strong resonance among the oxygen atoms is generated. It is found that the *p*, *d* and *f* scattering waves at the oxygen atoms make the quasi-bound states for the peak A. The Ce *d* components are to a small extent involved in these states and have σ- and π-type couplings along the Ce – O axis. This conclusion is in contrast with early work (23) where this peak was interpreted as Ce 4*f* contributions with a higher order photoabsorption transition than the dipole.

The peak B has mainly e_g wavefunctions such as shown in Fig 2(b) and the peak C has mainly t_{2g} wavefunctions as shown in Fig 2(c). These wavefunctions are extremely localized inside the O_8 cube though their energies are

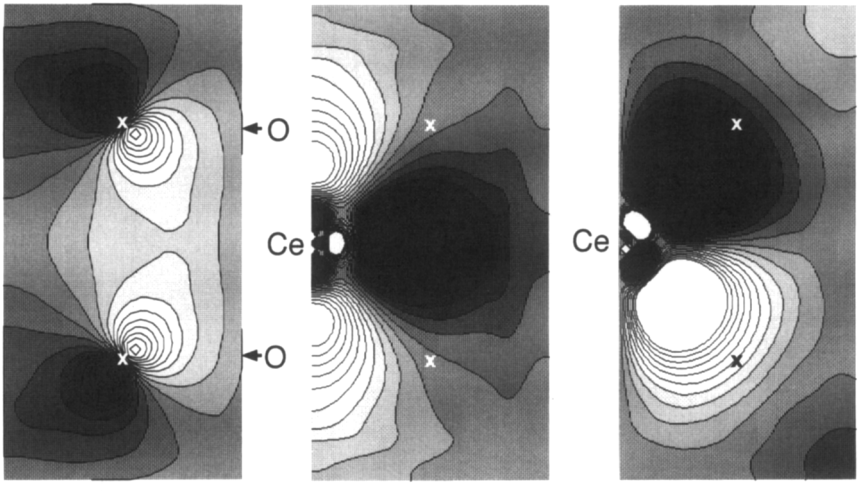

Fig 2. Sectional views of wavefunctions for resonances in CeO_2. A half of X-Y plane; (a) including O_4 plane for peak A, (b) including Ce for peak B and (c) including Ce for peak C in Fig 1. Shading is a measure of the wavefunction value at each location. The brightest and darkest parts mean the top and bottom. The X marks indicate locations of O in (a) and intersections with lines connecting two O atoms in (b) and (c).

much larger than the work function for the ionization. The local components of Ce *d*, in particular Ce 5*d*, are dominant in these quasi-bound states. Therefore, it is found that strong resonances due to the oxygen cage confine these states inside the cage.

The e_g wavefunctions point to the side of the O_8 cube and the t_{2g} ones point to the edge of the cube. According to the directions of these wavefunctions, the t_{2g} states have a shorter distance to approach the oxygen atoms, that is, the entities for the scattering. Wavefunctions with a shorter distance for the resonance require larger wave numbers and therefore higher energies (11). The peaks B and C arise from the cage effect and split, depending on the wavefunction directions to the oxygen cube. Additionally, the t_{2g} quasi-bound states are confined in a smaller volume than the e_g states as found in Fig 2(b) and (c). The explanation is that in the O_8 sphere, the O_2

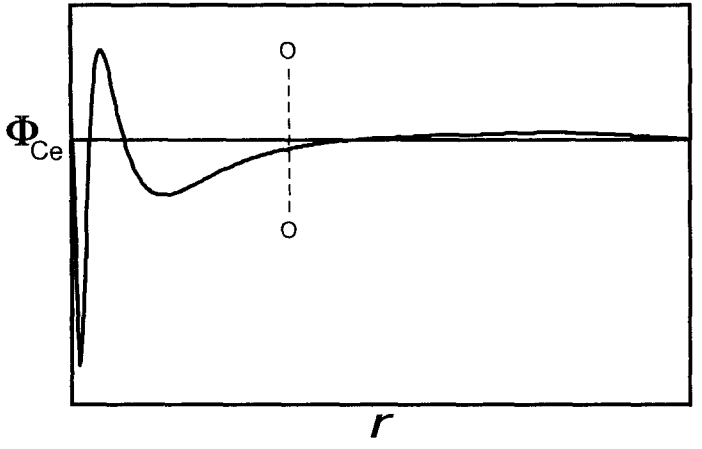

Fig 3. Radial section of the wavefunction corre-sponding to Fig 2(c) in [110] direction from Ce. Broken line indicates an intersection with a line connecting two O atoms.

edges provide harder boundaries than the O_4 planes. Actually, the potential experienced by t_{2g} along the edge is deeper than that experienced by e_g around the plane.

Figure 3 shows a sectional view of the details of the quasi-bound wave-function in Fig 2(c). The quasi-standing wave is observed inside the O_8 cage and the progressive wave lies outside the cage. The cage effect is so significant in the states involved in the X-ray absorption that the wavefunctions are remarkably localized.

The field of the O_8 cube results in the splitting of the $5d$ components into e_g and t_{2g} in the O_h symmetry. However, the area ratio between these peaks is far from 2:3 due to their multiplicities because the cross sections for the X-ray absorption are determined by the strength of the confinement of the quasi-bound states. This splitting of the B and C peaks arises from the different scatterings by the oxygen cube, though only the symmetric properties are the same as those in the crystal field.

The present theoretical spectrum by the first-principles method does not produce the peak D and indicates a conclusion that the single electron configuration provides only the peaks A-C. Another process is considered to explain this extra peak. The details of the low peaks lying beyond 7530eV are

out of the range of the present work. To discuss the details of the higher energy region, larger extended basis sets are required (1).

There are some papers which have produced the theoretical spectra including the peak D (3-6). All of them considered some Ce electron configurations such as $4f^0$ and $4f^1$. Jo and Kotani (5) attributed the B and C peaks to states with the Ce $4f^1$ and $4f^2$ components and the D peak to states with Ce $4f^0$ and $4f^2$. The split between the peaks B and C was obtained by assuming a structure for the $5d$ band. Their theoretical spectrum with some adjustable parameters agreed well with the experimental one. However, the assumed mixed valence model where Ce had three valences in the ground state of the CeO_2 crystal has not been supported by the experiments on magnetic properties and photoelectron spectra which observed no population in the $4f$ band (2, 24).

Delley and Beck (4) took a shake-up process during the X-ray absorption as a source of different $4f$ configurations and the peaks B, C and D were attributed to combinations of spin-orbit splitting and configurations of Ce $4f^0$ and $4f^1$. The parameters used were those which provided a theoretical Ce $3d$ photoelectron spectrum which was in good agreement with the experimental one. However, the intervals between the obtained peaks did not agree with the experimental X-ray spectrum.

Bianconi et al. adopted the Anderson impurity model and assumed prominent change of the electronic structure which resulted in the shake-up (3). This restructuring of the bands was attributed to a large $4f$ – core hole interaction. Soldatov et al. took the same shake-up model and successfully got theoretical XANES with the peaks A-D, by convoluting multiple-scattering XANES spectra obtained for the two electron configurations for the final states due to the shake-up (6).

3.2. $CeO_{1.75}$ spectrum

Blokhin el at. compared XANES spectra of CeO_2 and $9CeO_{1.75} \cdot La_2O_3$ (25). The solid solution with La_2O_3 was prepared to reduce the high reactivity due to the oxygen vacancies in $CeO_{1.75}$. We take a vacancy-including cluster $CeO_7\square_1$ (where $\square$ means an oxygen vacancy) with the same geometry as the CeO_8 cluster as representing a local electronic structure for the CeO_2 crystal.

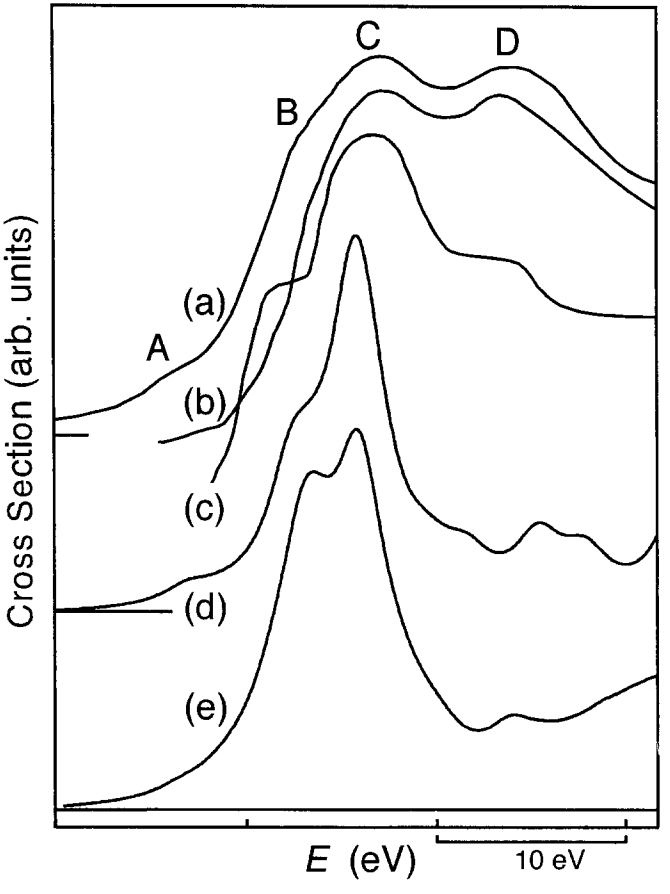

Fig 4. Ce L_3 X-ray absorption spectra for CeO_2 and $CeO_{1.75}$: (a), (b) experimental for CeO_2 (22), (25), respec-tively, (c) experimental for $CeO_{1.75}$ (25), and (d), (e) theoretical spectra for CeO_2 and $CeO_{1.75}$.

Figure 4 shows the present theoretical spectra and the experimental spectra (25). In the theoretical spectrum for the vacancy-containing cluster, the peaks A-C appear as well as for CeO_2. The peak A becomes blurred because the resonances among the oxygen atoms are weakened due to the oxygen defect. The part for the peak A was not reported for the experimental spectrum.

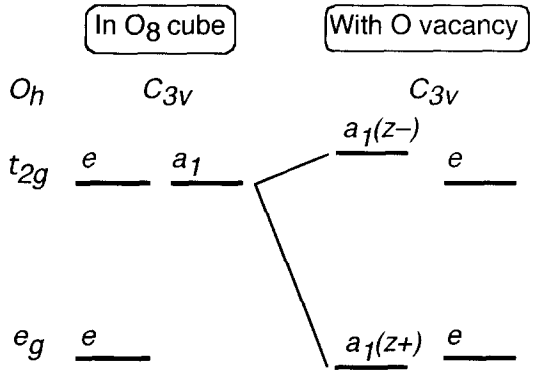

Fig 5. Level scheme for effect of oxygen vacancy. CeO_2 has O_h local symmetry and $CeO_{1.75}$ is assumed to have C_{3v}.

The prominent change due to the oxygen vacancy takes place at the peak B which is larger in $CeO_{1.75}$ than in CeO_2. The theoretical spectra show this change qualitatively. A problem in the comparison between the experimental and theoretical spectra is that the spectrum of CeO_2 of Ref. (25) was quite different from the other experimental ones (2-3, 22), in particular at the peak B in question. With the data available at present, we just discuss the qualitative change due to the vacancy.

The spectral change due to the presence of the vacancy has been analyzed with the obtained wavefunctions and the features revealed are illustrated in Fig 5. As explained in the previous section, the Ce $5d$ resonances are split into two groups e_g and t_{2g}. The local symmetry of O_h around Ce in CeO_2 degrades to C_{3v} due to the vacancy. The vacancy generation stabilizes the a_1 state which is oriented to the vacancy, denoted by a_1(z+). One of the two oxygen atoms which hold the a_1 quasi-bound state is missing and the symmetric degradation induces p contributions to a_1. These two factors make the a_1 state split and broad. Therefore, the vacancy creation makes the B peak larger and broader.

Valence fluctuation of Ce possibly occurs due to the oxygen defects. To examine the energy change with the Ce valency, the locations of the peaks B, C for Ce(III) and Ce(IV) in the CeO_7 cluster are compared. It is found that the peaks for Ce(III) are lower by about 0.5eV than for Ce (IV). The explanation is that this decrease in energy is attributed to the upward shift of

the L_3 level of Ce(III) due to the additional electron to Ce(IV) while the quasi-bound states are almost determined by the atomic arrangement. Therefore, the valency change of Ce possibly caused by the vacancy formation is undistinguishable in the present spectra and less effective than the local structure change.

4. CONCLUDING REMARKS

XANES spectra for CeO_2 and vacancy-including $CeO_{1.75}$ are obtained in the framework of the L^2 method applied to the first-principles molecular orbital method. For the Ce L_3 X-ray absorption spectra, the peaks are assigned to quasi-bound states which are generated by the cage effect due to the eight oxygen atoms surrounding the Ce atom. The cage effect is so significant in this X-ray absorption that the quasi-bound states are dominated by the local Ce *d* components. These states are split into e_g and t_{2g} depending on their directions with respect to the oxygen cage. A low peak close to the Ce *4f* band is attributed to quasi-bound states among the oxygen atoms with slight involvement of Ce *d*. One peak is missing in the present results which were obtained for the one-electron excitation in the photoabsorption processes. This peak is possibly due to a change of electron configuration during the photoabsorption.

A change originating from the oxygen vacancy is observed in the present theoretical spectra. It is found that the valence fluctuation of Ce possibly caused by the vacancy formation is less effective than the structural change and undistinguishable in the spectra. The local atomic arrangement substantially determines the XANES spectra for CeO_2 and $CeO_{1.75}$.

ACKNOWLEDGMENT

The present work was supported by a Grant-in-Aid for Scientific Research from the Ministry of Education, Science and Culture in Japan.

REFERENCES

(1) Nakamatsu, H.; Mukoyama, T.; Adachi, H. *J. Chem. Phys.* **1991**, *95*, 3167 (1991).

(2) Rohler, J. In "Handbook on the physics and chemistry of rare earths", Gschneider, Jr., K.A.; Eyring, L.; Hufner, S., Ed.; North-Holland: Amsterdam, 1987; Vol.10, 453 and references therein.

(3) Bianconi, A.; Marcelli, A.; Dexpert, H.; Karnatak, R.; Kotani, A.; Jo T.; Petiau, J. *Phys. Rev.* **1987**, *B35*, 806.

(4) Delley, B.; Beck, H. *J. Magn. Magn. Mat.* **1985**, *47&48*, 269.

(5) Jo, T.; Kotani, A. *Solid State Commun.* **1985**, *54*, 451.

(6) Soldatov, A.V.; Ivanchenko, T.S.; Dellalonga, S.; Kotani, A.; Iwamoto, Y.; Bianconi, A. *Phys. Rev.* **1994**, *B50*, 5074.

(7) Bianconi, A. *Chem. Anal.* **1988**, *92*, 573.

(8) Langhoff, P.W.; Padial, N.; Csanak, G.; Rescigno, T.N.; McKoy, B.V. *Int. J. Quantum Chem. Symp.* **1980**, *14*, 285.

(9) Nakamatsu, H.; Mukoyama, T.; Adachi, H. *Jpn. J. Appl. Phys.* **1993**, *32*, suppl. 32-2 23.

(10) Nakamatsu, H.; Adachi, H.; Mukoyama, T. *Bull. Inst. Chem. Res.; Kyoto Univ.* **1994**, *72*, 45.

(11) Nakamatsu, H. *Chem. Phys.* **1995**, *200*, 49.

(12) Ueda, K.; Shimizu, Y.; Chiba, H.; Okunishi, M.; Ohmori, K.; West, J.B.; Sato, Y.; Hayashi, T.; Nakamatsu, H.; Mukoyama, T. *Phys. Rev. Lett.* **1997**, *79*, 3371.

(13) Ikeda, T.; Kobayashi, H.; Ohmura, Y.; Nakamatsu, H.; Mukoyama, T. *J. Phys. Soc. Jpn.* **1997**, *6*, 1079.

(14) Nakamatsu, H.; Adachi, H.; Mukoyama, T. *Chem. Phys. Lett.* **1995**, *247*, 168.

(15) Adachi, H.; Tsukada, M.; Satoko, C. *J. Phys. Soc. Jpn.* **1978**, *45*, 875.

(16) Wyckoff, R.W.G. "Crystal Structures"; Robert E. Krieger: Florida, 1982; second ed. Vol. 1, p. 241.

(17) Liberman, D.A.; Cromer, D.T.; Waber, J.T. *Comp. Phys. Commun.* **1971**, *2*, 107.

(18) Nakamatsu, H.; Mukoyama, T.; Adachi, H. *Chem. Phys.* **1990**, *143*, 221.

(19) Adachi, H.; Taniguchi, K. *J. Phys. Soc. Jpn.* **1980**, *49*, 1944.

(20) Song, B.; Nakamatsu, H.; Sekine, R.; Mukoyama, T.; Taniguchi, K. *J. Phys.*

Cond. Matter **1998**, 10, 9443.

(21) Reinhardt, W.P. *Comp. Phys. Commun.* **1979**, *17*, 1.

(22) Bauchspiess, K.R.; Boksch, W.; Holland-Moritz, E.; Launois, H.; Pott, R.; Wohlleben, D. In "Valence Fluctuations in Solids", eds. Falicov, L.M.; Hanke, W.; Maple, M.B., Ed.; North-Holland: Amsterdam, 1981, p. 417.

(23) Troneva, N.V.; Marchikova, I.D.; Borovskiy, I.B. *Fiz. Met. & Metalloved.* **1958**, *6*, 141.

(24) Wuilloud, E.; Delley, B.; Schneider, W.-D.; Y. Baer, *Phys. Rev. Lett.* **1984**, *53*, 202.

(25) Blockin, S.M.; Kuznetsov, F.A. *Theor. & Exp. Chem. Acad. Sci. Ukr. SSR* **1966**, *2*, 321.

CO shakeup calculations with the DV-Xα method

Akio Shigemi*, Hirohide Nakamatsu and Takeshi Mukoyama

Institute for Chemical Research, Kyoto University, Uji, Kyoto 611-0011, Japan.

Shigero Ikeda

Ritsumeikan University, Kusatsu, Shiga, 525-8577, Japan.

(Recieved November 13, 1999)

C1s photoemission shakeup satellites for the CO molecule are obtained using the spin-polarized discrete variational Xα method (DV-Xα) in combination with the transition state method. The satellite peaks are assigned to shakeup transitions between the molecular orbitals. The present results agree reasonably well with the experimental peak positions and are compared with other theoretical results.

KEYWORDS: shakeup satellite, spin-polarized DV-Xα method, transition state concept, CO, XPS.

*Corresponding author: e-mail akio@elec.kuicr.kyoto-u.ac.jp

ADVANCES IN QUANTUM CHEMISTRY, VOLUME 37

0065-3276/01 $35.00

1. INTRODUCTION

The main peaks in X-ray Photoelectron Spectroscopy (XPS) for molecules appear because of the photoionization of core electrons. In addition, satellite peaks on the high binding energy side of the main peak have often been observed. These peaks are generally referred to as 'shakeup satellite' peaks. In the sudden approximation, the shakeup process which accompanies photoionization can be considered as a two-step process. First, a core electron is emitted as a photoelectron, creating an inner shell vacancy. In the next step, electron(s) in the same molecule transfer from valence orbital(s) to unoccupied orbital(s) with relaxation of orbital energies. It is important to study these satellites in order to understand the valence and excited states of molecules (1).

Satellite structures can be easily observed in simple molecules. The C1s spectrum of CO is especially interesting, because this molecule can be considered to be a typical example of a small unsaturated molecule. The satellite peaks which accompany the C1s spectrum of CO have been studied both experimentally and theoretically by many researchers. Experimental studies have been performed by Gelius (2), Hemmers et al. (3), Schirmer et al. (4), and Reich et al. (5). Schirmer et al. (4) proved that some satellite peaks caused by inelastic scattering appear near to the shakeup satellite peaks which accompany C1s photoionization in comparison with CO energy loss spectra. Hemmers et al. (3) and Reich et al. (5) performed higher resolution measurement. In particular, Hemmers et al. (3), from studying the angle-resolved high-resolution photoelectron spectra of CO C1s satellite lines, indicated that in the shakeup case the final ionic state is $^2\Sigma^+$ while in the conjugate shakeup case, where the photoelectron ends up in a bound state and the valence electron is ejected, it is either $^2\Delta$ or $^2\Sigma^-$. On the other hand, theoretical calculations have been made using the spin-polarized scattering-wave Xα (SW-Xα) method by Tse (6), the multiconfiguration Hartree-Fock (MCHF) method by Guest et al. (7), and the fourth-order Green's function method (ADC4) by Angonoa et al. (8).

Until now, the satellite peaks accompanying the C1s spectrum of CO were assigned using the various calculation methods described above. However, theoretical results are not in such good agreement with experimental data and the peak assignments do not agree with each other. Better theoretical calculations are needed to explain the experimental data and to assign the satellite peaks. We performed energy calculations and assigned these satellite peaks using spin-

polarized DV-Xα methods together with the transition state concept.

In the present work we tried to interpret the satellite peaks which accompany the CO C1s spectrum as a shakeup process. The values we calculated are used to assign the experimental spectrum. The results are also compared with assignments by other calculation methods.

2. COMPUTATION

In the shakeup process accompanying the inner-shell photoionization, the electrons are excited from occupied orbitals to unoccupied orbitals. In the case of a one-electron shakeup, there are three open shells in the final state. We represent their orbitals as a, b, c, and denote the up-spin electron by +, the down-spin electron by -. We can write the determinantal wave function of the final state with open shell structure in the following form (6):

$$\Psi_1 = \frac{1}{\sqrt{2}}\{|a^- b^+ c^+| - |a^+ b^- c^+|\} \quad , \tag{1}$$

$$\Psi_2 = \sqrt{\frac{2}{3}}|a^+ b^+ c^-| - \frac{1}{\sqrt{6}}\{|a^- b^+ c^+| + |a^+ b^- c^+|\} \quad , \tag{2}$$

$$\Psi_3 = \frac{1}{\sqrt{3}}\{|a^- b^+ c^+| + |a^+ b^- c^+| + |a^+ b^+ c^-|\} \quad , \tag{3}$$

$$\Psi_4 = |a^+ b^+ c^+| \quad , \tag{4}$$

where Ψ_1 and Ψ_2 are doublets, and Ψ_3 and Ψ_4 are quartets, respectively. These wave functions were obtained by first coupling a and b into a singlet or triplet state and then by coupling c to each of them. Since the shakeup process is a monopole transition, transitions to the quartet state are forbidden by the monopole selection rule. Therefore, we have to calculate the doublet energies, that is the Ψ_1 and Ψ_2 eigenenergies, $E(\Psi_1)$ and $E(\Psi_2)$. If we define the elements of above wave functions to be $D_1 = |a^+ b^- c^+|$, $D_2 = |a^- b^+ c^+|$, $D_3 = |a^+ b^+ c^-|$, $D_4 = |a^+ b^+ c^+|$, we can write $E(\Psi_1)$ and $E(\Psi_2)$ in the following form (6).

$$E(\Psi_1) = \frac{1}{2}\left[4E(D_1) - E(D_4) - E(D_3)\right] \quad , \tag{5.1}$$

$$E(\Psi_1) = \frac{1}{2}\left[4E(D_2) - E(D_4) - E(D_3)\right] \quad , \tag{5.2}$$

$$E(\Psi_2) = \frac{1}{2}\left[3E(D_3) - E(D_4)\right] \quad . \tag{6}$$

Next, we describe how we calculate the satellite peak energies which are observed for the shakeup transition in XPS. The energy of the shakeup peaks observed in XPS can be represented by the wave functions Ψ_n ;

$$I_s(\Psi_n) = E(\Psi_n) - E_0 \quad , \tag{7}$$

where $I_s(\Psi_n)$ is the energy of the Ψ_n state which is observed in XPS, $E(\Psi_n)$ is the total energy of the Ψ_n state, and E_0 is the total energy of ground state. On the other hand, the energy of the main peak, i.e. the ionization energy for a core hole, is represented by

$$I_p = E_i - E_0 \quad , \tag{8}$$

where E_i is the total energy of the ionization state. Then we can express the shakeup excitation energy, ΔI_s, which is the difference between the shakeup peak energy and the main peak energy, as,

$$\Delta I_s(\Psi_n) = I_s(\Psi_n) - I_p \quad . \tag{9}$$

This equation can be rewritten using Eqs.(7) and (8) as

$$\Delta I_s(\Psi_n) = E(\Psi_n) - E_i \quad . \tag{10}$$

In the case of the Ψ_1 state, $E(\Psi_1) - E_i$ can be expressed in terms of the components using Eq.(5.1).
We obtain

$$\begin{aligned}\Delta I_s(\Psi_1) &= \frac{1}{2}\left[4E(D_1) - E(D_4) - E(D_3)\right] - E_i \\ &= \frac{1}{2}\left[4\left\{E(D_1) - E_i\right\} - \left\{E(D_4) - E_i\right\} - \left\{E(D_3) - E_i\right\}\right] \quad ,\end{aligned} \tag{11}$$

where $E(D_n) - E_i$ is the difference between the total energy of the $D_n(n=1,2,3,4)$ component and the ionization energy. For the Ψ_2 wave function, we can also write a similar difference equation.

The difference between the total energy of the $D_n(n=1,2,3,4)$ component and the ionization energy can be expressed in terms of a, b and c orbitals as follows :

$$E(D_n) - E_i = E(a^1 b^1 c^1) - E(a^1 b^2 c^0) \quad , \tag{12}$$

where $E(a^i b^j c^k)$ is the state total energy, and i, j and k indicate the number of electrons in a, b and c, respectively. This equation corresponds to the transition energy for excitation of one electron from the b orbital to the c orbital. When we use the Xα method, the transition energy can be estimated from the transition state method (9), i.e. the difference between the energy eigenvalues of the initial and final orbitals, where one half electron is removed from the initial orbital and added to the final orbital. Using the transition state method, Eq.(12) can be expressed as follows :

$$E(D_n) - E_i = \varepsilon_c(a^1 b^{1.5} c^{0.5}) - \varepsilon_b(a^1 b^{1.5} c^{0.5}) \quad , \tag{13}$$

where $\varepsilon_c(a^1 b^{1.5} c^{0.5})$ and $\varepsilon_b(a^1 b^{1.5} c^{0.5})$ are the energy eigenvalues of the c and b orbitals in the case where one electron is removed from the a orbital and a half electron is excited from the b orbital to the c orbital.

Next, we describe how we calculate the shakeup transition energy for two electrons. When these two electrons are excited to the same orbital, the energy can be expressed as

$$\begin{aligned}\Delta I_s &= I_s - I_p \\ &= [E(a^1 b^0 c^2) - E(a^2 b^2 c^0)] - [E(a^1 b^2 c^0) - E(a^2 b^2 c^0)] \\ &= E(a^1 b^0 c^2) - E(a^1 b^2 c^0) \quad .\end{aligned} \tag{14}$$

Using the transition state procedure, this equation can be written as,

$$\Delta I_s = 2[\,\mathcal{E}_c(a^1 b^1 c^1) - \mathcal{E}_b(a^1 b^1 c^1)\,] \quad , \tag{15}$$

where the coefficient of 2 originates from the fact that two electrons are excited.

In the present work, we have performed the calculations using the spin-polarized DV-Xα molecular orbital method. The details of the software used are described elsewhere (10, 11). The carbon monoxide (= CO) molecule is a linear molecule which is considered to have the $C_{\infty v}$ symmetry and a C-O bond length of 1.1282Å. Numerical atomic orbitals (1s to 3p for the C and O atoms) were used as a basis set for the MO calculations. The Slater exchange parameter was chosen to be $\alpha = 0.7$ for all the calculations.

3. RESULT AND DISCUSSION

Table I. summarizes experimental and theoretical shakeup energies for CO C1s photoemission, together with the assignment of the shakeup peaks. Within the limits of the present work, six peaks and a shoulder are found in the vicinity of the main peak. The experimental results contain contributions from three groups (3-5).

An occupied and a vacant molecular orbitals involved in the shakeup excitation produce a doublet. The energies for the 1π to $2\pi^*$ transition obtained in the present work are 9.7eV and 11.3eV. They correspond to peaks 1 and 2 in the experimental spectra. The $5\sigma \rightarrow 6\sigma^*$ and $5\sigma \rightarrow 7\sigma^*$ transitions agree with the peaks 3, 5 and 4, 6, respectively. For comparison with the previous assignment, the energies for double shakeup excitations were also estimated and found to be 14.0eV for $5\sigma^2 \rightarrow 2\pi^2$ and 19.9eV for $1\pi^4 \rightarrow 1\pi^2 2\pi^2$.

In previous works, Tse (6) used the spin-polarized scattering wave Xα method (SW-Xα), Guest et al. (7) adopted the multiconfiguration Hartree-Fock method (MCHF) and Angonoa et al. (8) applied the fourth-order Green's function method (ADC4) to estimate the shakeup energies for CO. The energies they obtained are also listed in Table I. Their assignments which are different from the present results are indicated in the parentheses just below the shakeup estimates.

Table I. Comparison of experimental and theoretical shakeup energies for CO C1s photoemission.

Peak	*E* (Experiment) (eV)			Intensity†	Assignment	*E* (Theory) (eV)			
	Hemmers[a]	Schirmer[b]	Reich[c]			This work	SW-Xα[d]‡	MCHF[e]‡	ADC4[f]‡
1	8.65(8)	8.34(6)	8.66(6)	s	$2\sigma^{-1}1\pi^{-1}2\pi^{1}$	9.7	9.12	8.54	9.11
2	15.09(6)	14.88(6)	15.2(1)	s	$2\sigma^{-1}1\pi^{-1}2\pi^{1}$	11.3	10.90	15.71	17.12
					$[2\sigma^{-1}5\sigma^{-2}2\pi^{2}]^{**}$	14.0			
							15.90* $(2\sigma^{-1}5\sigma^{-1}6\sigma^{1})$		
3	17.77(5)	17.85(5)	18.09(5)	s	$2\sigma^{-1}5\sigma^{-1}6\sigma^{1}$	17.5	16.20 $(2\sigma^{-1}5\sigma^{-2}2\pi^{2})^{**}$ 18.29 $(2\sigma^{-1}1\pi^{-2}2\pi^{2})^{**}$	18.15 $(2\sigma^{-1}5\sigma^{-2}2\pi^{2})^{**}$ 18.26 $(2\sigma^{-1}1\pi^{-2}2\pi^{2})^{**}$	19.89
							18.88* $(2\sigma^{-1}5\sigma^{-1}7\sigma^{1})$		
4	19.17(4)	19.22(5)	19.48(4)	s	$2\sigma^{-1}5\sigma^{-1}7\sigma^{1}$	19.8	20.71 $(2\sigma^{-1}5\sigma^{-1}6\sigma^{1})$		21.18 $(2\sigma^{-1}5\sigma^{-1}6\sigma^{1})$
					$[2\sigma^{-1}1\pi^{-2}2\pi^{2}]^{**}$	19.9			20.79
5	20.05(5)	20.09	20.42(5)	s	$2\sigma^{-1}5\sigma^{-1}6\sigma^{1}$	21.9	24.23 $(2\sigma^{-1}5\sigma^{-1}7\sigma^{1})$		21.64 $(2\sigma^{-1}5\sigma^{-1}7\sigma^{1})$
5'	20.94(8)	21.10(10)		sh					22.31 $(2\sigma^{-1}1\pi^{-2}2\pi^{2}$, $2\sigma^{-1}5\sigma^{-1}7\sigma^{1})$
6		23.2(1)		s	$2\sigma^{-1}5\sigma^{-1}7\sigma^{1}$	23.6			

[a]Ref.3, [b]Ref.4, [c]Ref.5, [d]Ref.6, [e]Ref.7, [f]Ref.8. † **s** means a sharp peak, and **sh** means a shoulder.
‡ Assignments different from the present ones are shown in the parentheses.
*Correspondence to a peak was undone by the author. **Double excitation.

Peaks 1 and 2 are attributed to the $1\pi \rightarrow 2\pi^*$ excitation in the present work and also by all the other workers. The present work assigned peak 3 to the $5\sigma \rightarrow 6\sigma^*$ transition, as did ADC4, while the SW-Xα and MCHF results attributed it to double excitations such as $5\sigma^2 \rightarrow 2\pi^2$ and $1\pi^4 \rightarrow 1\pi^2 2\pi^2$. The present calculations assign peaks 4 and 5 to the $5\sigma \rightarrow 7\sigma^*$ and $5\sigma \rightarrow 6\sigma^*$ transitions respectively. These assignments are reversed in the SW-Xα and ADC4 results. Only ADC4 obtained a peak 5 shoulder 5'. Only the present work estimates peak 6 as an excitation of $5\sigma \rightarrow 7\sigma^*$. In addition, Tse failed to find the peaks for the lower energy parts of the $5\sigma \rightarrow 6\sigma^*$ and $5\sigma \rightarrow 7\sigma^*$ excitations.

We make further comparison with the SW-Xα results where the multiplet was estimated in the same way as in the present work. Component energies for the $1\pi \rightarrow 2\pi^*$ transition obtained by the present DV-Xα method and the SW-X α method are shown in Table Ⅱ.

Table Ⅱ. Component energies for the $1\pi \rightarrow 2\pi^*$ transition obtained by the present DV-Xα method and the SW-Xα method.

	Component energy (eV)	
	DV-Xα	SW-Xα
$\mathcal{E}(D_1)$	9.8	8.36699
$\mathcal{E}(D_2)$	9.2	9.24850
$\mathcal{E}(D_3)$	9.0	8.35665
$\mathcal{E}(D_4)$	7.7	6.83904

The ordering of $\mathcal{E}(D_1)$ and $\mathcal{E}(D_2)$ is found to be reversed. This analysis is based on the atomic constituents of the molecular orbitals. The main 2σ, 1π and 2π components involved in the shakeup process in question are the atomic orbitals of the carbon, oxygen and carbon atoms, respectively. As the exchange interaction works more effectively between molecular orbitals with larger spatial

wave function overlap, the 2π spin orbital is lowered by the electrons in 2σ with the same spin than 1π spin orbital. Following the allocation used in the SW-Xα calculations, the D_1 and D_2 states are ($1\pi^+$, $2\pi^-$, $2\sigma^+$) and ($1\pi^-$, $2\pi^+$, $2\sigma^+$), respectively. Therefore, 2π is lowered by the 2σ electrons in the D_2 state but not by the 2σ electrons in the D_1 state. This means that the component energy for D_2 is lower than that for D_1. This is as obtained by the present DV-Xα calculations.

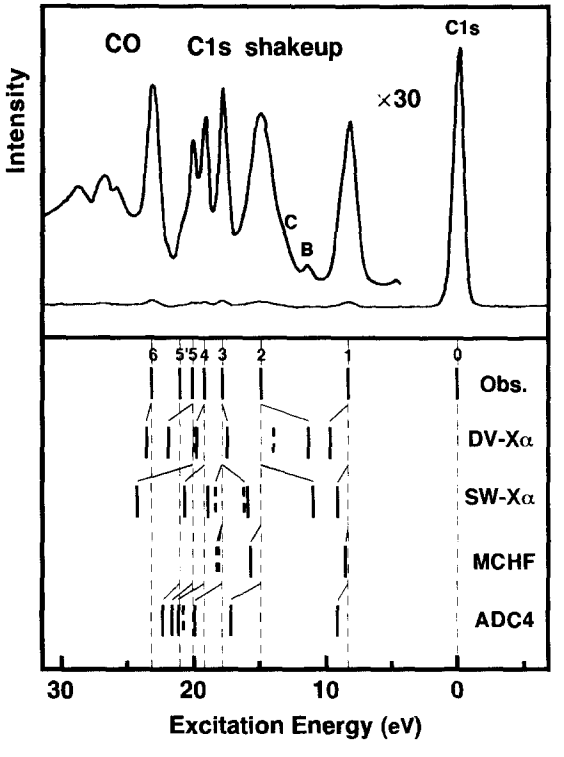

Fig 1. C1s shakeup spectrum for CO quoted from Ref.4 and peak positions obtained by theoretical estimations. Solid lines indicate positions for single excitations and broken lines, positions for double excitations. The origin of the excitation energy is at the C1s ionization energy. See text for the explanation of the B and C in the spectrum.

In Fig.1, the theoretical shakeup energies are compared with the experimental spectrum reported by Schirmer et al. (4). The main peak for the C1s photoemission is set to 0eV. Schirmer et al. pointed out that peaks B, C and a small part of peak 1 arise from inelastic scattering of photoelectrons by other molecules. The observed peak positions are marked 1-6 and connected by thin lines to the calculated ones in the present and previous works. The present estimates reproduce all the sharp peaks 1-6 and agree well with the experimental peak positions, except for peak 2. The SW-Xα results show larger deviations and MCHF provides only two excitations, furthermore the ADC4 results are shifted to higher excitation energies by 1-2 eV.

4. SUMMARY

C1s photoemission shakeup satellites for the CO molecule were calculated with the spin-polarized discrete variational Xα method. The transition state method was applied to the estimation of multiplet peak positions for the shakeup transitions and the results are in reasonable agreement with the experimental values.

A pair of molecular orbitals involved in the shakeup process produces two states and all the sharp peaks in the experimental spectrum can be assigned to the calculated states. The present and previously reported assignments agree with each other for the first two shakeup excitations due to the $1\pi \rightarrow 2\pi^*$ transition, however the other assignments depend on the theoretical model. The present multiplet calculations are basically performed in the same way as the SW-Xα method but are in better agreement with the experimental results. One of the improvements was analyzed by considering the exchange interaction and the atomic constituents of the molecular orbitals concerned.

The present results indicate that the DV-Xα method in combination with the transition state method is quite useful for the study of shakeup satellites in XPS for molecules.

REFERENCES

(1) Siegbahn, K.; Nordling, C.; Johansson, G.; Hedman, J.; Hede'n, P. F.; Hamrin, K.; Gelius, U.; Bergmark, T.; Werme, L. O.; Hanne, R.; Baer, Y. "ESCA Applied to Free Molecules"; North-Holland, Amsterdam, 1969.

(2) Gelius, U. *J. Electron Spectrosc. Relat. Phenom.* **1974,** *5*, 985.

(3) Hemmers, O.; Whitfield, S. B.; Berrah, N.; Langer, B.; Wehlitz, R.; Becker, U. *J. Phys. B : At. Mol. Opt. Phys.* **1995,** *28*, L693.

(4) Schirmer, J.; Angonoa, G.; Svensson, S.; Nordfors, D.; Gelius, U. *J. Phys. B : At. Mol. Phys.* **1987,** *20*, 6031.

(5) Reich, T.; Heimann, P. A.; Petersen, B. L.; Hudson, E.; Hussain, Z.; Shirley, D. A. *Phys. Rev. A* **1994,** *49*, 4570.

(6) Tse, J. S. *J .Chem. Phys.* **1980,** *73*, 5734.

(7) Guest, M. F.; Rodwell, W. R.; Darko, T.; Hillfer, I. H.; Kendrick, J. *J. Chem. Phys.* **1977,** *66*, 5447.

(8) Angonoa, G.; Walter, O.; Schirmer, J. *J. Chem. Phys.* **1987,** *87*, 6789.

(9) Slater, J. C. "Quantum Theory of Molecules and Solids", McGraw-Hill, 1974, vol. 4.

(10) Adachi, H.; Tsukada, M.; Satoko, C. *J. Phys. Soc. Jpn.* **1978,** *45*, 875.

(11) Adachi, H.; Shiokawa, S.; Tsukada, M.; Satoko, C.; Sugano, S. *J. Phys. Soc. Jpn.* **1979,** *47*, 1528.

$K\beta/K\alpha$ x-ray intensity ratios in 3*d* elements by photoionization and electron-capture decay

Takeshi Mukoyama*

Institute for Chemical Research, Kyoto University, Uji, Kyoto 611-0011, Japan

Kazuo Taniguchi

Department of Solid State Electronics, Osaka Electro-Communication University, Neyagawa, Osaka 572-8530, Japan

Hirohiko Adachi

Department of Materials Science and Engineering, Faculty of Engineering, Kyoto University, Kyoto 606-8501, Japan

(Received November 20, 1999)

The $K\beta/K\alpha$ x-ray intensity ratios by photoionization and electron-capture decay have been calculated for several chemical compounds of 3*d* elements by the use of the discrete-variational Xα (DV-Xα) molecular orbital method. The calculated results indicate that the $K\beta/K\alpha$ ratios depend on the excitation mode as well as the chemical effect. For the similar chemical environments the $K\beta/K\alpha$ ratio by photoionization is larger than that by electron-capture decay, due to the excess 3*d* electron in the latter case. However, the difference is small, sometimes negligible in comparison with the chemical effect. Possible reasons for large difference in earlier experiments are discussed and future experiments are suggested.

KEYWORDS: $K\beta/K\alpha$ ratio, electron-capture decay, photoionization
*Corresponding author, e-mail: mukoyama@elec.kuicr.kyoto-u.ac.jp

ADVANCES IN QUANTUM CHEMISTRY, VOLUME 37

0065-3276/01 $35.00

1. INTRODUCTION

The $K\beta/K\alpha$ x-ray intensity ratio is an easily measurable quantity with relatively high precision and has been studied extensively for K-x-ray emission by radioactive decay, photoionization, and charged-particle bombardment (1-3). Except for the case of heavy-ion impact where multiple ionization processes are dominant, it is generally accepted that this ratio is a characteristic quantity for each element. The experimental results are usually compared with the theoretical values for a single isolated atom and good agreement is obtained with the relativistic self-consistent-field calculations by Scofield (4).

However, Hansen *et al.* (5) measured K-x-ray intensity ratios following K-capture decay of radioactive nuclei and pointed out that there is considerable difference between $K\beta/K\alpha$ ratios by electron-capture decay and those by x-ray or electron bombardment. Later, Paic and Pecar (6) found that the $K\beta/K\alpha$ x-ray intensity ratios for $3d$ transition elements depend on the mode of excitation. The $K\beta/K\alpha$ ratios by electron-capture decay (EC) are smaller by almost ten per cent for Ti, V, Cr, and Fe than those by photoionization (PI). However, no appreciable difference was observed for Cu and Zn. A similar experiment was performed for Mn by Arndt *et al.* (7). They pointed out that the reason for this difference is due to the $3d$ excess electron in EC and the strong shakeoff process accompanying PI. Tamaki *et al.* (8) measured the $K\beta/K\alpha$ ratios for various chemical compounds of V, Cr, and Mn excited by PI and EC.

On the other hand, Rao *et al.* (9) measured the $K\beta/K\alpha$ ratios for Mn and Fe as well as for six elements between $49 \leqq Z \leqq 82$ following K-capture decay and PI. They found that for Mn and Fe the $K\beta/K\alpha$ ratios by EC is $4\sim5\%$ smaller than those by PI, but no dependence on the mode of excitation for high-Z elements. From these results they concluded that the dependence of the $K\beta/K\alpha$ ratios on the excitation mode observed for Mn and Fe is attributed to the chemical effect. Similar experiments were performed by Büyükkasap *et al.* (10) for Cr, Mn, Fe, Cs, and Ba. They observed that the $K\beta/K\alpha$ intensity ratios for $3d$ elements are affected by the mode of excitation, but the effect is smaller for Cs and Ba.

Recently, Bé *et al.* (11) showed that the absolute value for $K\beta/K\alpha$

ratio with PI in 3*d* elements increases by taking into account the $K\beta'$ and $K\beta_{2,5}$ peaks and the radiative Auger effect in data analysis measured with a solid-state detector (SSD). Combining their data with those by EC (12), they found no systematic difference in $K\beta/K\alpha$ ratios in 3*d* elements between two excitation modes.

It is well known that *K*-x-ray spectra depend on the chemical surroundings of the atom (13) and extensive experimental studies for the chemical effects on the $K\beta/K\alpha$ x-ray intensity ratios of 3*d* transition elements have been reported (14). Recently we have measured the $K\beta/K\alpha$ ratios for some chemical compounds of Cr and Mn with a high-energy resolution spectrometer and compared the experimental results with the theoretical calculations (15,16). Several theoretical estimations of the chemical effects on the *K*-x-ray intensity ratios have also been made (15-18).

In the case of EC, the daughter atom is considered as an impurity atom in the chemical compound of the parent atom and its chemical state is different both from that in ordinary chemical compounds of parent element and from that of daughter element. In addition, the outer-shell electron configuration of the parent atom is preserved after EC and the daughter atom has an excess electron in the outer shell in comparison with the PI case. These facts indicate that in order to compare the $K\beta/K\alpha$ ratios by PI with those by EC, the difference in the chemical surroundings should be taken into consideration as well as the difference in the number of electrons in the atom.

In the present work, we have calculated the $K\beta/K\alpha$ x-ray intensity ratios for 3*d* transition elements excited by PI and EC, taking into account both effects described above. The calculations were made using the discrete-variational (DV) $X\alpha$ molecular orbital (MO) method (19). The electronic states and wave functions in molecules were obtained for tetrahedral (Td) and octahedral (Oh) clusters. The x-ray emission rates were estimated by the DV integration method (20) with the MO wave functions in the dipole approximation. The calculated results are compared with the experimental data.

2. COMPUTATIONAL METHOD

The MO calculations were performed by the use of the DV-Xα method, which has been described in detail elsewhere (19). In this method, the atomic Hartree-Fock-Slater (HFS) calculations are made for each atom in the molecule. The atomic orbital (AO) wave functions obtained in the numerical form are used as the basis functions in the MO calculations. The molecular wave function for the λth MO is expressed in terms of the AO's as

$$\psi_\lambda = \Sigma_i \; C_{i\lambda} \; \phi_i , \qquad (1)$$

where ϕ_i is the AO and $C_{i\lambda}$ is the eigenvector to be determined variationally from the MO calculations. The wave function in Eq. (1) is used to derive the secular equation and the matrix element is evaluated in the DV integration method (20).

The *K*-ray emission rate in the dipole approximation is given by (21,22)

$$I_\lambda \propto E_\lambda^{\,3} D_\lambda^{\,2} \qquad (2)$$

Here E_λ is the energy difference and D_λ is the dipole matrix element between the *K* shell and the λth MO. Using Eq. (1), the dipole matrix element can be written as

$$D_\lambda = \Sigma_i \; C_{i\lambda} \langle \phi_K | \boldsymbol{r} | \phi_i \rangle \quad , \qquad (3)$$

where ϕ_K is the *K*-shell wave function and $\boldsymbol{r}$ is the position vector.

In the present work, Eq. (3) is calculated in the DV method, i.e. the integration is evaluated as the weighted sum of the integrand values at the discrete points distributed randomly according to a certain sampling function (20). The validity of the DV integration scheme in the calculation of the dipole matrix element has been already tested (23).

For simplicity, we assumed that all the compounds are the cluster with Td symmetry or Oh symmetry, where the 3*d* transition metal atom is located at the center and surrounded by four or six ligand atoms. In the case of EC, it is also assumed that there is no change in the chemical environment by electron capture, but only the atomic number of the central atom decreases by one. The internuclear distance is taken to be same as that of the parent atom and the electron configuration of the parent atom is used.

The chemical compounds and clusters used in the present

calculations are shown in Table I. The symbol $Cr[MnO_4^{2-}]$ means that the central Mn atom in MnO_4^{2-} cluster is replaced by Cr. The 1*s*-4*p* AO's are used as basis functions for metal atoms, while 1*s*-2*p* orbitals are employed for oxygen and 1*s*-3*p* AO's for chlorine. The Slater's exchange parameter is always taken to be $\alpha = 0.7$.

3. Results and discussion

All the numerical calculations in the present work have been made on the FACOM VP-30E computer in the Information Science Center of Osaka Electro-Communication University.

The calculated results of $K\beta/K\alpha$ ratios for EC and PI are listed in Table II. It is clear that, except for the $V[CrO_4^{2-}]$ and VO_4^{3-} pair, the $K\beta$

Table I. Compounds and clusters used in the calculations.

Compound	Symmetry	Cluster	Bond length (Å)	Reference
$K_2{}^{54}MnO_4$	Td	$Cr[MnO_4^{2-}]$	1.81	24
K_2CrO_4	Td	CrO_4^{2-}	1.65	25
$K_2{}^{51}CrO_4$	Td	$V[CrO_4^{2-}]$	1.65	25
Na_3VO_4	Td	VO_4^{3-}	1.74	26
$^{54}MnO_2$	Oh	$Cr[MnO_6^{8-}]$	1.89	27
CrO_2	Oh	CrO_6^{8-}	1.90	27
$^{51}CrO_2$	Oh	$V[CrO_6^{8-}]$	1.90	27
VO_2	Oh	VO_6^{8-}	1.93	27
$^{54}MnCl_2$	Oh	$Cr[MnCl_6^{4-}]$	2.51	28
$CrCl_2$	Oh	$CrCl^{4-}$	2.55	29
$^{51}CrCl_3$	Oh	$V[CrCl_6^{3-}]$	2.38	30
VCl_3	Oh	VCl_6^{3-}	2.45	31

Table II. Calculated results for $K\beta/K\alpha$ ratios.

EC	$K\beta/K\alpha$ ratio	PI	$K\beta/K\alpha$ ratio
$V[CrO_4^{2-}]$	0.1210	VO_4^{3-}	0.1201
$V[CrO_6^{8-}]$	0.1149	VO_6^{8-}	0.1154
$V[CrCl_6^{3-}]$	0.1125	VCl_6^{3-}	0.1133
$Cr[MnO_4^{2-}]$	0.1201	CrO_4^{2-}	0.1227
$Cr[MnO_6^{8-}]$	0.1171	CrO_6^{8-}	0.1172
$Cr[MnCl_6^{4-}]$	0.1127	$CrCl_6^{4-}$	0.1146

$/K\alpha$ ratio for PI is larger than that for EC. This fact is consistent with the experimental results of Hansen *et al.* (5), Paic and Pecar (6), Arndt *et al.* (7), and Rao *et al.* (9). In the case of $V[CrO_4^{2-}]$, its equivalent electronic structure for PI is not the VO_4^{3-} cluster, but VO_4^{2-}. The formal oxidation number of vanadium atom in the former cluster is 5, while that in the latter is 6. Since the $K\beta/K\alpha$ intensity ratio for 3*d* elements increases generally with increasing formal oxidation number (32), the $K\beta/K\alpha$ ratio for VO_4^{3-} is considered to be smaller than that for VO_4^{2-}, and also that for $V[CrO_4^{2-}]$.

As has been discussed in the previous work (15), the calculated values for single isolated atoms in the present model are smaller than the experimental data because of neglection of the exchange and overlap effects. Taking into account this fact, it is useful to express the calculated values as a relative ratio of the calculated $K\beta/K\alpha$ ratio by EC to that by PI with the similar chemical form. Comparison of the calculated and measured values for the relative $K\beta/K\alpha$ ratios in EC to those in PI, $(K\beta/K\alpha)_{EC}/(K\beta/K\alpha)_{PI}$, is given in Table III. The values for Na_3VO_4 and $K_2{}^{51}CrO_4$ are not included in the table due to the difference in formal oxidation numbers of V atoms, as described above.

It can be seen from the table that the relative ratio depends on the chemical form of the compound. In order to study the dependence of the excitation mode on the $K\beta/K\alpha$ ratios, comparison should be made for the compounds with the same chemical state. It is also clear that for the same chemical compound, the $K\beta/K\alpha$ ratios for EC are smaller Table

III. Comparison of calculated and measured relative ratios, $(K\beta/K\alpha \text{ ratio})_{EC}/(K\beta/K\alpha \text{ ratio})_{PI}$.

Element	Compound	Calculated	Measured	Reference
V	VO_2	0.996		
	VCl_3	0.993	1.007±0.016	8
	not specified		0.903±0.020	6
	not specified[a]		1.058±0.028	11
Cr	K_2CrO_4	0.979	1.041±0.018	8
	CrO_2	0.999		
	$CrCl_2$	0.983		
	not specified		0.948±0.021	6
	not specified[a]		1.045±0.041	10
	not specified[a]		1.008±0.019	11

[a]Pure element was used for PI.

than those for PI, but the dependence of the excitation mode is small, less than a few % and the relative ratio is almost unity for many cases.

However, when the chemical forms of the samples used for radioactive sources and target for PI are different, the relative ratio becomes a sum of two effects, the chemical effect and the effect of the excitation mode, and can be a larger value. For example, if we take the largest value for PI and the smallest value for EC from Table II, the relative ratio is 0.937 (VO_4^{3-} and $V[CrCl_6^{3-}]$) for V and 0.917 (CrO_4^{2-} and $Cr[MnCl_6^{3-}]$) for Cr. These values are in better agreement with the values of Paic and Pecar (6).

For the experimental values by Paic and Pecar (6), the detailed information on the chemical states is not given and it is probable that the chemical state for EC is different from that for PI and this gives their large experimental values. Nevertheless, it can be said that at least their experimental results give smaller values for EC than for PI and are in qualitative agreement with the present theoretical calculations.

Although the experimental data for EC by Büyükkasap *et al.* (10) and Bé *et al.* (11) are larger than those for PI, the chemical forms of the samples are different in two excitation modes. The ratio for chromium is

small and almost unity within the experimental errors. On the other hand, the relative ratio for vanadium is larger than the experimental uncertainty. This is because the value for EC is considerable larger in comparison with other elements, as pointed out by them (11). Both groups used pure elements for PI, but chemical compounds for EC. The chemical states of the radioactive sources were not reported. This fact suggests that their results be ascribed to the chemical effect.

In the data of Tamaki *et al.* (8), there are several $K\beta/K\alpha$ ratios measured with similar chemical states for EC and PI. Although their values for relative ratios are larger than unity, the experimental errors are large. The theoretical value for VCl_3 is within the experimental uncertainty. In the case of K_2CrO_4, the experimental relative ratio is considerable larger than unity. However, if we use the PI value for $(NH_4)_2CrO_4$, which corresponds to the same theoretical value for CrO_4^{2-} cluster, the experimental relative ratio is 1.022 ± 0.018 and very close to unity.

Arndt *et al.* (7) explained smaller values for EC due to the 3*d* excess electron in EC and larger shake probabilities in PI. They also demonstrated that the experimental results of Paic and Pecar and their own result for Mn can be fitted well, if the number of 3*d* electrons in PI is assumed to be smaller by two than that in EC. In order to examine the effect of the shake process on the $K\beta/K\alpha$ ratio, we estimated the shakeoff and shakeup probabilities accompanying EC and PI. For this purpose, we calculated the shakeoff-plus-shakeup probabilities accompanying PI and EC using the method of Carlson and Nestor (33). In the case of PI, the calculations were made in the similar manner to that of Mukoyama and Taniguchi (34) with the HFS wave functions (35). The corresponding values for EC were obtained by taking into account the change in nuclear charge as well as existence of a *K*-shell vacancy due to EC. In the case of EC, the parent atoms, i.e. Cr for V and Mn for Cr, were used as the initial states.

The numerical results for V and Cr are listed in Table IV. The valence electron configurations for V, Cr, and Mn are assumed to be $(3d)^3(4s)^2$, $(3d)^5(4s)^1$, and $(3d)^5(4s)^2$, respectively. From the table, it is clear that for EC the shakeoff and shakeup probabilities are negligibly small, while those in PI are about 5% for 3*p* electrons and about 10% for 3*d* electrons. Similar calculations for Mn have been reported by Arndt *et al.*

Table IV. Shakeoff and shakeup probabilities for *K*-shell photoionization and *K*-electron capture.

	V		Cr	
Shell	PI	EC	PI	EC
1*s*	4.91(-5)[a]	5.15(-4)	4.55(-5)	4.70(-4)
2*s*	1.59(-3)	1.13(-3)	1.52(-3)	1.03(-3)
2*p*	8.16(-3)	1.61(-4)	7.51(-3)	1.50(-4)
3*s*	6.79(-3)	1.16(-3)	6.59(-3)	9.54(-4)
3*p*	5.43(-2)	1.10(-4)	4.15(-2)	9.81(-5)
3*d*	8.45(-2)	5.17(-4)	1.49(-1)	3.75(-4)
4*s*	1.24(-1)	7.87(-4)	7.86(-2)	9.44(-4)

[a]4.91(-5) means 4.91×10^{-5}.

(7). Using the total shake (shakeoff plus shakeup) probabilities in Table IV, we modified the the number of 3*p*, 3*d*, and 4*s* electrons and calculated the $K\beta/K\alpha$ ratios after PI. Comparing the $K\beta/K\alpha$ ratios for PI with and without the shake processes, the increase in the $K\beta/K\alpha$ ratio due to the shake processes is found to be less than 0.5% for V and less than 0.4% for Cr. This fact indicates that the shakeoff and shakeup processes increase the $K\beta/K\alpha$ ratios for PI, but play a minor role in the difference between EC and PI.

However, for 3*p* and 3*d* electrons the final excited states in the shakeup process should be expressed as MO's, while the calculations in Table IV were made for AO's. In order to estimate the contributions of the shakeup process to the total shake probability in Table IV, we calculated the shakeup probabilities accompanying *K*-shell PI by the use of the method similar to that used in our previous work (36). The shakeup probabilities in PI were obtained to be about 30-40% of the total probability in Table IV for 3*p* electrons and about 40-50% for 3*d* electrons. In the shakeup probabilities, the dominant contributions come from the 3*p*-4*p* and 3*d*-4*d* transitions. For V, the former transition amounts to 27% of the total 3*p* shake probability and the latter is 35% of the total shake probability of 3*d*

electrons. The corresponding values for Cr are 21% and 48%, respectively. These large shakeup probabilities suggest that the chemical effect on the shakeup process is large and the shakeup probability should be estimated with MO wave functions. If we use MO's in the shakeup calculations, the contributions of the shake processes to the $K\beta/K\alpha$ ratio may change and become appreciable.

The present results seems to indicate that the dependence of the excitation mode on the $K\beta/K\alpha$ ratios is difficult to observe experimentally. However, it should be noted that all the experimental values discussed above were measured with SSD, such as Si(Li) and Ge(Li) detectors, and obtained by assuming single Gaussian shape for $K\alpha$ and $K\beta$ x-ray peaks. We have already pointed out (15) that the chemical effect on the $K\beta/K\alpha$ intensity ratios in $3d$ elements is sensitive to the intensities of $K\beta''$ and $K\beta_{2,5}$ peaks, which cannot be observed separately with SSD. This means that if these peaks are measured separately from the $K\beta_{1,3}$ diagram line, it may be possible to detect the difference due to excitation modes more clearly.

As has been pointed out by Bé *et al.* (11), the $K\beta/K\alpha$ ratio depends on the method of data analysis and it is essential to take into account the non-diagram lines, such as $K\beta_{2,5}$ line. Except for their work, all other experimental data were analyzed by the use of a single Gaussian for $K\beta$ lines. However, it should be noted that Bé *et al.* (11) neglected the contributions from $K\beta''$ peak, which is weak in metal but appreciable in some chemical compounds.

Recently, Bergmann *et al.* (37) measured the *K*-capture x-ray spectra of ^{55}Fe metal and $^{55}Fe_2O_3$ with high-energy-resolution crystal spectrometer and compared them with the x-ray excited spectra for Mn metal and MnO. Unfortunately they did not evaluate the $K\beta/K\alpha$ ratio, but demonstrated the difference in the peak shapes for $K\beta$ spectra between two excitation modes. Considering these facts, future experimental studies on the $K\beta/K\alpha$ ratio for $3d$ elements should be performed with high-resolution spectrometers, or at least with careful data analysis of the SSD spectra.

4. Conclusion

We have calculated the $K\beta/K\alpha$ x-ray intensity ratios for several chemical compounds of 3*d* elements by PI and EC with the DV-Xα method. The results indicate that the ratio depends on the excitation mode as well as the chemical state and both effects should be considered to compare with the experimental data. For similar chemical environments, the ratio by PI is larger than that by EC. This can be ascribed to the presence of an excess 3*d* electron in the latter case and partially to difference in the shake process between two excitation modes. However, the dependence on the excitation modes is very small and easily masked by the chemical effect.

The present results suggest that large difference in the $K\beta/K\alpha$ ratios observed in earlier experiments can be ascribed to the combination of the effect of the excess 3*d* electron in EC and the chemical effect in the samples used in two difference excitation modes. Since in the shakeup process the final excited states should be expressed as a molecular wave functions, it is interesting to calculate the shakeup probabilities by the use of MO's.

In order to compare with the present theoretical calculations, further experimental studies with high-resolution x-ray spectrometers and with more elaborate data analysis are hoped in the same chemical states for EC and PI.

REFERENCES

(1) Salem, S.I. In "Proceedings of the International Conference on Inner Shell Ionization Phenomena and Future Applications", Fink, R.W.; Manson, S.T.; Palms, J.M.; Rao, P.V., Eds.; USAEC: Oak Ridge, Tenn., 1973; 285.

(2) Salem, S.I.; Panossian, S.L.; Kreuse, R.A. *At. Data Nucl. Data Tables* **1974**, 14, 92.

(3) Berényi, D. *Bull. Inst. Chem. Res., Kyoto Univ.* **1979**, 57, 139.

(4) Scofield, J.H. *Phys. Rev. A* **1974**, 9, 1041.
(5) Hansen, J.S; Freund, H.U.; Fink, R.W. *Nucl. Phys. A* **1970**, 142, 604.
(6) Paic, G; Pecar, G. *Phys. Rev. A* **1976**, 14, 2190.
(7) Arndt, E.; Brunner, G; Hartmann, E. In "Proceedings of the International Seminar on High-Energy Ion-Atom Collisions", Berényi, D; Hock, G, Eds.; Akadéiai Kiadó: Budapest, 1982, 253; *J. Phys. B*, **1982**,15, L887.
(8) Tamaki, Y.; Omori, T.; Shiokawa, T. *Radiochem. Radioanal. Lett.* **1975**, 20, 255; *ibid.* **1979**, 37, 39; *Jpn J. Appl. Phys.* **1978**, 17, S245.
(9) Rao, N.V.; Reddy, S.B.; Sastry, D.L. *Nuovo Cimento* **1987**, 97A, 1.
(10) Büyükkasap, E.; Küçükönder, S.; Sahin, Y.; Erdgan, H. *J. Radioanal. Nucl. Chem. Lett.* **1994**, 186, 471.
(11) Bé, M. M.; Lépy, M.C.; Plagnard, J.; Duchemin, B. *Appl. Radiat. Isot.* **1998**, 49, 1367.
(12) Lépy, M.C.; Bé, M.M.; Plagnard, J. In "Application of Accelerators in Research and Industries", Duggan, J.L.; Morgan, I.L., Eds., AIP Press: New York, 1997, 1067.
(13) Meisel, A.; Leonhardt, G; Szargan, R. "Rötgenspektren und Chemische Bindung", Geest & Portig: Leipzig, 1977.
(14) Brunner, G.; Freyer, A.; Thomas, H.-J. "Akademie der Wissenschaften der DDR, Zentralinstitut für Isotopen- und Strahlenforschung, Zfi-Mitteilungen, Leipzig", Nr. 105, 1985, 63.
(15) Mukoyama, T.; Taniguchi, K.; Adachi, H. *Phys. Rev. B* **1986**, 34, 3710.
(16) Taniguchi, K.; Mukoyama, T.; Adachi, H. *J. Phys. (Paris) Colloq.* **1987**, 48, C9-77.
(17) Brunner, G.; Nagel, M.; Hartmann, E.; Arndt, E. *J. Phys. B* **1982**, 15, 4517.
(18) Band, I.M.; Kovtun, A.P.; Listengarten, M.A.; Trzhaskovskaya, M.B. *J. Electron Spectrosc. Relat. Phenom.* **1985**, 36, 59.
(19) Adachi, H.; Tsukada, M.; Satoko, C. *J. Phys. Soc. Jpn.* **1978**, 45, 875.
(20) Averill, F.W.; Ellis, D.E. *J. Chem. Phys.* **1973**, 59, 6412.
(21) Bethe, H.A.; Salpeter, E.E. "Quantum Mechanics of One- and Two-Electron Systems", Springer: Berlin, 1957, 248-269.
(22) Adachi, H.; Taniguchi, K. *J. Phys. Soc. Jpn.* **1980**, 49, 1944.
(23) Mukoyama, T.; Taniguchi, K.; Adachi, H. *Bull. Inst. Chem. Res., Kyoto Univ.* **1984**, 62, 13.
(24) Jasinski, J.P.; Holt, S.L. *J. Chem. Soc., Farady Trans. II* **1976**,

72, 1304.
(25) Colloti, G.; Conti, L.; Zocchi, M. *Acta Crystallogr.* **1959**, 12, 416.
(26) Troller, J.; Barnes, W.H. *Can. Mineralogist* **1958**, 6, 162.
(27) Bauer, W.H. *Acta Crystallogr.* **1976**, B32, 2200.
(28) Ohno, H.; Furukawa, K. *J. Chem. Soc. Farady Trans. I* **1978**, 74, 804.
(29) Oswald, H.R. *Helv. Chim. Acta* **1961**, 44, 1049.
(30) Wooster, N. *Z. Kristallogr. Kristallgeom. Kristallphys. Kristallchem.* **1930**, 74, 363.
(31) Klemm, W.; Krose, E. *Z. Anorg. Allgem. Chem.* **1947**, 253, 218.
(32) Tamaki, Y. *X-Ray Spectrom.* **1995**, 24, 235.
(33) Carlson, T.A.; Nestor, C.W. *Phys. Rev. A* **1973**, 8, 2887.
(34) Mukoyama, T.; Taniguchi, K. *Phys. Rev. A* **1987**, 36, 693.
(35) Herman, F.; Skillman, S. "Atomic Structure Calculations", Prentice-Hall: Englewood Cliffs, N.J., 1963.
(36) Mukoyama, T.; Taniguchi, K. *Bull. Inst. Chem. Res., Kyoto Univ.* **1992**, 70, 1.
(37) Bergmann, U.; Glatzel, P.; de Groot, F.; Cramer, S.P. *J. Am. Chem. Soc.* **1999**, 121, 4926.

A structural study of dibromo(1,4,8,11-tetraazacyclotetradecane)copper(II) and diaqua(1,4,8,11-tetraazacyclotetradecane)copper(II) difluoride four hydrate complexes in crystal and in aqueous solution by X-ray absorption near edge structure measurements and DV-Xα calculations

Shuji Matsuo, Toshio Yamaguchi, and Hisanobu Wakita*

Department of Chemistry, Faculty of Science, Fukuoka University, Nanakuma, Jonan-ku, Fukuoka 814-0180, Japan

(Received November 2, 1998)

Dibromo(1,4,8,11-tetraazacyclotetradecane)copper(II) ([$CuBr_2$(cyclam)]) and diaqua(1,4,8,11-tetraazacyclotetradecane)copper(II) difluoride four hydrate ([Cu(cyclam)$(H_2O)_2$]$F_2 \cdot 4H_2O$) were synthesized and were subjected to single crystal structure analysis and X-ray absorption near-edge structure (XANES) measurements in crystals and in aqueous solution. DV-Xα calculations for the both complexes have also been performed by a Slatar's transition state method based on the crystal structures to interpret the different XANES spectral patterns in both states. The results of the calculations suggest that the different spectral patterns are caused by exchanging one axial Br^- with an H_2O molecule to Cu(II) in aqueous solution and that the predominant complex in aqueous solution is [CuBr(cyclam)(H_2O)]$^+$. The net charge and bond order calculated for the complexes have shown that the exchange of the atoms in the axial positions affects the bond character between Cu(II) and N atoms in the equatorial positions. It has been found that the slight difference of the XANES spectral patterns for [Cu(cyclam)$(H_2O)_2$]$F_2 \cdot 4H_2O$ in crystal and in aqueous solution is due to the different contribution of Cu $4p_z$ and $5p_z$ orbitals by the bond character of the Cu-O bond.

KEYWORDS: Copper(II)-cyclam complex, XANES, DV-Xα method, electronic transition probability

*Corresponding author, e-mail: wakita@SUNSP1.sc.fukuoka-u.ac.jp

ADVANCES IN QUANTUM CHEMISTRY, VOLUME 37

0065-3276/01 $35.00

1. INTRODUCTION

Structures of 1,4,8,11-tetraazacyclotetradecanecopper(II) complexes ($[Cu(cyclam)]^{2+}$) with F^-, Cl^-, and Br^- have been determined in crystals (1-3). The effect of solvents on the axial ligation constants of (C-*meso*- (L^1) and C-*rac*-5,5,7,12,12,14-hexamethyl-cyclam (L^2))copper(II) complexes with Cl^- and Br^- have been studied in water and in methanol, suggesting an interesting

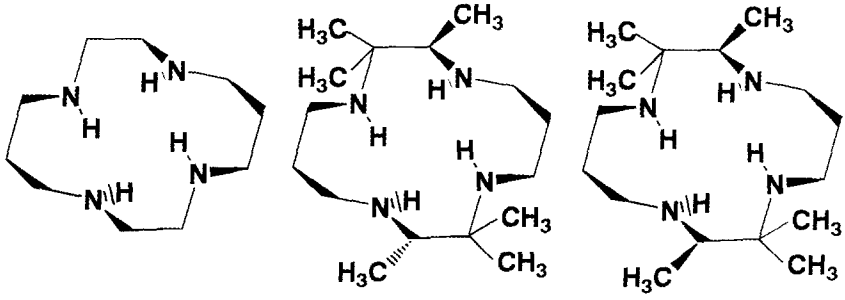

cyclam L^1 L^2

result that the ligation constant for Br^- is slightly larger than that for Cl^- in water, while the ligation constant for Br^- is much smaller than that for Cl^- in methanol (4). The structures of $[Cu(cyclam)]^{2+}$ complex with Cl^- in aqueous solution have been investigated from solution X-ray diffraction (5), and Br^- from extended X-ray absorption fine structure (EXAFS) measurements (6). The former method revealed that the $[Cu(cyclam)]Cl_2$ complex in aqueous solution forms a distorted octahedron with two H_2O molecules in the axial positions. However, the latter one could not reveal the details of the axial coordination sites for the both complexes because the interactions between Cu(II) and the anions at the axial positions little contribute to the EXAFS functions. Thus the structure of the $[Cu(cyclam)]^{2+}$ complexes with the halide ions, especially Br^- which is more likely than Cl^- to coordinate to Cu(II) in aqueous solution, remains ambiguous.

In the present study, we synthesized dibromo(1,4,8,11-tetraazacyclotetradecane)copper(II) ($[CuBr_2(cyclam)]$) and diaqua(1,4,8,11-tetraazacyclotetradecane)copper(II) difluoride four hydrate ($[Cu(cyclam)-(H_2O)_2]F_2{\cdot}4H_2O$) complexes and performed single crystal structure analysis and X-ray absorption near-edge structure (XANES) measurements in crystals and in aqueous solution. Furthermore, DV-Xα molecular orbital calculations have been made for models based on these results, and the structures and electronic states of the $[Cu(cyclam)]^{2+}$ complexes in crystals and in aqueous solution are discussed, in particular, on the axial coordination to Cu(II).

2. EXPERIMENTAL

2.1. Synthesis and Single Crystal Structure Analysis of [$CuBr_2$(cyclam)] complex

[$CuBr_2$(cyclam)] complex was synthesized according to the literature (7). $CuBr_2$ and cyclam were mixed in 1 : 1 ratio (5 mmol each) in 40 ml of methanol and refluxed with stirring for 3 h. The residue obtained by evaporation was dissolved in a small quantity of methanol, and brown solid was obtained by addition of a large quantity of ether. This solid was filtered and left in a desiccator. The dried solid was purified by recrystallization twice from water, then dissolved in water and left to stand. After three days needle magenta crystals were separated. The single crystal structure analysis was performed for this single crystal obtained (3). Found: C, 27.68; H, 5.40; N, 13.21 %. Calcd for [$CuBr_2(C_{10}H_{24}N_4)$] (MW = 423.68): C, 28.35; H, 5.71; N, 13.22 %. Crystal data: monoclinic, space group $P2_1/c$, a = 7.113(1), b = 12.527(1), c = 8.890(2) Å, β = 110.64(1) °, U = 741.3(2) $Å^3$, Z = 2, D_c = 1.898 g cm^{-3}, F_{000} = 422, λ = 0.7107 Å, μ(MoK_α) = 68.66 cm^{-1}, crystal dimensions 0.48 × 0.26 × 0.04 mm. The structure was resolved by the heavy-atom Patterson method and subsequent Fourier techniques. Structural refinement was made by a full-matrix least-squares method on non-hydrogen atoms with anisotropic temperature factors. The final values of the discrepancy indices R and R_w were 0.051 and 0.056, with a weighting scheme of w = 1 / $\sigma^2(F)$, respectively. Selected bond lengths are 2×Cu-N(1) 2.026(4) Å, 2×Cu-N(2) 2.033(5) Å, 2×Cu-Br 2.963(8) Å.

2.2. Synthesis of [Cu(cyclam)$(H_2O)_2$]$F_2 \cdot 4H_2O$ complex

[Cu(cyclam)$(H_2O)_2$]$F_2 \cdot 4H_2O$ complex was synthesized as reported in the literature (2) and obtained as large purple crystals by leaving to stand for three days after recrystallization twice from ethanol. Found: C, 29.98; H, 8.05; N, 13.32 %. Calcd for [Cu$(C_{10}H_{24}N_4)(H_2O)_2$]$F_2 \cdot 4H_2O$ (MW = 409.96): C, 29.30; H, 8.85; N, 13.67 %.

2.3. Collection of XANES Data

Cu K-edge spectra were collected at the Photon Factory, KEK, Tsukuba, by using the unfocused bending magnet beam line 10B station with

an Si (311) channel-cut monochromator, in the range of 8950 - 9050 eV with 0.3 eV step. The time to collect X-ray photons was 1 s at each measuring point. Crystal samples were measured in pellets as a mixture of the sample and cellulose to an optimized thickness. Aqueous solution samples (~0.4 mol dm^{-3}) prepared by dissolving the crystal sample in deionized water were measured in a solution cell made of stainless steel with Mylar films as window material.

2.4. Models and DV-Xα Calculations

DV-Xα molecular orbital (MO) calculations (8, 9) were performed for four models; [$CuBr_2$(cyclam)], [CuBr(cyclam)$(H_2O)]^+$, and two [Cu(cyclam)$(H_2O)_2]^{2+}$ that Cu-O bond lengths are different, hereafter referred to models A, B, C and D, respectively, and their atomic coordinates and structures are shown in Table 1 and Fig. 1, respectively. The structure of the cyclam ligand in all the models was based on the crystal structure of the [$CuBr_2$(cyclam)] with the H atoms that are crystallographically evaluated from the positions of non-H atoms. The bond length between Cu(II) and O atoms in H_2O at the axial positions for models B, C, and D was set at the value obtained for $[Cu(cyclam)]^{2+}$ in aqueous solution by the X-ray diffraction measurement (5) and for [Cu(cyclam)$(H_2O)_2]F_2 \cdot 4H_2O$ by single crystal structure analysis (2).

The DV-Xα calculations were made with C_i symmetry for models A, C, and D, and without symmetry for model B. Numerical atomic orbitals of 1*s* to 5*p* for Cu, and 1*s* to 2*p* for C, N and O, and 1*s* for H were used as a basis set for the DV-Xα calculations in the ground and transition states. The sample points used in the numerical integration were taken up to 30000 for each calculation. Self-consistency within 0.001 electrons was obtained for the final orbital populations. Transition probabilities calculated for each model were convoluted by a Gaussian function with a half-width at half-height (HWHH) of 1.0 eV to make transition peak shapes comparable with experimental XANES spectra.

3. RESULTS AND DISCUSSION

Fig. 2 shows the experimental XANES spectra for [$CuBr_2$(cyclam)] and [Cu(cyclam)$(H_2O)_2]F_2 \cdot 4H_2O$ in crystal and in aqueous solution. The profile at 8980 ~ 8990 eV for spectrum **a** is remarkably different from that for **b**, whereas the profile in the range for spectrum **d** is very similar to that for **c**. These results indicate that the coordination structure of Cu(II) within [$CuBr_2$(cyclam)] in crystal is different from that in aqueous solution, whereas

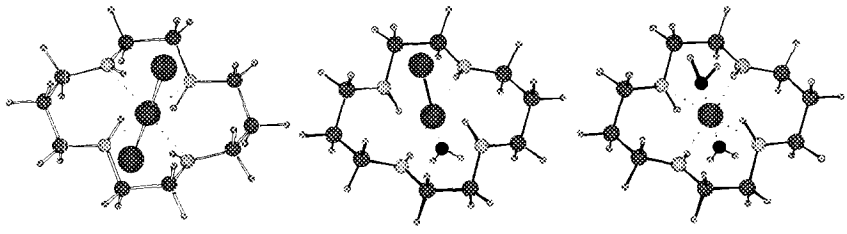

Fig 1. Schematic model structures used for the DV-Xα MO calculations. Cu-O bond length of model C is shorter than that of model D.

Table I. Atomic positions (Å) of models A, B, C, and D used in the DV-Xα calculations

Atom	x	y	z	Atom	x	y	z	Atom	x	y	z
----------**cyclam**----------				H	0.667	2.747	1.290	----**Axial positions**			
Cu	0.000	0.000	0.000	H	-0.667	-2.747	-1.290	**for model B**----			
N	1.373	-1.479	-0.181	H	-2.537	1.198	-1.449	Br	0.000	0.000	2.957
N	-1.373	1.479	0.181	H	2.537	-1.198	1.449	O	0.000	0.000	-2.770
N	-1.364	-1.501	0.147	H	-2.549	-1.235	-1.471	H	-0.768	0.000	-3.346
N	1.364	1.501	-0.147	H	2.549	1.235	1.471	H	0.768	0.000	-3.346
C	0.711	-2.736	0.280	H	-3.308	-0.003	0.944	----**Axial positions**			
C	-0.711	2.736	-0.280	H	3.308	0.003	-0.944	**for model C**----			
C	-0.717	-2.748	-0.339	H	-1.204	3.493	0.019	O	0.000	0.000	2.770
C	0.717	2.748	0.339	H	1.204	-3.493	-0.019	O	0.000	0.000	-2.770
C	-2.684	1.274	-0.515	H	1.200	3.510	0.049	H	0.768	0.000	3.346
C	2.684	-1.274	0.515	H	-1.200	-3.510	-0.049	H	-0.768	0.000	-3.346
C	2.682	1.303	0.535	H	-3.252	2.014	-0.339	H	-0.768	0.000	3.346
C	-2.682	-1.303	-0.535	H	3.252	-2.014	0.339	H	0.768	0.000	-3.346
C	3.351	0.000	0.007	H	3.248	2.046	0.348	----**Axial positions**			
C	-3.351	-0.000	-0.007	H	-3.248	-2.046	-0.348	**for model D**----			
H	1.559	-1.580	-1.107	H	4.259	-0.006	0.281	O	0.000	0.000	2.484
H	-1.559	1.580	1.107	H	-4.259	0.006	-0.281	O	0.000	0.000	-2.484
H	-1.543	-1.625	1.071	----**Axial positions**				H	0.768	0.000	3.060
H	1.543	1.625	-1.071	**for model A**----				H	-0.768	0.000	-3.060
H	-0.657	2.748	-1.228	Br	0.000	0.000	2.957	H	-0.768	0.000	3.060
H	0.657	-2.748	1.228	Br	0.000	0.000	-2.957	H	0.768	0.000	-3.060

the coordination structure of Cu(II) within $[Cu(cyclam)(H_2O)_2]F_2 \cdot 4H_2O$ in crystal is the same as that in aqueous solution. Furthermore, the profile in the same range for spectrum **b** is different from that for **c**, in spite of both samples are aqueous solution. Thus, these different profiles for spectra **a**, **b**, and **c** will reflect the change of coordination structure between Cu(II) and atoms in the axial positions.

The calculated transition probabilities and peaks for models A, B, C, and D are shown in Fig. 3. The energy scale was calibrated by assigning the calculated $1s \rightarrow 3d$ peak to the corresponding pre-edge peak in each experimental XANES spectrum. The calculated peaks for models A, B, C, and D reproduce the experimental spectral features well for both crystal and solution samples of $[CuBr_2(cyclam)]$ and $[Cu(cyclam)(H_2O)_2]F_2 \cdot 4H_2O$, respectively, except for the region above 9000 eV, in which more outer atomic orbitals of Cu will be required to obtain a good fit. A shoulder at 8980 ~ 8990 eV for spectrum **a** is assigned to molecular orbital $54a_u$ for model A, a feature at 8980 ~ 8990 eV for spectrum **b** to orbitals 94, 95, and 99 for model B, and

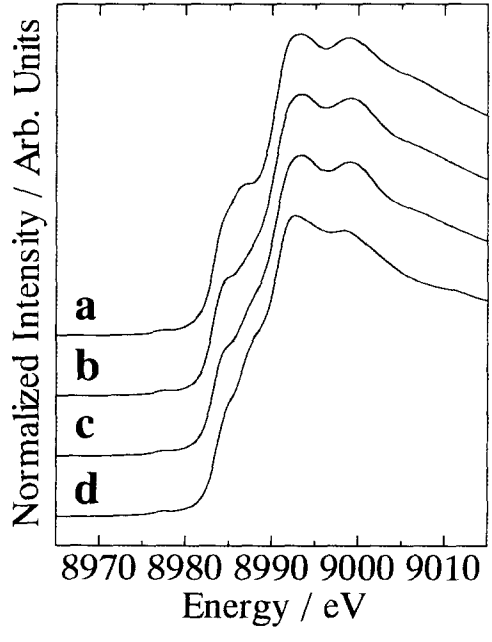

Fig 2. Cu *K* XANES spectra for $[CuBr_2(cyclam)]$ in crystal (**a**), and in aqueous solution (**b**), and for $[Cu(cyclam)(H_2O)_2]F_2 \cdot 4H_2O$ in aqueous solution (**c**), and in crystal (**d**).

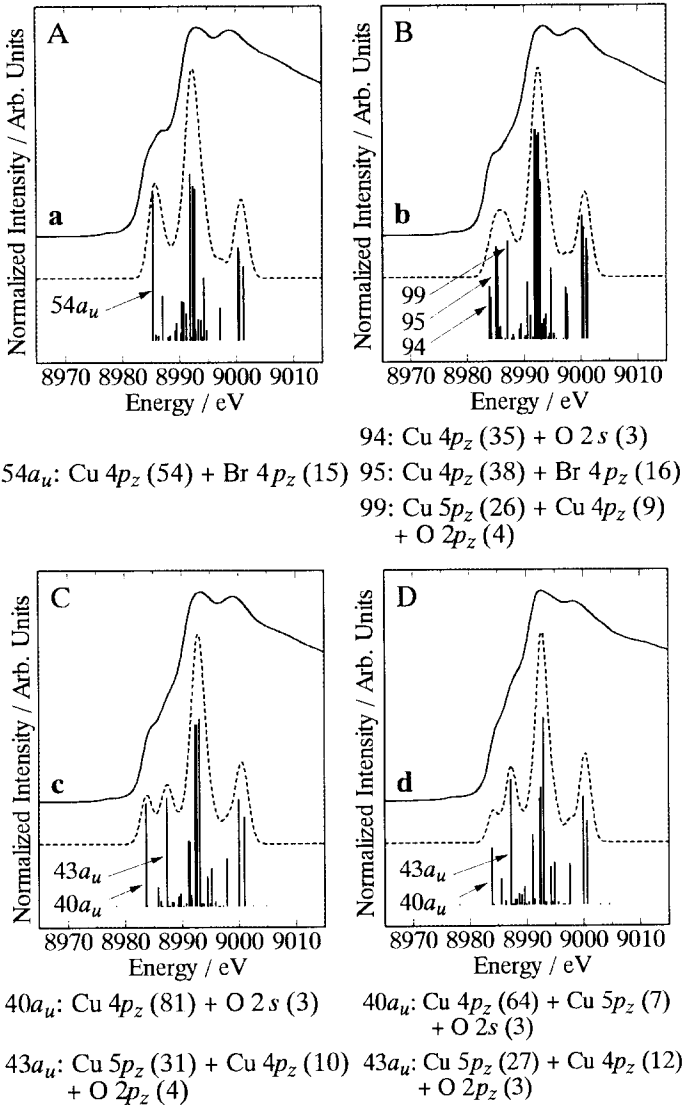

54a_u: Cu 4p_z (54) + Br 4p_z (15)

94: Cu 4p_z (35) + O 2s (3)
95: Cu 4p_z (38) + Br 4p_z (16)
99: Cu 5p_z (26) + Cu 4p_z (9) + O 2p_z (4)

40a_u: Cu 4p_z (81) + O 2s (3)

43a_u: Cu 5p_z (31) + Cu 4p_z (10) + O 2p_z (4)

40a_u: Cu 4p_z (64) + Cu 5p_z (7) + O 2s (3)

43a_u: Cu 5p_z (27) + Cu 4p_z (12) + O 2p_z (3)

Fig 3. Calculated transition probabilities (vertical bars) and peaks (dashed lines) for models A, B, C, and D. The experimental XANES spectra (solid lines) are given for reference. The important vertical bars are labeled with the MOs and their contributions.

two shoulders at 8980 ~ 8990 eV for spectra **c** and **d** to orbitals $40a_u$ and $43a_u$ for models C and D, respectively.

Constituent atomic orbitals and proportion of the MOs at 8980 ~ 8990 eV for each model are shown in Fig. 3. The orbital $54a_u$ for model A, orbitals 94, 95, and 99 for model B, and orbitals $40a_u$ and $43a_u$ for models C and D are mainly occupied by Cu $4p_z$ and $5p_z$ orbitals. Furthermore, orbital $54a_u$ for model A and orbitals $40a_u$ and $43a_u$ for models C and D are contributed partially from Br and O orbitals, respectively. For model B, orbital 95 is contributed from Br orbital, and orbitals 94 and 99 from O orbitals.

These results demonstrate that the profile at 8980 ~ 8990 eV for spectrum **b** without two clear shoulders like that for **c** is due to orbital 95 including Br orbital between orbitals 94 and 99 including O orbitals, and that the well observed shoulder in the low energy side at 8980 ~ 8990 eV for spectrum **c** than for **d** is due to larger proportion of Cu $4p_z$ in orbital $40a_u$.

It has been reported by Kosugi *et al.* about the profiles at 8980 ~ 8990 eV for Cu(II) compounds that the two features at 8985 and 8987 eV in Fig. 2 are assigned to $1s$-$4p\pi$ transitions based on well-screened and poorly screened core-hole states, respectively (10). However, the profiles at 8980 ~ 8990 eV for Cu(II) complexes have been reproduced satisfactorily by DV-Xα calculations on the coordination structure of Cu(II) (11, 12) as well as in the present work. Thus, it is suggested that the profiles at 8980 ~ 8990 eV for Cu(II) compounds are influenced by not only the ligand-to-metal charge transfer (LMCT) effects but change in the coordination structure of Cu(II).

Table 2 shows the net charges and bond orders obtained for each model. Positive charge on Cu and negative charge on N decrease in the order C > B > A. The Cu-N bond order decreases in the order C > B > A, and the

Table II. Net charge[a] (above) and bond order[b] (below)

	A	B	C	D
Cu	0.212	0.925	1.706	1.874
N	-0.298	-0.336	-0.427	-0.456
Br	-0.070	-0.044	——	——
O	——	-0.899	-0.968	-1.007
H	——	0.458	0.496	0.494
	A	B	C	D
Cu-N	-0.064	0.009	0.074	0.057
Cu-Br	1.031	1.016	——	——
Cu-O	——	0.018	0.023	-0.070
O-H	——	0.581	0.572	0.589

[a] 1 / atom, [b] 1 / bond

Cu-O bonds in the order C > B. The Cu-Br bond order for model B slightly decreases compared with that for model A, but the Cu-Br bond for model B still has covalent character. This is probably due to increased covalent character in the Cu-N bonds by replacement of one axial Br^- with an H_2O molecule. This may be a reason why another Br^- is difficult to be exchanged with an H_2O molecule in aqueous solution.

It has been found that the structure of $[Cu(cyclam)]^{2+}$ complex with Br^- in aqueous solution is different from that with Cl^- in aqueous solution obtained by Ohtaki *et al.* (5). The different axial coordination within both structures correspond to the larger ligation constants of CuL^1 and CuL^2 with Br^- than those with Cl^- in water (4). Therefore, it is concluded that the predominant complex in the aqueous solution of $[CuBr_2(cyclam)]$ is model B, $[CuBr(cyclam)(H_2O)]^+$.

Positive charge on Cu and negative charge on N and O for model C are large compared with those for model D. The Cu-N and Cu-O bond orders for model C slightly increase compared with those for model D. These trends are caused by more covalent character of the Cu-O bond for model C than that for model D. It shows that the Cu-O bond in aqueous solution is more stable than in crystal. Thus, it is considered that the difference of the shoulders at 8985 eV for spectra **c** and **d** is due to the different contribution of Cu $4p_z$ and $5p_z$ orbitals to orbitals $40a_u$ and $43a_u$ by the bond character of the Cu-O bond for $[Cu(cyclam)(H_2O)_2]F_2{\cdot}4H_2O$ in crystal and in aqueous solution.

4. CONCLUSION

The structures and electronic states of the $[CuBr_2(cyclam)]$ and $[Cu(cyclam)(H_2O)_2]F_2{\cdot}4H_2O$ in crystal and in aqueous solution were investigated from XANES and DV-Xα calculations. It has been found that the Cu *K*-edge XANES patterns at 8980 ~ 8990 eV for these Cu(II) complexes are influenced by not only LMCT effects but by change of the coordination structure of Cu(II), especially of axial coordination structure. The structure of the $[CuBr_2(cyclam)]$ in aqueous solution has been concluded to be $[CuBr(cyclam)(H_2O)]^+$ as predominant complex species, because another Br^- is difficult to exchange with an H_2O molecule in aqueous solution due to increased covalent character in the Cu-N bonds by replacement of one axial Br^- with an H_2O molecule. It has been found that the slight difference of the XANES spectral patterns at 8985 eV for $[Cu(cyclam)(H_2O)_2]F_2{\cdot}4H_2O$ in crystal and in aqueous solution is due to the different contribution of Cu $4p_z$ and $5p_z$ orbitals by the bond character of the Cu-O bond.

ACKNOWLEDGEMENT

This work was performed under the approval of the Photon Factory Program Advisory Committee (Proposal No. 93G148).

REFERENCES

(1) Studer, M.; Riesen, A.; Kaden, T. A. *Helv. Chim. Acta*, **1989**, *72*, 1253.
(2) Emsley, J.; Arif, M.; Bates, P. A.; Hursthous, M. B. *J. Mol. Struct.*, **1990**, *220*, 1.
(3) After we had performed single crystal structure analysis of the $[CuBr_2(C_{10}H_{24}N_4)]$ complex, the following paper was just published: Chen, X.; Long, G.; Willett, R. D.; Hawks, T.; Molnar S.; Brewer, K. *Acta Crystallogr.*, **1996,** *C52*, 1924.
(4) Liang, B. F.; Tsay, Y. K.; Chung, C. S. *J. Chem. Soc. Dalton Trans.*, **1983**, 995.
(5) Ohtaki, H.; Seki, H. *J. Macromol. Sci. – Chem.*, **1990**, *A27*, 1305.
(6) Yoshida, N. Master Thesis, Fukuoka University, 1993.
(7) Bhattacharya, P. K. *Indian J. Chem.*, **1980**, *19A*, 1086.
(8) Adachi, H.; Tsukada, M.; Satoko, C. *J. Phys. Soc. Jpn.*, **1978**, *45*, 875.
(9) Adachi, H.; Taniguchi, K. *J. Phys. Soc. Jpn.*, **1980**, *49*, 1944.
(10) Kosugi, N.; Tokura, Y.; Takagi, H.; Uchida, S. *Phys. Rev.*, **1990**, *B41*, 131.
(11) Valli, M.; Matsuo, S.; Wakita, H.; Yamaguchi, T.; Nomura, M. *Inorg. Chem.*, **1996**, *35*, 5642.
(12) Yamashita, S.; Fujiwara, M.; Kato, Y.; Yamaguchi, T.; Wakita, H. In "Adv. Quantum Chem.", Löwdin P. O., Ed.; Academic Press: Tokyo, 1997; Vol. 29, 357-371.

A Method of Incorporating the Composition into the Calculation of the O K_α X-ray Emission Spectrum of the Glassy State SiO_2-Na_2O Binary Slag with the DV-Xα Molecular Orbital Calculation

Masao Morishita[*1], Koichiro Koyama[*1], Tadayoshi Kikko[*2], Masahiko Morinaga[*3] and Hirohiko Adachi[*4]

[*1] *Department of Materials Science and Engineering, Faculty of Engineering, Himeji Institute of Technology, 2167 Shosha, Himeji 671-2201, Japan.*
[*2] *Graduate Student of Himeji Institute of Technology.*
[*3] *Department of Materials Science and Engineering, NagoyaUniversity, Furocho, Chigusa-ku, Nagoya, 464-0814 Japan.*
[*4] *Department of Materials Science and Engineering, Kyoto University, Yoshida Honmachi, Sakyo-ku, Kyoto, 606-8317 Japan.*

(Received October 26, 1998)

O K_α X-ray emission spectra for SiO_2-Na_2O binary slags simulated with the DV-Xα molecular orbital calculation were compared with ones measured by EPMA. The composition of the slag has been incorporated into the O_{2p} partial density of states (PDOS) calculation. The O_{2p} PDOS, as a function of the Na_2O content, agreed well with the measured O K_α X-ray emission spectra for the glassy state 66.7mol%SiO_2−33.3mol%Na_2O and 42.0mol%SiO_2−58.0mol%Na_2O binary slags. The present method was found to provide a very useful means of clarifying the change in the ionic configuration of the slag with the metal oxide content, and also of understanding the basicity.

KEYWORDS : SiO_2-Na_2O binary slag, glassy state, O K_α X-ray emission spectrum, partial density of states as a function of Na_2O content, basicity

*Corresponding author : e-mail morisita@mse.eng.himeji-tech.ac.jp

ADVANCES IN QUANTUM CHEMISTRY, VOLUME 37

0065-3276/01 $35.00

1. INTRODUCTION

Molten slags are important substances for iron and steel making. Recently, the optical method (1-3) has been widely utilized to determine the basicity of such slags. In this method, Pb^{2+} ions are added to slag as probe ions. The reduction in the Pb^{2+} 6s−6p energy gap caused by electron donation from oxygen ions can be measured from the shift in frequency in the UV absorption band. The reduction in the Pb^{2+} 6s−6p energy gap is related to the oxygen activity and has been adopted as a basicity scale (1-3). However, this method can only tell us about average electron donation. It therefore can not clarify the change in the local electronic state of Si^{4+} and oxygen ions as the metal oxide content changes.

Previously we have proposed a method to incorporate the Na_2O content into the calculation of the Si_{3p} partial density of states (PDOS) of the SiO_2−Na_2O binary slag (4-6). The Si_{3p} PDOS agreed well with the experimental Si K_β X-ray emission spectra of the binary slag (5,6). Furthermore, with this method, we were able to explain the reason for the change in the shape of the Si K_β X-ray emission spectrum of the slag as its metal oxide content changes.

In order to obtain better understanding of slag basicity, we have attempted to apply the same method to the investigation of the change in shape of O K_α X-ray emission spectrum of the oxygen ion in slags as the metal oxide content changes. In the present study, we simulated the O K_α X-ray emission spectra of 66.7mol%SiO_2 − 33.3mol%Na_2O and 42.0mol%SiO_2−58.0mol%Na_2O binary slags, and compared them with ones measured by EPMA.

The fine shapes appearing in X-ray emission spectra can be measured more accurately with electron excitation methods (e.g. EPMA) rather than X-ray excitation methods (e.g. X-ray fluorescence analysis) (7,8). In the present study, therefore, we undertook to measure the O K_α X-ray emission spectra of the 66.7mol%SiO_2− 33.3mol%Na_2O and 42mol%SiO_2−58mol%Na_2O binary slags using EPMA.

X-ray emission spectra have been precisely calculated (9) using Slater's transition state method (10). Furthermore, it was also found that the spectra could be approximately interpreted using the partial density of states (PDOS) of the ground state (11-14). In particular, calculation of PDOS using the DV-Xα (15,16) method is well known to be very useful for the interpretation of the X-ray emission spectra of pure solid state materials. Tanaka et.al. interpreted the shape of the pure SiO_2 spectrum from O_{2p} PDOS (14) using the DV-Xα method. However, changes in the shape of the O K_α X-ray emission spectra due to changes in the composition of glassy or liquid state

materials have never been treated, either by the DV-Xα method, or by other methods such as the semi-empirical method or the ab-initio Hartree-Fock method. In the present study, therefore, we attempted to incorporate the Na_2O content into O_{2p} PDOS DV-Xα calculation, and to simulate the O K_{α} X-ray emission spectra of the 66.7mol%SiO_2−33.3mol%Na_2O and 42mol%SiO_2−58mol%Na_2O binary slags.

2. METHODS OF EXPERIMENT AND SIMULATION

2.1. Measurement of X-ray emission spectrum

Commercial SiO_2 and Na_2CO_3 powders were used as starting materials. The 66.7mol%SiO_2−33.3mol%Na_2O and 42.0mol%SiO_2−58.0mol%Na_2O glassy state slag specimens were prepared by melting the mixtures of these starting materials in a platinum vessel at 1573 K in air and then pouring them onto a stainless steel plate (Na_2CO_3 decomposes to Na_2O on heating). These flat specimens we obtained were immediately put into a vacuum chamber where thin carbon film evaporated onto their surfaces, and then they were immediately put into the spectrometer. Other specimens, prepared the same way, were submitted to X-ray diffraction analysis. These preparations were all carried out as quikly as possible to avoid absorption of moisture from the air. We therefore judge that silanol groups had negligible effects on the spectra.

The O K_{α} X-ray emission spectra of the 66.7mol%SiO_2−33.3mol%Na_2O and 42.0mol%SiO_2−58.0mol%Na_2O glassy state slags were measured on EPMA (Joel JXA 8900R). TAP (Thallium acid phthalate) was used as the analyzing crystal. The emission current and acceleration potential were set at 2×10^{-7} A and 10 kV, respectively. The X-ray photon energy was calibrated using the main peak in the pure SiO_2 O K_{α} spectrum.

The second order Na K_{α} X-ray emission spectrum and the O K_{α} X-ray emission spectrum were seen to overlap, the real intensity of the former being twice that of the latter. Thus, we eliminated the second order Na K_{α} X-ray using a single channel analyzer (SCA).

2.2. Simulation method

2.2.1. Cluster model

The covalent bond between Si^{4+} ion and O^{2-} ion is very strong in molten SiO_2. This is the reason for the formation of the highly polymerized network structure of molten SiO_2. However, when large amount of basic metal oxides such as Li_2O, Na_2O, K_2O, CaO and MgO are added to molten SiO_2, the Si^{4+} ions capture O^{2-} ions of the metal oxides to have an electron configuration of an Ar-like closed shell (17), and consequently the polymerized network structure decomposes to form discrete anions, SiO_4^{4-}, $Si_2O_7^{6-}$, $Si_3O_{10}^{8-}$, etc.(17-21) On the other hand, the metal ions, like Na^+, K^+ and Ca^{2+}, coordinate edge-shared sites of the unit cell of the tetrahedron SiO_4^{4-} (22,23).

Figure 1 shows the cluster models adopted for the present calculations. They are the discrete anions SiO_4Na^{3-}, $Si_2O_7Na^{5-}$, $Si_3O_{10}Na^{7-}$, $Si_3O_9Na^{5-}$ and $Si_4O_{12}Na^{7-}$. In SiO_4Na^{3-}, only four non-bridging oxygen ions (O_{NB}) coordinate Si^{4+} ion. In $Si_2O_7Na^{5-}$, $Si_3O_{10}Na^{7-}$, $Si_3O_9Na^{5-}$ and $Si_4O_{12}Na^{7-}$, however, bridging oxygen ions (O_B), as well as O_{NB}, coordinate Si^{4+} ion. It is envisaged that more Na^+ ions coordinate each discrete anion. However for the purpose of the present study it is sufficient to consider only these cluster models. The configurations and interatomic distances obtained from the X-ray diffraction (24,25) were adopted.

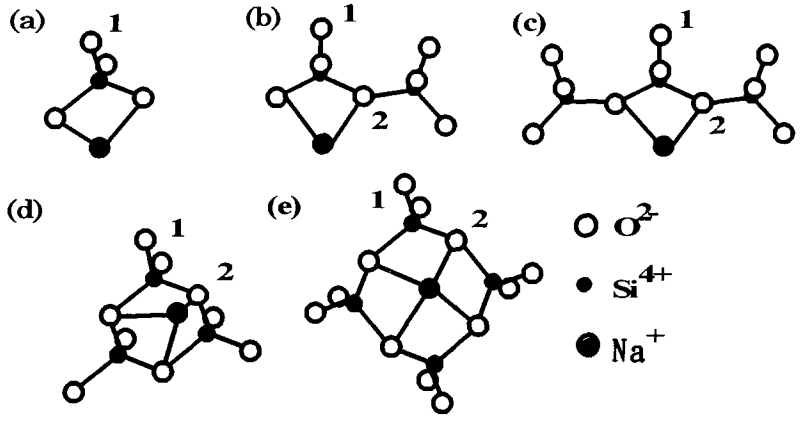

Fig 1. Cluster models adopted in the calculation: (a)SiO_4Na^{3-}, (b)$Si_2O_7Na^{5-}$, (c)$Si_3O_{10}Na^{7-}$, (d)$Si_3O_9Na^{5-}$ and (e) $Si_4O_{12}Na^{7-}$.

2.2.1. A method to calculate density of states as a function of composition

We devised a method to calculate glassy state slag Si_{3p} PDOS where the Na_2O content is incorporated (4-6). In the present study, we calculated the O_{2p} PDOS for the 66.7mol%SiO_2−33.3mol%Na_2O and 42mol%SiO_2−58mol%Na_2O glassy state binary slags by the same way as in the previous calculation of the Si_{3p} PDOS (4-6).

PDOS (Q_i) can be approximately evaluated from the coeffients, C_{vl}, for each molecular orbital and overlap matrices, S_{vj} (15). Initially, we calculated each O_{2p} PDOS (Q_{2p}) for the cluster models SiO_4Na_3, $Si_2O_7Na^{5-}$, $Si_3O_{10}Na^{7-}$, $Si_3O_9Na^{5-}$ and $Si_4O_{12}Na^{7-}$, shown in Fig.1(a)~(e), in the same way as in the previous studies (4-6).

$$Q_{2p} = \Sigma(j,l) C_{2pl} C_{jl} S_{2pj} \quad (1)$$

In order to evaluate the relative ratio of Q_{2p} for each cluster model to the total of the O_{2p} PDOS for the 66.7mol%SiO_2−33.3mol%Na_2O and 42mol%SiO_2−58mol%Na_2O slags, we multiplied Q_{2p} by a coefficient, m_i, such that,

$$m_i Q_{2p} = \Sigma(j,l)\, m_i C_{2pl} C_{jl} S_{2pj} \quad (2)$$

where m_i was the molar fraction of each discrete anion as shown in Table I.

Table I. Molar fractions of discrete anions (27).

	Molar fraction (m_i)	
Discrete anion	33.3mol%Na_2O	58mol%Na_2O
SiO_4Na^{3-}	0	0.14
$Si_2O_7Na^{5-}$	0.03	0.18
$Si_3O_{10}Na^{7-}$	0.20	0.32
$Si_3O_9Na^{5-}$	0.43	0.26
$Si_4O_{12}Na^{7-}$	0.34	0.10

Recently, Sawaguchi et.al., by a molecular dynamics calculation (27), succeeded in determining the change in molar fraction of each discrete anion with the Na_2O content at 1500 K. In the present study, we used their results for the 66.7mol%SiO_2−33.3mol%Na_2O and 42mol%SiO_2−58mol%Na_2O slags as the coefficients, m_i (Table I). The total of O_{2p} PDOS, Q^{total}_{2p} for the 66.7mol%SiO_2 − 33.3mol%Na_2O and 42mol%SiO_2−58mol%Na_2O slags were calculated from the total of each $m_i Q_{2p}$, that is,

$$Q^{total}_{2p} = \Sigma(i)\, m_i Q_{2p} = \Sigma(i)\Sigma(j,l) m_i C_{2pl} C_{jl} S_{2pj} \quad (3)$$

The Q^{total}_{2p} was compared with the measured O K_α X-ray emission spectra from the 66.7mol%SiO_2 − 33.3mol%Na_2O and 42mol%SiO_2 − 58mol%Na_2O slags. The calculated molecular orbital energies of each cluster model were nolmalized on the non-bonding O_{2p} level.

3. RESULT AND DISCUSSION

3.1. O_{2p} PDOS (m_iQ_{2p}) as a function of Na_2O content

Figure 2 shows the O_{NB} 2p PDOS (m_iQ_{2p}) for SiO_4Na^{3-} in the 42mol%SiO_2—58mol%Na_2O slag. The m_iQ_{2p} main peak was near -2.5 eV. The SiO_4Na^{3-} m_iQ_{2p} was high because the SiO_4Na^{3-} molar fraction in the 42mol%SiO_2—58mol%Na_2O slag was high, and this contributed to the O K_α X-ray emission spectrum. The 66.7mol%SiO_2—33.3mol%Na_2O slag has no SiO_4Na^{3-} (Table I). Therefore, the SiO_4Na^{3-} m_iQ_{2p} was not able to contribute to the O K_α X-ray emission spectrum.

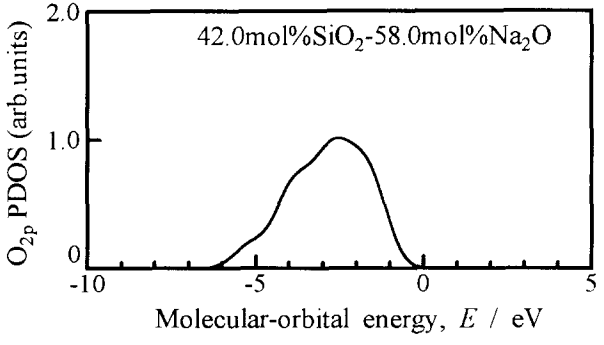

Fig 2. Calculated O_{NB} 2p PDOS (m_iQ_{2p}) for SiO_4Na^{3-} in molten 42.0mol%SiO_2—58.0mol%Na_2O.

Figure 3 shows the O_{2p} PDOS (m_iQ_{2p}) for $Si_2O_7Na^{5-}$ in the 66.7mol%SiO_2—33.3mol%Na_2O and the 42mol%SiO_2—58mol%Na_2O slags. The dashed line (—·—·) shows the O_{NB} m_iQ_{2p} (No.1 in Fig 1(b)). The dotted line (·····) shows the O_B m_iQ_{2p} (No.2 in Fig 1(b)). The solid line (——) shows their total. The total m_iQ_{2p} for both slags were split into a main peak, near —2 eV, and sub peaks, near —5 and —7.5eV. The total m_iQ_{2p} for the former slag was much lower than that of the latter because the $Si_2O_7Na^{5-}$ molar fraction in the former is much smaller than that in the latter (Table I).

Figure 4 shows the O_{2p} PDOS (m_iQ_{2p}) for $Si_3O_{10}Na_7$ in the 66.7mol%SiO_2—33.3mol%Na_2O and the 42mol%SiO_2—58mol%Na_2O slags. The dashed line (—·—·) shows the O_{NB} m_iQ_{2p} (No.1 in Fig 1(c)). The dotted line (·····) shows the O_B m_iQ_{2p} (No.2 in Fig 1(c)). The solid line (——) show their total. The total

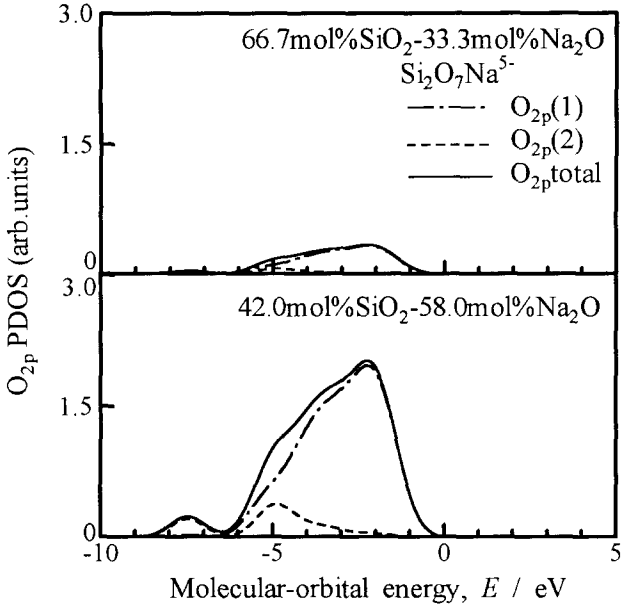

Fig 3. Calculated O_{NB} and O_B 2p PDOS (m_iQ_{2p}), and their total for $Si_2O_7Na^{5-}$ in molten 66.7mol%SiO_2—33.3mol%Na_2O and 42.0mol%SiO_2—58.0mol%Na_2O.

m_iQ_{2p} for both slags were split into a main peak, near −2.5 eV, and sub peaks, near −5.5 and −8eV. The total m_iQ_{2p} for the former slag was lower than that of the latter slag because the $Si_3O_{10}Na^{7-}$ molar fraction in the former is much smaller than that in the latter (Table I).

Figure 5 shows the O_{2p} PDOS (m_iQ_{2p}) for $Si_3O_9Na^{5-}$ in the 66.7mol%SiO_2−33.3mol%Na_2O and the 42mol%SiO_2−58mol%Na_2O slags. The dashed line (−·−·) shows the O_{NB} m_iQ_{2p} (No.1 in Fig 1(d)). The dotted line (·····) shows the O_B m_iQ_{2p} (No.2 in Fig 1(d)). The solid line (——) shows their total. The total m_iQ_{2p} for both slags were split into a main peak, near −4 eV, and sub peaks, near −2 and −7eV. The total m_iQ_{2p} for the former slag was much higher than that of the latter because the $Si_3O_9Na^{5-}$ molar fraction in the former is much larger than that in the latter (Table I).

Figure 6 shows the O_{2p} PDOS (m_iQ_{2p}) for $Si_4O_{12}Na^{7-}$ in the 66.7mol%SiO_2−33.3mol%Na_2O and the 42mol%SiO_2−58mol%Na_2O slags. The dashed line (−·−·) shows the O_{NB} m_iQ_{2p} (No.1 in Fig 1(e)). The dotted line (·····) shows the O_B m_iQ_{2p} (No.2 in Fig 1(e)). The solid line (——) shows their total. The total m_iQ_{2p} for both slags were split into a main peak, near −2 eV, and sub peaks, near

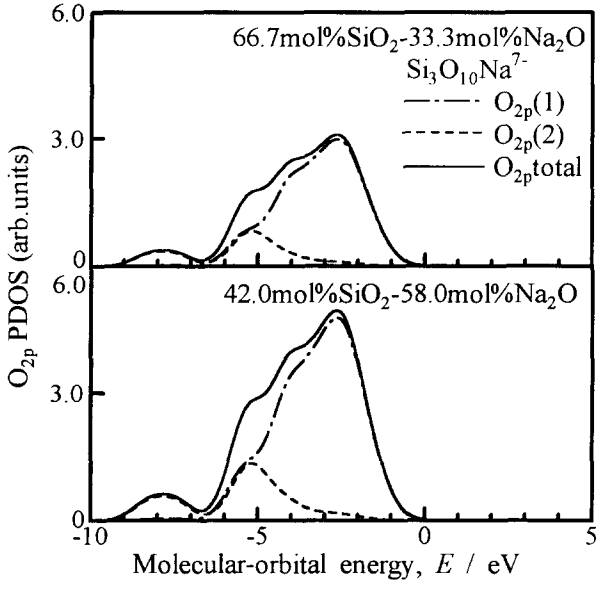

Fig 4. Calculated O_{NB} and O_B 2p PDOS (m_iQ_{2p}) and their total for $Si_3O_{10}Na^{7-}$ in molten 66.7mol%SiO_2—33.3mol%Na_2O and 42.0mol%SiO_2—58.0mol%Na_2O.

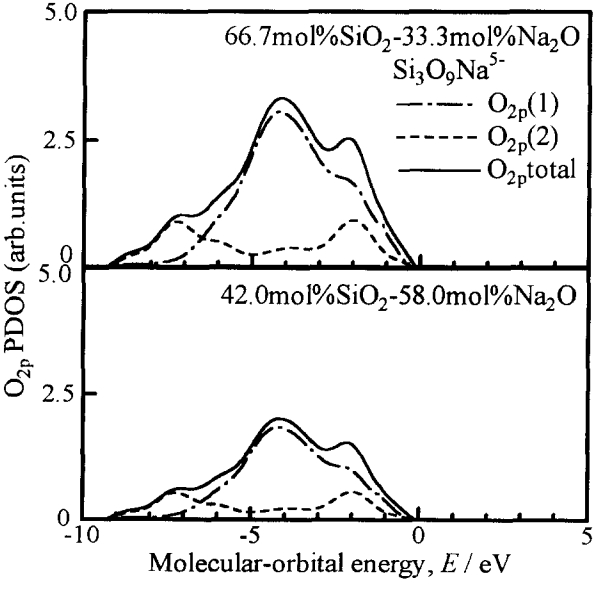

Fig 5. Calculated O_{NB} and O_B 2p PDOS (m_iQ_{2p}) and their total for $Si_3O_9Na^{5-}$ in molten 66.7mol%SiO_2—33.3mol%Na_2O and 42.0mol%SiO_2—58.0mol%Na_2O.

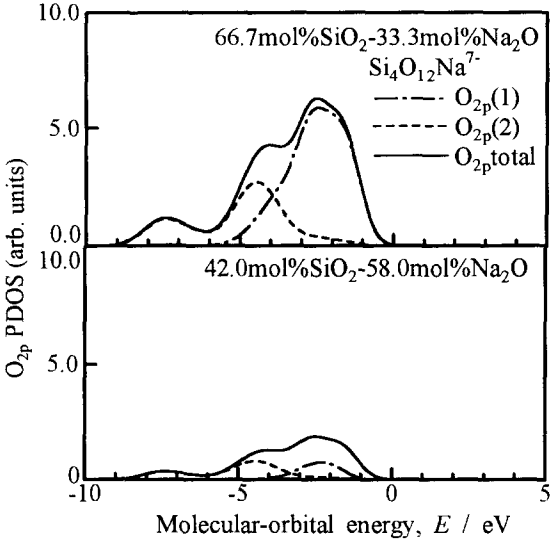

Fig 6. Calculated O_{NB} and O_B 2p PDOS ($m_i Q_{2p}$) and their total for $Si_4O_{12}Na^{7-}$ in molten 66.7mol%SiO_2—33.3mol%Na_2O and 42.0mol%SiO_2—58.0mol%Na_2O.

−4 and −7.5eV. The total $m_i Q_{2p}$ for the former slag was much higher than that of the latter because the molar fraction of $Si_4O_{12}Na^{7-}$ in the former is much larger than that in the latter (Table I).

Figure 7 shows the calculated total O_{2p} PDOS (Q^{total}_{2p}) for the 66.7mol%SiO_2—33.3mol%Na_2O slag, compared with the measured O K_α X-ray emission spectrum. In the measured O K_α EPMA spectrum, a main peak (mark A) can be seen near the X-ray energy 526 eV while two sub peaks (mark B and C) can also be seen near 524 eV (mark B) and 520.5 eV (mark C). In the Q^{total}_{2p}, a main peak (mark a) can be seen near −2eV and two sub peaks (mark b and c) can also be seen near −4eV and −7.5eV. Therefore, as can be seen, the Q^{total}_{2p} agreed well with the experimental O K_α X-ray emission spectrum.

Judging from these results, it can be said that the present discrete anion model well reproduces the real liquid state of the 66.7mol%SiO_2—33.3mol%Na_2O slag at high temperature. That is, the main peak (mark A in Fig 7) in the O K_α X-ray emission spectrum consists of the main peaks in the $Si_2O_7Na^{5-}$, $Si_3O_{10}Na^{7-}$ and $Si_4O_{12}Na^{7-}$ O_{2p} PDOS ($m_i Q_{2p}$) (Figs 3, 4 and 6) and the $Si_3O_9Na^{5-}$ sub peak (Fig 5). The higher energy sub peak (mark B) consists of the $Si_3O_9Na^{5-}$ main peak (Fig 5) and the $Si_2O_7Na^{5-}$, $Si_3O_{10}Na^{7-}$ and $Si_4O_{12}Na^{7-}$ sub peaks (Figs 3, 4, and 6). In the lower energy sub peak (mark C) consists of the $Si_2O_7Na^{5-}$, $Si_3O_{10}Na^{7-}$, $Si_3O_9Na^{5-}$ and $Si_4O_{12}Na^{7-}$ sub peaks (Figs 3, 4, 5 and

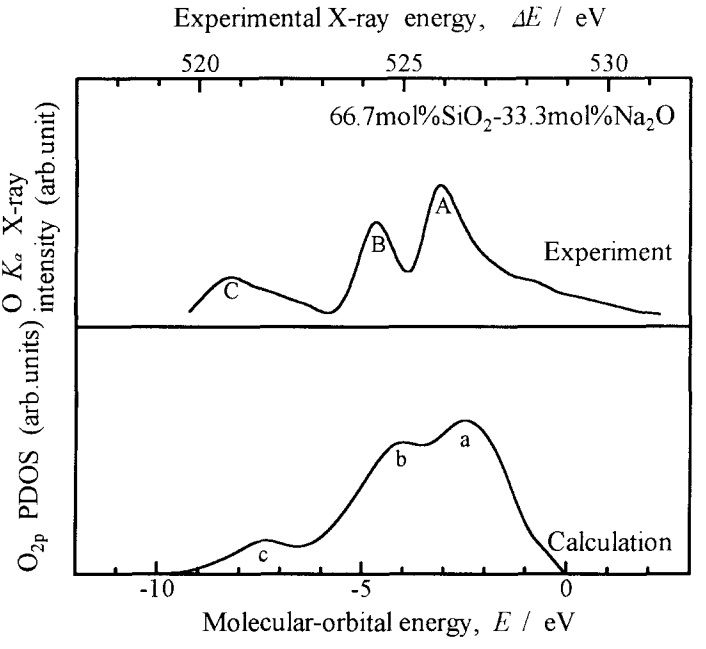

Fig 7. The calculated total O2p PDOS (Q^{total}_{2p}) and the measured O K_α EPMA spectrum for rapidly quenched 66.7mol%SiO_2—33.3mol%Na_2O.

6). Therefore, this new method is very useful for clarifying the reason for the split in the measured O K_α X-ray emission spectrum as well as the Si K_β X-ray emission spectrum of the glassy state slag (4-6).

Figure 8 shows the calculated total O_{2p} PDOS (Q^{total}_{2p}) for the 42.0mol%SiO_2—58.0mol%Na_2O slag, compared with the measured O K_α X-ray emission spectrum. In the measured O K_α X-ray emission spectrum, a main peak (mark A) can be seen near the X-ray energy 526 eV, and two sub peaks (mark B and C) can also be seen near 524 eV (mark B) and 520.5 eV. The positions of these 3 peaks are almost the same in both the 42.0mol%SiO_2—58.0mol%Na_2O slag and 66.7mol%SiO_2—33.3mol%Na_2O slag. However, the higher energy sub peak in the 42.0mol%SiO_2—58.0mol Na_2O slag (mark B in Fig 8) was lower than that in the 66.7mol%SiO_2—33.3mol%Na_2O (mark B in Fig7).

There has been no way hitherto to explain the change in shape and intensity for the O K_α X-ray emission spectrum as the composition of the SiO_2—Na_2O slag changes. Now we can explain the reason for this in the same way as in the previous study of the Si K_β X-ray emission spectrum (4-6). The $Si_3O_9Na^{5-}$ and $Si_4O_{12}Na^{7-}$ m_iQ_{2p} are much smaller in the 42.0mol%SiO_2—58.0mol%Na_2O slag than in the 66.7mol%SiO_2—33.3

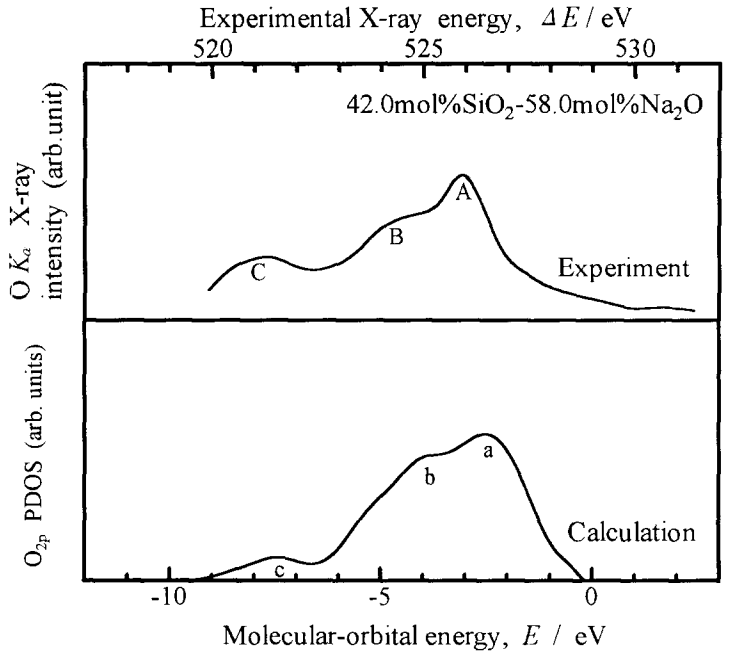

Fig 8. The calculated total O_{2p} PDOS (Q^{total}_{2p}) and the measured O K_α EPMA spectrum of rapidly quenched 42.0mol%SiO_2—58.0mol%Na_2O.

mol%Na_2O slag. That is why the higher energy sub peak in the measured O K_α X-ray emission spectrum was lower in the former (mark B in Fig 8) than in the latter (mark B in Fig 7). There were almost no differences in both the height of the main peak (mark A in Figs 7 and 8) and of the sub peak (mark C in Figs 7 and 8) between the 66.7mol%SiO_2 — 33.3mol%Na_2O slag and 42.0mol%SiO_2 — 58.0mol%Na_2O slag. We considered that this is due to the fact that the $m_i Q_{2p}$'s for SiO_4Na^{3-}, $Si_2O_7Na^{5-}$ and $Si_3O_{10}Na^{7-}$ were larger in the latter slag than in the former slag, while the $m_i Q_{2p}$'s for $Si_3O_9Na^{5-}$ and $Si_4O_{12}Na^{7-}$ were smaller in the latter slag than in the former slag. That is, it is due to the offset effect.

Furthermore, it was found for 42.0mol%SiO_2—58.0mol%Na_2O slag that the SiO_4Na^{3-} $m_i Q_{2p}$ was the main contribution to the main peak (mark A in Fig 8) in the O K_α X-ray emission spectrum, but did not contribute to the formation of the sub peaks (mark B and C in Fig 8).

The O K_α X-ray emission spectra energy range was measured to be almost the same for both slags. This means that their 1s orbital energies were almost the same. Therefore, we did not take the effect of the 1s orbital on the spectrum into the

consideration present study.

Gaskell (20,21) theoretically calculated the entropies of mixing for SiO_2—CaO, SiO_2—FeO and SiO_2—MnO slags on the basis of Guggenheim's expression for the configuration entropy of a system of linear and branched chain polymer molecule. The value he derived deviated from the experimental values (20,21). He attributed the reason for this deviation to the existence of a ring discrete anion of $Si_3O_9^{6-}$ (20,21). As above described, the main peaks in the O_{2p} PDOS (m_iQ_{2p}) for $Si_3O_9Na^{5-}$ (Fig 5) contributed to the appearance of the higher energy sub peak (mark B in Figs 7 and 8). Therefore, our present measurements and molecular orbital calculations of O K_α X-ray emission spectrum support Gaskell's prediction (20,21).

Recently Kowada et.al. (28-31) explained the optical properties of silicate glasses based on energy level structures calculated using glassy state cluster models. However they have not yet treated the problem of why the optical properties change with metal oxide content (28-31). We think that PDOS as a function of composition can be used to understand how the optical properties of glasses depend on the metal oxide content.

However, in view of the charge neutrality, the electric field around each discrete anion should affects its electronic states. There has been no way to incorporate the electric field around liquid state cluster models into the calculation. This problem should be further investigated.

3.2. Discussion for basicity

In the iron and steel making processes, sulfur in molten iron reacts with free oxygen ion and is transferred into slag according to the following equation (32).

$$S(\text{molten iron}) + O^{2-}(\text{molten slag}) = S^{2-}(\text{slag}) + 1/2O_2 \qquad (4)$$

Thus, the chemical equilibrium of the reaction proceeds to the right hand side as the concentration of free oxygen in the slag increases.

Masson (19) studied the equilibrium between the discrete anions and free oxygen ions on the basis of the statistical thermodynamics. He proposed a model in which free oxygen ions dissociated during polymerization of discrete anions. We also succeeded in explaining the equilibrium between free oxygen ions and discrete anions in molten slags based on the electronic states calculated with the DV-X α method (26).

One of the equilibria between the discrete anions and free oxygen ions can be expressed as (19-21,26)

$$Si_2O_7^{6-} + Si_2O_7^{6-} = Si_4O_{12}^{8-} + 2O^{2-} \quad (K_{2,2}) \qquad (5)$$

where $K_{2,2}$ is an equilibrium constant of the reaction. Therefore, the free oxygen ion,

O^{2-}, content is approximately given by (19)

$$O^{2-} = \{K_{2,2} \cdot m_i(Si_2O_7^{6-}) \cdot m_i(Si_2O_7^{6-}) / m_i(Si_4O_{12}^{8-}) \}^{1/2} \quad (6)$$

The free oxygen ion contents of the 66.7mol%SiO_2—33.3mol%Na_2O and the 42.0mol%SiO_2—58.0mol%Na_2O slags were calculated by substituting m_i (Table I) in eq.(6). The free oxygen ion content of the former slag was 0.003 $(K_{2,2})^{1/2}$ while the latter was 0.569 $(K_{2,2})^{1/2}$. The free oxygen ion content of the latter was therefore found to be 190 times higher than that of the former. Other reactions can be envisaged to occur in this system, but for the purpose of the present discussion it is sufficient to consider the reaction given by eq.(5). The desulfurization happens much more in the latter slag than in the former slag, is well known. Thus, we conclude that the latter slag has significantly higher basicity than the former.

Therefore, the present method was found to provide a very useful means to clarify changes in the structure of the slag with the metal oxide content, and also of understanding the basicity.

4. SUMMARY

O K_α X-ray emission spectra for SiO_2—Na_2O binary slags simulated with the DV-Xα molecular orbital calculation were compared with ones measured by EPMA. The composition of the slag has been incorporated in the calculation of the O_{2p} partial density of states (PDOS). The O_{2p} PDOS agreed well with the measured O K_α X-ray emission spectra of the glassy state 66.7mol%SiO_2 — 33.3mol%Na_2O and 42.0mol%SiO_2—58.0mol%Na_2O binary slags. Therefore, the present method was found to provide a very useful means of clarifying the changes in the ionic configuration of the slag with the metal oxide content. Furthermore, better understanding of the concept of basicity was obtained from the determination of the ionic configuration of the slag.

REFERENCES

(1) Duffy, J. A.; Ingram, M. D. *J. American. Chem. Soc.*, **1971,** *93*, 6448.

(2) Duffy, J. A.; Ingram, M. D. ; Sommerville, I. D. *J. Chem. Soc. Faraday Trans.*, **1978,**

74, 1410.
(3)Sumita, S.; Matsumoto, Y.; Morinaga, K.; Yanagase, T. *Trans. JIM.*, **1982,** *23*,360.
(4) Morishita, M.; Koyama, K.; Morinaga M.; Adachi, H. Mater. *Trans. JIM.*, **1997,** *36*, 724.
(5) Morishita, M. ; Koyama, K. ; Kikko, T. ; Morinaga ,M. ; Adachi, H. *Molten Salts*, **1997,** 222 [in Japanese].
(6) Morishita, M. ; Koyama, K. ; Kikko, T. ; Morinaga M.; Adachi, H. *Proc. Of 2nd Intern. Congress on Sci. and Tech. of Iron Making (ICSTI'98),* Iron & Steel Soc., Toronto, **1998,** 1933.
(7) Yamada, K. ; Takahashi, T. ; Motoyama, M. *J. Jpn. Inst. Met.*, **1996,** *60*, 100 [in Japanese].
(8) Takahashi, H. ; Okamura, T. ; Seo, Y. *J. Jpn. Inst. Met.*, **1989,** *53*, 349 [in Japanese].
(9) Adachi, H. ; Taniguchi, K. *J. Phys. Soc. Jpn.*, **1980,** *49*, 1944.
(10) Slater, J. C. "The Calculation of Molecular Orbitals", translated by Sugano, S. ; Adachi, H. ; Tsukada, M. Tokyo Univ. Shuppan-kai, Tokyo, **1982,** 58 [in Japanese].
(11) Kawai, J. ; Maeda, K. ; Higashi, I. ; Takami, M. ; Hayashi, Y. ; Uda, M. *Phys. Rev.*, **1990,** *B42*, 5693.
(12) Uda, E. ; Kawai J. ; Uda, M. *Nucl. Instruments and Methods Phys. Res.*,**1993,** *B75*, 24.
(13) Kawai, J. ; Maeda, K. ; Takami, M. ; Muramatsu, Y. ; Hayashi, T.; Motoyama M. ; Saito, Y. *J. Chem. Phys.*, **1993,** *98*, 3650.
(14) Tanaka, I. ; Kawai, J. ; Adachi, H. *Phys. Rev.*, **1995,** *B52*, 11733.
(15) Adachi, H. ; Tsukada ,M. ; Satoko, C. *J. Phys. Soc. Jpn.*, **1978,** *45*, 875.
(16) Adachi, H. "Introduction to Quantum Materials Chemistry Approach with DV-Xα Method", Sankyo Syuttpan, Tokyo, **1991,** 26,50 [in Japanese].
(17) Yokokawa, T. *Tetsu to Hagane*, **1982,** 68, 26 [in Japanese].
(18) Toop C. W. ; Samis, C. S. *Trans. Met. Soc. AIME.*, **1962,** 224, 878.
(19) Masson, C. R. *Proc. Roy. Soc.*, **1965,** *A287*, 201.
(20) Gaskell, D. R. *Met Trans.*, **1977,** *8B*, 131.
(21) Gaskell, D. R. *Proc. of 5th Intern. Conf. on Molten Slags, Fluxes and Salts '97*, Iron & Stell Soc. AIME., **1997,** 11.
(22) Levin, E. M. ; Block, S. J. American Ceramic *Soc.*, **1957,** *40*, 95.
(23) Nakajima, K. *Tetsu to Hagane*, **1994,** *80*, 19 [in Japanese].
(24) Waseda, Y. "The structure of Non-crystalline Materials", McGraw-Hil, New York, **1980,** 138.
(25) Waseda ,Y. ; Suito, H. *Tans. ISIJ.*, **1977,***17*, 82.
(26) Morishita, M. ; Koyama, K. ; Hatamoto, A. ; Morinaga, M. ;Adachi, H. "Advances

in Quantum Chemistry", **1997,** *29*, 285.

(27) Sawaguchi, N. ; Kawamura, K. ; Yokokawa, T. *Proc. of the 27th Symp.on Molten Salt Chem.*, Yokohama, **1995,** *27*, 102 [in Japanese].

(28) Kowada, Y. ; Adachi, H. ; Tatsumisago, M. ; Minami, T. *J. Non-Cryt. Solids*, **1992,** 150, 318.

(29) Kowada, Y. ; Adachi, H. ; Minami, T. *J. Ceramic Soc. Jpn.*, **1993,** *101*, 1330.

(30) Kowada, K. ; Adachi, H. ; Tatsumisago, M. ; Minami, T. *J. Non-Cryt. Solids*, **1994,** *177*, 286.

(31) Kowada, Y. ; Adachi, H. ; Tatsumisago, M. ; Minami, T. *J. Non-Cryt. Solids*, *192&193*, 316.

(32) Tokuda, M. *Tetsu to Hagane*, **1983,** *69*, 1699 [in Japanese].

The electronic states in Ca-doped $BaTiO_3$ ceramics

Myung Chul Chang*, Soo-Chang Yu †

Department of Materials Science and Engineering, Department of Chemistry †, Kunsan National University, Kunsan 573-701, Korea

(Received November 2, 1998)

We investigated the electronic structures for the ceramic compositions given by $Ba_{1-x}Ca_xTiO_3$ and $BaTi_{1-y}Ca_yO_3$. The measured XPS shapes for the O1s molecular orbitals were changed a lot due to the addition of Ca into $BaTiO_3$. The O1s spectra of Ti site doped samples show strongly split energy peaks. On the other hands, there was little change to the spectra for the Ba site doped samples. Through DV-X α calculations we observe that the replacement of Ca^{2+} ion for Ti^{4+} sites in $Ba_8Ti_7O_6$ cluster model introduces the strong splitting of the O1s molecular orbital energies. From the O1s pDOS for $Ba_8Ti_7O_6$, $Ba_6Ca_2Ti_7O_6$ and $Ba_8Ti_5Ca_2O_6$ cluster models the O1s energy splitting for the $BaTi_{1-y}Ca_yO_3$ composition was proven to be caused by the aliovalent ion (Ca^{2+}) substitution for Ti^{4+} ion sites.

KEYWORDS: barium titanate, calcium incorporation, XPS

*Corresponding author: e-mail mcchang@ks.kunsan.ac.kr

0065-3276/01 $35.00

1. INTRODUCTION

$BaTiO_3$-based ceramics are well known as PTC thermistor and ceramic capacitors. Ca is frequently added to $BaTiO_3$ to control the electrical conductivity and the grain size in the production of the ceramic capacitors and PTCR ceramics (1-2). The reaction whereby Ca is incorporated into the $BaTiO_3$ ceramics greatly influences the electrical properties. There have been many studies aimed at understanding the Ca-incorporation reaction in $BaTiO_3$ on a basis of defect chemistry. It is generally accepted that acceptor levels are formed in $BaTiO_3$ band gap by the Ca incorporation reaction (3,4). However, there has been some debate about the incorporation of Ca ions into Ti sites because of the difference in the ionic radii. To evaluate the evidence of Ca_{Ti}'''' in $BaTiO_3$, electronic energy states in Ca-doped $BaTiO_3$ ceramics were investigated through XPS and the DV-X α calculations (5).

2. EXPERIMENT AND COMPUTATIONAL METHOD

2-1 Sample Preparation and XPS measurement

Ca-doped $BaTiO_3$ ceramics were prepared by conventional ceramic processing. $(Ba_{1-x}Ca_x)TiO_3$ (x = 0.015) compositions were used for the Ba site doped ceramics and $Ba(Ti_{1-y}Ca_y)O_3$ (y= 0.01, 0.02) compositions were used for the Ti site doped ceramics. We used $BaCO_3$, $CaCO_3$ and TiO_2 as the precursor raw materials (with purities above 99.9%). We carefully kept the Ba/Ti ratio to 0.999 to reduce the unreacted $BaCO_3$. The pressed disks were sintered at 1350 ℃ for one hour in air and the sintered disks were used as the samples for the XPS measurements. XPS measurements were carried out at room temperature. For the XPS measurements, an Mg anode X-ray source was used with an excitation voltage of 15 kV and a current of 15mA. When the homogeneous mixtures of $BaCO_3$, TiO_2 and $CaCO_3$ reacted at the sintering temperature, the actual reaction where Ca is incorporated into $BaTiO_3$ can be considered as follows.

$$(Ba_{1-\delta}Ca_{\delta})TiO_3 \quad (1)$$

$$Ba(Ti_{1-\delta}Ca_{\delta})TiO_3 \quad (2)$$

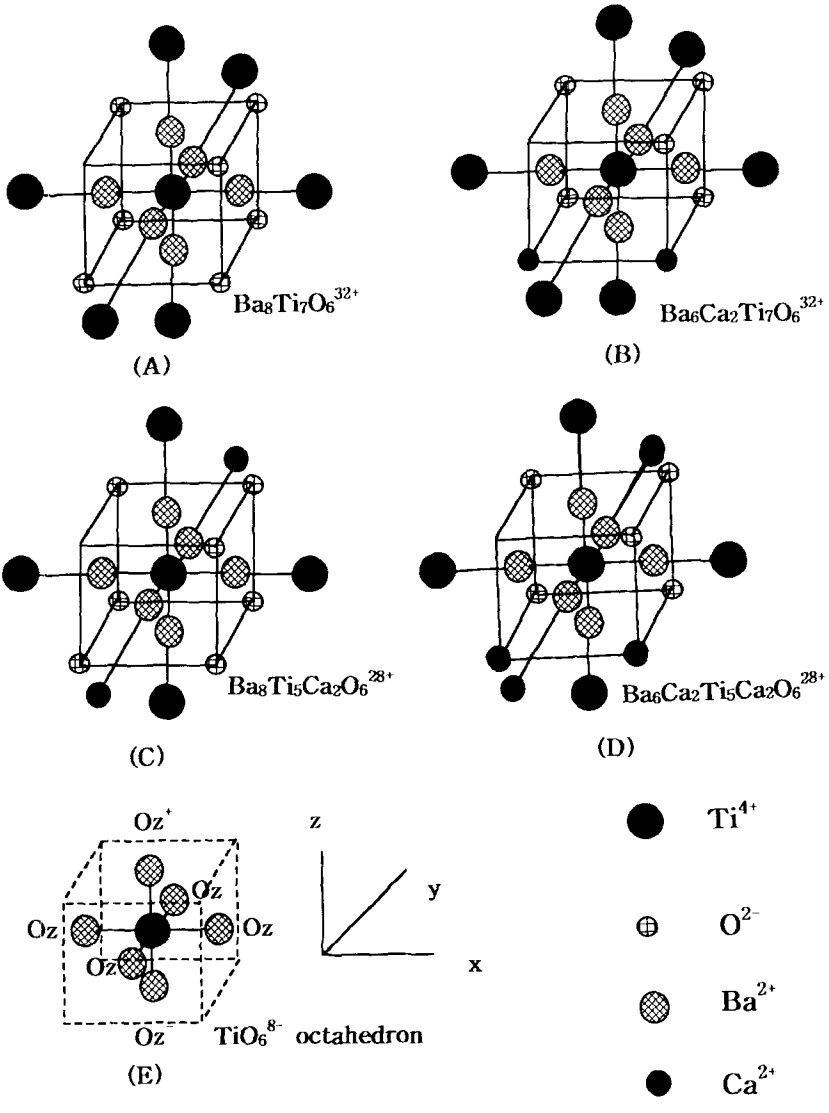

Fig. 1 The model clusters used for the DV-Xα calculation, which are (A) $Ba_8Ti_7O_6^{32+}$(the initial charges are Ba^{2+}, Ti^{4+}, O^{2-}, Ca^{2+}), (B) $Ba_6Ca_2Ti_7O_6^{32+}$, (C) $Ba_8Ti_5Ca_2O_6^{28+}$, (D) $Ba_6Ca_2Ti_5Ca_2O_6^{28+}$ and (E) TiO_6. For the cubic clusters the cluster models are abbreviated as c-BT21, c-BTC21, c-BCT21, c-BCTC21 and c-TiO6 for (A), (B), (C), (D) and (E), respectively. For the tetragonal clusters these are written as t-BT21, t-BTC21, t-BTC21 , t-BCTC21 and t-TiO_6, respectively

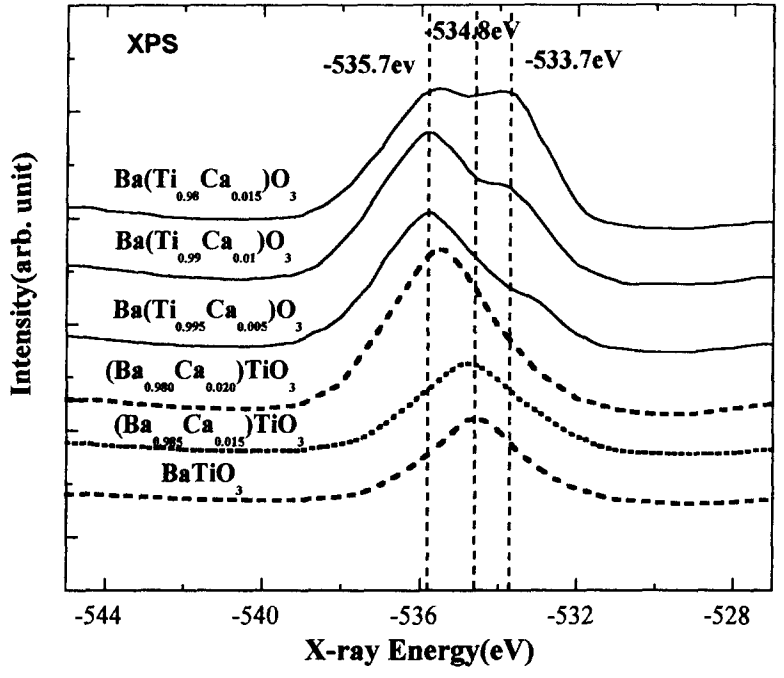

Fig. 2 Experimental XPS spectra for $BaTiO_3$, $(Ba_{1-x}Ca_x)TiO_3$(x= 0.015, 0.020) and for $Ba(Ti_{1-y}Ca_y)O_3$(y=0.005, 0.010, 0.015)

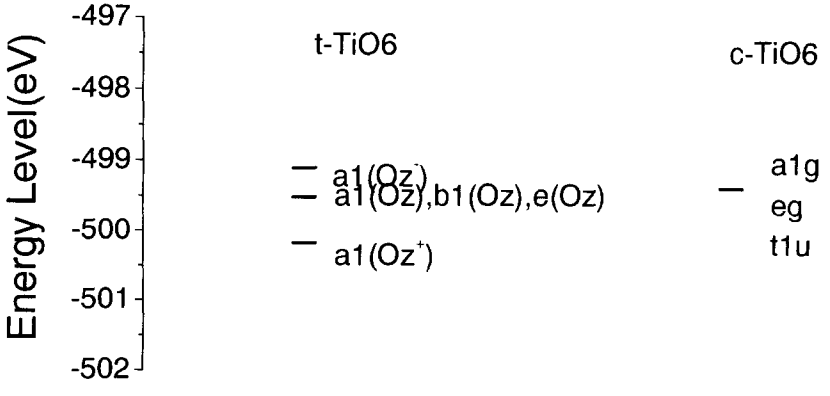

Fig. 3 Calculated energy levels for O1s molecular orbitals for the tetragonal TiO_6^{8-} cluster and the cubic TiO_6^{8-} cluster.

$$(Ba_{1-\delta}Ca_{\delta})(Ti_{1-\delta}Ca_{\delta})O_3 \quad (3)$$

If an excess amount of Ca is added for Ba site in $BaTiO_3$, the Ca atoms may be incorporated according to the equation (3) after high temperature reaction.

2-2 Computational Method

Perovskite $BaTiO_3$ shows phase transitions such as Cubic → Tetragonal → Orthorombic → Trigonal, when it is cooled from high temperature. $BaTiO_3$ crystal exists in the cubic state above 120 ℃ and in the tetragonal state below 120 ℃. So, the DV-Xα calculations were carried out for both the cubic clusters and the tetragonal clusters, respectively. For the DV-Xα calculations we chose the cluster models $Ba_8Ti_7O_6^{32+}$ (the initial charges were Ba^{2+}, Ti^{4+}, O^{2-}, Ca^{2+}), $Ba_6Ca_2Ti_7O_6^{32+}$, $Ba_8Ti_5Ca_2O_6^{28+}$, $Ba_6Ca_2Ti_5Ca_2O_6^{28+}$ and TiO_6^{8-} as shown in Fig. 1(A), (B), (C), (D), (E), respectively. For the cubic model we used Oh symmetry for $Ba_8Ti_7O_6^{32+}$, D2h symmetry for $Ba_8Ti_5Ca_2O_6^{28+}$ and Ci symmetry for $Ba_6Ca_2Ti_7O_6^{32+}$ and $Ba_6Ca_2Ti_5Ca_2O_6^{28+}$. We used the C4v symmetry for the tetragonal $Ba_8Ti_7O_6^{32+}$ and the C2 symmetry for the other tetragonal clusters. We adopted a = 4.012 Å as the unit cell parameter of the cubic $BaTiO_3$ while for the tetragonal $BaTiO_3$ we adopted a = 3.992 Å and c = 4.032 Å. The space group (Oh symmetry) for the cubic phase was Pm3m (221) and we took the coordinates as (0, 0, 0) for Ti, (1/2, 1/2, 1/2) for Ba and (1/2, 0, 0) for O. The space group (C4v symmetry) for the tetragonal phase is known to be P4mm (99) and we took (0,0,0) for Ti, (1/2, 1/2, 1/2 - 0.014) for Ba, (0, 0, 1/2 - 0.037) for O and (1/2, 0, -0.028) for O as the coordinates of the ions. We set point charges corresponding to 6 x 6 x 6 unit cells to create the madelung potential around the clusters.

3. Results and discussion

3-1 XPS spectra

Figure 2 shows the measured XPS spectra of the O1s molecular orbitals for $BaTiO_3$, $Ba_{1-x}Ca_xTiO_3$(x=0.015, 0.020), and $BaTi_{1-y}Ca_yO_3$(y = 0.005, 0.010, 0.015) samples. In $Ba_{1-x}Ca_xTiO_3$(x=0.015. 0.020) samples we can not observe

the energy shoulder and the energy peak position moves to higher energy side with the increase of Ca. The structure of XPS spectra for $Ba_{1-x}Ca_xTiO_3$(x=0.015. 0.020) compositions is little changed, compared with $BaTiO_3$. However, in $BaTi_{1-y}Ca_yO_3$(y = 0.005 ,0.010 ,0.015) compositions we can observe the strong development of the energy shoulder with the increase of Ca contents. Consequently we can assume that the development of O1s molecular orbital energies are significantly influenced by the Ca position in $BaTiO_3$. Molecular orbital structure of $BaTiO_3$ is likely to be considerably influenced by the substitution of Ca for Ti sites. The energy change of O1s molecular orbitals will be analyzed through DV-Xα calculations.

3-2 MO Energy Calculation

Figure 3 shows the band energy levels of the O1s molecular orbitals obtained by the DV-Xα calculations for the TiO_6^{8-} cluster (as shown in Fig. 1(E)). The C4v symmetry and the Oh symmetry were used for the tetragonal cluster and the cubic cluster, respectively. We placed the point charges (Ba^{2+}, Ti^{4+}, O^{2-}) in over 1,000 positions for the perovskite $BaTiO_3$ structure to create the madelung potential around the TiO_6^{8-} cluster. The O1s molecular orbital energy levels for the tetragonal TiO_6^{8-} cluster were widely split because of the tetragonality (lattice ratio of a/c). The band energy structure for the tetragonal cluster was mainly caused by the a1(Oz^+) and a1(Oz^-) discrete energy splitting. Here, a1(Oz^+) represents the O1s molecular orbital energy for the oxygen atom(Oz^+) located in the positive z direction in TiO_6^{8-} and a1(Oz^-) indicates that for the oxygen atom(Oz^-) located in the negative z direction in TiO_6^{8-} as shown in Fig. 1(E). e(Oz) is the doubly degenerated O1s molecular orbital energy level for the oxygen atoms located in Oz positions in Fig. 1(E).

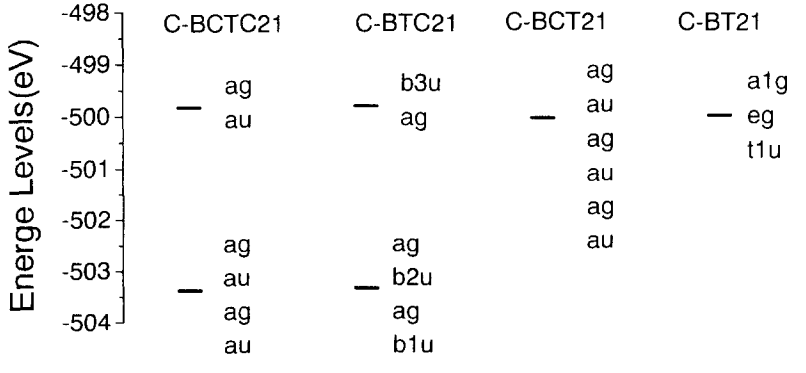

Fig. 4 Calculated energy levels of O1s molecular orbitals for the cluster models is c-BT21, c-BTC21, c-BCT21 and c-BCTC21.

Figure 4 shows the band energy levels for the O1s molecular orbitals obtained by DV-Xα calculations for the cubic clusters such as $Ba_8Ti_7O_6^{32+}$ (abbreviated as c-BT21), $Ba_6Ca_2Ti_7O_6^{32+}$ (c-BCT21), $Ba_8Ti_5Ca_2O_6^{28+}$ (c-BTC21) and $Ba_6Ca_2Ti_5Ca_2O_6^{28+}$ (c-BCTC21). For the c-BT21 cluster the 6 molecular orbital energy levels (a1g, eg, t1u) for O1s were concentrated at the around -500eV. This band structure is almost same as that of the cubic TiO_6^{8-} cluster(Fig. 3). The band structure for the t-BCT cluster also shows a similar structure. However, the c-BTC cluster and the c-BCTC cluster show the strong energy splitting at -503.3 eV and -499.8 eV. That is, the replacement of Ca^{2+} into Ti^{4+} site contributes to the splitting of the O1s molecular orbital energies. Figure 5 shows the O1s partial DOS for the above cluster models. Double energy peaks strongly developed for both c-BTC21 and c-BCTC, while little change was observed in c-BCT21 cluster model. As a result we can assume that the formation of $Ca_{Ti}^{''''}$ (Ca replacement into Ti site) greatly contributes to the energy splitting of the O1s molecular energy levels.

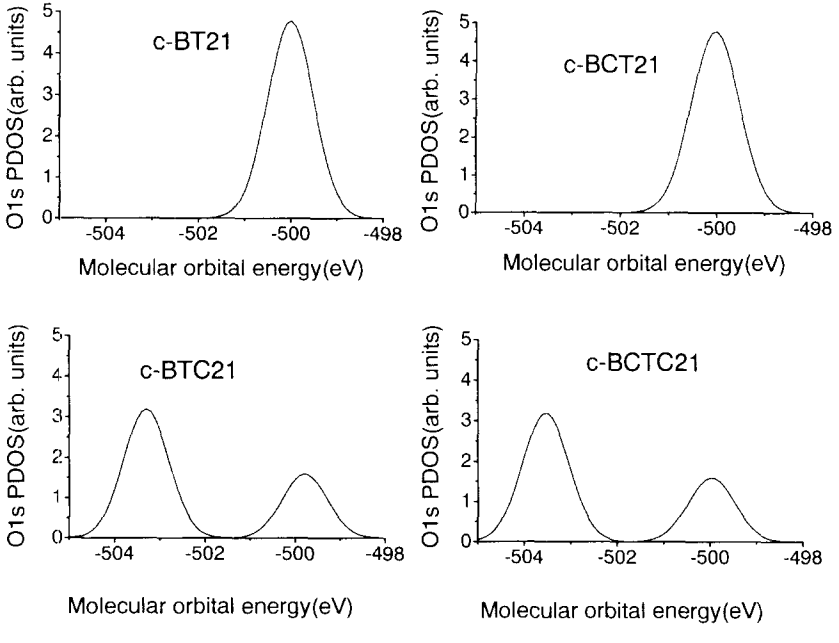

Fig. 5 O1s PDOS for the c-BT21, c-BTC21, c-BCT21 and c-BCTC21 cluster models.

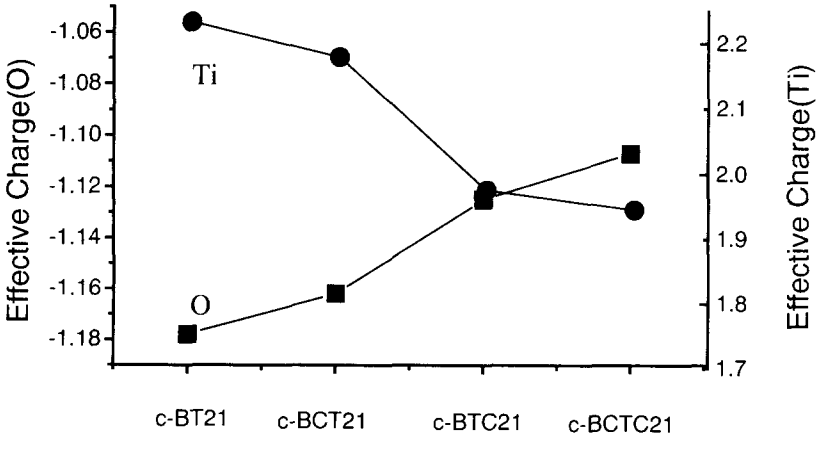

Fig. 6 The effective charge variation of the titanium ion and the oxygen ion in the TiO_6 octahedron for the c-BT21, c-BCT21, c-BTC21 and c-BCTC21 model clusters. Ti(center) indicates the Ti atom located at the center of the cluster.

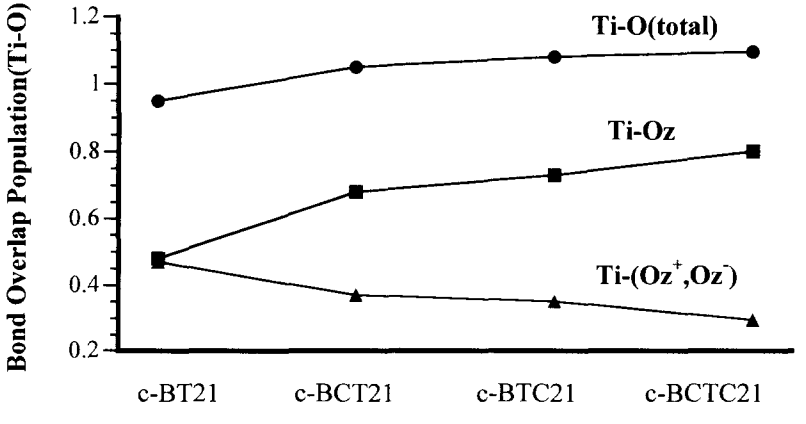

Fig. 7 Bond overlap population of the Ti-O bond in the TiO_6 octahedron for the c-BT21, c-BCT21, c-BTC21 and c-BCTC21 model clusters. Ti(center) indicates the Ti atom located at the center of the cluster. Oz^+, Oz and Oz^- indicate the corresponding atom positions as shown in Fig. 1(E).

Figure 6 shows the effective charges for the cubic clusters. The charge of the oxygen increases as c-BT21, c-BCT21, c-BTC21, c-BCTC21. The charge of Ti decreases as c-BT21, c-BCT21, c-BTC21, c-BCTC21. The replacement of Ca^{2+} into the cation site(Ba^{2+} or Ti^{4+}) contributes to the reduction of the charge difference between the O ions and the Ti ions. That is, the effective charge is decreased by the formation of Ca_{Ba}^{x} and Ca_{Ti}''''. Certainly, the formation of Ca_{Ti}'''' strongly contributes to the change of the effective charge. Figure 7 shows the bond overlap populations for the cubic cluster models. The total bond overlap population is increased by the Ca replacement into the cation site and the formation of Ca_{Ba}^{x} and Ca_{Ti}'''' contributes to the development of the covalent bond between Ti and Oz. However, the bond overlap populations for Ti-Oz^{-} bond and Ti-Oz^{+} bond decrease on formation of Ca_{Ba}^{x} and Ca_{Ti}''''. The formation of Ca_{Ti}'''' strongly influences the bond overlap population for the Ti-O bond.

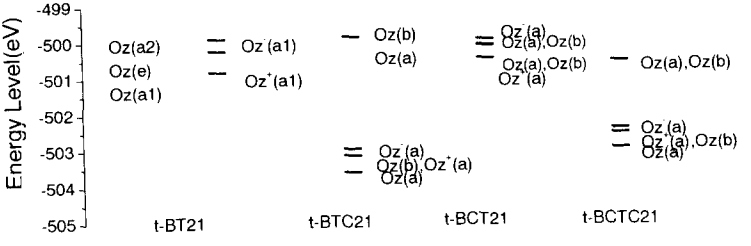

Fig. 8 Calculated energy levels for the O1s molecular orbitals for the cluster models t-BT21, t-BCT21, t-BTC21 and t-BCTC21. Oz^{+}, Oz and Oz^{-} indicate the corresponding atom positions as shown in Fig. 1(E).

Fig. 9 Calculated energy levels for O1s molecular orbitals for the cluster models t-BTC21xy and t-BTC21yz. In Fig. 1(C) the positions of Ca ions in t-BTC21 are located in the xy plane. When Ca ions are located in the yz plane, we refer to this cluster as t-BTC21yz.

Figure 8 shows the molecular orbital energy levels for the tetragonal clusters t-BT21, t-BCT21, t-BTC21 and t-BCTC21. The energy level structure of the O1s molecular orbitals for the t-BT21 cluster is very similar to that of the tetragonal TiO_6^{8-} cluster(Fig.3). The t-BT21 cluster shows an energy splitting between -499.7 eV and -501.22 eV. In t-BT21 the Oz^+ and Oz^- molecular orbital energy levels are placed at the both ends of the energy distribution for the O1s orbitals in a similar way to the t-TiO_6^{8-} cluster. The t-BCT21 cluster shows the similar energy level structure to the t-BT21 cluster. For the t-BTC21 cluster the molecular orbital energies of the Oz^+ and Oz^- positions were closely located in a similar way to the t-BT21 cluster, but the O1s orbital energy levels for the 4 Oz positions were very split. The splitting of the Oz molecular orbitals are the main cause of the splitting of O1s molecular orbital energy levels. In the above case the Ca atoms were placed on the x-y plane of the TiO_6 octahedron. If we place the Ca atoms in the y-z plane of the TiO_6 octahedron, we can observe the molecular orbital energy levels as shown in Fig. 9. Figure 10 shows the O1s partial DOS for the t-BTC21 clusters with the different Ca positions. We can observe the similar energy level structures for the t-BCTC cluster model (Fig. 11).

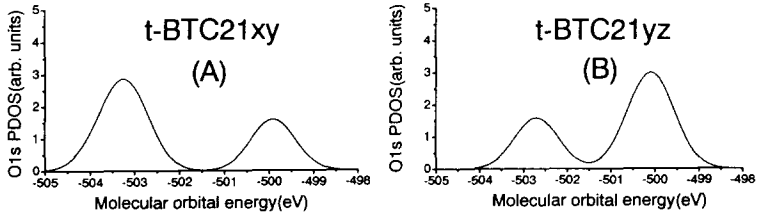

Fig. 10 O1s PDOS for t-BTC21xy and t-BTC21yz.

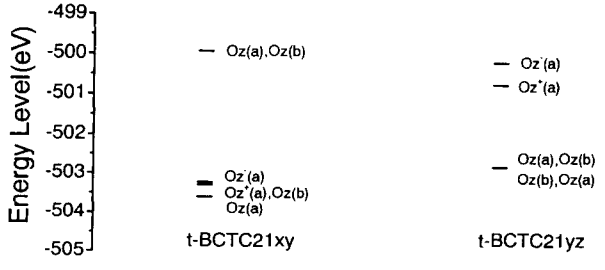

Fig. 11 Calculated energy levels for O1s molecular orbitals for the cluster models of t-BCTC21xy and t-BCTC21yz. In Fig. 1(D) the positions of the Ca ions in t-BCTC21 are located in the xy plane. When Ca ions are located in the yz plane, we refer to this cluster as t-BCTC21yz.

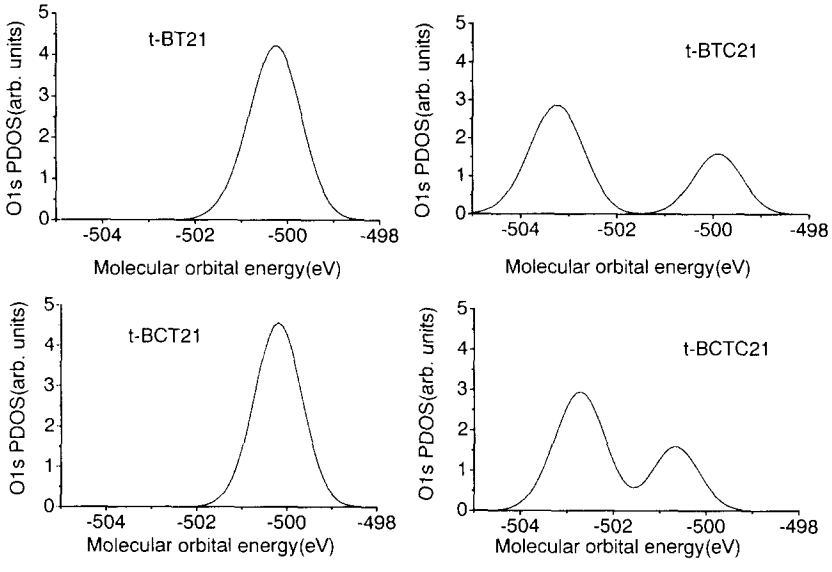

Fig. 12 O1s PDOS for the cluster models t-BT21, t-BCT21, t-BTC21 and t-BCTC21.

Figure 12 shows the O1s partial DOS for t-BT21, t-BTC21, t-BCT21 and t-BCTC clusters. The peak positions are -500.3 eV for both t-BT21 and t-BCT21. For t-BTC 21 we can see two peak positions at -501.2 eV and -499.8 eV. Similarly, for t-BCTC21 we can observe two peak positions at -502.7 eV and -500.7 eV. Figure 13 shows the effective charges of the Ti and O ions for the above tetragonal clusters. The Ti ion charge significantly decreased on formation of Ca_{Ti}''''. The total charges of the oxygen ions greatly increased on formation of Ca_{Ti}''''. That is, the formation of Ca_{Ti}'''' greatly contributes to changes in the charges of Ti and O ions. The effective charges of the O ions in the Oz atom position increased with the formation of Ca_{Ti}'''' and Ca_{Ba}^{x}, but the effective charges of the O ions in Oz^{-} atom position decreased on formation of Ca_{Ti}'''' and Ca_{Ba}^{x}. That is, the electrons from Oz atoms are moved to the Oz^{-} atom on formation of Ca_{Ti}'''' and Ca_{Ba}^{x}. From Fig. 14 the total bond overlap population for the Ti-O bond increases on the formation of Ca_{Ti}'''' and Ca_{Ba}^{x}. The formation of Ca_{Ba}^{x} decreased the bond overlap population of Ti-Oz bond and increased that of the $Ti\text{-}Oz^{+}$ bond and the $Ti\text{-}Oz^{-}$ bond. The formation of Ca_{Ti}'''' increased the Ti-Oz bond overlap population, but decreased that of the $Ti\text{-}Oz^{+}$ bond and the $Ti\text{-}Oz^{-}$ bond. The influence of Ca_{Ti}'''' on the Ti-O bond overlap population was greater than that of Ca_{Ba}^{x}.

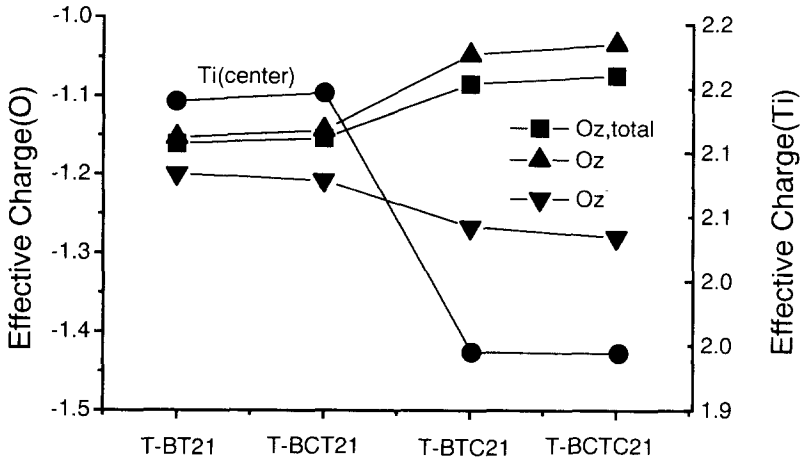

Fig. 13 The effective charges of Ti and O ions in the TiO_6 octahedron for the cluster models t-BT21, t-BCT21, t-BTC21 and t-BCTC21.

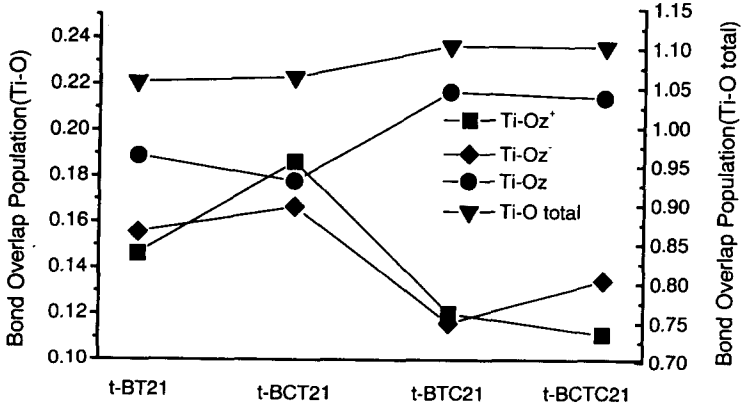

Fig. 14 Ti-O Bond overlap population in the TiO_6 octahedron for the cluster models t-BT21, t-BCT21, t-BTC21 and t-BCTC21.

4. SUMMARY

When Ca^{2+} is added into the Ti^{4+} site of $BaTiO_3$ the formation of Ca_{Ti}'''' strongly contributes to the O1s MO energy splitting. The evidence for Ca_{Ti}'''' was analyzed by XPS measurement and DV-X α calculations. If Ca is excessively doped at Ba site for $BaTiO_3$ we can suppose the splitting in the O1s molecular orbital energy spectra. A partial incorporation of Ca for Ti site in $(Ba,Ca)_{1+\delta}TiO_3$ ceramic compositions can be assisted by the t-BCTC cluster model.

REFERENCES

(1) D. V. Lewis and C.R.A. Catlow, J. Am. Ceram. Soc.,1990, 73, 669
(2) Y. Sakabe, Am. Ceram. Soc. Bull., 1987, 66, 1338
(3) Y. H. Han, J. B. Appleby and D. M. Smyth, J. Am. Ceram. Soc., 1987, 70, 96
(4) M. C. Chang, S. H. Hur and S. J. Park, Ceramic Transactions 41, Grain Boundaries and Interfacial Phenomena in Electronic Ceramics. edited by L..M.Levinson and S. Hirano, The American Ceramic Society 1993, 177-184
(5) H. Adachi, M. Tsukada, and C. Satoko, J. Phys. Soc. Jpn., 1978, 45, 875

Characteristics of Electronic Structures in Hydrogen Storage Alloys

Hiroshi Yukawa* and Masahiko Morinaga

Department of Materials Science and Engineering,
Graduate School of Engineering,
Nagoya University, Furo-cho, Chikusa-ku, Nagoya 464-8603, JAPAN

(Received January 22, 1999)

The electronic structures of hydrogen storage alloys are calculated by the DV-Xα molecular orbital method. It is found that hydrogen interacts more strongly with hydride non-forming elements, B, (e.g., Ni, Mn, Fe) than hydride forming elements, A, (e.g., La, Zr, Ti, Mg) in every hydrogen storage alloy, despite that there is a larger affinity of A element for hydrogen than B element in the binary metal-hydrogen system. The presence of such a metal-hydrogen interaction is characteristic of hydrogen storage alloys. Also, it is shown that the stability of hydrides can be elucidated in view of the crystal structural evolution in the course of hydrogenation. Furthermore, it is found that the A/B compositional ratio of hydrogen storage alloys is understood in terms of a simple parameter, 2 Bo(A-B) / [Bo(A-A)+Bo(B-B)], where the Bo(A-B), Bo(A-A) and the Bo(B-B) are the bond orders between atoms given in the parentheses.

KEYWORDS: electronic structure, hydrogen storage alloys hydride stability, alloy design

*Corresponding author, e-mail: hiroshi@numse.nagoya-u.ac.jp

0065-3276/01 $35.00

1. INTRODUCTION

Advanced energy conversion materials have been in great demand for the development of new clean energy systems in the next century. In particular, hydrogen storage alloy is very important, because hydrogen fuel is one of the most clean energy resources obtained easily by the electrolysis of water. A large amount of hydrogen is stored in the alloy by forming metal hydrides. A variety of hydrogen storage alloys have been developed and alloying effects have also been investigated experimentally in order to further improve the hydriding properties of them (1-7). Owing to these extensive studies, several empirical rules have been found and used for the alloy development. For example, there is a close correlation between the interstitial hole size (or the unit cell volume of the alloy) and the stability of hydrides formed in hydrogen storage alloys (8,9). Namely, the larger the interstitial hole size (or the unit cell volume) is, the more stable the hydride is. However, there are some exceptions to this rule (e.g., $CaNi_5$ and Mg_2Ni (10)). In addition, reminding that a total amount of hydrogen stored in any alloys is still low in view of practical applications, we should make an alternative approach to the understanding of the hydriding properties of these alloys and their alloying effects as well. In this study an electronic approach is made to solve a variety of problems relevant to hydrogen storage alloys in a fundamental manner. The DV-Xα cluster method is employed for this purpose.

2. DV-Xα CLUSTER METHOD AND CLUSTER MODELS

The DV-Xα cluster method is a molecular orbital method, assuming a Hartree-Fock-Slater (HFS) approximation. With this method, local electronic structures around hydrogen can be calculated accurately. In this method, the exchange-correlation between electrons, V_{XC}, is given by the following Slater's Xα potential,

$$V_{XC} = -3\alpha\left[\frac{3}{8\pi}\rho(r)\right]^{1/3} \quad (1)$$

where $\rho(r)$ is the density of electrons at position r, the parameter α is fixed at 0.7 and the self-consistent charge approximation is used in this calculation. The matrix elements of Hamiltonian and the overlap integrals are calculated by a random sampling method. The molecular orbitals are constructed by a linear combination of numerically generated atomic orbitals (LCAO).

Depending on the crystal structure, appropriate cluster models are employed in the calculation. Here, 'cluster' means a hypothetical molecule to represent a metal crystal. For example, a cluster model used for the $ZrMn_2$ system is shown in Fig.1. This is constructed based on the crystal structure of $ZrMn_2H_3$ (11). Hydrogen atoms are located at the central site of one tetrahedron, the corners of which are occupied by two Zr atoms and two Mn atoms.

For a characterization of the electronic structure, the spatial electron density distributions, the bond order between atoms and ionicities of each atom in the cluster are estimated according to the Mulliken population analysis (12). The overlap population, $Q_{\nu\nu'}$, of electrons between two atoms ν and ν' is defined as,

$$Q_{\nu\nu'} = \sum_l \sum_{ij} C_{il}^{\nu} C_{jl}^{\nu'} \int \Psi_i^{\nu} \Psi_j^{\nu'*} dV \quad (2)$$

where Ψ_i^{ν} and $\Psi_j^{\nu'}$ are the wavefunctions of the i and j orbitals of ν and ν' atoms, respectively. C_{il}^{ν} and $C_{jl}^{\nu'}$ are coefficients which show the magnitude of

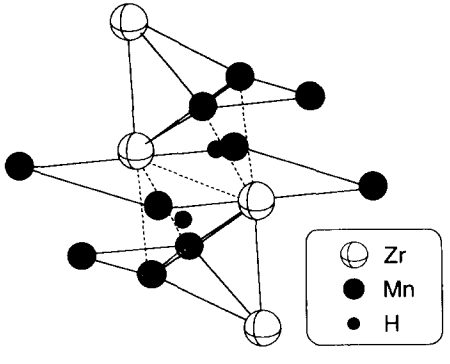

Fig.1.Cluster model used in the calculation for $ZrMn_2$ system.

the linear combination of atomic orbitals in the lth molecular orbital. The sum over l runs only over the occupied orbitals. Here, this $Q_{vv'}$ is called the bond order and used as a measure of the strength of the covalent bond between v and v' atoms. Further detailed explanation of the calculation method is given elsewhere (13-18).

3. ELECTRONIC STRUCTURE OF HYDROGEN IN PURE TRANSITION METALS

Before showing the results of hydrogen storage alloys, a brief summary is given for the electronic structure of hydrogen in pure transition metals (19), because it helps to understand how hydrogen storage alloys are treatable using an electronic approach. A schematic illustration is shown in Fig.2 of the energy level structure of hydrogen in pure transition metals. Here, Ti is selected as an example, but any other transition metal has a similar electronic structure. As shown in Fig.2, the Fermi energy level, Ef, lies on the Ti-3d band. When hydrogen is introduced into Ti, a bonding level between the H-1s and the Ti-3d electrons appears just below the Ti-3d band. The charge transfer takes place from Ti atom to hydrogen, and the effective ionicity of hydrogen becomes about -0.2. Also, the Fermi energy level, Ef, rises slightly due to the hydrogenation (20).

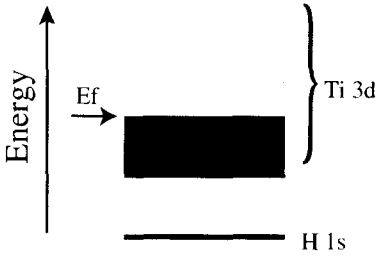

Fig.2. Schematic illustration of the energy level structure.

For a series of 3d transition metals, M, it is found that the bond orders between atoms change with the hydrogenation of M, as shown in Fig.3 (20). The bond order between hydrogen and metal atoms is large for the left-side metals, and it decreases gradually as the position of M moves to the right-side in the

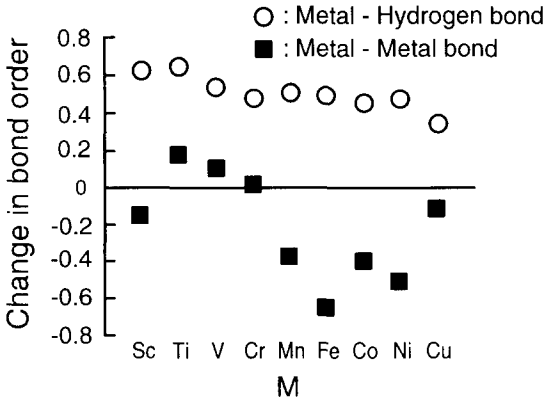

Fig.3. Change in bond order between atoms with hydrogenation in 3d transition metals, M (20).

periodic table. However, all the M-H bond orders have positive values, regardless of M.

On the other hand, the bond order between metal atoms changes largely with M. For example, when hydrogen is introduced into metal, the bond strength increases for Ti, but decreases for Fe. This is because, for the left-side metals such as Ti, the Fermi energy level, Ef, lies on the energy region where the bonding-type interaction is operating between Ti-3d electrons. In such a case, the Ti-Ti bond is strengthened since the bonding-type d-d component further increases with rising Ef due to the hydrogenation. On the other hand, for the right-side metals such as Fe, the Fermi energy level lies on the energy region where the antibonding-type interaction is operating between the Fe-3d electrons. In this case, to the contrary to the case of Ti, the Fe-Fe bond is weakened since the antibonding d-d component further increases with rising Ef due to the hydrogenation. This is the reason why the left-side metals have a larger affinity for hydrogen than the right-side metals in the periodic table, as is found experimentally.

Here, it is important to note that not only the metal-hydrogen interaction but also the metal-metal interaction is important in understanding the hydriding property of metals. This is also the case for hydrogen storage alloys, as explained later.

4. ELECTRONIC STRUCTURE OF HYDROGEN STORAGE ALLOYS

4.1 CHEMICAL BOND STATE OF HYDROGEN

Hydrogen storage alloys such as $LaNi_5$ (AB_5-type), $ZrMn_2$ (AB_2-type), TiFe (AB-type) and Mg_2Ni (A_2B-type) consist of hydride forming elements, "A", and non-forming elements, "B". We may speculate about the role of each element in the following way. The hydride forming element (e.g., Zr) may make a strong chemical bond with hydrogen, whereas the hydride non-forming element (e.g., Mn) may work to reduce such a strong A-H bond, so that hydrogen is released readily from the A atom in the hydrogen desorption process. However this naive understanding is not true (21-25).

For the $ZrMn_2$ hydride, the contour map of the electron densities is shown in Fig.4(a) on the lattice plane containing the Zr, Mn and H atoms. As shown in this figure, the relatively high electron-density region near hydrogen extends

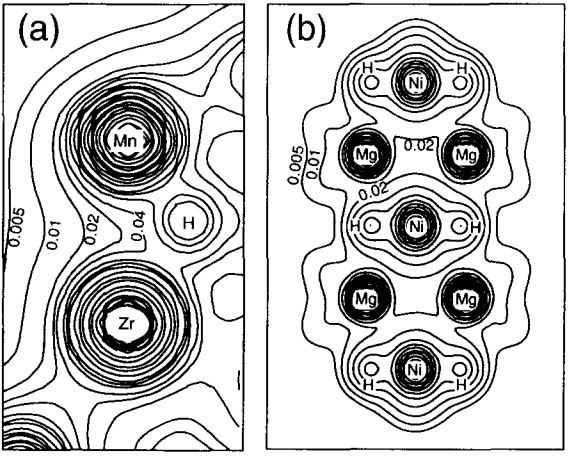

Fig.4. Contour map of the electron densities in (a) $ZrMn_2$ system and (b) Mg_2Ni system. The denoted numbers indicate the nubmers of electrons per $a.u^3$ (1a.u.=0.0529nm).

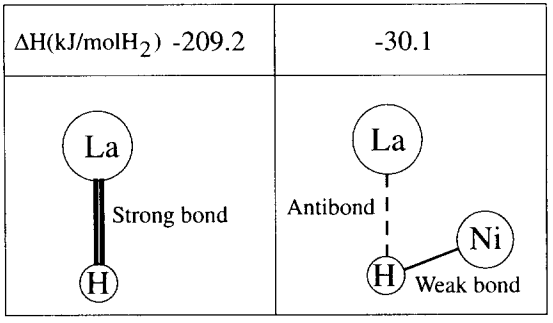

Fig.5. Schematic illustration of metal-hydrogen interactions in (a)LaH_2 and (b) $LaNi_5H_6$

towards the Mn atom site, but does not towards the Zr atom site. This result clearly indicates that hydrogen has a larger affinity for Mn atoms than Zr atoms in the $ZrMn_2$ system (21). Similar results are also obtained for Mg_2Ni system (22) (see Fig.4(b)), $LaNi_5$ system (23) and TiFe system (24), where hydrogen atoms interact more strongly with B atoms (Ni or Fe) rather than A atoms (Mg, La or Ti). However, this B-H (e.g., Ni-H) interaction is still weaker compared to the A-H (e.g., La-H) interaction in pure metal hydride, AH_2, (e.g., LaH_2). For example, as shown in Fig.5, the heat of formation, ΔH, is compared between LaH_2 and $LaNi_5H_6$. It is -209.2 kJ/mol H_2 for LaH_2 and -30.1 kJ/mol H_2 for $LaNi_5H_6$. As explained above, the Ni-H interaction is stronger than the La-H interaction in the $LaNi_5$ system, but this Ni-H interaction is supposed to be still weaker than the La-H interaction in LaH_2, judging from the heat of formation of hydrides shown in Fig.5. The hydrogen desorption process can be activated readily because of weak interactions with hydrogen operating in hydrogen storage alloys (25). On the other hand, LaH_2 is too stable to be dehydrided at moderate temperatures. In this sense, it may be said that the existence of weak metal-hydrogen interactions is characteristic of hydrogen storage alloys.

4.2. ROLES OF HYDRIDE FORMING AND NON-FORMING ELEMENTS

However, the hydride forming element, A, also plays an important role for the formation of the B-H bond (26). In order to make clear the roles of hydride forming and non-forming elements in hydrogen storage alloys, a series of calculations of the electronic structures is performed using a Ni-based octahedral cluster, M_2Ni_4H, shown in an insert in Fig.6, where M's are various elements presented on the horizontal axis. From this figure, it is evident that the Ni-M bond order is large when the M-H bond order is small. In particular, the Ni-H bond order is enhanced when M's are the hydride forming elements such as Na, Sr, and Ba. This means that hydrogen interacts strongly with Ni atoms if the hydride forming elements exist in the neighborhood, in agreement with the previous calculations of electronic structures of Ni-containing hydrides (22, 23). On the other hand, when M's are the hydride non-forming elements such as Fe, Co, and Ni, the Ni-H bond order is very small. Thus, it is apparent from Fig.6

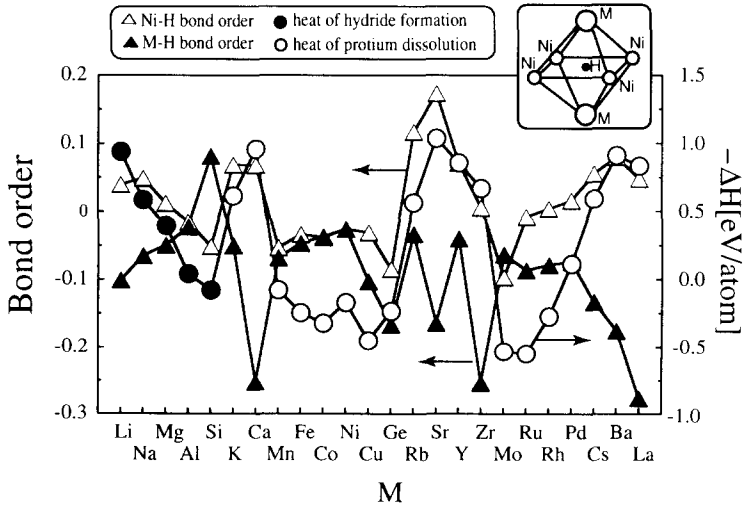

Fig.6. Bond orders between Ni and H atoms and between M and H atoms in the HM_2Ni_4 cluster, and comparison with the heat of hydride formation of M metal or heat of hydrogen dissolution in M metal.

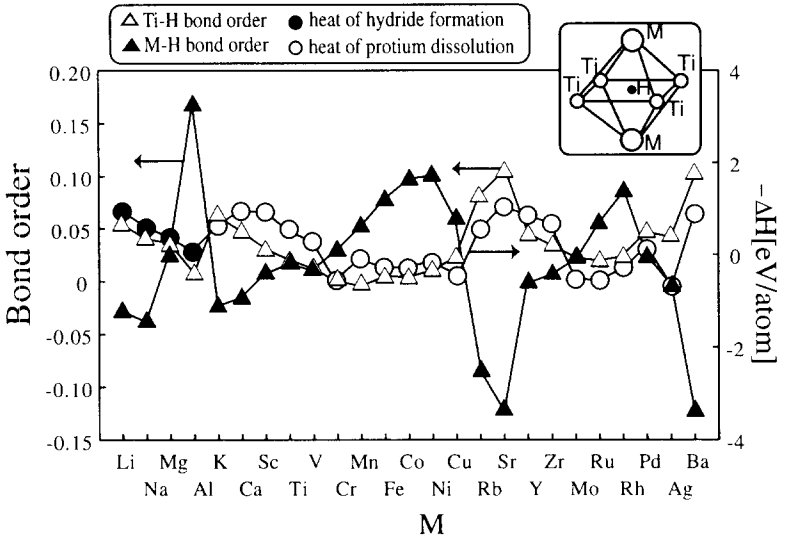

Fig.7. Bond orders between Ti and H atoms and between M and H atoms in the HM_2Ti_4 cluster, and comparison with the heat of hydride formation of M metal or heat of hydrogen dissolution in M metal.

that the magnitude of the Ni-H bond order correlates well with the heat of hydride formation of M metal or the heat of hydrogen dissolution in M metal.

Similar results are also obtained for the Ti-based octahedral cluster, M_2Ti_4H. Here, Ti is a hydride forming element, in contrast to the hydride non-forming element, Ni, in the M_2Ni_4H cluster. As shown in Fig.7, when M's are the hydride non-forming elements such as Fe, Co and Ni, the Ti-H bond order is smaller than the M-H bond order. When M's are stronger hydride forming elements than Ti, for example Sr, Y and Ba, the Ti-H bond order is larger than the M-H bond order. As a result, the Ti-H bond order curve resembles the -ΔH curve as shown in Fig.7. Similar results are also obtained for the Mg-based octahedral cluster, M_2Mg_4H (27). Therefore, there is a general trend that the B-H bond becomes strong only when the hydride forming element, A, exists adjacent to B and H atoms. Otherwise, it remains weak or even antibonding, resulting in the no-chance for hydrogen to be absorbed in the alloy. Thus, both the hydride forming and non-forming elements are essential elements in hydrogen storage alloys.

4.3. ALLOYING EFFECT ON THE STABILITY OF HYDRIDES

When an alloying element, M, is added into the mother alloy, chemical interactions between atoms change in some ways depending on M, and hence the stability of the hydride is modified by alloying. This can be understood in terms of the chemical bond strengths between metal atoms sitting on the corners of a polyhedron where hydrogen is located (25, 28), as far as the crystal structure of hydrides is a derivative one of the mother alloy. On the other hand, in case when the crystal structure of hydrides is not derivative but completely new one, the importance of metal-hydrogen interactions further increases in considering the hydride stability.

3.4.1 HYDRIDE WITH DERIVATIVE CRYSTAL STRUCTURES

As described above, the hydride stability is treated in view of the crystal structural evolution in the course of hydrogenation. For example, the crystal structure of $LaNi_5H_6$ is not substantially different from that of $LaNi_5$, since only the lattice expansion and the lattice distortion are introduced into the alloy during hydrogenation. Therefore, it is supposed that the easiness of the lattice expansion and distortion during hydrogenation is important in considering the hydride stability. This will be controlled mainly by the nature of the chemical bonds between metal atoms in the starting alloy, rather than by the magnitude of the direct metal-hydrogen interaction.

For example, in case of the $LaNi_5$ system, as shown in Fig.8(a), when a hydrogen atom is located at the center of a small metal octahedron, the hydrogen interacts strongly with the Ni atoms rather than the La atoms. As a result, the Ni-Ni interaction in this octahedron is reduced significantly by the hydrogenation (23). In such a case, lattice expansion may occur so as to recover the Ni-Ni interaction to some extent. However, the occurrence of such a recovery is supposed to be hard if the La-Ni interaction is significantly large. This is because, the La atoms stick to the Ni atoms because of the presence of strong La-Ni interaction, which suppresses the movement for the Ni atoms to go away from a central hydrogen atom in the octahedron. In this way, the presence of

strong La-Ni interaction results in barring the way for lattice expansion. For this reason, the stability of the hydride decreases with increasing La-Ni interaction and probably with decreasing Ni-Ni interaction. So, the ratio of the La-Ni bond order to the Ni-Ni bond order is assumed to be a measure of the hydride stability. The hydride becomes more unstable with increasing ratio, so that the ratio will

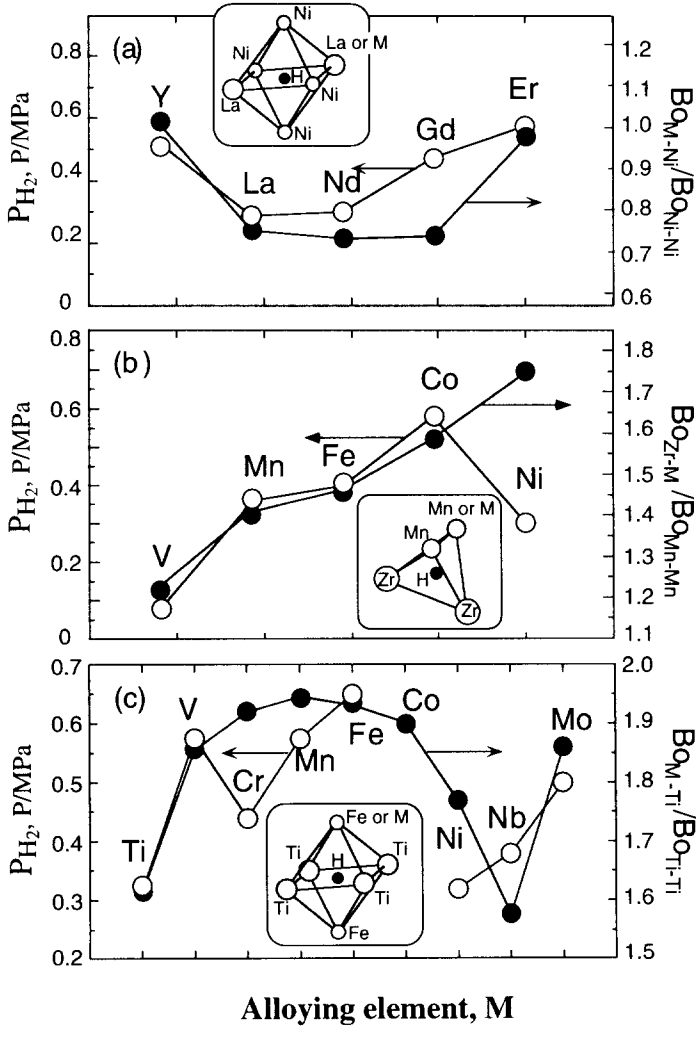

Fig.8.Comparison between the bond order ratios and the experimental plateau pressures for (a) $LaNi_5$ system, (b) $ZrMn_2$ system and (c) TiFe system.

proportional to the equilibrium plateau pressure of hydrogen in the hydride formation reaction. In fact, as shown in shown in Fig.8(a), the ratios are approximately similar to the experimental results for $La_{0.8}M_{0.2}Ni_5$ alloys.

In case of the $ZrMn_2$ system (21), as shown in Fig.8(b), a hydrogen atom occupies the central site of a small tetrahedron and interacts strongly with Mn atoms. In this case, the ratios of the Zr-Mn bond order to the Mn-Mn bond order are calculated and the results are shown in Fig.8(b). It is evident that the calculated bond order ratios correlate well with the experimental results of the equilibrium plateau pressure of hydrogen for $ZrMn_{1.8}M_{0.2}$ alloys.

Similar results are also obtained for the TiFe system (24). As shown in Fig.8(c), the ratios of the Fe-Ti bond order to the Ti-Ti bond order are approximately similar to the experimental results for $TiFe_{0.96}M_{0.04}$ alloys. A discrepancy observed at Cr may be attributable to the difficulties involving in the activation process of the Cr-containing alloy.

The hydrides formed in all these systems have a derivative crystal structure of the starting alloys. Thus, the metal-metal interaction on a small polyhedron and its change with alloying elements, M, will determine the stability of hydrides.

4.3.2 HYDRIDE WITH COMPLETELY NEW CRYSTAL STRUCTURES

On the other hand, in case of the Mg_2Ni system, the hydride, Mg_2NiH_4, of having a completely different crystal structure from that of Mg_2Ni appears in the course of hydrogenation above 518K. In this case, the importance of the metal-hydrogen interaction increases as well as the metal-metal interaction (25, 28). In fact, as shown in Fig.9, the measured heat of the hydride formation in $Mg_2Ni_{0.75}M_{0.25}$, changes in an approximately similar way as does the M-Mg or the M-H interaction (22). It is noticed that the M-H chemical bond plays a more important role in the hydride stability in this Mg_2Ni, compared to $LaNi_5$, TiFe and $ZrMn_2$. The importance of the M-H interaction further increases in b.c.c.V (29). In fact, the V-V interaction is very small in the VH_2 hydride with the CaF_2-type structure, since V forms a f.c.c. lattice instead of the original b.c.c. lattice in it. In this case, the ionicity difference between H and M atoms, $\Delta Io(Io[H]-Io[M])$,

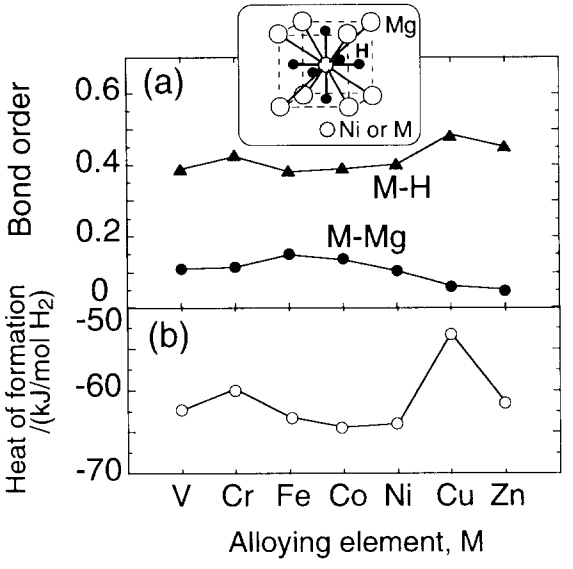

Fig.9. Conparison between (a) the bond orders and (b) the heat of formation for the hydride in Mg_2Ni system.

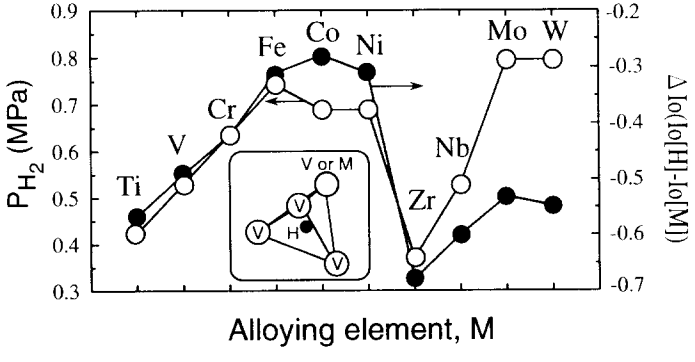

Fig.10. Comparison between the calculated ionicity differences and the experimental plateau pressures for VH_2 system.

which is a measure of the ionic interaction through the charge transfer between them, is responsible mainly for the relative stability of alloyed VH_2 hydride as shown in Fig.10 (27).

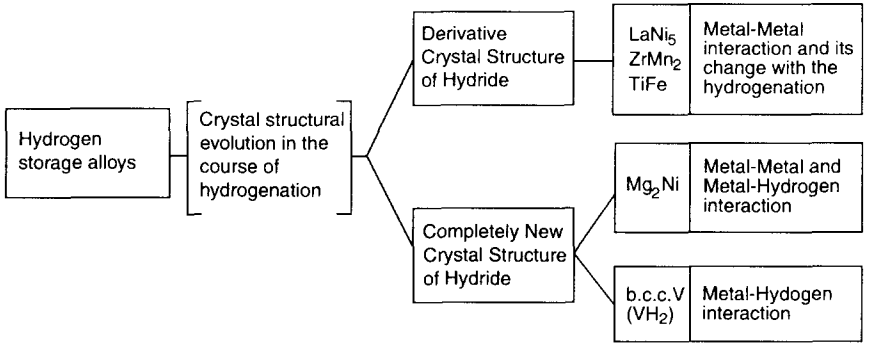

Fig.11. Classification of hydrogen storage alloys in terms of crystal structural evolution in the course of hydrogenation.

All these results are summarized in Fig.11. However, in any cases, the stability of hydrides is well understood in terms of the nature of the chemical bond between atoms in small metal polyhedra and also of the crystal structural evolution in the course of hydrogenation (25, 28).

4.4. CRITERIA FOR ALLOY DESIGN

4.4.1 OPTIMUM ATOMIC ARRANGEMENTS ON METAL POLYHEDRA

Some criteria for the design of hydrogen storage alloys will be discussed in this section. For the design of new alloys, it is important first to select the constituent elements and then to determine the alloy composition.

As mentioned before, the constitution of both the hydride forming elements, A, and non-forming elements, B, is essential for hydrogen storage alloys. This is because the presence of the B-H interaction is characteristic of hydrogen storage alloys, and this interaction is enhanced only when A elements exist near the B elements in the alloy. Also, the effective number of the B-H bonds will increase when the concentration of A element is high, as might be expected from the

results shown in Fig.6 and 7. As a result, the amount of hydrogen absorbed in the alloy will increase with increasing A/B compositional ratio. However, a disproportionation reaction tends to take place, if the concentration of A element is too high in the alloy. Let's explain this assuming that there are three types of tetragonal clusters in the A-B binary alloy as shown in Fig.12. Here, if the A/B compositional ratio is high, or the A-A bond is stronger than the A-B or the B-B bond, the clusters shown in Fig.12(a) are dominant in the alloy. In such a case, hydrogen will interact mainly with A elements when hydrogen is introduced into the alloy, resulting in the formation of strong A-H bonds. And the disproportionation reaction, $AB + H \rightarrow AH + B$, will take place easily in it. AH is so stable that the onset of this reaction is undesirable in view of the hydrogen desorption.

By contraries, when the A/B compositional ratio is low, or the B-B bond is stronger than the A-A or the A-B bonds, the clusters shown in Fig.12(c) are dominant in the alloy. In this case, it is very hard for hydrogen to be absorbed in such a B atom-abundant cluster.

Therefore, in order to absorb and desorb hydrogen smoothly without the onset of any disproportionation reaction, the A/B compositional ratio should be controlled in a proper manner, depending on the chemical bond strength between

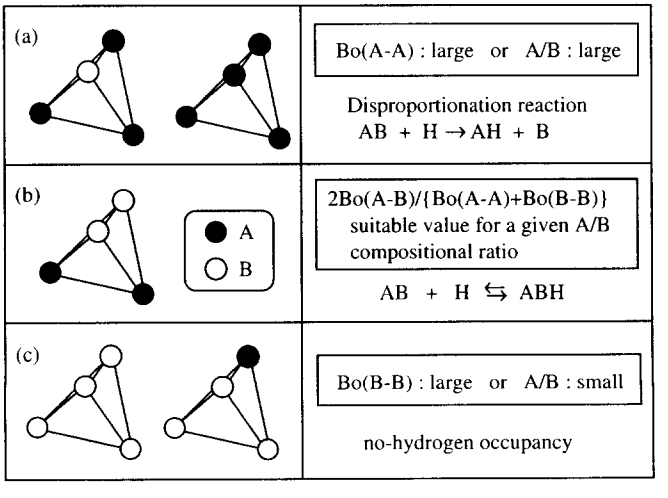

Fig.12. Tetrahedral clusters and hydriding reactions.

the A and the B elements as shown in Fig.12(b). In other words, optimum clusters are made in the alloy only when the bond order ratio, 2 Bo(A-B) / [Bo(A-A)+Bo(B-B)], takes a suitable value for a given A/B compositional ratio.

4.4.2 ALLOY COMPOSITIONS

A series of calculation is performed to obtain the bond order ratio, 2 Bo(A-B) / [Bo(A-A)+Bo(B-B)], for various alloy systems using the tetrahedral or the octahedral clusters, and the results are shown in Fig.13 and 14, respectively. Here, this bond order ratio has a physical meaning similar to the interaction parameter, Ω_{AB} ($=V_{AB}-1/2(V_{AA}+V_{BB})$), where V_{AB}, V_{AA}, V_{BB} are the respective bond strengths between atoms given in the subscript. As described earlier, if this bond order ratio has a suitable value for a given alloy composition, the hydrogen absorption and desorption reaction, AB + H $\leftrightarrow$ ABH, is expected to take place readily in the alloy. In fact, as shown in Fig.13, there exists a strong correlation between the A/B compositional ratio and the bond order ratio. For example, all

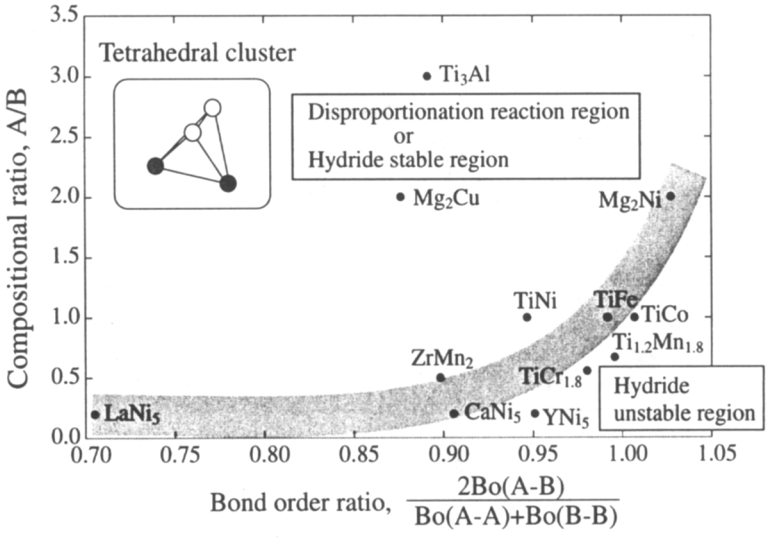

Fig.13. Correlation between the A/B compositional ratio and the bond order ratio for tetrahedral cluster.

the typical hydrogen storage alloys, e.g., $LaNi_5$, $ZrMn_2$, TiFe and Mg_2Ni, locate on a narrow band illustrated in Fig.13.

Also, all the alloys located in the upper region above this narrow band (e.g., Mg_2Cu and Ti_3Al) tend to decompose during the hydrogenation. For example, in case of Mg_2Cu, the disproportionation reaction, $Mg_2Cu + 2H_2 \rightarrow 2MgH_2 + Cu$, occurs during the hydrogenation. Therefore, the region lying above the narrow band is called the disproportionation reaction region.

On the other hand, the alloys located in the region below this narrow band, tend to form unstable hydrides. YNi_5 is an example, as its equilibrium pressure of hydrogen is very high. Therefore, this region is called the hydride unstable region.

Here, the Mg-Ni system has the largest bond order ratio among the alloys shown in Fig.13. This means that the Mg-Ni bond is much stronger than the Mg-Mg bond. This is the reason why any disproportionation reaction does not occur up to the high Mg/Ni compositional ratio in this system. On the other hand, in case of the La-Ni system, the La/Ni compositional ratio is low because the La-La bond is stronger than the La-Ni bond. Therefore, it is supposed that the disproportionation reaction will occur during the hydrogenation as the La/Ni

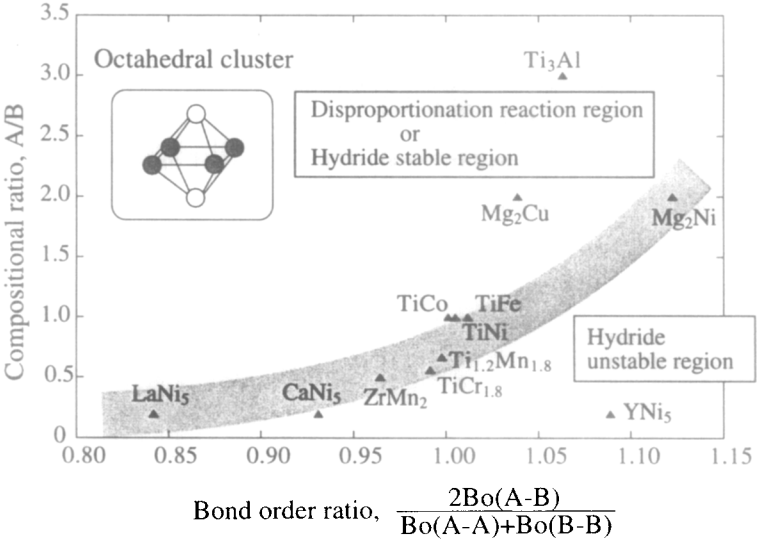

Fig.14. Correlation between the A/B compositional ratio and the bond order ratio for octahedral cluster.

compositional ratio increases. Even in such a case, the onset of the disproportionation reaction may be suppressed by controlling the bond order ratio in some ways. For example, the substitution of Mg atoms for La atoms in the La-Ni system may increase the average bond order ratio, and hence the onset of the disproportionation reaction may be suppressed even in the alloy with a relatively high La concentration.

Similar results are also obtained for the octahedral clusters as shown in Fig.14. Thus, the present result is independent of the clusters used for the calculation. Once A and B elements are chosen, the A/B compositional ratio is determined following a relationship with the bond order ratio shown in Fig.13 or Fig.14.

5. CONCLUSION

An electronic approach is presented to the understanding of hydrogen storage alloys in a fundamental manner. From a series of the DV-Xα molecular orbital calculations, it is shown that the roles of hydride forming and non-forming elements in the alloys, and stability changes of hydrides with alloying elements are understood consistently in view of the nature of chemical bond and its modification in the course of hydrogenation. Also, some criteria for alloy design (e.g., optimum alloy compositions) are proposed in this study.

ACKNOWLEDGMENTS

The authors would like to express sincere thanks to Messrs. Y.Takahashi, T.Matsumura, K.Nakatsuka, M.Takagi and M.Nakai, all the graduate students of Nagoya University, for their great helps in the DV-Xα molecular orbital

calculations. We also acknowledge the Computer Center, Institute for Molecular Science, Okazaki National Institute for the use of the SX-3/34R computer. This research was supported by the Grant-in-Aid for Scientific Research from the Ministry of Education, Science, Sports and Culture of Japan.

REFERENCES

1. Van Mal, H. H.; Buschow, K. H. J.; Miedema, A. R. *J. Less-Common Met.*, **1974**, 35, 65.
2. Fujitani, S.; Yonezu, I.; Saito, T.; Furukawa, N.; Akiba, E.; Hayakawa, H.; Ono, S. *J. Less-Common Met.*, **1991**, 172-174, 220.
3. Reidinger, F.; Lynch; J. F.; Reily, J. J. *J. Phys. F*, **1982**, 12, L49.
4. Darnaudery, J. P.; Darriet, B.; Pezat, M. *Int. J. Hydrogen Energy.*, **1983**, 8, 705.
5. Mealand, A. J.; Libowitz, G. G.; Lynch, J. F.; Rak, G. *J. Less-Common Met.*,**1984**, 104, 133.
6. Libowitz, G. G.; Mealand, A. J. *Mater. Sci. Forum*, **1988**, 31, 177.
7. Kagawa, A.; Ono, E.; Kusakabe, T.; Sakamoto,Y. *J. Less-Common Met.*, **1991**, 172, 64.
8. Lundin, C. E.; Lynch, F.E.; Magee,C.B. *J. Less-Common Met.*,**1977**, **56**, 19.
9. Mendelsohe, M. H.; Gruen, D.M.; Dwight, A.E. *J. Less-Common Met.*, **1979**, 63, 193.
10. Darnaudery, J. P.; Darriet, B.; Pezat, M. *Int. J. Hydrogen Energy.*, **1983**, 8, 705.
11. Soubeyroux, J. L.; Pontonnier, L.; Miraglia, S.; Isnard, O.; Fruchart, D. *Z. Phys. Chem, Bd.* **1993**, 179, 187.
12. Mulliken, R. S. *J. Chem. Phys.*, **1955**, 23, 1833, 1841, 2338, 2343.
13. Adachi, H.; Tsukada, M.; Satoko, C. *J. Phys. Soc. Japan*, **1978**, 45, 874.
14. Adachi, H.; Shiokawa, S.; Tsukada, M.; Satoko, C.; Sugano, S. *J. Phys. Soc. Japan*, **1979**, 47, 1528.

15. Tsukada, M.; Adachi, H.; Satoko, C. *Progr. in Surface Sci.*, **1983**, 14, 113.
16. Morinaga, M.; Yukawa, N.; Adachi, H. *J. Phys. Soc. Jpn.*, **1984**, 53, 653.
17. Morinaga, M.; Yukawa, N.; Adachi, H. *J. Phys. F*, **1985**, 15, 1071.
18. Morinaga, M.; Yukawa, N.; Adachi, H.; Mura, T. *J. Phys. F.*, **1987**, 17, 2147.
19. Yukawa, H.; Morinaga, M. *Materia Japan*, **1998**, 37, 578.
20. Adachi, H.; Imoto, S. *J. Phys. Soc. Jpn.*, **1979**, 46, 1194.
21. Matsumura, T.; Yukawa, H.; Morinaga, M. *J. Alloys Comp.*, **1998**, 279, 192.
22. Takahashi, Y.; Yukawa, H.; Morinaga, M. *J. Alloys Comp.*, **1996**, 242, 98.
23. Yukawa, H.; Takahashi, Y.; Morinaga, M. *Intermetallics*, **1996**, 4, S215.
24. Yukawa, H.; Takahashi, Y.; Morinaga, M. *Computational. Mat. Sci.*, **1999**, 14, 291.
25. Yukawa, H.; Morinaga, M. *Advances in Quantum Chemistry*, **1997**, 29, 83.
26. Nakatsuka, K.; Yoshino, M.; Yukawa, H.; Morinaga, M. *J. Alloys Comp.*, **2000**, 293-295, 222.
27. Nakatsuka, K.; Takagi, M.; Nakai, M.; Yukawa, H.; Morinaga, M. *"Proc. of the Inter. Conf. on Solid-Solid Phase Transformations '99 (JIMIC-3)"*; Koiwa. M; Otsuka, K; Miyazaki, T, Eds.; The Japan Institute of Metals, **1999**, 681.
28. Yukawa, H.; Matsumura, T.; Morinaga, M. *J. Alloys Comp.*, **2000**, 293-295, 227.
29. Matsumura, T.; Yukawa, H.; Morinaga, M. *J. Alloys Comp.*, **1999**, 284, 82.

Application of DV-Xα calculations in ceramics science

Isao TANAKA

Department of Energy Science and Technology, Kyoto University, Sakyo, Kyoto, 606-8501 Japan.

(Received; 24th February, 1999)

We have been using DV-Xα calculations as a tool for materials selection/design of advanced ceramics. It uses numerical atomic orbitals that are "optimized" for given chemical environment. Therefore, reliable electronic structures can be obtained with compact basis-sets, which is very useful for gaining our insight into chemical bondings. Recent results on transparent oxide conductors by our group are reviewed here. Oxides of group 11 to 14 metals in the 4th and 5th row of the periodic table are investigated with special interests on metal-metal bondings that determine the nature of the bottom of the conduction band, thus the n-type conductivity. Electron energy loss near edge structures (ELNES) is a very useful tool to investigate the metal-metal bondings by experiments. The present type of calculations are successful for interpretation and reproduction of the ELNES.

KEYWORDS: transparent oxide conductors, chemical bondings, electron energy loss near edge structures (ELNES), indium oxides, oxygen vacancy

e-mail : tanaka@dvxa4.MTL.kyoto-u.ac.jp

ADVANCES IN QUANTUM CHEMISTRY, VOLUME 37

0065-3276/01 $35.00

1. INTRODUCTION

Macroscopic properties of ceramic materials are often dominated by localized imperfections such as defects, impurities, surfaces and interfaces. Systematically-doped polycrystalline materials exhibit wider variety of properties as compared with monolithic single crystals. Some of them serve key roles in high-tech society and they are referred to as fine ceramics or advanced ceramics. An ultimate objective of the ceramic science and technology is to understand the nature and functions of the localized imperfections in order to achieve desired performances of materials intellectually without too much accumulation of empirical knowledge.

Recent development of computational technology in quantum mechanical calculations as well as vast increase in computer resources enable us to conduct electronic structure calculations of realistic systems without including empirical parameters, i.e., from first principles. Electronic mechanisms behind the roles of the localized imperfections are expected to be understood clearly with the aid of the first principles calculation, leading to guiding principles for materials design.

We have been applying the DV-Xα calculation for various aspects in ceramic science. The advantage to employ the DV-Xα cluster calculations as compared with other computational techniques can be summarized as follows:

1. It uses numerically generated "optimum" atomic orbitals as basis functions that are obtained as solutions of radial part Schrödinger equation for each atoms in a given chemical environment. Molecular orbital calculations using minimal or nearly minimal number of basis functions thus provide reliable electronic structures. The compact-basis calculations are very useful for gaining insight into chemical bondings.
2. Because of the use of the atomic orbital basis, all kinds of elements in the periodic table can be examined under the same computational accuracy within non-relativistic approximation.
3. Calculations are made entirely from first principles; thus no adjustable parameters are included in the calculation.
4. Cluster calculations can be made for any atomic arrangement without imposing artificial boundary conditions. The convergence of properties of interest with the cluster size can be explicitly revealed. This is extremely important when we deal with imperfection-induced states that are localized within some extent.
5. All electrons including those of core-orbitals are used. The core-states are often frozen in other methods for computational economy. For quantitative reproduction of the X-ray spectra, however, inclusion of a core-hole is sometimes mandatory.

In the present paper, some of our recent results are reviewed after brief introduction to the computational procedures.

2. COMPUTATIONAL PROCEDURE

A non-relativistic first principles molecular orbital (MO) method using model clusters using the computer code named SCAT(1), a modified version of an original discrete variational (DV)-Xα program(2), has been employed throughout the present work. Numerical atomic orbitals (NAO) were used as basis functions. They were generated flexibly by solving radial part Schrödinger equation for a given environment. Minimal basis-sets were used in order to clarify the simple relationship between spectral features and chemical bondings. Integrations to obtain energy eigenvalues and eigenfunctions were made in a numerical manner. Population analyses were made in a standard Mulliken's manner(3). The overlap population between i-th atomic orbital and j-th atomic orbital at the ℓ-th MO is given by

$$Q_{ij}^{\ell} = C_{i\ell} C_{j\ell} S_{ij} \quad , \qquad (1)$$

where S_{ij} is the overlap integral given by

$$S_{ij} = \int \chi_i \chi_j \, \mathrm{d}r \quad . \qquad (2)$$

χ_i and $C_{i\ell}$ are i-th atomic orbital and its coefficient for the ℓ-th MO. The overlap population between atom A and B is given by

$$Q_{AB}^{\ell} = \sum_{i \in A} \sum_{j \in B} Q_{ij}^{\ell} \quad . \qquad (3)$$

Overlap population diagrams were made by broadening of Q^{ℓ}_{AB} at individual MOs using Gaussian functions. The sum of Q^{ℓ}_{AB} over occupied orbitals is called bond-overlap population, Q_{AB}, as defined by

$$Q_{AB} = \sum_{\ell} f_{\ell} Q_{AB}^{\ell} \quad , \qquad (4)$$

where f_ℓ is the occupation number of the ℓ-th MO. The orbital population of the i-th orbital is given by

$$Q_i = \sum_{\ell} f_{\ell} \sum_{j} Q_{ij}^{\ell} \quad . \qquad (5)$$

Net charge of each atom ΔQ_A is obtained by

$$\Delta Q_A = Z_A - \sum_{i \in A} Q_i \tag{6}$$

where Z_A is the atomic number of atom A. Model clusters were embedded in Madelung potential generated by point charges of formal values. Convergence of the Madelung potential with respect to dipole and quadrupole sums(4) was found to be established within an accuracy of 0.1%.

3. ELECTRONIC STRUCTURES AND CHEMICAL BONDINGS IN In_2O_3

Indium oxide film is transparent in visible region and semiconductive when donor impurities such as Sn ions are present. The Sn-doped In_2O_3 is specially denoted by ITO (indium tin oxides). They are widely used for transparent electrodes in solar cells, display devices etc. Despite its technological importance, no first principles calculation of In_2O_3 was reported prior to the recent work by the present authors(5). Since the properties of these films are sensitively changed by small amount of additional dopants and their preparation conditions, first principles calculations should be valuable in order to have guiding principles for materials/processing design. In the present paper, we review our results from the viewpoint of chemical bondings.

Indium oxide has a C-type rare earth structure (space group Ia3, No.206) similar to many trivalent rare-earth oxides, such as Yb_2O_3 and Dy_2O_3. They are composed of eight fluorite-type unit cells with systematic anion vacancies. The unit cell is composed of 8 In(1) atoms at the b site, 24 In(2) atoms at the d site, and 48 oxygen atoms at the e sites according to the Wyckoff's notation. A model cluster, $(In_{43}O_{120})^{111-}$ is used in the present study. Figure 1 displays local and partial density of states (PDOS) obtained near the center of the cluster. Total density of states (DOS) was computed as a sum of two times PDOS for In-orbitals and three times for O-orbitals. All of these curves are made by broadening the discrete energy eigenvalues by Gaussian functions of 0.5 eV FWHM.

Small contribution of In-4d, 5s and 5p orbitals in O-2s and O-2p bands can be recognized. The presence of In-5s and 5p orbitals in the O-2p band is natural for ionic compounds with partial covalency. Mulliken's population analysis found that the bonding of In_2O_3 does not fit the fully ionic picture. Net charges evaluated for atoms near the center of the cluster are +2.03 for In and -1.65 for O, respectively. There should be a small covalent bonding

between In and O. The manner of covalent bonding can be clearly understood using overlap population diagrams in which the quantity given by eq(1) is shown as a function of MO energy after broadening by Gaussian functions. The diagrams for In-O, In-In and O-O bonds obtained near the center of the cluster are shown in Fig. 2. The right part of each diagrams shows the bonding contribution and the left part shows the antibonding contribution. The integration of both bonding and antibonding contributions up to the highest occupied MO (HOMO) provides the bond overlap population for each bond. These values show that the major covalency in In2O3 crystal is due to the bonding of the In-O. Regarding the In-O interaction, the O-2s band (-15 to -17 eV) is completely bonding. The In-4d band (-10 to -12 eV) displays both bonding and antibonding contributions for almost the same amount.

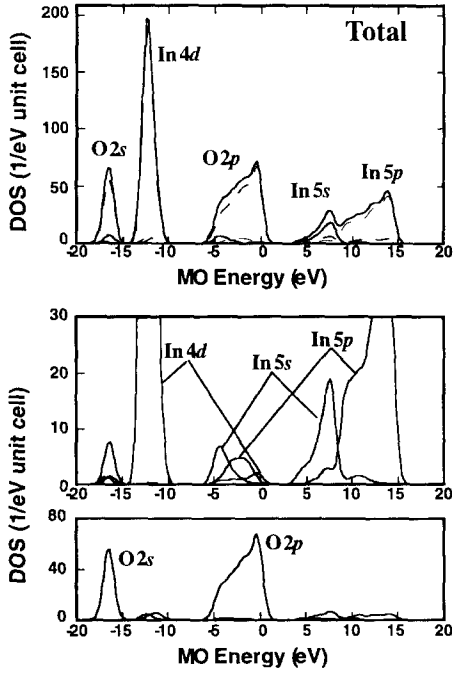

Fig 1. Total and partial density of states of In_2O_3 obtained by local density of states of atoms near the center of the $(In_{43}O_{120})^{111-}$ cluster. Highest occupied molecular orbital (HOMO) was taken to be zero in the MO energy.

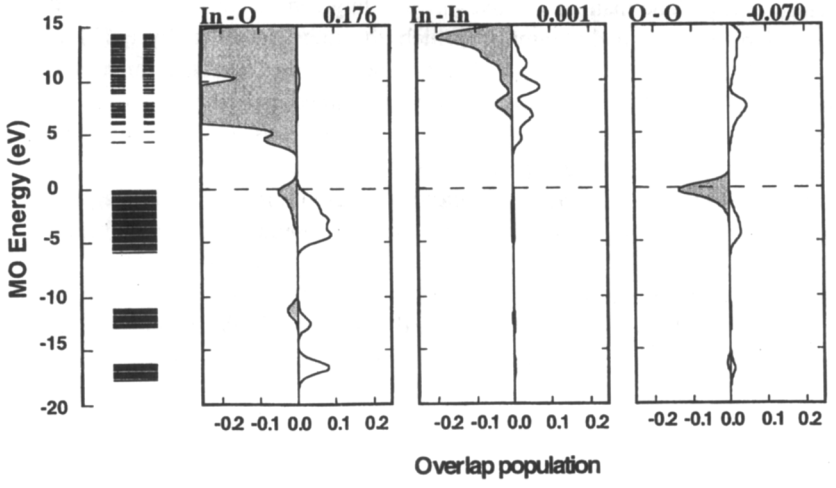

Fig 2. Overlap population diagrams of In_2O_3 obtained near the center of the $(In_{43}O_{120})^{111-}$ cluster.

The major part of the O-2p band (0 to -5 eV) shows bonding contribution. However, there is an antibonding contribution due to the interaction between O-2p and In-4d orbitals near the top of the valence band.

The O-O bond is less significant than the In-O bond. The balance of the bonding and antibonding contributions in all of the O-2s, 2p and In-4d bands makes the net bond-overlap-population to be a small negative value. The In-In interaction is much weaker than the other two kinds of bonds. There are two groups of In-In distances depending upon the manner of the InO_6 octahedral linkage in the In_2O_3 crystal. It is around 3.36 Å when the neighboring octahedra are edge-shared, and around 3.83 Å when they are corner-shared. Irrespective of the linkage, the direct In-In covalent bond is found to be weak. It should be noted, however, the overlap population between In orbitals are strong in the unoccupied band where the In-5sp orbitals are dominant. Although they play little role for the chemical bonding of the ideal In_2O_3 at the ground state, the In-In interaction becomes important at the excited states as well as doped or defective crystals where these higher energy states are partially occupied by electrons.

Oxygen of In_2O_3 is slightly deficient in air at elevated temperatures. The O-vacancy introduces excess electrons in order to maintain the charge neutrality, which is widely accepted to be the origin of the n-type conductivity. Changes of the electronic states and chemical bondings associated with the presence of O-vacancy is therefore of great interest. In order to emphasize the effect of the oxygen vacancy, a model cluster that has an oxygen at the center, i.e.

$(In_4O_{17})^{22-}$ cluster, is employed. Top panel of Fig. 3 displays the MO level structure and overlap population diagram of the $(In_4O_{17})^{22-}$ cluster. Comparison of the overlap population diagram with that of the $(In_{43}O_{120})^{111-}$ cluster shown in Fig. 2 finds that the framework structures of these two diagrams are the same except for a small difference in the unoccupied In-5sp band. The $(In_4O_{16})^{22-}$ cluster that contains an oxygen vacancy at the center of the $(In_4O_{17})^{22-}$ cluster with two excess electrons is shown together.

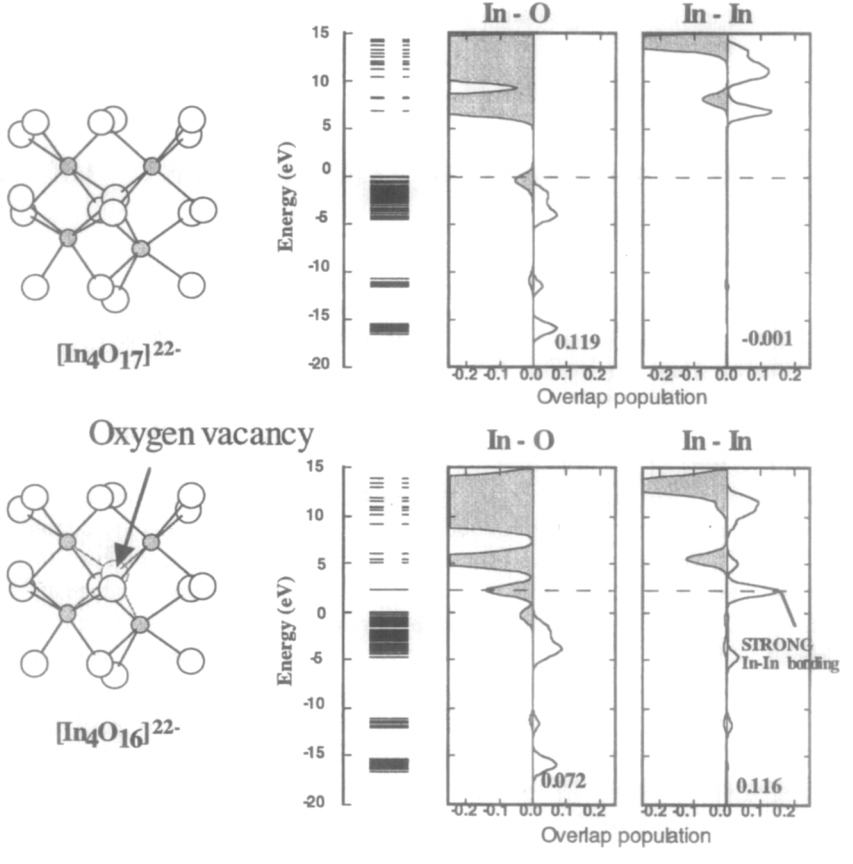

Fig 3. Oxygen vacancy level and overlap population diagrams around the vacancy by model clusters of $(In_4O_{17})^{22-}$ and $(In_4O_{16})^{22-}$. MO energy of the defective cluster is alligned with that of the perfect crystal at the top of the O-2p band.

When the oxygen vacancy is present, two phenomena can be noticed: 1) Decrease in the energy of the In-5sp bands by 3 eV, and 2) formation of a discrete level in between the band-gap. The shape of the overlap population diagrams is not significantly altered by the presence of the vacancy. It is simply shifted in energy. However, the discrete level that is newly appeared is strong antibonding for the In-O and strong bonding for the In-In interaction. This level may be called the vacancy level. The extra charges associated with the O-vacancy occupy the vacancy level, which significantly alter the chemical bonding around the vacancy. The In-In bond is reinforced remarkably in exchange for the reduction in In-O bonding. The M-M interaction is therefore important in determining relative stabilities of O-vacancies among metal-oxides in general.

4. TOWARD BETTER TRANSPARENT OXIDE CONDUCTORS

Oxides of group 11 to 14 metals in the 4th and 5th row of the periodic table, such as ZnO, Ga_2O_3 and CdO exhibit n-type conductivity due to the oxygen deficiency similar to In_2O_3. They have been doped and/or mixed in order to optimize properties as transparent oxide conductors for optical devices.

The n-type conductivity is determined by the product of the reciprocal effective mass of electrons and the concentration of carriers in a semi-classical viewpoint. The effective mass is often calculated by fitting the dispersion curve near the bottom of the conduction band. The bottom is mainly composed of M-4s/5s orbitals in the oxides of the present interest, and the curvature is mainly determined by the M-M interactions. The situation is schematically shown in Fig. 4. The strong interaction among M-4s/5s orbitals should bring about wider M-4s/5s band-width and smaller effective mass. On the other hand, weaker M-4s/5s interactions result in narrower band-width and larger effective mass. With the increase of the atomic number in the same row of the periodic table, the M-4s/5s orbitals tend to be contracted. Assuming the M-M distance is the same, the M-4s/5s interactions should be weakened with the atomic number, in general.

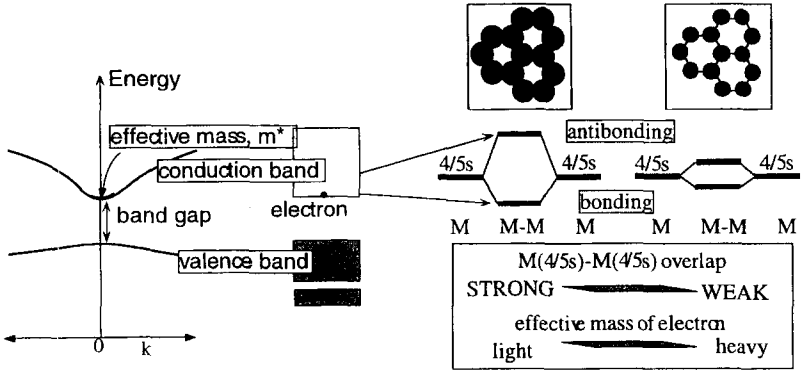

Fig 4. Schematic view of the bottom of the conduction bands of oxides of group 11 to 14 metals.

The molecular orbital calculations of 4th-row metal-oxides, i.e., Cu_2O, ZnO, Ga_2O_3, and GeO_2 were made using model clusters that have cation at the center(6). They contain the first nearest-neighbor cations and oxygen ions surrounding those cations. They were embedded in Madelung potential generated by point charges in order to minimize the surface effects. Figure 5 shows two times of the mean radius of the M4s atomic orbital, $2\langle r\rangle_{4s}$, used in the present calculation divided by the mean M-M distance, $d_{M\text{-}M}$, in the real crystals. The quantity may be used as a good measure for the magnitude of the M4s interactions. It should be noted that atomic orbitals are often fixed in molecular orbital calculations. In our program, the atomic orbitals are optimized for given chemical environments. The mean radius of the atomic orbitals is a more meaningful quantity as merely a parameter of a basis-function. As expected by a simple argument, $2\langle r\rangle_{4s}/d_{M\text{-}M}$ decreases monotonously with rising the atomic number.

The overlap population between M4s orbitals at the lowest unoccupied molecular orbital (LUMO) obtained by the cluster calculation is shown in Fig. 5. Differently from $2\langle r\rangle_{4s}/d_{M\text{-}M}$, the value is smaller in Cu_2O than in ZnO. This can be explained by the remarkably smaller M4s population in the LUMO only in Cu_2O, as can be seen in Fig. 5. LUMO of Cu_2O cannot be treated similarly to the later oxides. Except for Cu_2O, however, M4s is dominant at the bottom of the conduction band. Therefore, the M4s interactions should play a determining role for the effective mass of electrons. With the increase of the atomic number, the effective mass is expected to increase, thereby reducing

the conductivity. It should also be noted that the increase of the M-M bonding interaction at the LUMO can contribute for the stability of O-vacancies in these oxides as discussed in the previous chapter. This also gives rise to the conductivity. It seems better n-type conductors can be obtained with metal oxides with lower atomic numbers as far as the major component of LUMO is M4s.

Experimental band-gap is shown in Fig. 6. As can be seen, the band-gap increases with rising the atomic number. The tendency of the experimental band-gaps is well reproduced by the LUMO-HOMO gap of the present cluster calculation. However, the absolute values are larger by the cluster calculation because of the use of the small clusters(6). In order to exhibit transparency, the experimental band-gap should be larger than 3.3 eV.

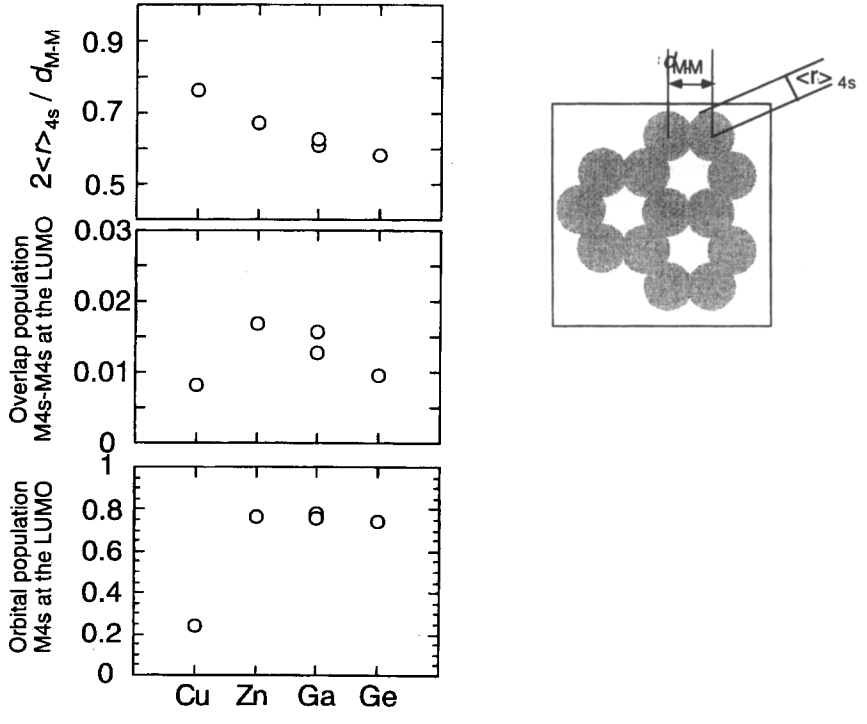

Fig 5.
(TOP) The ratio of the mean radius of M4s orbital, $\langle r \rangle_{4s}$, and the averaged near-neighbour metal-metal distance, $d_{M\text{-}M}$. (MIDDLE) The M4s-4s overlap population at the LUMO. (BOTTOM) The M4s orbital population at the LUMO.

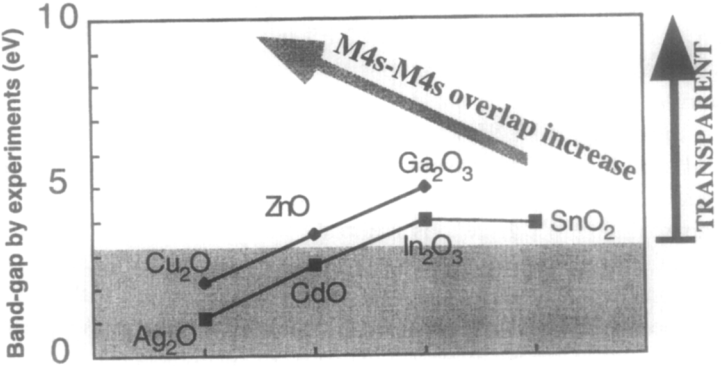

Fig 6. Band gaps by experiments for oxides of 11-14 group metals in 4th and 5th row of the Periodic table.

The condition is satisfied for ZnO and later oxides of 4th row elements. Since the M4s interactions are strongest in ZnO, it is the best candidate for transparent oxide conductors among binary oxides of 4th row elements. Ternary or more complicated oxides may be analyzed in the same manner considering the balance of two factors; 1) the band-gap and 2) the M-M interactions. An effort to design new transparent oxide conductor is in progress by the combination of experiments and molecular orbital calculations for $InGaZnO_4$ and its derivatives by Orita, the present author and others(7).

5. ELECTRON ENERGY LOSS SPECTROSCOPY AS A TOOL TO INVESTIGATE THE M-M INTERACTIONS

Electron energy loss spectrometer (EELS) is often equipped in modern transmission electron microscope (TEM), which constitutes a versatile tool in solid-state physics/chemistry as well as in materials science. The structures within approximately 20 eV from the core-loss edge is usually referred to as

electron-energy loss near edge structures (ELNES), which is analogous to NEXAFS (near edge X-ray absorption fine structures) that is a synonym of XANES (X-ray absorption near edge structure). On the core-loss process, an electron is excited from a core level to an unoccupied state by an electric dipole transition. As a result, experimental ELNES is related to unoccupied partial density of states of the selected atom that is allowed by the electric dipole selection rule.

Efforts to reproduce ELNES by first principles calculations are not always successful even today. The reasons for the disagreement between theoretical spectra and experimental spectra may be twofold: 1) Even when LDA (local-density approximation) calculations are made from first principles, results of unoccupied density of states show stronger dependence on the choice of the basis-functions as compared with the occupied states especially at high energies. Theoretical spectra in early days-literature are sometimes differ from those by more sophisticated methods. 2) Most of theoretical calculations that have been used to compare with the experimental spectra were done for the ground state. In other words, presence of a core-hole has been completely ignored. On the absorption phenomenon, an electron is excited from a core-level to an unoccupied orbital leaving a core hole. Unoccupied band structure is in general changed by the presence of the core-hole. Calculation at the ground state reproduces experimental spectrum only when the core-hole effect is not significant.

First principles cluster-calculations on the basis of molecular orbital (MO) theory have been successful for reproduction of ELNES of some oxides(8-12). Core-hole effects can be rigorously included into the self-consistent calculations, which were pointed out to be essential for the ELNES calculation(10-12). Since excited electron is localized near the core-hole, cluster-calculations should be advantageous for the ELNES reproduction as compared with band-structure methods unless a sufficiently large super-cell is chosen. Very recently, the present authors have reported the effects of a core-hole in the unoccupied density of states using model clusters of hexagonal boron-nitride(13). Wave functions are found to localize significantly near the core hole, thereby changing their energies as well as spatial distribution. They are very different from the Bloch states assumed in a band-structure calculation on the basis of a structural unit-cell. When the presence of the core-hole is ignored, in other words at the ground state, small clusters exhibit better agreement with the experiment as compared with large clusters because wave-functions are made to localize in the small clusters.

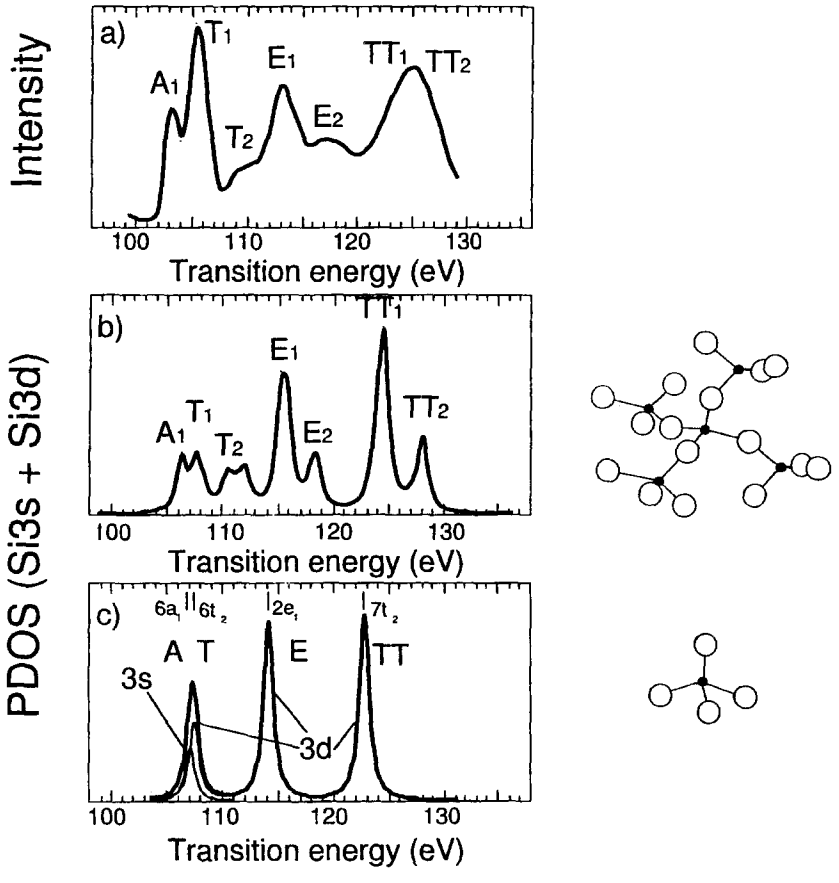

Fig. 7 (a) Experimental Si-$L_{2,3}$ edge ELNES from α-quartz in comparison with theoretical sum of PDOSes of Si-3s and 3d obtained at the center of b) a $(Si_5O_{16})^{12-}$ cluster, and c) a $(SiO_4)^{4-}$ cluster in T_d symmetry.

As described in the previous chapters, the bottom of the conduction band of metal oxides of group 12-14 elements is composed of empty M-s orbitals. The density of state features as observed by ELNES is therefore determined by the M-M interactions. An example of the effect of the M-M interaction on the

ELNES can be found in SiO_2 at the Si-L_{23} edge. Figure 7 compares experimental Si-L_{23} edge ELNES of SiO_2 (α-quartz) in comparison with theoretical spectra obtained as a sum of PDOSes of Si3s and 3d. Similar to most of SiO_2 polytypes, α-quartz has a $(SiO_4)^{4-}$ tetrahedron as a unit of the structure as shown in Fig. 7. The neighbouring tetrahedra share their corner oxygen to make it two-fold coordinated. Calculations by the tetrahedral unit $(SiO_4)^{4-}$, and a larger one including the second shell, i.e., $(Si_5O_{16})^{12-}$ are compared. The $(SiO_4)^{4-}$ cluster was made to have the regular tetrahedral symmetry, (T_d), for simplicity, although it is distorted in α-quartz. The larger cluster, $(Si_5O_{16})^{12-}$ were cut from real crystal structure. The $(SiO_4)^{4-}$ cluster of regular tetrahedron exhibits only four unoccupied molecular orbitals when basis-functions are restricted to be minimal and Si-3d, i.e., 1s - 2p for O and 1s - 3d for Si. These molecular orbitals are $6a_1$ (Si-3s), $6t_1$ (Si-3p/3d), 2e (Si-3d) and $7t_1$(Si-3d). The atomic orbitals shown in the parentheses are major components in each of molecular orbitals. They will be called A, T, E and TT for convenience. e and t_1 are doubly and triply degenerated. When the tetrahedra are linked, Si-Si interactions make these orbitals split. For example, Si3d-3d interactions make the E to be E_1 and E_2. It is interesting that the major features that appear in the experimental spectrum can be interpreted in this way using the $(Si_5O_{16})^{12-}$ cluster. The M-M bondings can be evaluated in this way through the detailed inspection of the ELNES. Works on oxides for transparent oxide conductors are now in progress.

6. CONCLUSION

Recent DV-Xα calculations using model clusters on transparent oxide conductors by our group are reviewed. Oxides of group 11 to 14 metals in the 4th and 5th row of the periodic table are investigated with special interests on metal-metal bondings that determine the nature of the bottom of the conduction band, thus the n-type conduction. Among binary oxides with 4th-row elements, ZnO is found to show the strongest M4s-4s interaction. It is then expected to have highest electron mobility. The interaction decreases with the increase of atomic number of cations in the same row. However, the band-gap also increases at the same time. The figure of merit as a transparent oxide conductors should therefore be determined by the balance of these two factors at least. An emphasis is placed on the use of ELNES as a tool to investigate the M-M interaction near the bottom of the conduction band. For the interpretation of the ELNES, DV-Xα calculations using model clusters have been successful for interpretation and reproduction of peaks in the spectrum.

ACKNOWLEDGMENT

This work was supported by Grant-in-Aid for General Scientific Research from Ministry of Education, Sports, Science and Culture of Japan.

REFERENCES

(1) H. Adachi, M. Tsukada, and C. Satoko, *J. Phys. Soc. Jpn.* **45**, 875 (1978).
(2) D.E. Ellis, H. Adachi, and F. W. Averill , *Surf. Sci.* **58**, 497 (1976).
(3) R. S. Mulliken, *J. Chem. Phys.* **23**, 1833 (1955).
(4) H. Coker, *J. Phys. Chem.*, **87**, 2512 (1983).
(5) I. Tanaka, M. Mizuno, and H. Adachi, *Phys.Rev.* B, **56**, 3536 (1997).
(6) M. Sone, Master thesis, Kyoto University 1999.
(7) M. Orita, H. Tanji, M. Mizuno, H. Adachi and I. Tanaka *Phys. Rev.* B **61** 1811 (2000).
(8) I. Tanaka , J. Kawai, and H. Adachi, *Solid State Commun.*, **93**, 533 (1995).
(9) I. Tanaka, T. Nakajima, J. Kawai, H. Adachi, H. Gu and M. Rühle, *Phil. Mag. Lett.* **75**, 21 (1997).
(10) I. Tanaka , and H. Adachi, *Phys. Rev.* B **54**, 4604 (1996).
(11) I. Tanaka , and H. Adachi, *J. Phys.* D **29**, 1725 (1996).
(12) H. Kanda, M. Yoshiya, F. Oba, K. Ogasawara, H. Adachi, and I. Tanaka, *Phys. Rev.* B **58**, 9693 (1998).
(13) I. Tanaka, H. Araki, M. Yoshiya, T. Mizoguchi, K. Ogasawara, and H. Adachi, *Phys. Rev.* B **60** 4944 (1999).

Prediction of change in the work functions due to stacking faults in Mg, Ti, Co, Cu and Zn

Y. Fujimoto[a)] *and M. Uda* [a,b)]

[a)] *Department of Materials Science and Engneering, Waseda University, 3-4-1 Ohkubo, Shinjuku-ku, Tokyo 169-8555, Japan.*

[b)] *Laboratory for Materials Science and Technology, Waseda University, 2-8-26 Nishi-Waseda, Shinjuku-ku, Tokyo 169-0051, Japan.*

(Received November 20, 1998)

We calculated the density of states (DOSs) of Mg, Ti, Co, Cu and Zn with stacking faults using the DV-Xα molecular orbital calculations, employing 13-atom h.c.p. and f.c.c. clusters. Here the stacking faults were prepared by mixing h.c.p. and f.c.c. structures. Our calculations predict that only Cu should show a lowering of its work function when its f.c.c. structure is contaminated with stacking faults, i.e. h.c.p. sequences, while the other metals show no change.

Keywords: DV-Xα, stacking fault, DOS, f.c.c., h.c.p.

Corresponding Author: M. Uda : muda@mn.waseda.ac.jp

ADVANCES IN QUANTUM CHEMISTRY, VOLUME 37

0065-3276/01 $35.00

1. Introduction

Electrons in a solid valence band are prevented from escaping by a potential barrier formed at the surface of the solid. Here the work function, i.e. the low energy threshold of the density of states (DOS) for the valence band is a measure of the height of this potential barrier. A large number of methods have been proposed and utilized to determine the work function[1]. The most common ones are based on thermionic emission and photoemission techniques[2]. However, experimental values obtained using any of these techniques show large variations even when the same material is being considered. This is due to differences in surface preparation and in measuring methods.

We previously measured the work functions of evaporated polycrystalline Ag, Au and Al before and after annealing at 500Å[3]. We found that annealing change the Ag work function from 4.35 to 4.64 eV, but that the Au and Al work functions remained almost unchanged; the change being from 5.38 to 5.42 eV for Au and from 4.31 to 4.29 eV for Al. The statistical deviations in the above measurements were smaller than $\pm$0.1eV. Annealing of the evaporated polycrystalline films at 350-500°C was responsible for the decrease in the number of stacking faults due to recrystallization. The DOSs of the Ag, Au and Al valence band were calculated using the discrete variational X-α (DV-Xα) molecular orbital calculation method[4], where we adopted 13-atom f.c.c. and h.c.p. clusters. Indeed the h.c.p. structure is considered to be a model structure for the stacking faults of the f.c.c. structure. Our calculations for Ag showed that the DOS of the h.c.p. cluster was situated at lower energy than the f.c.c. cluster, but the DOSs for both Au and Al were situated at almost the same energy for both clusters. This suggests that the change in the Ag work function during annealing may be due to decrease in the number of

stacking faults. In order to extend this stacking fault model, we have applied the DV-Xα method to the calculation of f.c.c. and h.c.p. clusters of Mg, Ti, Co, Cu and Zn. This should be helpful for the prediction of change in the work functions of these metals before and after annealing.

2. Calculation

We wish to compare the valence band density of states (DOS) of f.c.c. and h.c.p. metals with and without stacking faults. We therefore adopt a mixture of the f.c.c. and h.c.p. structures as a representative of the stacking fault structure of either of these structures. To calculate the DOS we summed up the squares of the coefficients of molecular orbital wave functions and convoluted the summed squares with the Gaussian of full width 0.5 eV at half maximum. For these DOS calculations we chose the metals Mg, Ti, Co, Cu and Zn. The model clusters employed here for both the f.c.c. and the h.c.p. structures were made of 13 atoms i.e., a central atom and 12 equidistant neighbor atoms. These structures are shown in Fig. 1. We reproduced the typical electronic structures in bulk materials by extracting the molecular orbitals localized only on the central atom from all the molecular orbitals which contributed - those localized on ligand atoms as well as on the central atom. To perform calculations we take the symmetry of the cluster as C_{3v}, and the number of discrete sampling points in one cluster as 4000. The lattice constants, basis sets and well potentials for these metals are summarized on Table 1.

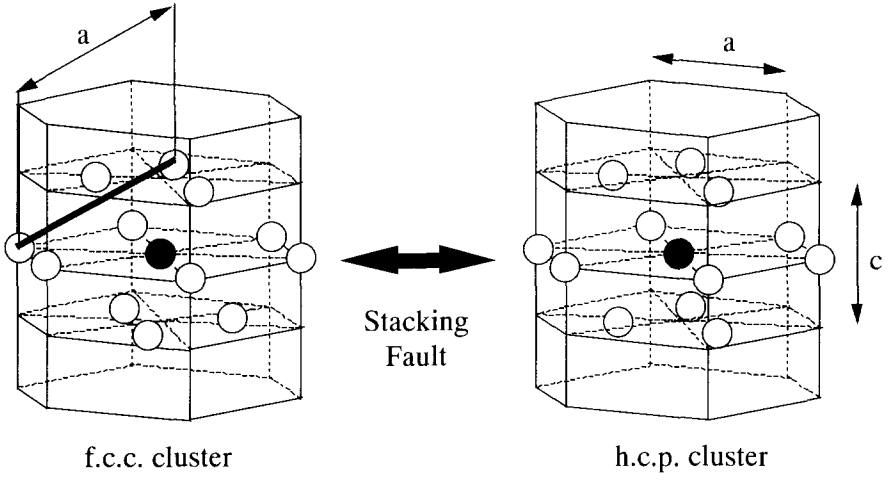

Fig.1. Model clusters for f.c.c. and h.c.p. structures

Table I. Lattice constants, basis sets and well potentials

	a ,c (Å)	basis sets	well potentials
Mg	3.21, 5.21	$1s^{-}3d$	$0.66 \times a_0$ -3.5 Hr
Ti	2.95, 4.69	$1s^{-}4p$	$0.72 \times a_0$ -3.5 Hr
Co	2.51, 4.07	$1s^{-}4p$	$0.89 \times a_0$ -2.0 Hr
Cu	3.61	$1s^{-}4p$	$0.93 \times a_0$ -2.0 Hr
Zn	2.66, 4.95	$1s^{-}4p$	$0.70 \times a_0$ -3.5 Hr

(a_0=bond length)

3. Results and Discussion

Shown in Fig. 2 (a)-(e) are the DOSs near the Fermi edge we calculated for Mg, Ti, Co, Cu and Zn. Here the mixing ratios of f.c.c. to h.c.p. structures are, for simplicity, assumed to be 1:1. For Mg, Cu and Zn, the DOSs of the f.c.c. and h.c.p. structures have different shapes, while for Ti and Co the shapes of the f.c.c. and h.c.p. DOSs are almost the same. For all the metals the DOSs for the h.c.p. structures we used are always situated at lower binding energy than the f.c.c. structure results. Mg, Cu and Zn take h.c.p., f.c.c. and h.c.p. structures, respectively, in equilibrium at room temperature. Therefore the stacking fault structures for these metals are characterized by h.c.p., f.c.c. and h.c.p. structures contaminated with f.c.c., h.c.p. and f.c.c. structures, respectively. This means that when the stacking faults are formed in these metals, the new DOS will appear at lower binding energy than the DOSs for f.c.c. Cu without stacking faults. While for Mg and Zn, the DOSs originating from the stacking faults should appear at higher binding energy than the DOSs for the h.c.p. structures without stacking faults. Then we expect, from the DV-X α molecular orbital calculation, that the Cu work function will fall when f.c.c. Cu is contaminated with h.c.p. Cu, i.e. when f.c.c. Cu is contaminated with stacking faults. However for the equilibrium h.c.p. structures of Mg, Ti, Zn and Co no change in the work function is expected when they are contaminated with the corresponding f.c.c. structures or stacking faults. Such predictions will be confirmed by experiments which are in progress.

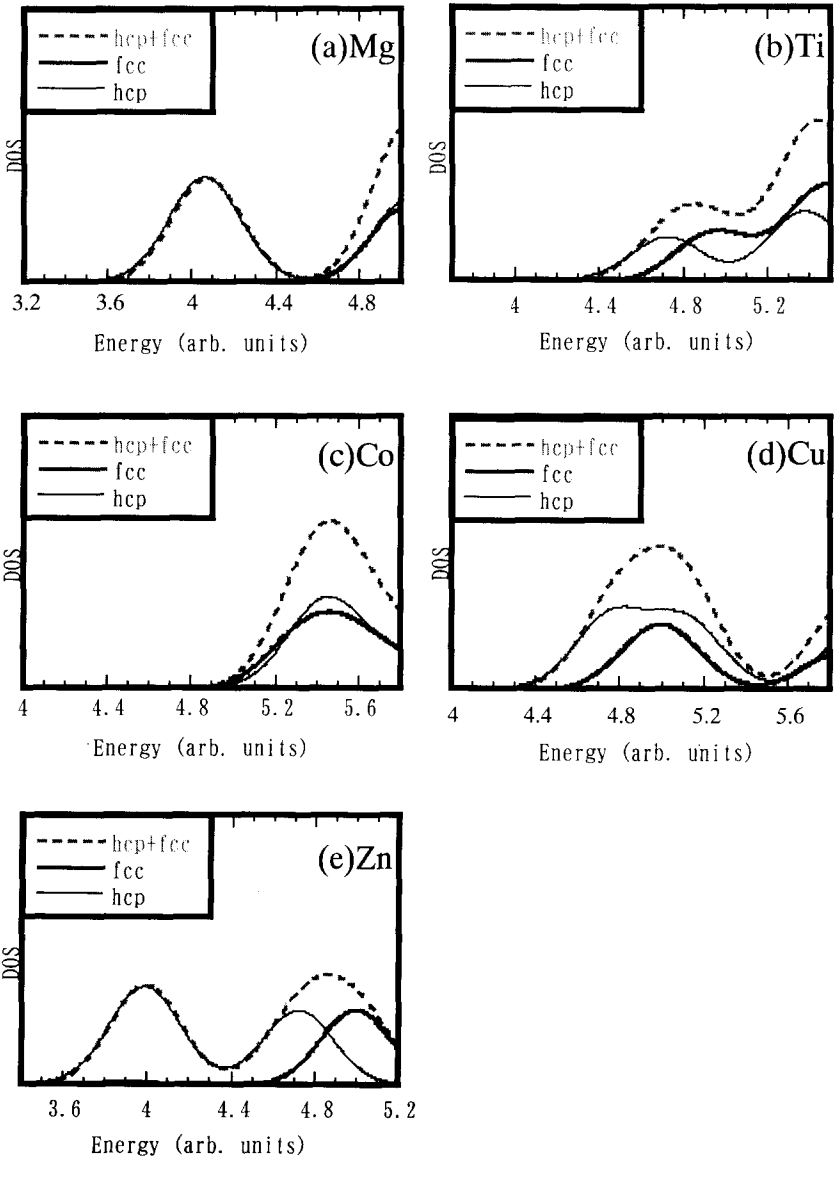

Fig.2. The calculated DOSs of (a) Mg, (b) Ti, (c) Co, (d) Cu and (e) Zn

4. Conclusion

We calculated the DOSs of Mg, Ti, Co, Cu and Zn with stacking faults using the DV-Xα molecular orbital calculation method. For all these metals the DOSs for the equilibrium h.c.p. structures were at lower energy than the corresponding f.c.c. structures. This suggests that the work function of Cu alone is expected to be lowered by formation of the stacking faults but those of the other metals remain unchanged.

References

[1] M. Cardona and L. Ley, Photoemission in Solids, Springer, Berlin, 1978, p. 19.

[2] R. H. Fowler, Phys. Rev. 38 (1931) 45

[3] M. Uda, A. Nakamura, T. Yamamoto and Y. Fujimoto, J. Electron Spectrosc. Relat. Phenom. 88-91 (1998) 643

[4] H. Adachi, M. Tsukada and C. Satoko, J. Phys. Soc. Jpn. 48 (1978) 875

Analysis of chemical bond in metal clusters: I. Alkali metal and alkaline earth metals

Rika Sekine* and Kumiko Tanaka

Department of Chemistry, Faculty of Science, Shizuoka University, 836 Ohya, Shizuoka, 422-8529 Japan.

Jun Onoe and Kazuo Takeuchi

The Institute of Physical and Chemical Research (RIKEN), 2-1 Hirosawa, Wako, Saitama, 351-0198 Japan.

Hirohide Nakamatsu

Institute for Chemical Research, Kyoto University, Uji, Kyoto, 611-0011, Japan.

(Received November 30, 1998)

We have performed molecular orbital calculations for small alkali metal (AM) and alkaline earth metal (AE) clusters, using a density-functional method. We found that tetramers of AM (Li_4, Na_4, and K_4) which take a rhombus (Rh) structure are energetically stable, while those of AE (Be_4, Mg_4, and Ca_4) prefer a tetrahedral (Td) structure. Analysis of the chemical bonding indicates that the AM tetramers are formed mainly by *s-s* and *s-p* bonding interactions, while in the AE tetramers *s-s* is antibonding and the *s-p* and *p-p* bonding interactions are larger. Charge distributions show that the AM tetramers have three-center bonding, while the AE clusters have a two-center character. A comparison between molecular orbital correlation diagrams for the Rh and Td geometries clarified the main factor in the determination of the AM and AE tetramers geometries.

KEYWORDS: alkali metal, alkaline earth metal, chemical bond, cluster, structure optimization

*Corresponding author: e-mail scrseki@ipc.shizuoka.ac.jp

ADVANCES IN QUANTUM CHEMISTRY, VOLUME 37

0065-3276/01 $35.00

1. INTRODUCTION

There are many reports concerning metal clusters in a variety of fields such as physics, chemistry, and engineering (1-3). The metal clusters are found to exhibit some properties which are different from those of the bulk material, for example bond length (4), ionization energy (1), magnetic moment (5), and so on. One of the most interesting features of the metal clusters is their geometrical structure which is often different from the bulk structure.

Many theoretical and experimental studies of the geometrical structure of alkali metal (AM) and alkaline earth metal (AE) clusters have been made (6-24). The geometric structures of sodium clusters have been investigated thoroughly and found to be isosceles triangle for Na_3 (6-9), rhombus for Na_4 (6-12), trapezoid for Na_5 (6,8,9,12), and bitriangle (D_{3h}) or pentagonal pyramid (C_{5v}) for Na_6 (6,8,9,12). Lithium and potassium clusters as far as the hexamers have geometries similar to those of Na clusters (6,7,10,11,13,14). On the other hand, magnesium clusters have structures different from those of the alkali metal clusters. The structure of Mg clusters are an equilateral triangle for Mg_3 (15-17), a tetrahedron for Mg_4 (15-20), a trigonal bipyramid for Mg_5 (15-17), and a square bipyramid or an octahedron for Mg_6 (16). Other AE clusters such as beryllium and calcium as far as the hexamers have structures similar to those of the corresponding Mg clusters (15,18,20-24).

The differences in the stable geometries of the AM and AE clusters have been investigated from the electronic structure view point. Ekhardt and Penzar, using a self-consistent jellium model, reported a more stable prolate structure than the spherical one for Na_4 (25). The model placed four valence electrons of the Na_4 cluster into a spherical potential. Two electrons occupy the $1s$ shell in the spherical potential and the other two electrons are accommodated in the $1p$ shell. Prolate distortion splits the $1p$ levels and then the lowered $1p_z$ level is filled with two electrons. Therefore, the Na_4 cluster prefers the prolate deformation. Using a molecular orbital method, Rao and Jena came to a conclusion which is consistent with the jellium results (13). The Li_4 cluster adopts a planar structure while the Be_4 cluster has a close packed structure since the latter cluster has eight valence electrons and the molecular orbitals corresponding to the $1p$ shell for the jellium model are completely filled with the electrons.

In this paper, we explain the stability of the AM and AE tetramers using molecular orbital energy correlation diagrams between the planar and close packed geometries. The relationship between the character of the highest occupied molecular orbitals and the shape of the cluster will be discussed. We focus our attention on differences in the charge distribution and in the nature of the chemical bonding. To this end, we will analyze charge distributions and orbital overlap populations.

2. COMPUTATIONAL METHOD

2.1. Structure Optimization

We optimized the structures of AM (Li, Na, K) and AE (Be, Mg, and Ca) tetramers, using a program package from the Amsterdam Density Functional (ADF) (26). We described the electronic states of the clusters with a triple-ζ Slater-type orbital (STO) basis set. With the exception of K and Ca, polarization functions were included in the basis set. For Li, Na, Be and Mg the $1s$ orbitals were treated with the frozen core approximation. For K and Ca, the $1s \sim 2p$ shells were regarded as the frozen core.

The interatomic distances for the tetramers were optimized for the tetrahedral geometry, however both the interatomic distances and angles changed within the rhombic structure. The structure optimization algorithm was based on a quasi Newton approach (29), using the Hessian of the total energy for computing changes in the geometry so as to make the Hessian vanish. The bonding energy was computed, using the transition state method, as the energy of the cluster minus the energy of the constituent atoms (30,31).

2.2. Analysis of chemical bonding

In order to elucidate the contribution of the individual atomic orbitals to the chemical bonding in the metal clusters, we used the discrete-variational (DV) Xα molecular orbital method (32). We used a code (33) where the molecular wavefunctions were expressed as a linear combination of atomic orbitals. The basis functions were obtained by numerically solving the Hartree-Fock-Slater equations in the atomic-like potentials derived from the spherical average of the molecular potential around the nuclei. Thus the atomic orbitals used as the basis functions were automatically optimized in the molecular potential (33). For this reason, the DV-Xα method was used to analyze the role of the individual atomic orbitals in chemical bonding (34,35). The ADF method introduced in the previous section makes use of the triple-ζ Slater-type orbital basis. This type of basis set is not suitable for analyzing chemical bonding, since the correspondence to the atomic orbitals is complicated. The computational details of the DV-Xα method have been described in Ref. 33.

Chemical bonds between atomic orbitals were extracted with the Mulliken population analysis (36). This analysis is useful for the qualitative discussion of chemical bonding of a series of similar molecules, and has been widely used. In population analysis, the bond overlap population $P_B(k,l)$ for a specific pair of atoms k and l in a polyatomic molecule is defined as

$$P_B(k,l) = \Sigma_{(i)} \Sigma_{(r,s)} 2N_{(i)} C^k_{ir} C^l_{is} \langle \phi^k_r | \phi^l_s \rangle, \qquad (1)$$

where $N_{(i)}$ denotes the occupation number of the electrons in the *i*th MO. The quantities C^k_{ir} and C^l_{is} represent respectively the coefficients of the normalized atomic orbitals ϕ^k_r and ϕ^l_s, in the linear combination of the atomic orbitals for the *i* th MO. Similarly, the orbital overlap population $P_O(k,r,l,s)$ for the atomic orbitals ϕ^k_r and ϕ^l_s is also defined as

$$P_O(k,r,l,s) = \Sigma_{(i)} 2N_{(i)} C^k_{ir} C^l_{is} <\phi^k_r \mid \phi^l_s>. \quad (2)$$

The basis functions used were $1s\sim2p$ for Li and Be, $1s\sim3p$ for Na and Mg, and $1s\sim4p$ (without $3d$) for K and Ca. All the DV-Xα calculations were performed with the Slater exchange parameter α of 0.7.

In order to estimate multi-center bonds in the rhombic (Rh) and tetrahedral (Td) AM and AE tetramers, we mapped the charge density distributions of the metal clusters. This analysis compensates for a shortcoming of the Mulliken population analysis, where the analysis estimates only one- and two- center charge distributions. We therefore examined the charge redistribution on the formation of the chemical bonds. We used the differential charge density Δρ defined as

$$\Delta\rho = \rho(\text{cluster}) - \rho(\text{atom}), \quad (3)$$

where ρ(cluster) means the charge density for the cluster and ρ(atom) means the sum of spherically averaged charge densities for neutral atoms positioned the same as in the cluster.

3. RESULTS AND DISCUSSION

3.1. Geometrical structure

Figure 1 shows Rh and Td tetramer structures examined using ADF. The interatomic distances, r_{11}, r_{12} and r were optimized for the AM and AE tetramers and the results are summarized in Table I (a). By looking at the bonding energy (B.E.) we can see that AM tetramers take up the 2-D

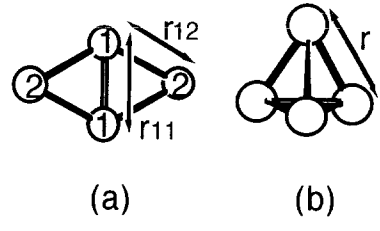

Fig 1. Tetramer structure investigated: (a) rhombus (Rh) and (b) tetrahedron (Td). Optimized values of r_{11}, r_{12}, and r are summarized in Table I (a).

rhombus structure as the energetically most stable structure, rather than the 3-D tetrahedral structure. On the contrary, AE clusters prefer the 3-D tetrahedral structure to the 2-D rhombus. These results, which were obtained using ADF, are consistent with previously reported results (6-24).

Table I (a). Optimized geometries for alkali metal and alkaline earth metal tetramers [present work]

		Rhombus (Rh)					Tetrahedron (Td)		
		B.E.	r_{12}	r_{11}	r_{12}/r_b	r_{11}/r_b	B.E.	r	r/r_b
AM	Li_4	-3.72	3.08	2.64	99%	85%	-3.02	3.02	97%
	Na_4	-2.73	3.30	2.95	86%	77%	-2.01	3.36	88%
	K_4	-2.06	4.60	4.19	97%	88%	-1.53	4.70	99%
AE	Be_4	-2.49	2.27	2.10	100%	93%	-4.40	2.11	93%
	Mg_4	-0.87	3.33	3.05	104%	95%	-1.52	3.18	99%
	Ca_4	-0.81	4.35	4.22	110%	107%	-1.28	4.09	103%

B.E.: Bonding Energy [eV], r_{11}: diagonal bond length [Å], r_{12}, r: side bond length [Å], r/r_b: ratio of bond length for cluster to that for bulk r_b.

The distances r_{11} and r_{12} in Table I (a) correspond to the diagonal bond length and the side bond lengths, respectively, for the rhombus shown in Fig. 1(a). The tetrahedron has only one structural parameter, r [see Fig. 1(b)]. For the AM clusters with the Rh structure, the side bond lengths r_{12} were estimated to be 3.08 Å for Li_4, 3.30 Å for Na_4, and 4.60 Å for K_4. These results are in good agreement with the previously reported values of 2.94-3.18 Å for Li_4 (7,10,11,13,14), 3.28-3.74 Å for Na_4 (6-11), and 4.42-4.91 Å for K_4 (6,7,10), which are summarized in Table I (b). For the diagonal bond lengths (r_{11}) we obtained 2.64 Å for Li_4, 2.95 Å for Na_4, and 4.19 Å for K_4. These results agree well with the reported values of 2.61-2.75 Å for Li_4 (7,10,11,13,14), 2.91-3.44 Å for Na_4 (6-11), and 3.92-4.46 Å for K_4 (6,7). For the AE clusters with the Td structure, the bond lengths (r) we obtained are 2.11 Å for Be_4, 3.18 Å for Mg_4, and 4.09 Å for Ca_4. These are also in good correspondence with the reported values of 2.06-2.10 Å for Be_4 (15,18,21,23), 2.97-3.39 Å for Mg_4 (15,16,18-20), 4.02-4.29 Å for Ca_4 (18,20,22).

The values r_{11}/r_b, r_{12}/r_b, and r/r_b, which are the bond lengths normalized by r_b, are also shown in Table I (a), where r_b represents the bond length for the

bulk structure. Excepting Ca_4, the stable structures for these tetramers have shorter bond lengths than those for the bulk.

In these results discussed above, we have found some remarkable differences in the stable geometries of the AM and AE tetramers. Why do AM tetramers prefer the Rh structure to the Td structure? Why do AE tetramers prefer the Td structure to the Rh structure? Next, we examine how the bond nature differs in AM and AE tetramers.

Table I (b). Optimized geometries for alkali metal and alkaline earth metal tetramers. [previous works]

	Rhombus (Rh)				Tetrahedron (Td)	
	r_{12}	r_{11}	ref.		r	ref.
Li_4	2.94	2.61	13	Be_4	2.06	15
	3.08	2.75	10		2.07	18
	3.09	2.61	7		2.08	23
	3.16	2.69	14		2.10	21
	3.18	2.69	11			
Na_4	3.28	2.91	9	Mg_4	2.97	16
	3.44	3.44	6		3.19 ~ 3.23*	18
	3.48	3.00	10		3.23	15
	3.53	3.10	7		3.33~3.39*	19
	3.68	3.21	11		3.39	20
	3.74	3.25	8			
K_4	4.42	3.92	7	Ca_4	4.02 ~ 4.20*	22
	4.46	4.46	6		4.16 ~ 4.19*	18
	4.91	---	10		4.29	20

r_{11}: diagonal bond length [Å], r_{12}, r: side bond length [Å].
*values depend on the basis set used.

3.2. Bond nature of AM and AE tetramers

In this section, we discuss the way the chemical bonds in the AM and AE tetramers differ in terms of bond overlap populations (P_B). In the discussion in the following sections B~D, we use the DV-Xα method. Table II shows P_B for the tetramers with the Rh and Td geometries, where the values are normalized by dividing by the number of bonds. Comparison of Tables I (a) and II shows that energetically more stable structures have larger P_B values. This indicates that P_B is a good indicator of the strength of the chemical bonding.

Table II. orbital overlap population (P_O) for alkali metal and alkaline earth metal tetramers

		Rhombus (Rh)								
	P_B	P_O								
		s-s			s-p			p-p		
		r_{11}	r_{12}	av	r_{11}	r_{12}	av	r_{11}	r_{12}	av
Li_4	0.466	0.226	0.114	0.136	0.206	0.286	0.270	0.164	0.034	0.060
AM Na_4	0.392	0.286	0.128	0.160	0.158	0.222	0.210	0.070	0.012	0.024
K_4	0.294	0.214	0.096	0.120	0.106	0.168	0.156	0.046	0.012	0.018
Be_4	0.322	-0.542	0.016	-0.096	0.554	0.224	0.290	0.272	0.092	0.128
AE Mg_4	0.196	-0.244	-0.158	-0.174	0.484	0.294	0.332	0.052	0.034	0.038
Ca_4	0.182	-0.124	-0.084	-0.092	0.278	0.242	0.250	0.032	0.022	0.024

		Tetrahedron (Td)			
		P_B	P_O		
			s-s	s-p	p-p
	Li_4	0.424	0.096	0.246	0.084
AE	Na_4	0.076	-0.136	0.184	0.028
	K_4	0.076	-0.050	0.118	0.008
	Be_4	0.376	-0.220	0.412	0.184
AE	Mg_4	0.234	-0.156	0.328	0.062
	Ca_4	0.228	-0.094	0.272	0.050

P_B: overlap population per bond, P_O: orbital overlap population per bond.
r_{11}: diagonal pair, r_{12}: side pair,
av: average, where $av = \{P_O(r_{11}) + 4\,P_O(r_{12})\} / 5$

As shown in eq. (2), P_B is divided into contributions P_O from the individual interactions between the valence atomic orbitals. Table II shows P_O for the *s-s*, *s-p*, and *p-p* atomic orbital pairs for the metal clusters. The Rh tetramers have two kinds of bonds; one is the diagonal bond (r_{11}) and the other is the side bond (r_{12}). The average value, $P_O(av)$, for the Rh tetramers, was estimated as $\{P_O(r_{12}) + 4P_O(r_{11})\}/5$. For the AM tetramers, $P_O(av)$ for the *s-p* interaction is larger than that for the *s-s* and *p-p* orbital interactions, and the *p-p* interaction is very weak for both the Rh and Td geometries. For the Rh geometry, the *s-s* interaction is strong for the diagonal pairs r_{11}. For the AE clusters, the P_O values for the *s-s* pairs are negative, except for r_{12} of Be_4, in contrast to the results for the AM tetramers. A negative P_O value means that antibonding interaction. These *s-s* antibonding interactions for the AE tetramers can be explained from the fact that AE metals have the $(s)^2$ valence

configurations and do not provide enough vacant *s* states to make bonding orbitals. On the other hand, the P_O values for the *s-p* pair interactions are large. Furthermore, the P_O values for the *p-p* pair interactions are not as small as those for the AM clusters in the same row in the periodic table.

For the AM tetramers, we find that the P_O values of the *s-s* interaction decrease markedly in going from the Rh to Td geometries, while those for the *s-p* and *p-p* interactions change only a little between these geometries. Accordingly, for the AM tetramers, the *s-s* antibonding contribution is determinant in avoiding the Td geometry. In the AE tetramers, the *s-p* and *p-p* bonding interactions increase markedly going from Rh to Td, exceeding the increase in the *s-s* antibonding interaction. We find that the *s-p* and *p-p* interactions are both dominant factors for determination of the geometry of the AE tetramers. Furthermore, we conclude from this discussion that the difference in the bonding character between AM and AE clusters originates from the *p* contribution, which is produced by the promotion of electrons from *s* orbitals.

3.3. Analysis of Charge Distribution

Although the Mulliken population analysis is useful for the discussion of two-center bonding, it is not sufficient for the description of the three- or four-center bonds that may exist in metal clusters. In order to elucidate the multi-center bonds, we examine contour maps of the charge densities of Na_4 and Mg_4 as typical tetramers of AM and AE, respectively. We use the differential charge density, $\Delta\rho$ defined by eq. (3)., to express the charge redistribution on the formation of chemical bonds.

First, we examine Na_4 on the basis of the $\Delta\rho$ plots. Figures 2(a)~(e) show the contour map and its cross sections for the differential charge density of Na_4 with Rh structure. Figure 2A (a) describes the structure of the Rh cluster. The point X is the midpoint between atoms "1" and "2". The point where the 2-2 and 1-X lines cross is shown as a hatched circle. Figure 2A (b) shows the $\Delta\rho$ contour map in the Na_4 rhombus plane. In this plot darker colors represent higher values of $\Delta\rho$. Figures 2A (c), (d), and (e) show the $\Delta\rho$ values in the 1-X direction, the 1-2 direction, and the 1-1 direction, respectively. Figures 2B (f)~(k) show contour maps, together with the corresponding sectional views, for the charge density of Na_4 with Td structure. In Fig. 2B(f), one side of the tetrahedron is along the X-axis. The point M is the midpoint between the atoms. The $\Delta\rho$ contour maps of one of triangles [Fig. 2B(g)] and of the XZ plane [Fig. 2B(h)] are shown. Figures 2B(i), (j), and (k) show the $\Delta\rho$ values in the X, Z, and 1-M directions, respectively. Here the symbol "1" indicates the two atoms which are out of the Z-X plane.

For Rh, the largest value of $\Delta\rho$ is 0.0038 [e/au^3]. This is at the triangle's center of gravity point, marked with the hatched circle in Figs. 2A(b) and (c).

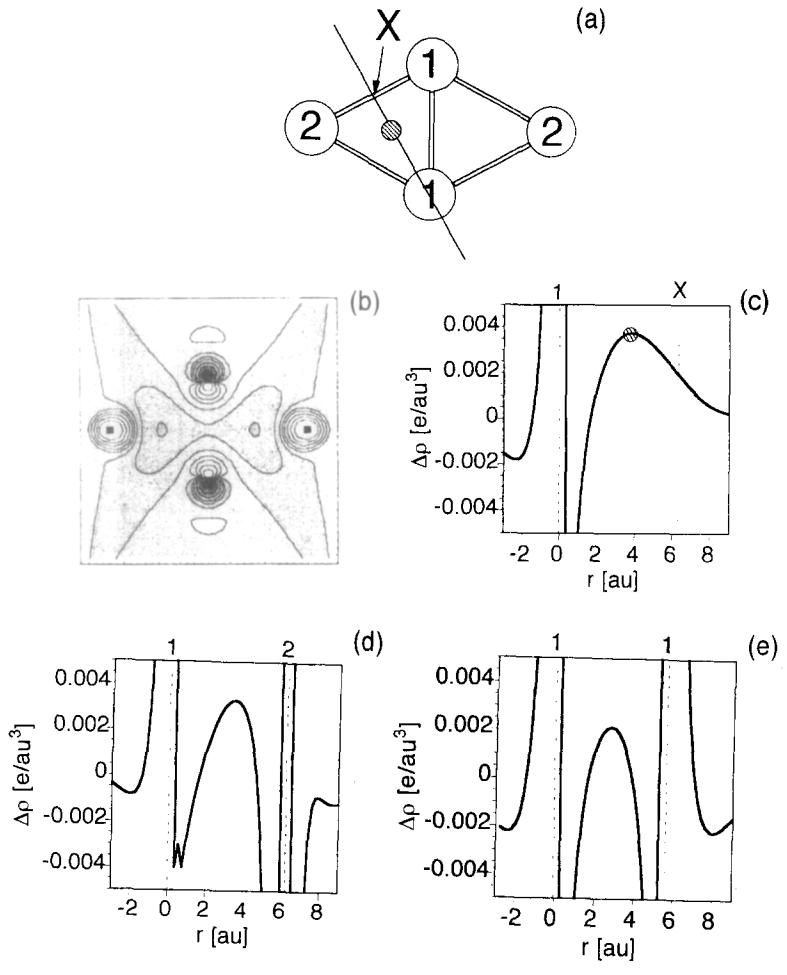

Fig 2A. Contour maps of $\Delta\rho$ and the corresponding sectional views for Na_4 in Rh. (a) structure of Rh cluster, (b) $\Delta\rho$ contour map in the rhombus plane, (c) $\Delta\rho$ in the 1-X direction, (d) the 1-2 direction, and (e) the 1-1 direction.

The values of $\Delta\rho$ found along the interatomic line are smaller than the value found at the center of the triangle; the values at the midpoint between the atoms 1-2 and 1-1 are 0.0033 [e/au^3] and 0.0021 [e/au^3], respectively, as shown in Figs. 2A(d) and (e). Figures 2B(h) and (j) show that, for Td, $\Delta\rho$ takes its highest value of 0.0027 [e/au^3] at the center of gravity of the tetrahedron. The

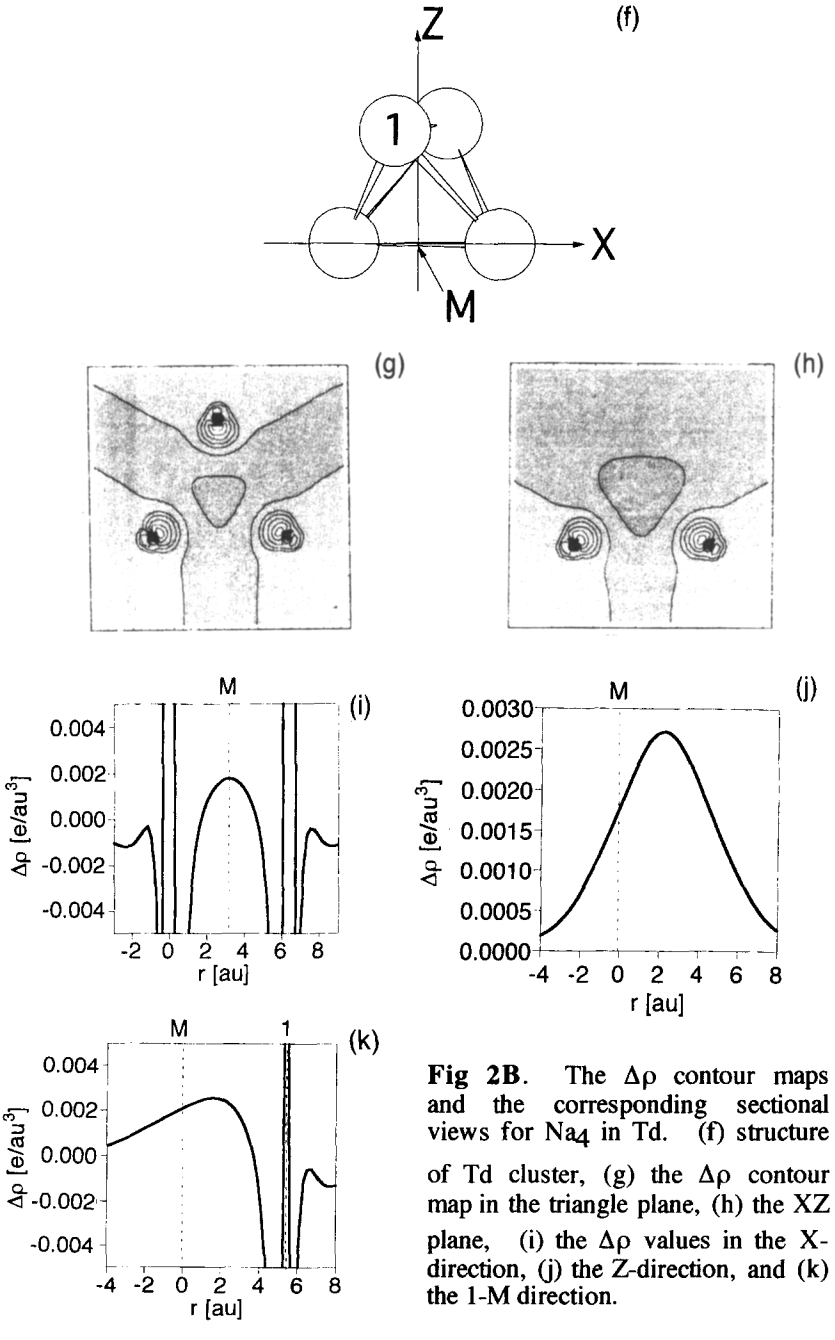

Fig 2B. The Δρ contour maps and the corresponding sectional views for Na_4 in Td. (f) structure of Td cluster, (g) the Δρ contour map in the triangle plane, (h) the XZ plane, (i) the Δρ values in the X-direction, (j) the Z-direction, and (k) the 1-M direction.

value at the center of gravity of the triangle is smaller [0.0026, Fig. 2B(k)] and the value at the midpoint between the atoms 1-1 is smaller still [0.0018, Fig. 2B(i)]. Consequently, in the sense of $\Delta\rho$ maximization, the Na_4 cluster makes stronger bond in the Rh geometry than in the Td geometry.

We next study Mg_4 which favors the Td geometry. Figure 3 shows contour maps, and their cross sections, for the charge densities of Mg_4 in both the Rh and Td structures. The cross sections and axes for the plots are the same as those for the Na_4 clusters. That is, Fig 3A(a)~(d) and Fig 3B(e)~(i) correspond to Fig 2A(b)~(e) and Fig 2B(g)~(k), respectively. The $\Delta\rho$ value at the center of gravity of the Rh triangle of is 0.0013 [e/au^3], as shown in Fig. 3A(b). On the other hand, the $\Delta\rho$ value at the 1-1 middle point is 0.0014 [e/au^3] [Fig 3A(d)], which is slightly larger than the value at the center of gravity.

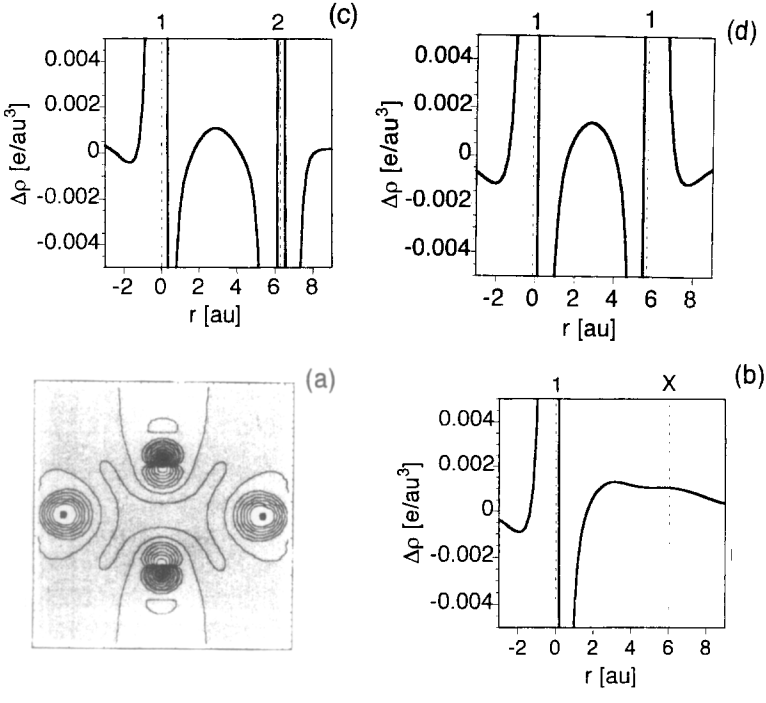

Fig 3A. Contour maps of $\Delta\rho$ and the corresponding sectional views for Mg_4 in Rh. (a) $\Delta\rho$ contour map in the rhombus plane, (b) $\Delta\rho$ in the 1-X direction, (c) the 1-2 direction, and (d) the 1-1 direction. The structure of the Rh cluster is the same as shown in Fig. 2A(a).

Consequently, Mg_4 has a more two-centered bond character than Na_4. For Td, the highest value $\Delta\rho$ is obtained is 0.0018 [e/au^3] at the midpoint (M) of the side of the Mg_4 cluster [Figs 3B(g), (h), and (i)]. Accordingly, Mg_4 also tends to form two-center bonds in the Td geometry, which are clearly seen in Figs 3B(e) and (f). Since the two-center bonds in the Rh and Td geometries do not differ greatly in strength, a larger number of atomic pairs is required to achieve a more stable cluster. For tetramers the maximum number of pairs is six, and this is attained in the Td geometry.

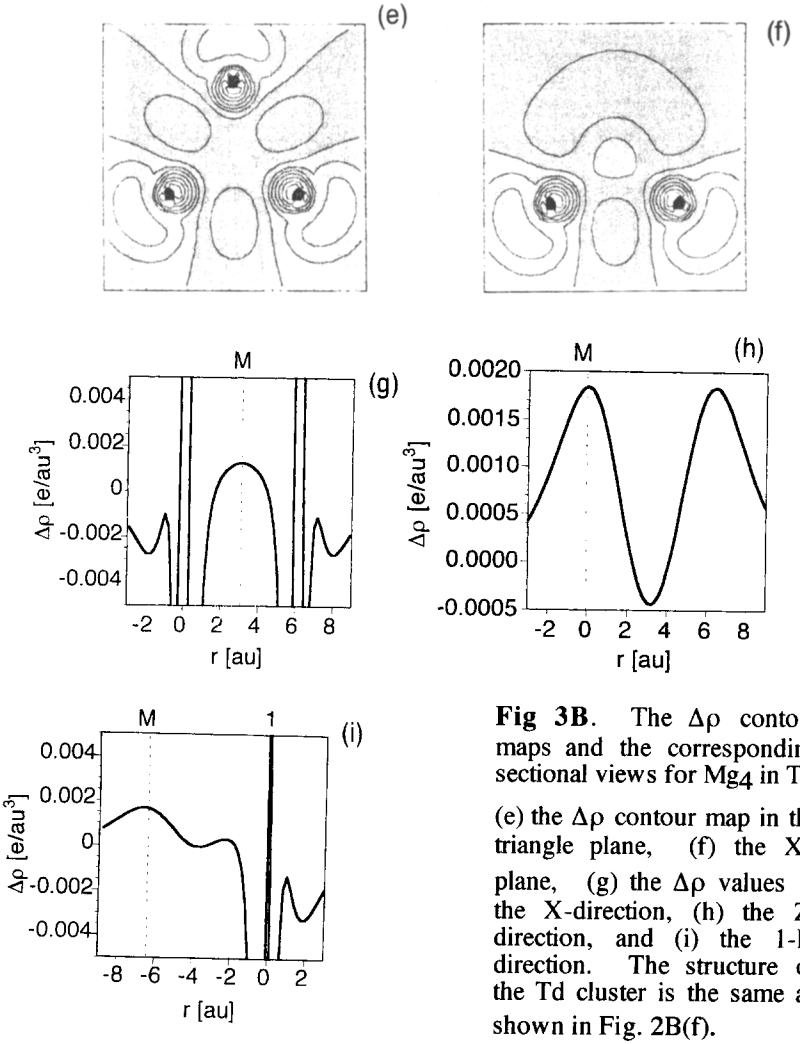

Fig 3B. The $\Delta\rho$ contour maps and the corresponding sectional views for Mg_4 in Td. (e) the $\Delta\rho$ contour map in the triangle plane, (f) the XZ plane, (g) the $\Delta\rho$ values in the X-direction, (h) the Z-direction, and (i) the 1-M direction. The structure of the Td cluster is the same as shown in Fig. 2B(f).

3.4. Molecular Orbital Correlation between Rh and Td

In this section, we analyze the stable geometries for the Na_4 and Mg_4 clusters, using molecular orbital (MO) correlation diagrams interpolating between geometries. Structure deformation is often correlated with symmetry breaking, *e.g.* the Jahn-Teller effect (37), which stabilizes the electronic structures of metal clusters.

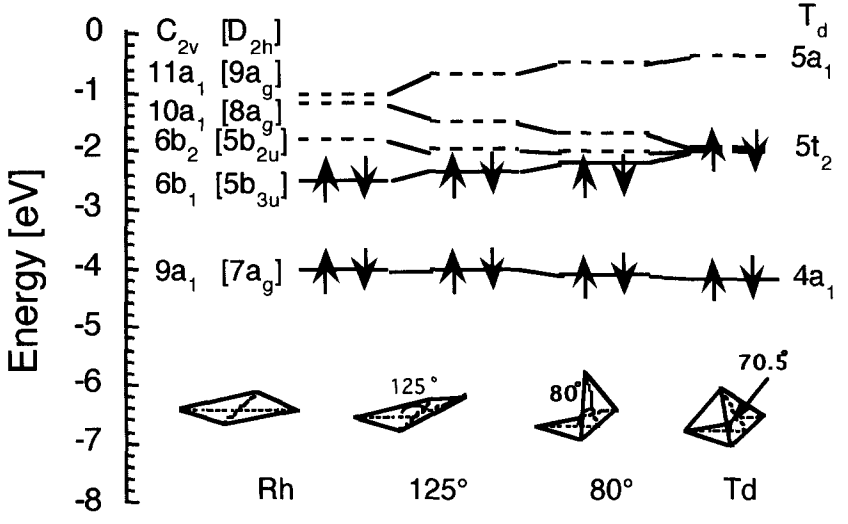

Fig 4. Molecular orbital correlation diagram interpolating between Rh and Td for Na_4. Names of MOs for C_{2v} and D_{2h} are indicated on the left side, while those for Td are on the right side.

Figures 4 and 5 show the molecular orbital diagrams for the Na_4 and Mg_4 clusters, respectively. The dihedral angle θ between two triangles changed from 180° (Rh) to 70.5° (Td). We examined MOs with θ=180°, 125°, 80° and 70.5° for Na_4, while for Mg_4 we examined those with θ=180°, 125°, and 70.5°. In the present diagrams, the side and diagonal bond lengths were fixed at 3.33 Å for Na-Na and 3.26 Å for Mg-Mg. These were averages of the bond lengths in the Td and Rh geometries. We assumed C_{2v} symmetry for all the structures. The irreducible representations of individual MOs of C_{2v} and of D_{2h} are

displayed on the left side. Those of Td are also shown on the right side. AM has $[RE](s)^1$, while AE has the $[RE](s)^2$ configuration, here [RE] denotes the electronic configuration of the noble gases. Thus Na_4 has four valence electrons while Mg_4 has eight.

Figure 4 shows that the $6b_1$ and $9a_1$ MOs in the C_{2v} expression are occupied and that there is a distinctive energy gap (0.70 eV) between the highest occupied MO (HOMO) $6b_1$ and the lowest unoccupied MO (LUMO) $6b_2$ for the Rh Na_4 cluster. As the θ value decreases, this energy gap becomes narrower and reaches zero at θ=70.5° corresponding to the Td structure. The $10a_1$, $6b_2$, and $6b_1$ MOs of the Rh geometry degenerate into the 5t2 MO of the Td geometry. This triply degenerate MO is partially occupied

The stability of Mg_4 with Td geometry can be explained on the basis of the MO diagram shown in Fig 5, which is drawn in a manner similar to that for Na_4. The Mg_4 cluster has eight valence electrons and these electrons occupy the $4a_1$ and $5t_2$ MOs of the Td geometry. The energy gap between the HOMO and the LUMO becomes smaller as θ increases. The $4a_1$ level at -7.3 eV for the Td geometry is shifted to -6.6 eV for the Rh geometry.

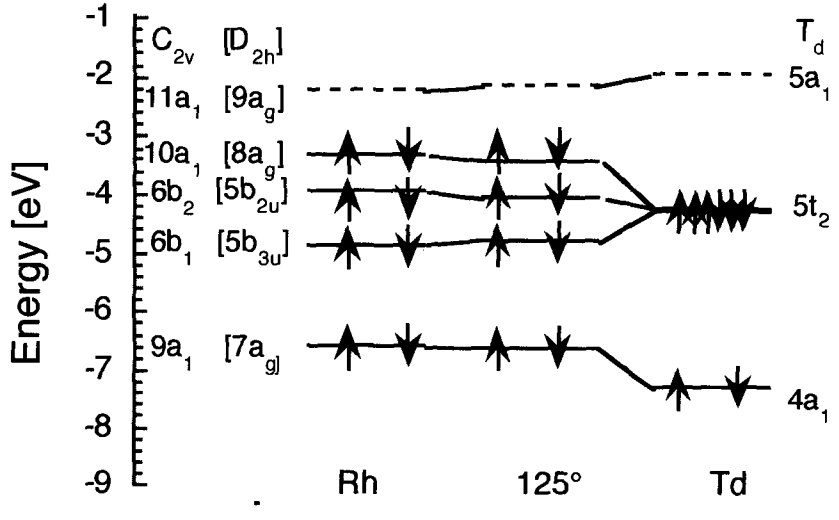

Fig 5. Molecular orbital diagrams for Mg_4. Names of MOs for C_{2v} and D_{2h} are indicated on the left side, while those for Td are on the right side.

To clarify the MO characters, Fig 6 shows contour maps of the wavefunctions for (a) HOMO $10a_1$, (b) the second highest MO below HOMO, $6b_2$, and (c) the third HOMO $6b_1$ for Mg_4 with the Rh geometry. These MO notations refer to the C_{2v} point group (see Fig 5). The atomic arrangement used here is shown in Fig 6 (d). These three MOs shown in Fig 6 are all occupied for Mg_4. The third HOMO b_1 is antisymmetric with respect to the YZ-plane, as shown in Fig 6 (c). When the rhombus is folded into the tetrahedron, the atoms in the XZ-plane approach each other. These atoms cannot make a bonding orbital since they have opposite phases. However, the HOMO $10a_1$ makes a bonding orbital between these atoms in the XZ-plane when the rhombus is folded about the Y-axis. With regard to the second HOMO $6b_2$, in the Td geometry the atoms in the XZ-plane make a weak bonding orbital, and the energy slightly decreases as shown in Fig 5.

The origin of the Rh geometry preference in Na_4 is attributed to the stabilized $6b_1$. The three levels $10a_1$, $6b_2$, and $6b_1$ are occupied in Mg_4 and the stabilization of $6b_1$ is canceled out by the destabilization of$10a_1$. The center of gravity of these three levels is lowered in the Td geometry. The other occupied levels, including $4a_1$ [in Td notation] become lower and stabilize the Td geometry. The closed structure of Td is attributed to the lowering of these levels because the overlap of the potentials of the constituent atoms produces the most stable molecular potential.

The molecular orbital correlation diagram can be connected to the jellium model (25). For example, the $1p_Z$ and $1p_{X,Y}$, subshells in the jellium model are correlated with the $6b_1$ (C_{2v} notation), $6b_2$, and $10a_1$ in the MO diagram. The X axis in the present work corresponds to the Z axis in the jellium model. Therefore the molecular orbital calculation gives essentially the same picture as the jellium model, with regard to the AM and AE clusters. The present work also gives a direct view of these molecular orbitals, as was shown in Fig 6.

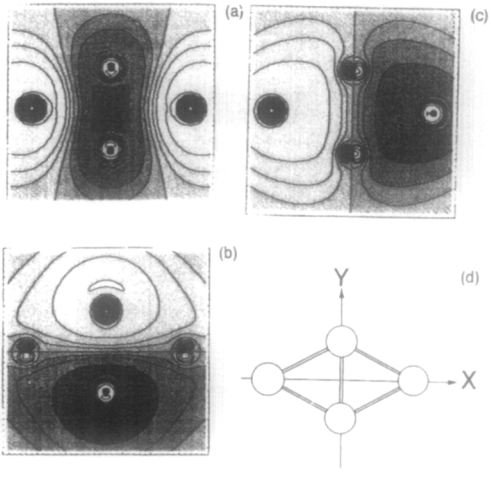

Fig 6. Contour maps: for the highest occupied molecular orbitals of Mg_4 in Rh in the rhombus plane. (a) the highest MO $10a_1$, (b) the second highest MO $6b_2$, and (c) the third highest MO $6b_1$, (d) structure of the Rh cluster.

4. SUMMARY

In order to clarify differences in bond nature between the AM and AE tetramers, we examined the electronic structures of Li_4, Na_4, K_4, Be_4, Mg_4, and Ca_4 tetramers. We found the energetically optimal structures for the tetramers using ADF. The rhombus geometry is stable for the AM tetramers, while the tetrahedral one is stable for the AE tetramers.

The stability of the AM and AE clusters can be explained from molecular orbital correlation diagrams, which are produced by changing the dihedral angle from 180° (Rh) to 70.5° (Td). For Mg_4, the three-fold degenerate $5t_2$ MO is the HOMO and it is fully occupied in the Td symmetry. The charge distribution is thus spherical for this cluster. On the other hand, Na_4 has fewer electrons than Mg_4 and prefers an anisotropic charge distribution. As a result the Na_4 cluster is stabilized by being distorted into D_{2h} (Rh) symmetry. Actually, we clarify the fact that the Na_4 HOMO is antisymmetric with respect to the folding plane. Therefore, the approach of the two atoms at the two apexes of the rhombus is not favorable for Na_4 but is favorable for Mg_4. These conclusions, derived from the correlation diagrams, are consistent with those obtained from the jellium model.

The cluster geometries were related to the interactions between atomic orbitals. The AM and AE tetramers orbital interactions were examine using the Mulliken overlap population analysis. The *s-s* antibonding contribution is the main factor that allows the AM tetramers to avoid the Td closely packing geometry. On the other hand, for the AE tetramers, the large *s-p* and *p-p* bonding interactions stabilize the tetrahedral geometry. This difference in the bonding character in the AE clusters arises from the increase of the *p* contribution. This *p* contribution originates from the promotion of *s* orbital electrons, which form a closed shell in an isolated AE atom.

Charge density distribution analysis revealed the multi-center bonding character of the *s*-orbitals. The Na_4 cluster is bound with three-center (and four-center) bonds. The charge density at the center of gravity is larger in the Rh geometry than in the Td geometry. For Mg_4, the atoms are connected by two-center bonds. These bonds are constructed mainly from the *p*-orbitals which have bonding directions. The necessary condition, which results in the Td geometry, is obtaining the maximum amount of two-center bonding,.

ACKNOWLEDGMENT

This work is supported partly by Grant-in-Aid for Scientific Research No. 08640735 from the Ministry of Education, Science and Culture, Japan and also partly by The Research Grant for Women from Esso Sekiyu KK.

REFERENCES

(1) de Heer, W. A.; *Rev. Mod. Phys.* **1993**, *65*, 611.
(2) Brack, M.; *Rev. Mod. Phys.* **1993**, *65*, 677.
(3) Haberland, H., Ed.; "*Clusters of Atoms and Molecules*"; Springer-Verlag: Berlin, 1994.
(4) Kimura, K.; *Phase Transitions* **1990**, *24-26*, 493.
(5) Billas, I. M. L.; Châtelain, A.; de Heer, W. A.; *Science*, **1994**, *265*, 1682.
(6) Spiegelmann, F.; Pavolini D.; *J. Chem. Phys.* **1988**, *89*, 4954 .
(7) Flad, J.; Igel, G.; Dolg, M.; Stoll, H.; Preuss, H.; *Chem. Phys.* **1983**, *75*, 331.
(8) Bonac˘ic´-Koutecky´, V.; Fantucci, P.; Koutecky´, J.; *Phys. Rev. B* **1988**, *37*, 4369.
(9) Martins, J. L.; Buttet, J.; Car, R.; *Phys. Rev. B* **1985**, *31*, 1804.
(10) Pacchioni, G.; Beckmann, H-O; Koutecky´, J.; *Chem. Phys. Lett.* **1982**, *87*, 151.
(11) Dahlseid, T. A.; Kappes, M. M.; Pople, J. A.; Ratner, M. A.; *J. Chem. Phys.* **1992**, 96, 4924.
(12) Chen, J.; Brink, D. M.; Wille, L. T.; *J. Phys. B* **1990**, *23*, 885.
(13) Rao, B. K.; Jena, P.; *Phys. Rev. B* **1985**, *32*, 2058.
(14) Boustani, I.; Pewestorf, W.; Fantucci, P.; Bonac˘ic´-Koutecky´, V.; Koutecky´, J.; *Phys. Rev. B* **1987**, *35*, 9437.
(15) Lee, T. J.; Rendell, A. P.; Taylor, P. R.; *J. Phys. Chem.*, **1990**, *94*, 5463.
(16) Reuse, F.; Khanna, S. N.; de Coulon, V.; Buttet, J.; *Phys. Rev. B* **1990**, *41*, 11743.
(17) Kumar, V.; Car, R.; *Z. Phys. D* **1991**, *19*, 177.
(18) Bauschlicher, C. W. Jr.; Bagus, P. S.; Cox, B. N.; *J. Chem. Phys.* **1982**, *77*, 4032.
(19) Chiles, R. A.; Dykstra, C. E.; Jordan, K. D.; *J. Chem. Phys.* **1981**, *75*, 1044.
(20) Pacchioni, G.; Koutecky´, J.; *J. Chem. Phys.* 1982, *77*, 5850.
(21) Rohlfing, C. McM.; Binkley, J. S.; *Chem. Phys. Lett.* **1987**, *134*, 110.
(22) Lee, T. J.; Rendell, A. P.; Taylor, P. R.; *Theor. Chim. Acta* **1992**, 83, 165.
(23) Sudhaker, P. V.; Lammertsma, K.; *J. Chem. Phys.* **1993**, *99*, 7929.
(24) Hearn, J. E.; Johnston, R. L.; *J. Chem. Phys.* **1997**, *107*, 4674.
(25) Ekhardt, W.; Penzar, Z.; *Phys. Rev. B* **1988**, *38*, 4273.
(26) Release 2.0.1 Scientific Computing & Modelling, *Theoretical Chemistry, Vrije Universiteit, De Boelelaan 1083; 1081 HV Amsterdam; The Netherlands*, e-mail adf@chem.vu.nl.
(27) Vosko, S. H.; Wilk, L.; Nusair, M.; *Can. J. Phys.* **1980**, *58*, 1200.
(28) Perdew, J. P.; Chevary, J. A.; Vosko, S. H.; Jackson, K. A.; Perderson, M. R.; Singh, D. J.; Fiolhais, C.; *Phys. Rev. B* **1992**, *46*, 6671.
(29) Fan, L.; Ziegler, T.; *J. Chem. Phys.* **1991**, *95*, 7401.
(30) Ziegler, T.; Rauk, A.; *Theor. Chim. Acta* **1977**, *46*, 1.
(31) Baerends, E. J.; Branchadell, V.; Sodupe, M.; *Chem. Phys. Lett.* **1997**, *265*, 481.
(32) Ellis, D. E.; Painter, G. S.; *Phys. Rev. B* **1970**, *2*, 2887.

(33) Adachi, H.; Tsukada, M.; Satoko, C.; *J. Phys. Soc. Jpn.* **1978**, *45*, 875.
(34) Onoe, J.; Takeuchi, K.; Nakamastu, H.; Mukoyama, T.; Sekine, R.; Kim, B-II.; Adachi, H.; *J. Chem. Phys.* **1993**, *99*, 6810.
(35) Onoe, J.; *J. Phys. Soc. Jpn.* **1997**, *66*, 2328.
(36) Mulliken, R. S.; *J. Chem. Phys.* **1955**, *23*, 1833; *ibid.*, 1841; *ibid.* , 2388; *ibid.*, 2343.
(37) Jahn, H. A.; Teller, E.; *Proc. Roy. Soc. (London)* **1937**, *A161*, 220.

Electronic structure calculations to determine the effects of impurities on ceramic properties

Kimichika Fukushima*

Power and Industrial Systems R&D Center, Toshiba Corporation, 4-1, Ukishima-cho, Kawasaki-ku, Kawasaki 210, Japan

(received Nov. 2, 1998)

We report electronic structure calculation results for two types of ceramics with impurities. First, we studied Si_3N_4 and SiC, and the results show that these materials have valence states composed mainly of N *sp* or C *sp* atomic orbitals and conduction states consisting mainly of Si *sp* atomic orbitals. The component atoms C and N have negative net charges, whereas Si atoms have a positive net charge. The orbital mixing between the *d* orbitals of the ion-implanted Fe, Mo and Hf and the *sp* orbitals of N or C and Si causes charge transfer between these atoms. The reduced ionicity of Si weakens the attack on ceramics by ionic atoms and improves the resistance of the ceramics to corrosion. In the second part of this work, we studied Cu oxide superconductors. At present, these Cu oxides do not have sufficient critical current density at 77 K in an applied magnetic field. In order to enhance the critical current density, it is necessary to introduce pinning centers for magnetic flux lines. In the case of impurities whose atomic orbitals contribute little to HOMO (highest occupied molecular orbital), most charge carriers cannot enter the impurity sites. Thus, the superconducting order parameter becomes small or vanishes, and such impurities are effective pinning centers.

KEYWORDS: ceranics, Si_3N_4, SiC, corrosion, flux pinning

*Corresponding author: e-mail kimichika.fukushima@toshiba.co.jp

ADVANCES IN QUANTUM CHEMISTRY, VOLUME 37

0065-3276/01 $35.00

1. INTRODUCTION

Material properties are frequently influenced by impurities in the materials. We focus on (1) the role of the atoms introduced by ion implantation in ceramics in improving corrosion resistance and (2) the effects of impurities in pinning magnetic flux lines in superconductors to enhance the critical current density in an applied magnetic field. The calculation of the electronic states of materials is one of the most effective methods of studying properties and is indispensable in the material design process. This paper is based on a presentation made at the Korea-Japan DV-Xα Joint Symposium '98 held in Korea in August 1998, and includes some of results reported in a previous paper[1] on the topics mentioned above. Regarding the first topic, in this paper we report the original results for the effect of the interstitial and substitutional ion-implantated atom in β-Si_3N_4 and α-SiC on the corrosion resistance. This paper includes a summary of the results for the interstitial atoms introduced by ion implantation in β-Si_3N_4 discussed in the previous paper[1]. Regarding the second topic, this paper presents a summary of the results treated previouly.

We first report on the effects of ion implantation on the corrosion resistance of the ceramics Si_3N_4 and SiC. These ceramics can be used at high temperatures, because they have a high degree of hardness, good friction resistance, low thermal expansion and low density even when the temperature is raised. For wider practical use of these ceramics, it is necessary to improve corrosion resistance to, for instance, liquids. In a previous study, we showed that the ionic interaction beween surface atoms and the atoms in a liquid play an important role in corrosion[1],[2]. For example, a positively charged atom at a surface exposed to a liquid may be attacked by a negatively charged atom in the liquid as impurity atoms in liquids may sometimes have a negative charge. Through this type of ionic interaction, surface atoms may be released into liquids. It seems reasonable to expect that the suppression of the ionic interaction will improve the corrosion resistance and that ion implantation promises to be a useful method for suppressing ionic interaction. In fact, we examined the effect of an interstitial atom introduced by ion implantation on the corrosion resistance of β-Si_3N_4. The effect of a substitutional atom introduced by ion implantation was not discussed in the previous paper, so we calculated the electronic structures of simulated implanted atoms that exist at interstitial sites in the ceramics or are substituted for component atoms of the ceramics. The properties of α-SiC, the ceramic with which the present paper is mainly

concerned, may differ in some respects from those of β-Si_3N_4. In the case of β-Si_3N_4, the crystal structure is hexagonal phenacite-like, and Si and N belong to the different group IV and V, respectively. Unkile β-Si_3N_4, α-SiC has the Wultzite type crystal structure, and Si and C both belong to group IV. α-SiC is an important ceramic from viewpoint of application, and it has not yet been examined thoroughly respecting the effect of ion-implantation on the corrosion resistance. We used these calculated electronic structures to predict whether or not the atoms introduced by ion implantation would suppress the ionicity of the component atoms of the ceramics.

We then report on the pinning effect of impurity atoms in high-temperature copper oxide superconductors. For the use of oxide superconductors at 77 K in an applied high magnetic field, it is necessary to enhance the critical current density. The improvement of the critical current density requires the introduction of strong pinning centers for the magnetic flux lines. In the case of impurities and insulating inclusions, only few charge carriers can enter these sites, and the superconducting order parameters will be small there. The impurity atoms and insulating inclusions are thus expected to improve the critical current density. In general, regions where charge carriers do not exist act as pinning centers for magnetic flux lines. Roughly speaking, this is because the normal electric conductivity necessary for superconductivity vanishes in such insulating regions. By solving the Ginzburg-Landau equation, it is shown that magnetic flux lines are more stable in the region without carriers than that with carriers. For a cylindrical insulating inclusion, we first numerically solved the Ginzburg-Landau equation exactly, and showed that a magnetic flux line is pinned by the insulating inclusion. These sites will therefore strongly pin the magnetic flux lines. We theoretically predicted the effect of impurities on improving pinning of magnetic flux lines, and examined the optimal size of the insulating inclusion [3],[4]. The results of experiments on the addition of fluorine were consistent with the predictions and showed a large enhancement of the critical current density in a high magnetic field at 77 K [5]. In this part of the study, we investigated the electronic states of F atoms substituted for O (oxygen) atoms and the effects of the impurities on the pinning of the magnetic flux lines.

2. IMPURITY EFFECT ON MATERIAL PROPERTIES

2.1 Corrosion Resistance of Ceramics

First, we carried out cluster calculations for the ceramics β-Si_3N_4 and

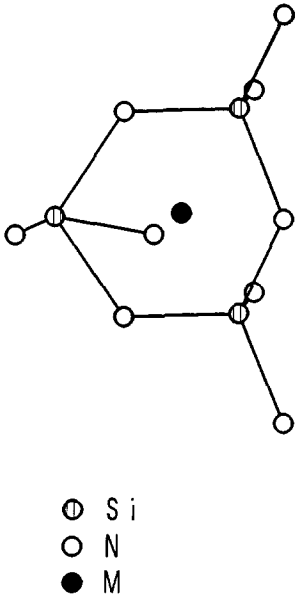

Fig 1. Model cluster for an interstitial atom introduced by ion implantation in Si_3N_4.

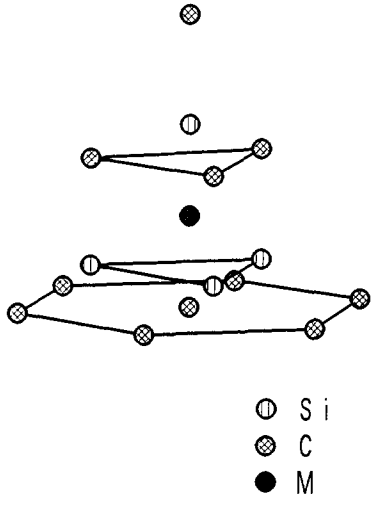

Fig 2. Model cluster for an interstitial atom introduced by ion implantation in SiC.

α-SiC in order to examine the corrosion resistance. Ion implantation was considered because it is expected to enable improvements in the corrosion resistance of materials. Simulation of the ion-implantation of Fe, Mo and Hf atoms into ceramics was performed for cases where the atoms introduced by ion implantation are (1) located at interstitial sites, and (2) substituted for Si atoms. Cluster model is an effective model to study local electronic structures. This paper focuses on the corrosion and corrosion resistance processes caused by an ionic interaction where the covalent bond is less important than the ionic interaction. For the analysis of ionic interactions, it is neccssary to calculate atomic charges, which are produced by the difference of the ionization energies for component elements. We consider the ceramics composed of two elements tetrahedrally bonded with the different ionization energies. The energy levels due to the dangling bonds do not form distinctive energy levels in an energy gap as is seen in the below results. This property is also observed in the case of GaAs, a III-V semiconductor, and the ionization energies for Ga and As are different, as we showed in ref.

(6). SiC is composed of elements belonging to the same IV group, but the ionization energies of Si and C are different. This energy difference does not result in distinctive energy levels in an energy gap due to the dangling bond such as those frequently seen in Si. Therefore, the essence of the ionic interaction in the corrosion and corrosion resistance processes treated in this study is well expressed by the present cluster model. β-Si_3N_4 has a hexagonal phenacite-like crystal structure with the unit lengths 7.606 Å and 2.909 Å in the directions of the a and c axes, respectively [7]. For the interstitial atom M (M = Fe, Mo or Hf) implanted into Si_3N_4, we used the model cluster Si_3N_9M shown in Fig. 1 and for the atom M substituted for an Si atom in Si_3N_4, we adopted the model cluster Si_2N_9M (Si replaced by M is indicated as S in Fig. 1). The crystal structure of α-SiC is the Wultzite type, and the unit lengths are 3.076 Å in the direction of the a axis and 5.048 Å in the direction of the c axis. As a model for an interstitial atom M implanted into SiC, we adopted the cluster $Si_4C_{11}M$ shown in Fig. 2. For the atom M substituted for an Si atom in SiC, we used the model $Si_3C_{11}M$ (Si replaced by M is indicated as S in Fig. 2). The electronic state calculations were performed using the non-spin-polarized molecular orbital method. At the beginning of the self-consistent iteration, the initial charges of Si, N and C were set to +4e, −3e and −4e, respectively. For the Fe atom introduced by ion implantation, we set neutral and +2e as the initial charges, whereas for the Mo and Hf atoms introduced by ion implantation, we assigned a neutral initial charge. The basis set used was composed of numerical atomic orbitals such as 1s-3p for Si, 1s-2p for N and C, 1s-3d for Fe, 1s-4d for Mo and 1s-5d for Hf. The point group used for producing symmetry orbitals was C_s for β-Si_3N_4 and C_{3v} for α-SiC. The electronic temperature for which calculations were carried out was 900 K. For Si_3N_4, the occupied valence states are composed mainly of N sp atomic orbitals and the unoccupied conduction states are composed mainly of Si sp atomic orbitals.

The energy level diagrams for intersitial atoms introduced by ion implantation in Si_3N_4 were reported in the previous paper [1]. Figure 3 shows the energy levels for Si_2N_9Fe, which is the model for an Fe atom introduced by ion implantation substituting for an Si atom in β-Si_3N_4. The energy levels from $19a'$ to $46a'$ are originated mailny from Si 3s and 3p atomic orbitals, N 2s and 2p atomic orbitals, and Fe 3d atomic orbitals. The orbitals from $19a'$ to $39a'$ are composed mainly of N 2s and 2p atomic orbitals. The energy levels $40a'$, $26a''$, $27a''$, $42a'$ and $43a'$ are originated mainly from Fe 3d atomic orbitals. The energy levels above the level $28a''$ have their origin in the Si 3s and 3p atomic orbitals. HOMO (highest

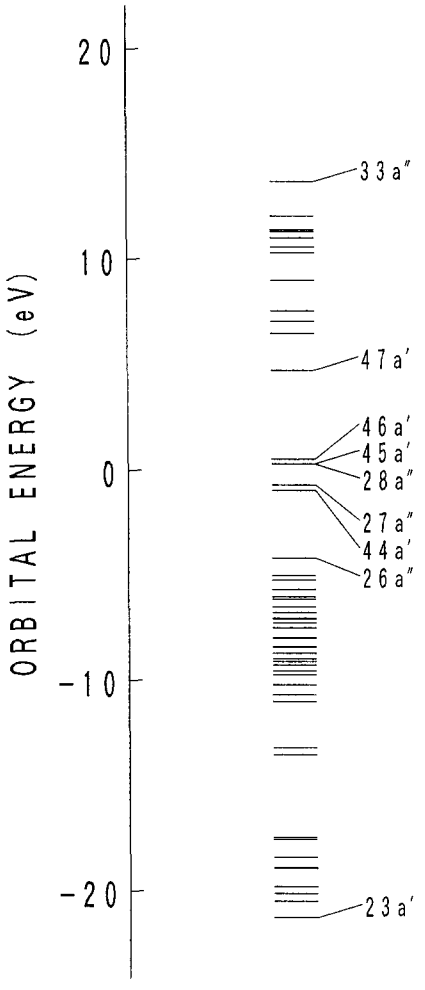

Fig 3. Energy levels for substitutional Fe introduced by ion implantation in Si_3N_4.

occupied molecular orbital) is $27a''$. Figure 4 shows the energy level diagram for Si_4C_{11}. The main components of the valence states (whose energy levels are from $12a_1$ to $22a_1$) are the C $2sp$ atomic orbitals and those of the conduction states (whose energy levels are from $24e$ to $27a_1$) are the Si $3sp$ atomic orbitals, and an energy gap exists between these states. The N and

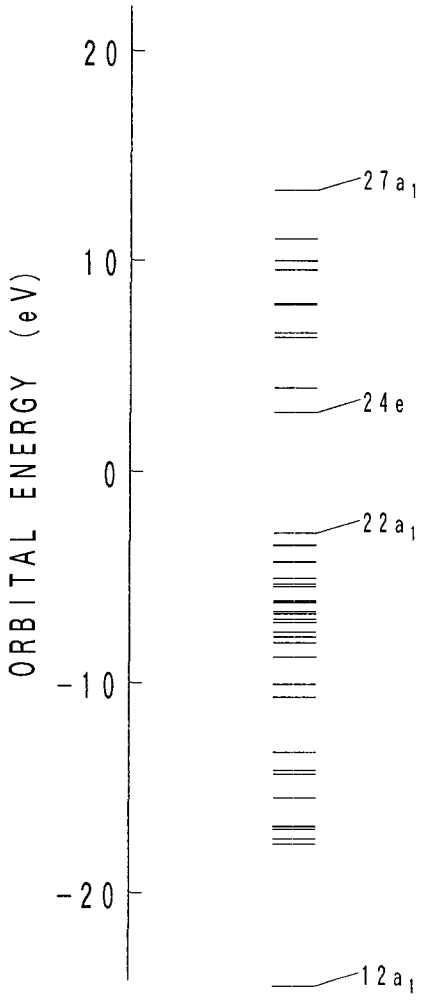

Fig 4. Energy levels for SiC.

C atoms thus have negative net charges, whereas the Si atoms have a positive net charge. Figure 5 shows the energy levels for $Si_4C_{11}Fe$, the model for simulation of the ion implantation of intersitial neutral Fe into SiC. The energy levels from $17a_1$ to $7a_2$ are valence states comprising of C *sp* orbitals and are occupied by electrons. The energy levels $28a_1$, $26e$ and

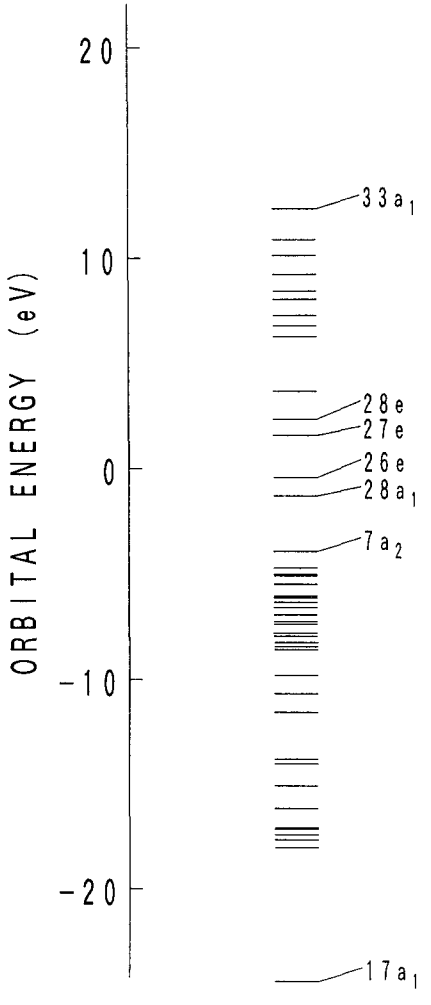

Fig 5. Energy levels for interstitial Fe introduced by ion implantation in SiC.

$27e$ located in the energy gap have their origin in the Fe $3d$ atomic orbitals. HOMO is $27e$. For interstitial Fe^{2+} introduced by ion implantation into SiC, the calculated energy levels are as shown in Fig. 6. The energies for the Fe $3d$ orbitals, which are indicated as $28a_1$, $26e$ and $27e$, become lower than those for neutral Fe. HOMO is $7a_2$, and the orbitals from $17a_1$ to $7a_2$

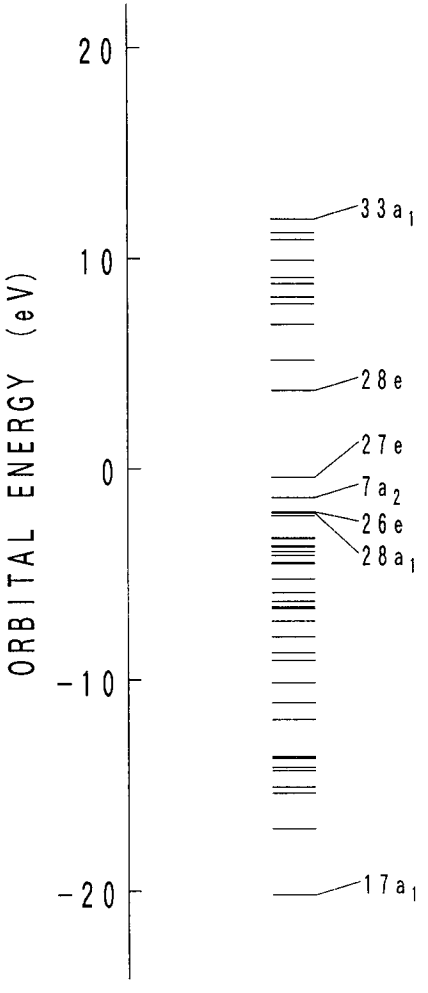

Fig 6. Energy levels for interstitial Fe^{2+} introduced by ion implantation in SiC.

except for the orbitals $28a_1$ and $26e$ have their origin mainly in the C $2sp$ atomic orbitals. The orbitals from $28e$ to $33a_1$ comprise mainly of the Si $3sp$ atomic orbitals. Figure 7 shows the calculated energy level diagram for an interstitial neutral Mo atom, introduced by ion implantation into SiC. The orbitals whose main component is The orbitals whose main component

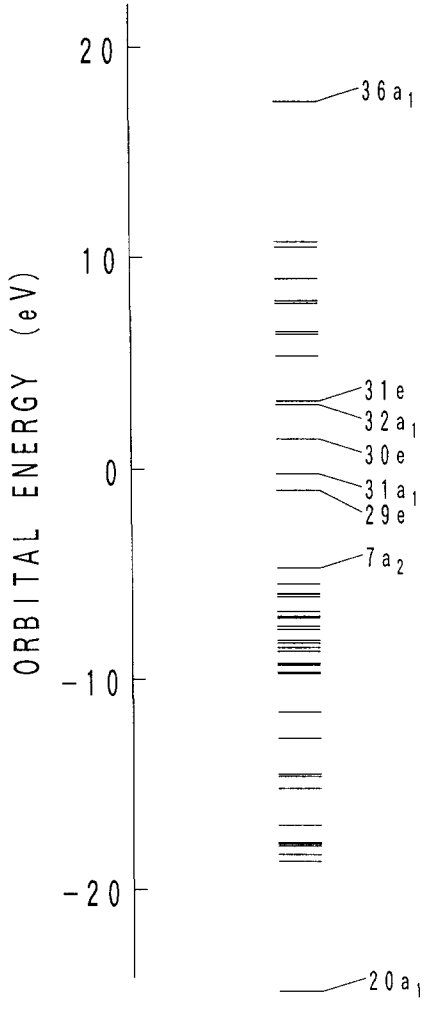

Fig 7. Energy levels for interstitial Mo introduced by ion implantation in SiC.

is Mo $4d$ are $29e$, $31a_1$ and $31e$, and their energies are higher than those for the Fe $3d$ atomic orbitals. The orbitals $30e$ and $32a_1$ consist mainly of the Si $3sp$ atomic orbitals.

Tables I to IV show the net charges of component atoms. For intersitial atoms introduced by ion implantation, the net charge of Si is the

Table I. Net charge of component atoms for ion-implanted β-Si_3N_4.

Implanted Ion	Atom	Charge (e)
No implantation	Si (average)	+1.99229
Interstitial Fe	Si (average)	+1.77957
	Fe	+0.75515
Interstitial Fe^{2+}	Si (average)	+1.72772
	Fe	+1.01611
Interstitial Mo	Si (average)	+1.71020
	Mo	+0.92802
Interstitial Hf	Si (average)	+1.64161
	Hf	+1.07785

Table II. Net charge of component atoms for ion-implanted β-Si_3N_4.

System	Atom	Charge (e)
Substitutional Fe	Si	+1.58497
	Fe	+1.38511
Substitutional Mo	Si	+1.46765
	Mo	+1.46237
Substitutional Hf	Si	+1.41711
	Hf	+1.79431

Table III. Net charge of component atoms for ion-implanted α-SiC.

System	Atom	Charge (e)
No implantation	Si	+1.8008
Interstitial Fe	Si	+1.50527
	Fe	+1.24051
Interstitial Fe^{2+}	Si	+1.51576
	Fe	+1.46981
Interstitial	Si	+1.40908
	Mo	+1.80691
Interstitial Hf	Si	+1.41003
	Hf	+1.66627

Table IV. Net charge of component atoms for ion-implanted α-SiC.

System	Atom	Charge(e)
Substitutional Fe	Si	+1.59754
	Fe	+1.49643
Substitutional Mo	Si	+1.51900
	Mo	+1.64978
Substitutional Hf	Si	+1.50478
	Hf	+1.96797

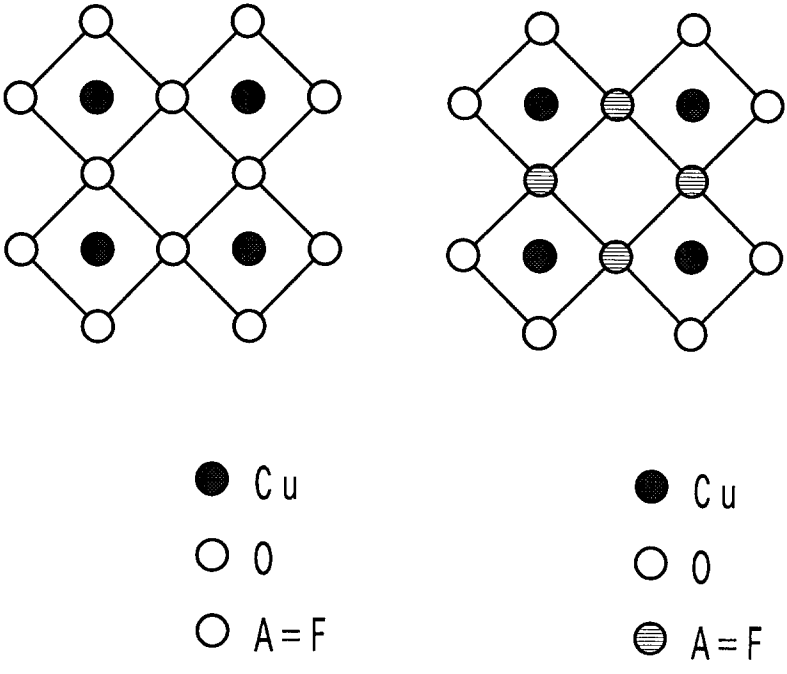

Fig 8. The atomic configuration in the *ab* plane for Cu oxides.

Fig 9. Model cluster for F substituted for O in Cu oxides.

average value for the first neighbor Si around the implanted atom, whereas for substitutional atoms introduced by ion implantation, the net charge of Si is the value for the second neighbor Si around the implanted atom. These results show that the ion implantation of Fe, Mo and Hf each reduces the ionicity of Si. This will suppress the ionic interaction between component atoms at the ceramic surface and liquids to which ceramics are exposed. Thus, the corrosion resistance of the ceramics will be enhanced.

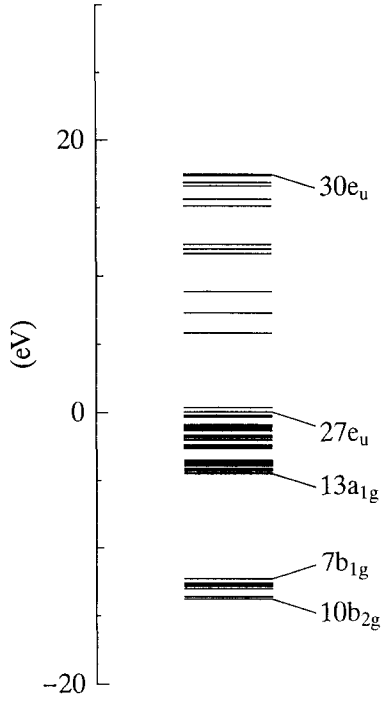

Fig 10. Energy levels for F substituted for O in Cu oxides.

2.2. Pinning Effect in Superconductors

In the second part of this study we examined copper oxide high-temperature superconductors. We used the model cluster $Cu_4O_{16}A_4$ (A=F), where oxygen atoms were replaced by halogen atoms, to analyze the effects of the impurity on the electronic states. Figure 8 and 9 show the atomic configuration in the *ab* plane for Cu oxides and the model cluster $Cu_4O_{16}A_4$, respectively. The model cluster has four octahedra composed of a central Cu atom and six O ligands. The distances between the Cu and O atoms in the *ab* plane and along the *c* axis are 1.894 Å and 2.428 Å, respectively. The basis set adopted was 1*s*-2*p* atomic orbitals for O and F and 1*s*-4*p* atomic orbitals for Cu. The initial charges were set to +2e for Cu, −2e for O and −1e for F. D_{4h} was used as the point group and one hole was

introduced into the cluster to treat the metallic state. Also, a Madelung potential was included in the Hamiltonian to describe the long-range electric field created by ions out of the cluster. The Madelung potential was calculated in 11×11×3 unit cells arrayed in the a, b and c directions. The lattice structure adopted was the K_2NiF_4 type. Figure 10 shows the calculated energy level diagram for F atoms substituted for O atoms in Cu oxides. The orbitals from $13a_{1g}$ to $27e_u$ have their origins mainly in the O $2p$ and Cu $3d$ atomic orbitals and they are occupied by electrons. HOMO is the state $27e_u$. The orbitals from $10b_{2g}$ to $7b_{1g}$ are comprised mainly of F $2p$ atomic orbitals. The energies of these F $2p$ orbitals are lower than the lowest energy of the O $2p$ and Cu $3d$ mixed states. Few charge carriers can enter the F sites, and superconducting states cannot be formed. Therefore, the F atoms act effectively as pinning centers for magnetic flux lines in Cu oxide superconductors. The experiments showed that the addition of F substantially enhanced the superconducting critical current at 77 K in magnetic field, and the critical current was maintained at least up to 3.5 T, a practical magnetic field from the viewpoint of engineering.

3. CONCLUSIONS

We investigated the effect of ion implantation on the interaction between component atoms of Si_3N_4 and SiC. In many cases, the ionicity of the component atoms of the ceramics was found to be reduced as a result of the charge transfer due to ion implantation. Ceramic atoms were attacked less stronglyby ionic atoms (such as O in liquid sodium) and the corrosion resistance of the ceramics was thus improved by ion implantation.

In addition, we performed electronic state calculations for impurity atoms in Cu oxide superconductors in order to examine the effects of these impurities on the pinning of magnetic flux lines. For impurity atoms such as F substituting for O atoms, the contribution of the atomic orbitals of these atoms to HOMO is small and most of the charge carriers generally do not exist at the impurity sites. Impurity atoms such as F thus effectively pin magnetic flux lines in Cu oxide superconductors.

REFERENCES

(1) Fukushima, K.;Endo, H. *Adv. Quant. Chem.* **1997**, *29*, 269.

(2) Fukushima, K.,; Endo H. *Jpn. J. Appl. Phys.* **1994**, *23*, 2613.

(3) Fukushima, K. *Physica C* **1993**, *212*, 407.

(4) Takezawa, N.; Fukushima, K. *Physica C* **1994**, *228*, 149.

(5) Tachikawa, K.;Kikuchi, A.;Kinoshita, T.; Komiya, S. In "Advances in Superconductivity VII" , Yamafuji, K.; Morishita T. Ed.; Springer-Verlag, 1995, p. 461.

(6) Fukushima K.; Adachi H., *Jpn. J. Appl. Phys.* **1989**, *28*, 1851.

(7) Wyckoff, R. W. G. "Crystal Structures" , Interscience: New York, 1964.

Embedded Cluster Models for Electronic States of Silicate Glasses

Y. Kowada*

Hyogo University of Teacher Education,
Yashirocho, Hyogo 673-14, Japan

D. E. Ellis
Department of Chemistry and Materials Research Center,
Northwestern University, Evanston, Illinois 60208

(Received July 17, 1999)

The discrete variational (DV) Xα method is applied to the study of the electronic structure of silicate glasses in embedded model clusters. The effects of the cluster size, the size of embedded units, and the Si-O-Si bond angles on the electronic states are discussed. Embedding units drastically improve the description of the electronic state, when compared to the isolated SiO_4^{4-} cluster, which is the structural unit of silicate glasses; e.g., the Fermi energy for the embedded cluster becomes smaller when compared to that of the
isolated cluster. Furthermore the Si and O ions both become more ionic in the embedded clusters. The electronic states localized around the center of the clusters, however, do not depend critically on either the size of the embedding units or size of the variational cluster. The range that the Si-O-Si bond angle takes leads to an energy shift and a broadening of each band which can be related to the spectroscopic peak broadening (XPS, IR, Raman, X-ray and neutron diffraction, etc.) observed in silicate glasses. The ionicities of both the Si and O ions decrease and the Si-O bond order increases with increasing Si-O-Si bond angle.

KEYWORDS: oxide glass, embedded method, DV-Xα, silicate
*Corresponding author, e-mail: ykowada@sci.hyogo-u.ac.jp

ADVANCES IN QUANTUM CHEMISTRY, VOLUME 37

0065-3276/01 $35.00

I. INTRODUCTION

Electronic states of oxide glasses are difficult to study by theoretical methods because of the structural randomness in their long-range order. In usual silicate glasses which are examples of typical oxide glasses, the glass structure is defined by SiO_4 tetrahedral units which are connected because they all share one corner oxygen ion. (1, 2) This structural unit is very similar to the structure that occurs in the corresponding silicate crystals; i. e. the short-range structure of silicate glasses is similar to that of silicate crystals. Due to this similarity in the short-range structure, many
experimental spectra of silicate glasses, such as X-ray photoelectron spectroscopy, infra-red spectroscopy, Raman spectroscopy and so on, are similar to the crystal spectra, except for a slight peak shift and increased peak widths. (3-7) This broadness is clearly related to the randomness of the long-range structure. In the case of SiO_2 glass, the SiO_4 unit connections occur with a variety of bond angles. The average Si-O-Si bond angle, connecting two SiO_4 units, is about 144° and this has a wide distribution in the range from 130° to 160°. (8)

The need to model this distribution means that it is difficult to theoretically study the electronic states of oxide glasses. There are several ways to theoretically study the electronic state of oxide materials, these include band calculations and molecular orbital methods. (9-13) The randomness is a problem for the band approach because it requires translational symmetry of the unit cell; a large super-cell may be chosen, but this is at the cost of increased computer time and possible spurious interactions between cells. On the other hand, the molecular orbital (MO) approach is usually applied to isolated molecules, (14-16) and can not handle infinite numbers of atoms as in the solid state. The embedded potential method is one of the improvements in molecular orbital methods which have been introduced in order to study solid state materials. (17) Basically, the cluster Hamilto-

nian is modified by adding pseudo potentials representing the solid state environment, and constraints are applied to localize cluster orbitals. This method has been used on many materials and many useful results have been obtained. (18) In order to apply this embedding method to glassy materials, several problems should be clarified, one of the most important being what effect the size of the embedding units has. To describe the glassy state, we need in principle many distinct embedding potentials and we cannot use translational symmetry. Consequently, it is necessary to study which embedding conditions are appropriate for giving a reasonable description of the potential in the glassy state. Therefore we need to study what effect the size of both variational clusters and embedding units has.

In this work we used several related clusters with different sizes and also studied clusters with modified Si-O-Si bond angles. We will discuss the effects of the embedding, the cluster size and Si-O-Si bond angle on the electronic states of silicate glasses.

2. Computational Details

We used the discrete variational (DV-Xα) method which uses a linear combination of atomic orbitals (LCAO) expansion of molecular orbitals to calculate the silicate cluster electronic state. (19, 20) In this method the exchange-correlation potentials are approximated by the simple Kohn-Sham-Slater form

$$V_{ex}(r) = -\alpha\left[\frac{3\rho}{4\pi}\right]^{\frac{1}{3}}$$

where α is a constant, fixed at 0.7, ρ is the electron density of the cluster. The basis sets are formed from numerical solutions of the Schrödinger equation.

Mulliken population analysis was used for the evaluation of the net charge of each atom and the bond overlap populations of each cluster.

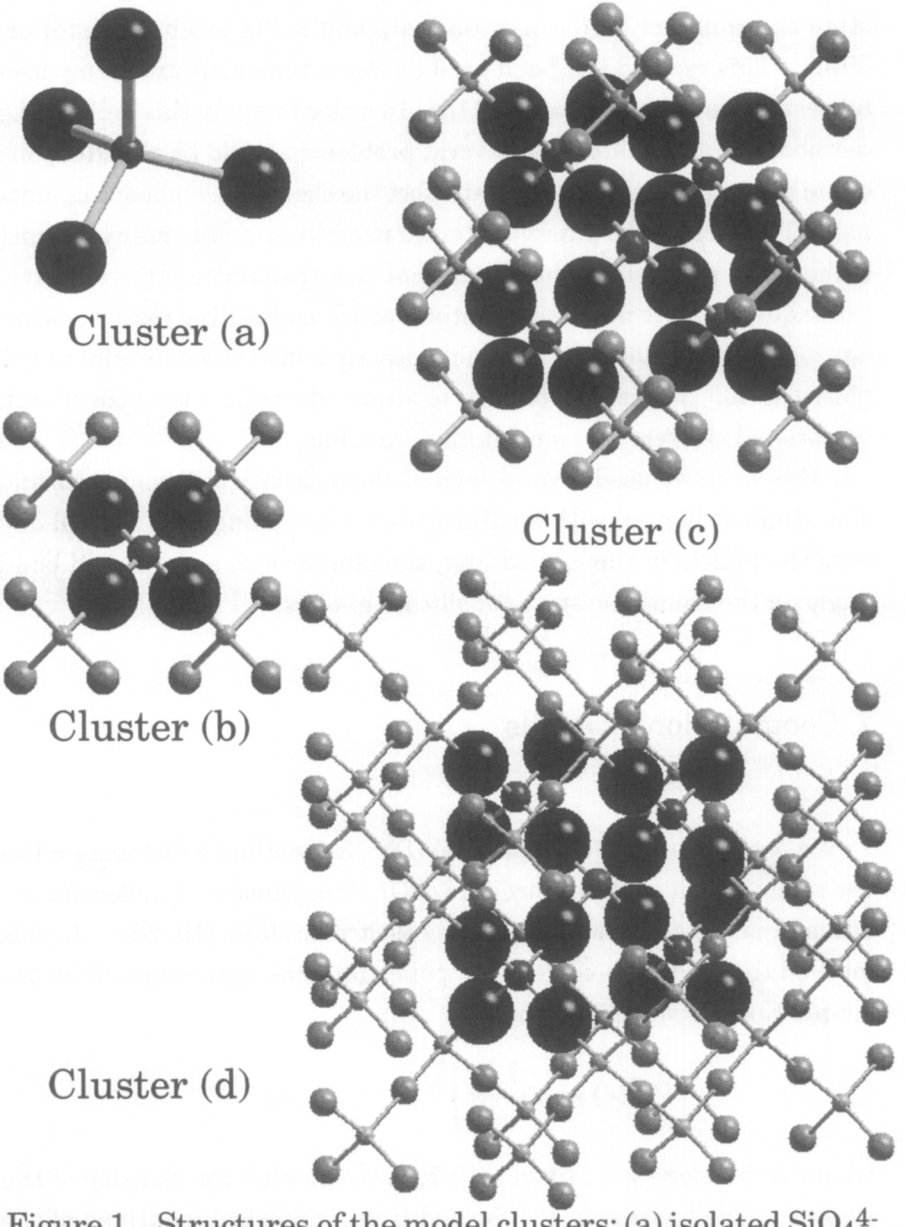

Figure 1. Structures of the model clusters: (a) isolated SiO_4^{4-}, (b) embedded SiO_4^{4-}, (c) embedded $Si_5O_{16}^{12-}$, (d) embedded $Si_5O_{16}^{12-}$ with second sheath of embedded units, (e) embedded $Si_{17}O_{52}^{36-}$, (f) embedded $Si_5O_{16}^{12-}$ with various Si-O-Si bond angles.

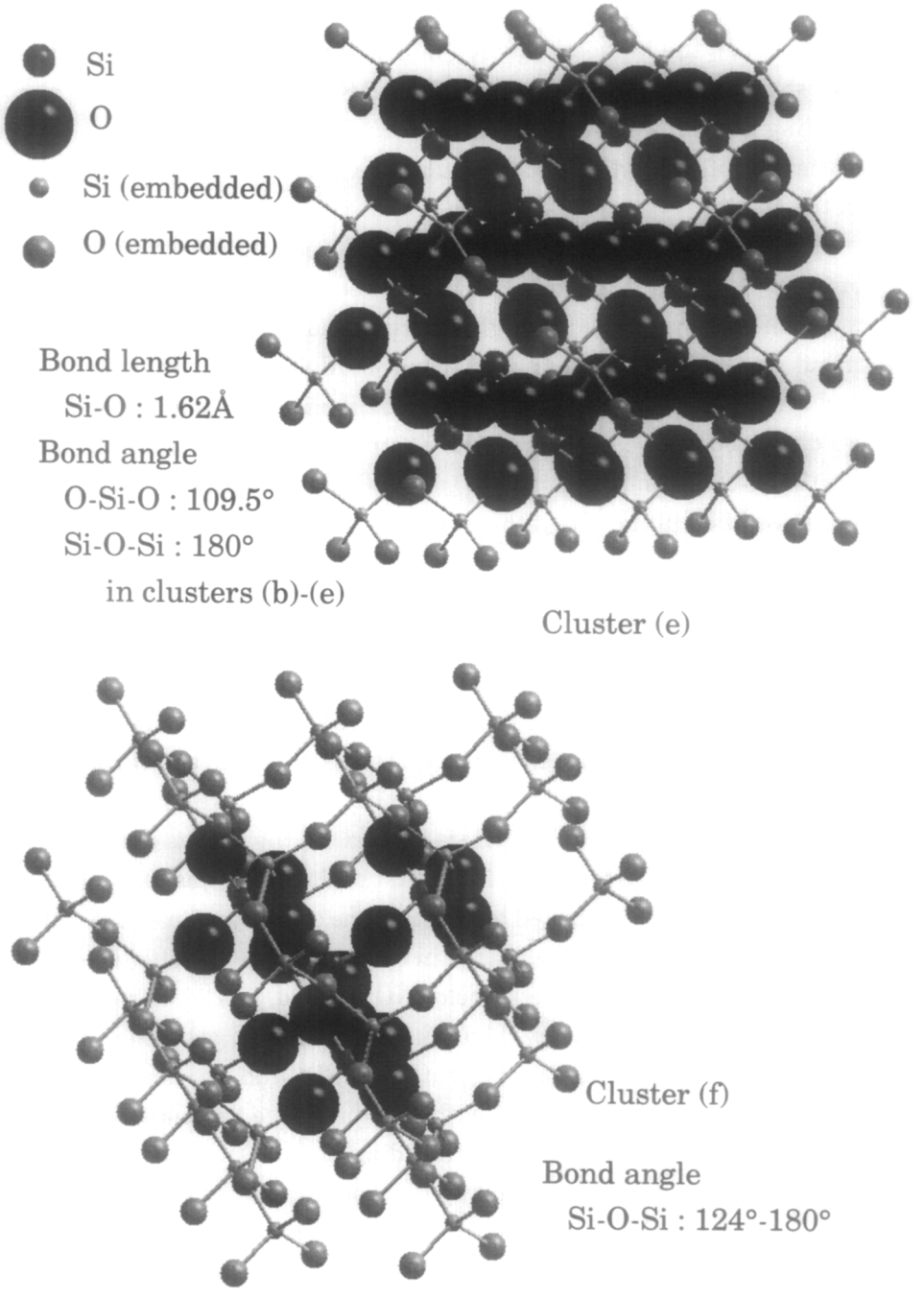

(Figure 1. continued)

The Fermi energy of each cluster was taken as the middle of the energy gap between the highest occupied molecular orbital (HOMO) and the lowest unoccupied molecular orbital (LUMO). In order to discuss the bonding nature, we used the bond order which
is the sum of the bond overlap populations between each pair of atoms in the cluster.

The six clusters shown in figure 1 were used to discuss the effects of the embedding, the cluster size, and the Si-O-Si bond angles. As mentioned above, the silicate glass structure has basically a wide distribution of Si-O-Si bond angles. Since studying both the size effects and the Si-O-Si bond angles at the same time is very complicated, first we discussed the size effects on the electronic states of clusters by taking the Si-O-Si bond angle as 180°, for both the variational cluster and the embedding units. Next the Si-O-Si bonds in a certain cluster were rotated from 180° to 124° simulating the distribution of Si-O-Si bond angles in the SiO_2 glass. Cluster (a) is an isolated SiO_4^{4-} cluster, a structural unit of general silicate glasses. Cluster (b) is the same cluster as (a) but with four embedding SiO_3^{+} units. Comparison of clusters (a) and (b) allows us to observe the most basic effects of the embedding. Cluster (c) includes five SiO_4 units ($Si_5O_{16}^{12-}$) in the variational space and twelve embedding SiO_3^{+} units. There are four bridging oxygens in this cluster. In clusters (b) and (c), the charge of each embedding Si ion was fixed at +3.4 and that of the O ion was -0.8. These charge values were optimized by calculations on clusters (a)-(e) and the charge of the O ion was decreased in order to make the clusters neutral, as discussed in more detail below. Cluster (d) has 24 more embedding SiO_3 units than cluster (c). In this case, the charges of the embedding Si and O ions in the first sheath are +3.4 and -1.8 respectively. After the O ion in the second sheath had its charge decreased in order to make the cluster neutral, the embedding Si and O ions in the second sheath had charges of +3.4 and -0.76, respectively. Cluster (e) is a $Si_{17}O_{52}^{36-}$ variational cluster with embedding consisting of twelve $SiO_2^{1.7+}$ units which are connected to two oxygen ions and twelve $SiO_3^{1.3+}$ units connected to one oxygen ion in the cluster. By using

clusters (b)-(e) it is possible to discuss what effect the size of the variational cluster and the embedding unit has on the electronic states.

We would also like to discuss what effect the physically important structural parameter, the bond angle, has. Experimentally, Si-O bond lengths and O-Si-O bond angles in silicate glasses are not so much different from those in crystals. The Si-O-Si bond angle, however, has a much broader distribution in the glasses than in the crystals. As mentioned previously, in silica glass Si-O-Si bond angle average at about 144° and take a broad distribution from 130° to 160°, though no such distribution is observed in silicate crystals. These experimental results suggest that many features of the silicate glass randomness might be modeled by variation of the Si-O-Si bond angles. We modified the Si-O-Si bond from 0 to 70 degrees in cluster (f), which has the same number of atoms and embedding ions as cluster (d). The real three dimensional Si-O-Si bond angles varied from 124° to 180°. The Si-O-Si angles in the embedding units were also modified to be the same as those in the variational cluster.

In clusters (a)-(f), the Si-O bond length was fixed at 1.62 Å and the Si-O-Si bond angle was fixed at 109°28'. These values are the average values as measured by X-ray and neutron diffraction in SiO2 glass. (21)

3. RESULTS AND DISCUSSION

Figure 2 shows the MO energy level structure for the valence states in clusters (a)-(d). The ordinate shows the energy of each MO in eV.

For the isolated SiO_4^{4-} unit, cluster (a), the occupied MOs are mainly constructed from O 2s and 2p orbitals while the unoccupied MOs are dominated by Si 3s-3d orbitals, as could be expected from the nominal Si^{4+}, O^{2-} charge states. The Fermi energy of this cluster is +23.8 eV since its total charge is -4 and there is no external environment. The

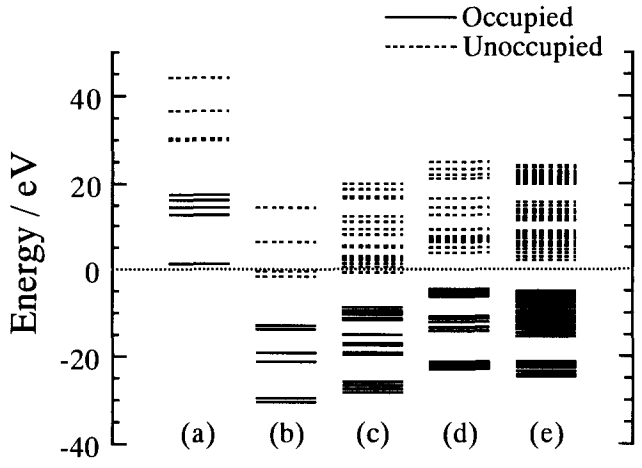

Figure 2. Valence energy level diagram for clusters (a)-(e).

energy gap between the HOMO and LUMO is 12.8 eV. Cluster (b) is the same as cluster (a) but with four additional SiO_3^+ embedding units. As a result of the embedding, the system, that is the cluster plus the embedding, becomes electrically neutral. This neutrality lowers the Fermi energy of the cluster to -7.20 eV, and produces an energy gap between the HOMO and the LUMO of 11.0 eV. The optical band gap in the SiO2 glass, obtained by experiment, is about 7.7 - 8.2 eV. (22, 23) The cluster (b) energy gap is larger than that for the SiO_2 glass, suggesting that only one SiO4 unit is not enough to represent the quantitative energy level structure of the bulk state. Though it is necessary to use transition state calculations and non-local functionals to precisely compare the HOMO-LUMO band gap with experimental results, the embedding method clearly improves the energy level structure of the SiO_4 cluster. (24, 25) There is another notable difference in the energy level structures of clusters (a) and (b). That is, the occupied "O 2p" band in cluster (b) near the HOMO is split into two parts. The top band near the HOMO is due to lone pair electrons and MOs which have a π type interaction with the embedding Si ions. The bottom band is due to σ type interactions with the embedding Si ions. This band structure corresponds to the formation of bridging oxygens. Ex-

cept for the Fermi energy shift and the splitting of the occupied band, the level structure of cluster (b) is similar to cluster (a). This result suggests that we can use isolated clusters to qualitatively discuss the electronic states of silicate glasses. We need, however, to use the embedding method to discuss electronic properties such as the energy gap and absorption spectra, and to make comparisons with experimental measurements.

Cluster (c) is a larger $Si_5O_{16}^{12-}$ variational unit with embedding ions which gives a much denser set of MO levels and a presumably better description of the energy bands of the solid. In this cluster, occupied orbitals are again constituted by O 2s and 2p orbitals and unoccupied orbitals arise primarily from Si 3s-3d orbitals. Basically, the energy level structure of cluster (c) is the same as that of cluster (b); the Fermi energy, however, shifts down to -4.64 eV. The HOMO-LUMO energy gap is 8.15 eV, quite close to that found in the SiO_2 glass. This result suggests that cluster (c) already has a similar energy level structure to that of the SiO_2 glass. Cluster (d) has a second sheath of embedding units added; this cluster should show still more similarity with the electronic states of silicate bulk, since now second and third neighbor interactions are included. The cluster's level structure is very similar to that of (c) with the Fermi energy ~ 0 eV. These results now appear quite satisfactory, both in relative and absolute energy distributions. Cluster (e) is the largest considered in this work; here, the MO level density in each band is considerably greater than in the smaller clusters. The HOMO-LUMO band gap of 7.53 eV is slightly smaller than that of cluster (d), and the E_F is -7.10 eV. This is caused by the smaller number of embedding units for this cluster, and might be improved by an additional sheath as in cluster (d).

The effects of the embedding units have obviously been seen in the energy level shifts and sub-band formation. More subtle changes in the net charge and bond order are also interesting, since these parameters are very important for the understanding of the ionicity and bonding nature of silicate glasses. Fig. 3 (a) and (b) show the net ionic charges in clusters (a)-(e). There are three kinds of Si and O ions in these clusters: every cluster has the center silicon shown as Si_C in Fig. 3 (a) and four

nearest-neighbor oxygens, shown as O_I in Fig. 3 (b). Clusters (c) and (d) have four silicon and twelve oxygen ions around the central SiO_4 unit. These outer ions are shown as Si_O and O_O. Cluster (e) has another twelve Si and thirty six O ions around the Si_5O_{16} unit, of the oxygen ions two kinds can be distinguished. One (Non-bridging) is connected to the $SiO_3^{1.3+}$ units and the other (Bridging) is connected to the $SiO_2^{1.7+}$ units by sharing that unit with two oxygens. These "third shell" ions are shown as Si_{O2}, O_{ONB} and O_{OB} in Fig. 3.

The net charge of the Si ion in the naked cluster (a) is 2.04 in comparison to the nominal +4 value; the embedding units drastically change the net Si charge. Thus, in cluster (b) the net Si_C charge becomes 3.52, which is much closer to the expected value. In cluster (c), however, the charge of Si_C ion is not much different to that in cluster (b), and the charges of the four Si_O are near to that of the Si_C. This result means that these two Si ions are in a similar condition
in this cluster. Since one the most important purposes of embedding is to place the cluster in the same environment as it would be in the solid, these results show that embedding units are very effective for improving the electronic state of the silicate clusters. Cluster (d) has two sheaths of embedding SiO_3 units. This increase in the number of embedding units makes the net charges of both Si_C and Si_O almost the same. This is an improvement in the environment around these two Si ions. On the other hand, the net charges of Si_O and Si_{O2} are a bit smaller than that of Si_C in cluster (e). This difference seems to be caused by the existence of two kinds of O ion in the exterior of the variational cluster (e). Though one of them, O_{ONB}, is connected to an embedding $SiO_3^{1.3+}$ unit, the other kind of oxygen, O_{OB}, is linked a $SiO_2^{1.7+}$ unit which is shared with an another O_{OB} ions. In this case the embedded $SiO_2^{1.7+}$ unit has larger charge and attracts electrons on the O_{OB} ions more than the $SiO_3^{1.3+}$ units. The Si_C charge, however, is little different from that in cluster (d). That is, center Si ion net charge doesn't change much in clusters
(b)-(e). This result suggests that the embedded method is very useful for improving the environment around the silicate clusters, though the cluster size does not have much effect on the electronic state around the cen-

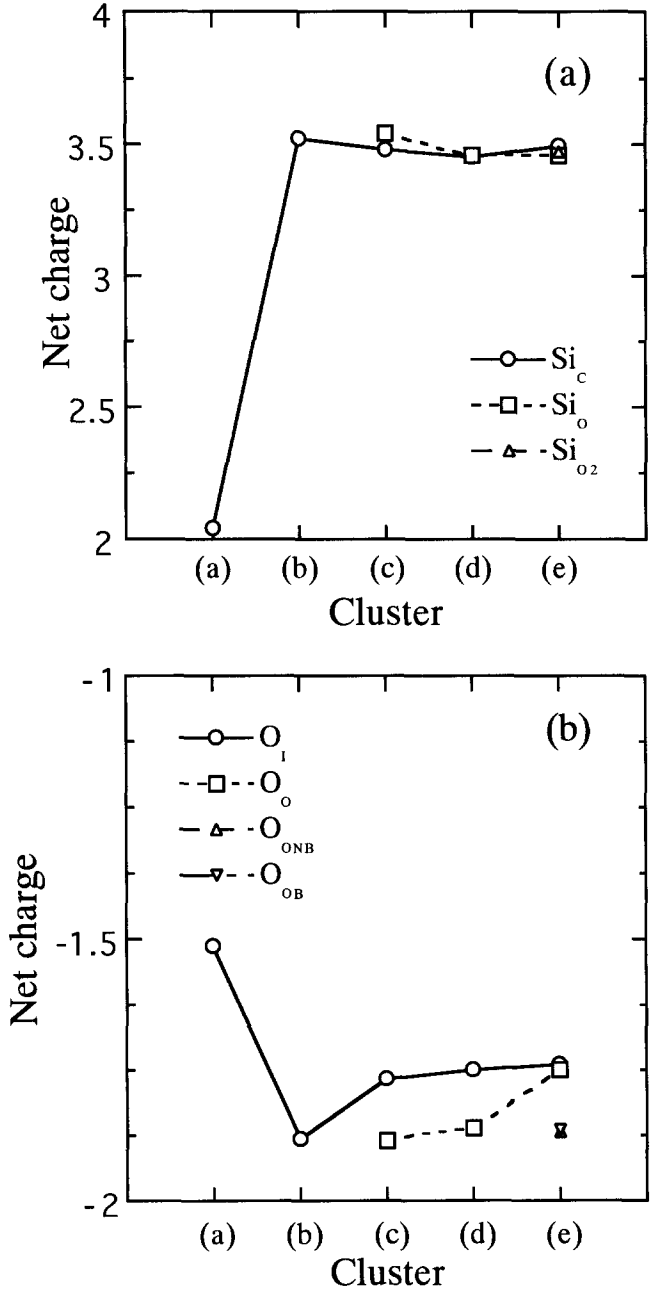

Figure 3. Net charge of Si (a) and O (b) ions in the clusters (a)-(e).

ter of cluster.

The oxygen ion net charges are shown in Fig. 3 (b). In the cluster (a), O_I has a charge of -1.51, and increases to -1.88 in cluster (b), with the embedding units. This change obviously corresponds to the change for Si in Fig. 3 (a). In cluster (c), the O_I and O_O ion charges become -1.77 and -1.88, respectively. The O_O charge is larger than that of O_I here, showing the different effect of the embedding units: since cluster electrons are attracted to the outside by the positive charge of embedding units, the O_O ions become more negative. The net charge of the O_I ions, however, is almost same as that in cluster (c), so the net balance is reasonable. In cluster (e), the O_O ions have almost same charge as the O_I ions, while the O_{ONB} and O_{OB} ions have larger negative charge than the others. These results suggest that the embedding units cause drastic changes in the net charge of the peripheral oxygen ions, while the O_I charge around the cluster center is only weakly affected, as in the Si ion case.

Fig. 4 shows bond orders between Si_C and O_I (Si_c-O_I), between Si_O and O_I ions (Si_O-O_I), and between Si_O and O_O ions (Si_O-O_O). For the cluster (e) case, there are in addition Si_{O2}, O_{ONB} and O_{OB} ions; their bond orders are shown as Si_{O2}-O_{ONB} and Si_{O2}-O_{OB}.

For cluster (a) the bond order between Si_C and O_I is 0.655, this decreases with the addition of embedding units to 0.614 in cluster (b). This result is consistent with the net charge of the Si and O ions, that is, these ion's charges increase with embedding; i.e., they become more ionic. In cluster (c) there are three different kinds of Si-O bonding, that is Si_C-O_I, Si_O-O_I, and Si_O-O_O, each has a corresponding bond order. The relative order, Si_O-O_O (0.767) > Si_C-O_I (0.656) > Si_O-O_I (0.492) is correlated with the effect of embedding units. Therefore Si_O-O_O receives the largest influence from embedding, and the Si_O-O_O bond order becomes larger; on the contrary, Si_O-O_I bond order becomes smaller under the same influence. The bond order of Si_C-O_I bonding in the cluster (c), however, is almost the same as in cluster (b), suggesting that the central region of the Si_C-O_I bonding is influenced less from the embedding than the peripheral structure is. This means

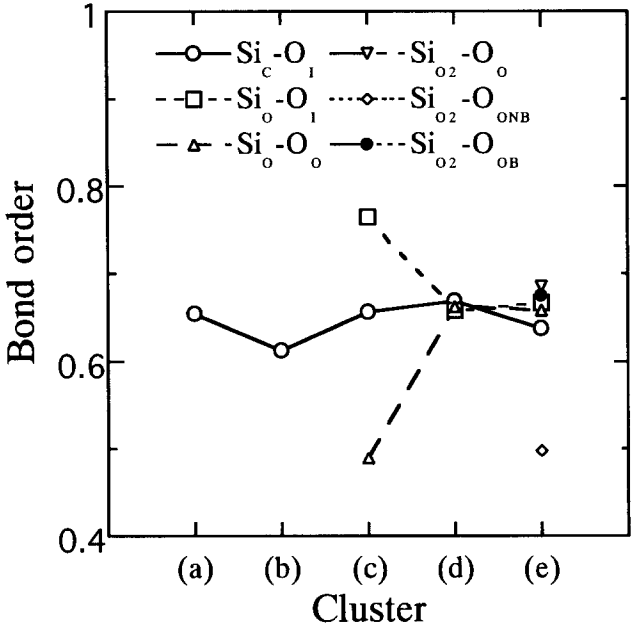

Figure 4. Bond order of Si-O in the clusters (a)-(e).

that the electronic states near the cluster centers are little affected by either the cluster size or the embedding units. In other words, electronic states localized near the center are stable in silicate clusters, and thus suitable for the analysis of glass properties.

The cluster (c) results suggest that a single sheath of embedding units is useful for putting the isolated cluster into a bulk-like state, but is not sufficient to produce a solid state environment in the "surface-layer" Si and O ions. After the addition of a second sheath of embedding units, the Si_O-O_O bond orders are much improved. In cluster (d), the three different Si-O bonding structures have almost the same bond order values. This result shows that variational cluster (d) comes close to the bulk-like state and that the second sheath of embedding units is needed to discuss the quantitative details of the electronic states of solid state silicates. Of course we can't regard cluster (d) as a complete model of the solid state, because the variational cluster has 12 negative charges and the outside oxygen ions have a larger negative

charge than the interior oxygen. We can discuss the electronic state of the silicate clusters quantitatively, however, using the results around the center of cluster (d).

In cluster (e) the Si-O bond orders are: Si_C-O_I, Si_O-O_I, Si_O-O_O, and Si_{O2}-O_O with values 0.635, 0.697, 0.659, and 0.609, respectively. These interior bonding structures are satisfactorily close to each other; however, the bondings of the terminal groups Si_{O2}-O_{OB} and Si_{O2}-O_{ONB} are different from the others. The Si_{O2}-O_{OB} bond order is 0.827; i. e., much larger than the interior values, while in contrast, the Si_{O2}-O_{ONB} bond order is 0.513 and is thus much smaller than the cluster (e) interior bonding. The analysis of these differences reveals the combined effects of the number of bonds shared and the embedding unit charges. Since O_{ONB} is connected to one embedding $SiO_3^{1.3+}$ unit, it feels less attraction to the variational cluster electrons and this makes the Si_{O2}-O_{ONB} bond order smaller. On the other hand, two O_{OB} share one embedding $SiO_2^{1.7+}$ unit, which has a larger positive charge. This larger charge in turn causes the Si_{O2}-O_{OB} bond order to get larger. In order to improve the Si_{O2}-O_{OB} and Si_{O2}-O_{ONB} bond orders we could add a second sheath of embedding units or optimize the charge of the embedding ions. The observed stability of the central region, and the fact that boundary-condition effects on the surface of the variational cluster are easily separated, permit the use of embedding methods for the quantitative discussion of the electronic states of solid state silicate.

Next we discuss how the silicate cluster electronic states change with the Si-O-Si bond angle. Fig. 5 shows the cluster (f) energy level diagrams. The bond angles for each case are shown at the bottom of each column. The 180° angle result is for cluster (d).

The level structure for the case where $\angle$Si-O-Si = 172°, is almost same as that for cluster (d). That is, the occupied levels are formed from three bands. One is centered around -28 eV and is mainly made up of O 2s orbitals, while two more bands mainly made up of O 2p lie between -10 and -20 eV. The level structure of the unoccupied levels is also very similar to that of cluster (d), being dominated by Si 3s-p-d

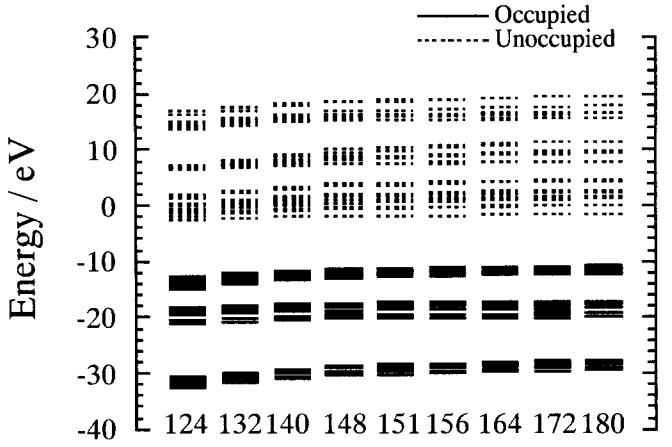

Figure 5. Valence energy level diagram for the cluster (f) with various bond angles of Si-O-Si.

orbitals. In the 164° case, compared with the 172° case, the level structure is slightly, but perceptibly changed; the energy of each band is lower. The 156 and 151° angles show the same tendency. Therefore the MO energies decrease gradually with the decrease in the Si-O-Si bond angle. This tendency gets somewhat accelerated after 140°. As mentioned above, in real silicate glasses the Si-O-Si bond angle averages at 144° with a wide distribution from 130° to 160°. The present results show that decrease of bond angles leads to a shift to lower energy of related MOs. Then, the observed energy level structure of real silicate glasses should be a result of the mixing of the various molecular orbitals caused by the variety of different Si-O-Si bond angles. In other words, this mixed band structure is observed as peak broadening in experimental spectra such as XPS, X-ray emission spectra and so on.

The cluster (f) net ionic charges are shown in Figs. 6 (a) and (b). In the 180° angle case, the net Si charge at the center (Fig. 6a) is almost the same as that of Si_O. The charge decreases continuously with the Si-O-Si bond angle. Even at the most extreme 124° angle the Si_C and Si_O charges are almost the same.

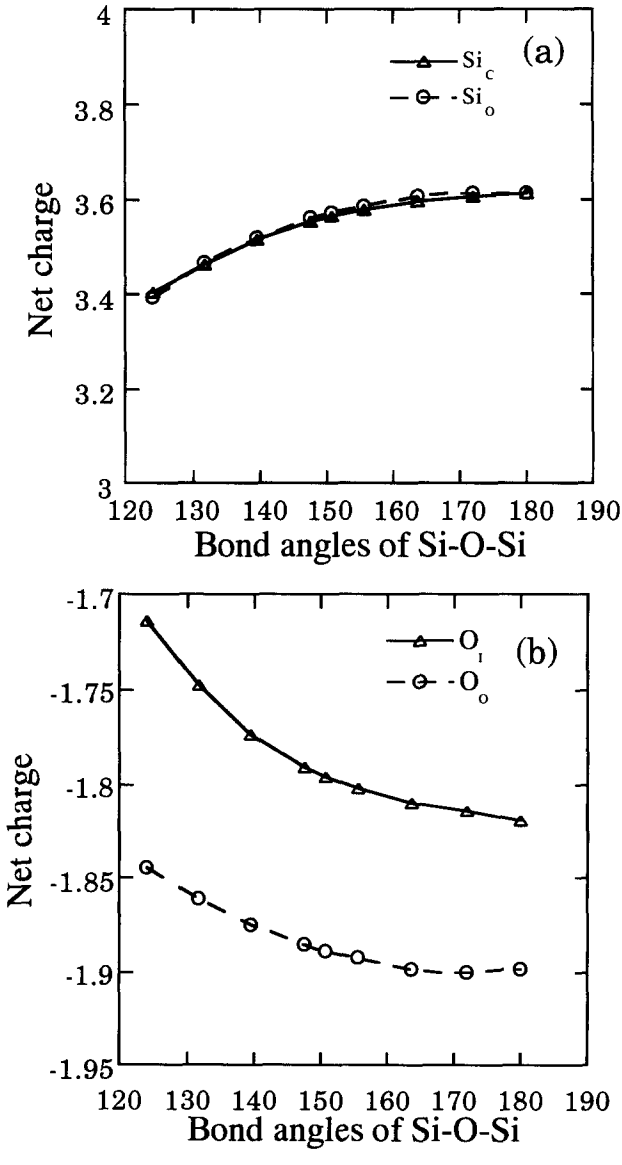

Figure 6. Relationship between the bond angle of Si-O-Si and the net charge of both Si (a) and O (b) in the cluster (f).

Fig. 6 (b) shows the net charges of the O ions. At 180° , the O_O net charge is -1.89 and is larger than that of O_I, -1.82. As explained above, this is due to the embedding units causing attraction of excess electrons from the variational cluster to the outside. The O ion negative charge decreases with the Si-O-Si bond angle, paralleling that of Si ions, while the O_I charge and the O_O charge maintain a nearly constant difference. The decrease in the net ionic charge implies a smaller ionic interaction between the Si and O ions for the lower Si-O-Si bond angles. This clarifies the role of this parameter.

In order to further discuss the Si-O bonding nature, we calculated the bond order for each Si-O pair in cluster (f). The results for Si_C-O_I, Si_O-O_I and Si_O-O_O bonds are shown in Fig. 7 as triangles, circles and squares, respectively. The Si_C-O_I, Si_O-O_I, and Si_O-O_O bond orders are almost equal at the Si-O-Si angle of 180°. The Si_C-O_I bond order increases with decrease in the Si-O-Si bond angle, whereas the Si_O-O_I and Si_O-O_O bond orders show the opposite tendency in the range 180° to 172°. In the region where the bond angle is smaller than 164°, however, all three bond orders increase with decreasing of bond angle. This increase shows two distinct regions, with a transition point at around 148°. This transition or bending point is very interesting because it falls at the average bond angle of the SiO_2 glass. As shown in Fig. 6, the Si-O ionic interaction decreases with the Si-O-Si bond angle. In contrast to this, we see here that the covalent interaction increases with decreasing Si-O-Si bond angle. This result suggests that there may be a total energy minimum which is obtained by simultaneous optimization of both the ionic and the covalent interactions. In order to verify this idea we need to calculate the cluster (f) total energy versus bond angle, this will be reported in the near future.

4. CONCLUSION

In order to study the effects of the cluster size, embedding units and the Si-O-Si bond angle on the electronic structure of silicate glasses

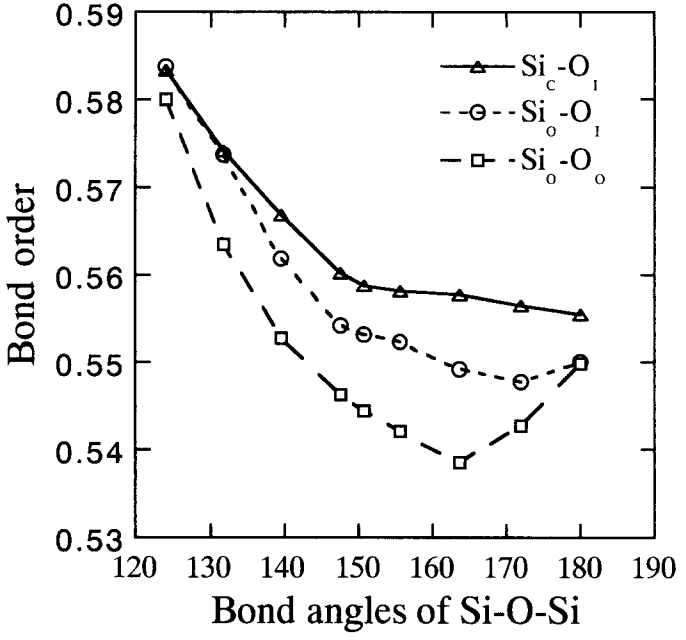

Figure 7. Relationship between the bond angle of Si-O-Si and the bond order of Si-O in the cluster (f).

we have used the DV-Xα method to analyze numerous silicate clusters. Clusters with a single sheath of $(SiO_4)^Q$ embedding units already show level structures and Fermi energies compatible with the bulk system. Addition of a second sheath of embedding units improves the net charge and the bond order in silicate clusters, particularly near the cluster surface. The electronic structure of silicate clusters changes with the Si-O-Si bond angle, with Si-O bond order increasing and ionic charge decreasing with decreasing Si-O-Si bond angle. The resulting band broadening and net shift to greater binding energy compare favorably with the experimental band broadening.

REFERENCES

(1) Wong, J.; and C. A. Angell, C. A. In "Glass Structure by Spectroscopy", Marcel Dekker, New York, 1976; 864.

(2) Sakka, S.; Matusita, K. J. Non-Cryst. Solids **1976**, *22*, 57.

(3) Brückner, R.; Chun H.-U.; Goretzk, H.; Sammet, M. J. Non-Cryst. Solids **1980**, *42*, 49.

(4) Stephenson, D. A.; Binkowski, N. J. J. Non-Cryst. Solids **1976**, *22*, 399.

(5) Sigel, Jr., G. H. J. Non-Cryst. Solids **1973/1974**, *13*, 372.

(6) Sigel, Jr., G. H. J. Phys. Chem. Solids **1971**, *32*, 2373.

(7) DiStefano, T. H.; Eastman, D. E. Phys. Rev. Lett. **1971**, *27*, 1560.

(8) Mozzi, R L.; Warren, B. E. J. Appl. Crystal. **1969**, *2*, 164.

(9) Ellis, E.; Johnson, D. W.; Breeze, A.; Magee, P. M.; Perkins, P. G. Phil. Mag. B **1979**, *40*, 105.

(10) Schneider, P. M.; Fowler, W. B. Phys. Rev. Lett. **1976**, *36*, 425.

(11) Tossell, J. A. ; Vaughen, D. J. ; Johnson, K. H. Chem. Phys. Lett. **1973**, *20*, 329.

(12) Pantelides, S. T.; Harrison, W. A. Phys. Rev. **1976**, *B13*, 2667.

(13) Chelikowsky, J. R.; Schlüter, M. Phys. Rev. **1977**, *B15*, 4020.

(14) Kowada, Y.; Adachi, H.; Tatsumisago, M.; Minami, T. J. Non-Cryst. Solids **1992**, *150*, 318.

(15) Kowada, Y. ; Adachi, H. ; Minami, T. J. Phys. Chem. **1993**, *97*, 8989.

(16) Kowada, Y.; Morimoto, K.; Adachi, H.; Tatsumisago, M.; Minami, T. J. Non-Cryst. Solids **1996**, *196*, 204.

(17) Understanding Chemical Reactivity Vol.12, "Density Functional Theory of Molecules, Clusters, and Solids", Ellis D. E., Eds.; Kluwer Academic Publishers Dordrecht: Boston, London 1955.

(18) Ellis, D. E. In "Physics and Chemistry of Metal Cluster Compounds", de Jongh, L. J., Ed.; Kluwer Academic Publishers Dordrecht: Boston, London 1994; 135. Ellis, D. E.; Guo, J.; Low, J. J. In "Quantum Chemistry proaches to Chemisorption and Heterogeneous Catalysis", Ruette, F.; Kluwer Academic Publishers, Dordrecht: Boston, London, 1992; 70.

(19) Ellis, D. E.; Painter, G. S. Phys. Rev. **1970**, *B2*, 2887.

(20) Rosen, A.; Ellis, D. E.; Adachi, H.; Averill, F. W. J. Chem. Phys. **1976**, *65*,

3629.

(21) Waseda, Y. "The Structure of Non-Crystalline Materials"; McGraw-Hill: New York, 1980; 133.

(22) Sigel Jr., G. H. J. Phys. Chem. Solids **1971**, *32*, 2373.

(23) Sigel Jr., G. H. J. Non-Cryst. Solids **1973/1974**, *13*, 372.

(24) Perdew, J. P.; Zunger, A. Phys. Rev. **1981**, *B23*, 5048.

(25) Gunnarsson, O.; Jonson, M.; Lundqvist, B. I. Phys. Rev. **1979**, *B20*, 3136.

Electronic structure of Ti_4O_7 using DV-Xα cluster calculation method

Hyunju Chang* and Jae Do Lee

Advanced Materials Division
Korea Research Institute of Chemical Technology
Taejon, 305-600, Korea

(Recieved November 20, 1998)

Ti_4O_7 has been attracted, because it shows temperature-induced semiconductor-semiconductor-metal transitions. These transitions have been known to be induced by charge delocalization of Ti ions. We have initiated self-consistent local-density calculations on Ti_4O_7, in order to investigate charge delocalization of Ti ions in metallic phase. Embedded cluster Discrete Variational (DV)-Xα method has been used to determine local charge distributions and density of states. Several model cluster calculations have been carried out for two different geometric structures in low-temperature semiconductor phase and high-temperature metallic phase of Ti_4O_7. The calculated projected density of states agreed well with the X-ray absorption spectra (XAS) for two different phases of Ti_4O_7. We have found that the charge delocalization within the cluster model is very small and a little change occurs in mainly Ti *3d* across the metal-nonmetal transition.

KEYWORDS: Ti_4O_7, cluster method, DV-Xα, metal-nonmetal transition

*Corresponding author, e-mail: hjchang@pado.krict.re.kr

ADVANCES IN QUANTUM CHEMISTRY, VOLUME 37

0065-3276/01 $35.00

1. INTRODUCTION

Ti_4O_7 has attracted considerable attention, since it shows interesting physical properties, such as temperature dependent conductivity. Especially, it has a moderate conductivity at room temperature, like graphite, which allows many possible applications. Ti_4O_7 shows metal - nonmetal transition. There are two steps of transition at 130K and 150K, semiconductor-semiconductor-metal transitions (1). Its electronic structure has been investigated extensively by many experimental tools, such as X-ray diffraction, electrical-resistivity measurement and magnetic-susceptibility measurement. However, this study is the first time to try to understand the electronic structure of Ti_4O_7 using theoretical tools, as far as we know. The structure of Ti_4O_7 is known as a Magneli structure. Crystal structure is triclinic and it consists of rutile octahedral units. The chains of rutile units form 2-dimensional slabs, which are separated with shear planes (1). The slabs consist of two types of chains, called as 4-2-2-4 and 3-1-1-3, as shown in Fig 1. Each Ti forms a rutile octahedron unit and shares oxygens at the corners and the edges of octahedron with its neighboring octahedra. At the end of each chain, Ti3 and Ti4 centered octahedra share oxygens at the surface as well as at the corners and the edges. It makes Ti_4O_7 different from TiO_2 units. Nonmetal-metal transition in Ti_4O_7 is known to occur through charge delocalization in Ti *3d* from many experiments (2).

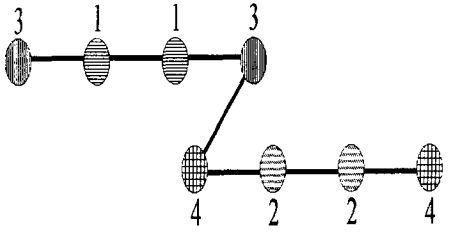

Fig 1. Two different chains in Ti_4O_7 ; Each Ti has 6 nearest neighboring oxygens.

At the low-temperature phase, Ti_4O_7 is a mixed valence compound with two equally populated, Ti^{4+} and Ti^{3+}. The 3-1-1-3 chains consist of Ti^{3+} ions, while the 4-2-2-4 chains consist of Ti^{4+} ions, as an ordered structure. At the medium temperature phase, these two valences are getting disordered. Finally, at the nonmetal-metal transition temperature, the charge of Ti's is delocalized and all the Ti's have 3.5 charge valence. It gives a jump in conductivity of Ti_4O_7 at the transition temperature. Our purpose of this study is to clarify this charge delocalization across the transition using cluster calculations.

2. COMPUTATIONAL PROCEDURE

We have used the DV-Xα embedded cluster method which is explained in detail elsewhere (3,4). Here we give a summary of main feature. The DV-Xα method is based on density functional theory in which the Coulomb and exchange potential energy is a functional of the electronic density.

The single particle Hamiltonian $\hat{h}$ can be written as (in hartree units)

$$\hat{h} = -\frac{1}{2}\nabla^2 + V_C(\vec{r}) + V_{X\alpha}(\vec{r}). \qquad (1)$$

Here, $V_C(\vec{r})$ is the Coulomb potential due to electrons and nuclei, and $V_{X\alpha}(\vec{r})$ is the exchange potential, with both of the potentials depending on $\rho(\vec{r})$. $V_{X\alpha}(\vec{r})$ is the so called Xα exchange potential and represented as $V_{X\alpha}(\vec{r}) = -3\alpha\left[\left(\frac{3}{8\pi}\right)\rho(\vec{r})\right]^{\frac{1}{3}}$. The value of 0.7 for α has been known to be optimal in reproducing experimental ionization energies and used through our calculations.

The total charge density of the system can be represented as the sum of cluster density and environmental host density,

$$\rho(\vec{r}) = \rho^{cluster}(\vec{r}) + \rho^{host}(\vec{r}) \tag{2}$$

The cluster densities are determined from molecular orbital (MO) wave functions, $\psi_i(\vec{r})$, that are solutions of Schrödinger equations of the Hamiltonian in Eq. (1). With the Fermi-Dirac occupation numbers n_i, the cluster density is written as

$$\rho^{cluster}(\vec{r}) = \sum n_i |\psi_i(\vec{r})|^2. \tag{3}$$

The host density is determined as the sum over contributing atom or ion charge densities,

$$\rho^{host}(\vec{r}) = \sum \rho_v(\vec{r}). \tag{4}$$

As in many molecular orbital methods, $\psi_i(\vec{r})$ in Eq. (3) is represented as a linear combination of atomic orbitals (LCAO),

$$\psi_i(\vec{r}) = \sum_{\mu} C_{i\mu} \chi_\mu(\vec{r}), \tag{5}$$

where the basis functions, $\chi_\mu(\vec{r})$, are taken as numerical solutions of Kohn-Sham equations for the free ions or atoms in a potential well. In the present calculations, the numerical basis functions of the free ions (Ti^{4+}, Ti^{3+}, and O^{2-}) are used.

Application of the variational method leads the secular matrix equation

$$HC = ECS, \tag{6}$$

where H and S are the Hamiltonian and the overlap matrices, respectively. The matrices, C and E, represent the coefficients in Eq. (5) and eigenvalues, respectively. The matrix elements are evaluated using numerical sampling, and the optimal C is obtained by the self-consistent-field (SCF) method described in Ref. (3,4).

The calculations involved determination of the projected densities of states (ProDOS)(5). The ProDOS were calculated near the Fermi energy, with approximate intensity for dipole allowed transitions from the core levels of selected site and parity. With the one-electron molecular orbitals of the clusters, as in Eq. (5), the ProDOS are defined in terms of the eigenvector coefficients of the orbitals and a Lorentzian (a localized line shape) of width σ, as

$$N_p(E) = \sum_i G_{pi} \frac{\sigma/\pi}{(E-\varepsilon_i)^2+\sigma^2} \tag{7}$$

where $G_{pi} = |C_{pi}|^2$ (8)

The ProDos differs from the usual partial density of states (PDOS) calculated in the previous works in the definition (6). The summation in the Eq. (7) is over the unoccupied final states, thus $N_p(E)$ will be proportional to the absorption cross section approximately (5). However, ProDos and PDOS are nearly the same, as far as the localized bound states are concerned. We have found that the ProDos of our clusters are very similar to PDOS of them. In this report, we concentrate our discussions on ProDOS of the central atom Ti to compare them with the XAS results of Ti_4O_7 (7).

Two different structural parameters were taken for the low-temperature phase at 115K, and the high-temperature metallic phase at 298K (8). We have focused these two temperatures to investigate the difference in electronic structure of at the low-temperature phase and the high-temperature metallic phase in Ti_4O_7. We have chosen the Ti1, Ti2, Ti3, and Ti4-centered clusters at each temperature, total 8 model clusters. Each cluster was taken within the radius 4.4 Å, which gives 32 or 33 atom cluster according to the structure. The cluster was embedded in the crystal environmental potential, which was driven from about 350 atoms within a sphere with the radius of 11 Å. It is a triclinic system, thus non-symmetry option was used in DV-Xα method. Fig. 2 shows the one of the clusters which contains 33 atoms, Ti_{12} and O_{21}. According to the structural parameters (8), at 115K, the shortest cation-cation bond is the Ti3-Ti1. At 298K, Ti3-Ti1 is getting farther and Ti3-Ti4 is the shortest bond, which shares oxygens at the surface as well as at the corners and the edges of octahedron.

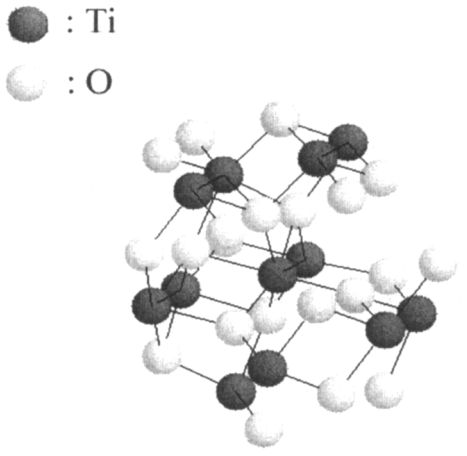

Fig 2. One of the Ti-centered model clusters: Ti 4-centered 33 atom cluster at 298K

3. RESULTS AND DISCUSSIONS

We have calculated the projected density of states (ProDOS), charge density, and Mulliken charge values for each Ti-centered cluster at 115K and 298K. The ProDOS of Ti *3d* at two temperatures were compared, since in the experimental XAS (7), main difference appears in Ti *3d* between the low-temperature phase and the high-temperature phase. In Fig. 3, the calculated ProDOS of Ti *3d* at high temperature shifts toward lower energy by 0.40 eV. That agrees with the experimental observation of 0.45 eV shift. The t_{2g} and e_g subbands in calculation split by about 2.0 eV. The separation is a little smaller than the experimental value, 2.4 eV. The similar shift is shown in all Ti-centered clusters. Overall trend of change in the calculations from low to high

temperature agrees with the experimental XAS. We have found that ProDOS of Ti *4sp* and O *2p* shows a very little change from 115K to 298 K. It indicates that main change across the transition occurs in Ti *3d*.

The opening of a band gap in the Ti_4O_7 low-temperature semiconducting phase has been estimated at 0.25 eV by a photoemission spectra (PES) experiment (9). However, the calculated ProDOS does not show any band gap opening at 115K, as shown in Fig. 3. It can be compared with the recent calculation of Ti_2O_3 using DV-Xα cluster method, which has successfully reproduced a band gap opening of Ti_2O_3 at low temperature insulating phase (10). Nakatsugawa and Iguchi (10) exclaims that electron-phonon interaction in Ti_2O_3 is weak, since the band gap can be seen in their DV-Xα cluster

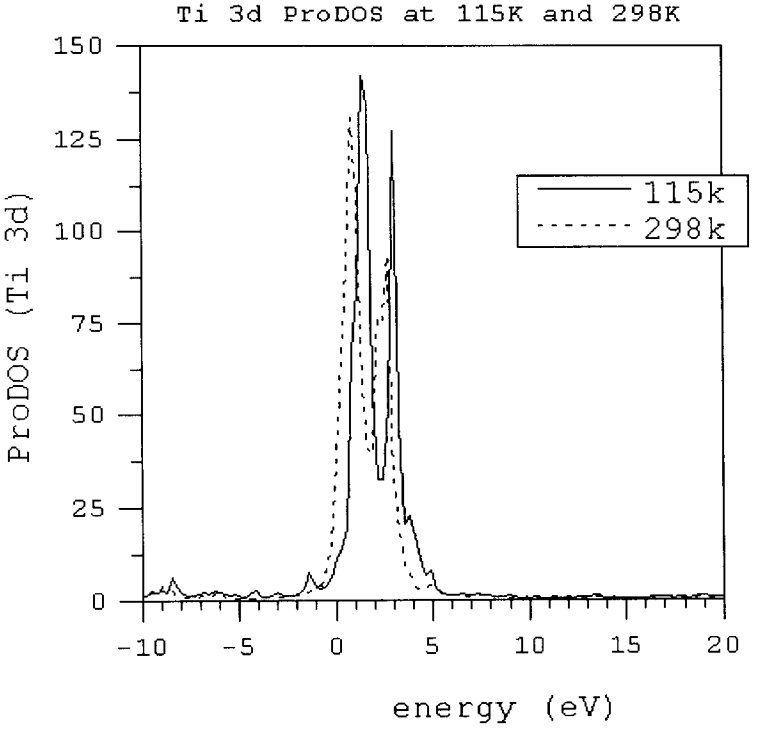

Fig 3. ProDOS of Ti *3d* calculated from the Ti4-centered clusters at 115K and 298K

Table I. Calculated Mulliken charge values compared with the experimentally determined values

Ti	Exp. (Schlenker, 1980)		Calculated	
	115K	298K	115K	298K
Ti4	3.90	3.47	3.06	2.92
Ti2	4.00	3.45	3.12	3.05
Ti3	3.09	3.60	2.87	2.92
Ti1	3.02	3.48	2.87	2.91

calculation without considering electron-phonon interaction. It implies that electron-phonon interaction might be important in Ti_4O_7, like VO_2.

We have also calculated the Mulliken charge values to clarify the charge delocalization across the transition. The values of 4 Ti's for each temperature are listed in the Table I. From the calculated values, there is an increase of valence charge in Ti1 and Ti3, while there is a decrease of valence charge in Ti2 and Ti4, from 115K to 298K. However, the amount of the change is very small. From the experiments, we expect the charge difference about 0.5, but the calculated results shows difference about 0.1. (Some are about 0.05.) The difference between two temperatures in calculation is only the structural difference which we took. We have also found no big change in charge density contour plots between two temperatures, as expected from the Mulliken charge values, but a little change was found along Ti3-Ti4. Fig. 4 shows some degree of charge delocalization along Ti3 and Ti4. Especially the charge around Ti3 is getting delocalized. We have plotted the similar charge density plots along other cation and cation pairs. They show very little change. It suggests that the charge delocalization occurs mostly along Ti3 and Ti4.

Across the nonmetal-metal transition, we have found a main but little change occurs in Ti *3d*, as agreed with the experimental XAS. However, the degree of charge delocalization is much smaller in calculation than that expected from experiment. We could not find a band gap opening at low-

temperature semiconducting phase. The electron-phone interaction could be strong in Ti_4O_7 in low-temperature, compared with Ti_2O_3, thus our method seem to have a limit to reproduce the band gap opening and enough charge delocalization in this case. Even in the limitation of the method, we could confirm the main change in Ti *3d* and the trend of charge delocalization in nonmetal-metal transition of Ti_4O_7 from our cluster calculations.

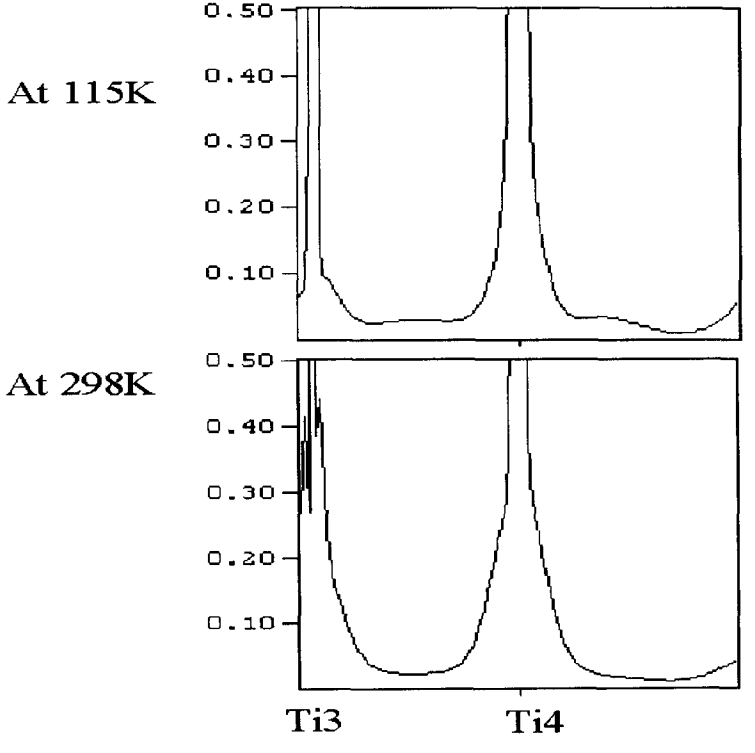

Fig 4. Charge density plot along Ti3 and Ti4 at 115K and 298K

REFERENCES

(1) Lakkis, S.; Schlenker, C. B.; Chakraverty, K.; Burder, R. *Phys. Rev. B* **1976**, 14, 1429.
(2) Schlenker, C.; Marezio, M. *Phil. Mag. B* **1980**, 42, 452.
(3) Baerends, E. J.; Ellis, D. E.; Ros, P. *Chem. Phys.* **1973**, 2, 41.
(4) Rosen, A.; Ellis, D. E.; Adachi, H.; Averill, F. W. *J. Chem. Phys.* **1976**, 65, 3629.
(5) Guo, J.; Ellis, D. E.; Goodman, G. L.; Alp, E. E.; Soderholm, L.; Shenoy, G. K. *Phys. Rev. B*, **1990**, 41, 82.
(6) Ellis, D. E.; Benesh, G. A.; Byrom, E. *Phys. Rev. B* **1977**, 16, 3308.
(7) Abbate M.; Potze, R.; Sawatzky, G. A.; Schelenker, C.; Lin, H. J.; Tjeng, L. H.; Chen, C. T.; Teehan, D.; Turner, T. S. *Phys. Rev. B* **1995**, 51, 10150.
(8) Le Page, Y.; Strobel, P. *J. Sol. St. Chem.* **1982**, 43, 314; Le Page, Y.; Marezio, M. *ibid.* **1984**, 53, 13.
(9) Abbate M.; Potze, R.; Sawatzky, G. A.; Schelenker, C.; Teehan, D.; Turner, T. S. *Solid State Comm.* **1995**, 94, 465.
(10) Nakatsugawa, H.; Iguchi, E.; *Phys. Rev. B* **1997**, 56, 12931.

The electronic structures of graphite and fullerene, and their compounds

Shinji Kawasaki*, Fujio Okino and Hidekazu Touhara

Faculty of Textile Science and Technology, Shinshu University, 3-15-1 Tokida, Ueda 386-8567, Japan.

Ning Liu and Toyohisa Nakajima

EPSON KOWA Corp., 1077-5 Shimonogo, Ueda 386-1214, Japan.

(Recieved November 2. 1998)

We report results of first-principles molecular orbital calculations on model clusters of graphite (C_{24}), alkali graphite intercalation compounds (MC_{48}: M = Li, Na, K, Rb, Cs), fullerene (C_{60}), and fluorinated fullerenes ($C_{60}F_x$: x = 18, 36, 48). The calculated partial densities of states (pDOS) are compared with measured x-ray absorption near edge structure (XANES) spectra, x-ray photoelectron spectra (XPS), x-ray emission spectra (XES), and ultraviolet photoelectron spectra (UPS). In the case of graphite and its compounds, the calculated pDOS well reproduce features of the observed XANES and UPS spectra. The calculated pDOS and the observed XPS, UPS and XANES of $C_{60}F_x$ (x = 0, 36, 48) are also in satisfactory accordance.

KEYWORDS: carbon, graphite, fullerene, XANES, UPS, XES

*Corresponding author, e-mail: skawasa@giptc.shinshu-u.ac.jp

ADVANCES IN QUANTUM CHEMISTRY, VOLUME 37

0065-3276/01 $35.00

1. INTRODUCTION

Carbon atoms crystallize in several forms. Graphite and diamond are well known carbon polymorphs. Fullerenes, which were discovered in the 1980's, have also been well characterized. Carbon materials show a variety of different physical and chemical properties. Because of this the electronic structure of carbon materials has been investigated using a number of different experimental techniques, for example, XPS, UPS and XANES. Theoretical studies of carbon materials have been also performed. However, experimentally observed spectra are not always consistent with theoretical predictions. Recently, in order to understand the various kinds of observed electronic spectra, DV-Xα calculations have been performed on a small cluster model. [1] In the present paper, we report results of DV-Xα calculations performed on the carbon materials: graphite, alkali graphite intercalation compounds (GIC), fullerene, and fluorinated fullerenes.

We previously reported the results of DV-Xα calculations on C_{60}, $C_{60}F_{36}$ and $C_{60}F_{48}$. [2] In that paper, we compared calculated DOS results with the observed spectra of fluorinated fullerenes with varying numbers of fluorine atoms. However, recently, new methods for the synthesization of high purity fluorinated fullerenes have been discovered. [3, 4, 5, 6] Since this discovery, a lot of spectra related to the electronic structure of pure fluorinated fullerenes have become available. In the present paper, we compare calculated DOS of these materials with the observed spectra. Furthermore, we also perform DV-Xα calculations on $C_{60}F_{18}$, a material which was discovered only recently. [7]

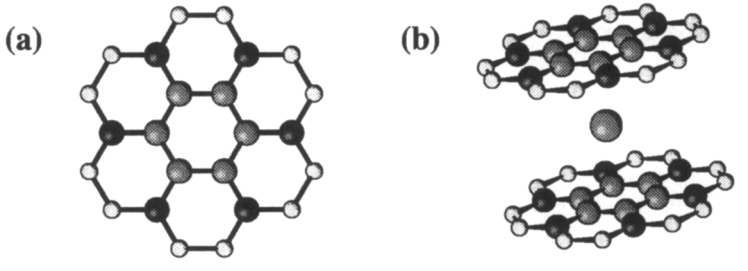

Fig. 1. (a) A C_{24} model cluster of graphite used for the ground state calculations. The three different circle symbols indicate the three types of carbon atoms. (b) A MC_{48} model cluster of the alkali GIC. The large circle indicates the alkali metal atom.

Table I. Interlayer distances I_c and C-C bond lengths d_{cc}.

	I_c (nm)	d_{cc} (nm)
C_{24}	0.333	0.14168
LiC_{48}	0.370	0.14324
NaC_{48}	0.478	0.14271
KC_{48}	0.535	0.14254
RbC_{48}	0.560	0.14248
CsC_{48}	0.599	0.14240

2. CALCULATION

2.1. Graphite and Alkali GICs

We used the C_{24} model cluster, which consists of seven carbon hexagons, to represent the graphite plane (Fig. 1 (a)). To perform the ground state calculations, we classified the carbon atoms into three types, and performed the calculations under D_{6h} symmetry. To avoid model cluster termination effects, we treated the electronic structure of the inner carbon atoms as that of graphite. When we performed Slater's transition state calculations, however, we took four types of carbon atom into account. This was because one of the inner carbon atoms, in which the 1s electron transits to an unoccupied level, should be distinguished from the other inner carbon atoms. Further we didn't use any symmetry orbitals for the transition state calculations.

The alkali GIC calculations were performed under D_{6h} symmetry on MC_{48} cluster models which had a sandwich-type structure (Fig. 1 (b)). The interlayer distances and the in-plane C-C bond lengths we used for the model clusters are summarized in Table I.

In all our calculations we used 5×10^4 sampling points. The atomic orbitals we used as basis sets were $1s$ - $3p$ for C, $1s$ - $2p$ for Li, $1s$ - $3p$ for Na, $1s$ - $3p$, $4s$, $4p$ for K, $1s$ - $3d$, $4s$, $4p$, $5s$, $5p$ for Rb, and $1s$ - $4d$, $5s$, $5p$, $6s$, $6p$ for Cs.

2.2. Fullerenes and Fluorinated Fullerenes

The atomic coordinates of $C_{60}F_{18}$ are described in Ref. [5]. The atomic positions of the 60 carbon and 18 fluorine atoms were optimized by PM3 calculations. We used almost the same conditions for the $C_{60}F_{18}$ DV-Xα calculations as those used for the $C_{60}F_{36}$ and $C_{60}F_{48}$ calculations. For details of these C_{60}, $C_{60}F_{36}$ and $C_{60}F_{48}$ calculations please see Ref. [2].

3. RESULTS & DISCUSSION

3.1. Graphite and Alkali GICs

Figure 2 (a) shows the observed and simulated XANES spectra of graphite. Shown in Figure 2 (a) are the observed spectra and the simulated XANES spectra for graphite. As can be seen, the simulated spectrum well reproduce the observed spectrum. The energy of the lowest peak, calculated by taking into account the spin-polarization during the transition, is in good agreement with the observed value, to within 0.5 eV.

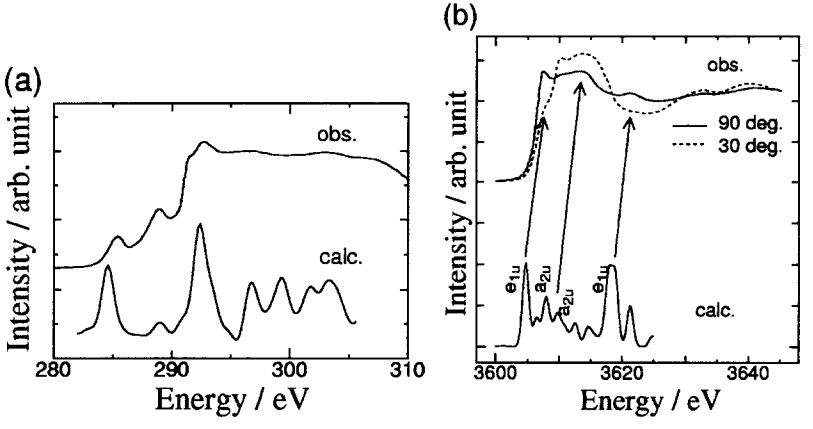

Fig. 2. (a) Comparison between the observed graphite C *K*-edge XANES spectrum and the calculated C-2*p* and 3*p* density of unoccupied states (DOUS). The transition energy was calculated as the energy difference between the DOUS and the C 1*s* orbital energy. The observed XANES spectrum was taken from Ref. [8]. (b) Comparison between the observed K *K*-edge XANES spectrum of KC_8 and the calculated K-3*p* and 4*p* DOUS. The transition energy was calculated as the energy difference between the DOUS and the K 1*s* orbital energy. The observed XANES spectrum was taken from Ref. [9].

The unoccupied K *p*-state DOS, shown in Fig. 2 (b), which we calculated for KC_{48} with Slater's transition state, is in good agreement with the observed K *K*-edge XANES spectra. [9] The calculation reproduced the edge energy to within 1.5 eV.

Figure 3 shows the alkali GIC DOS calculated near the Fermi energies (E_F). We calculated the DOS of the graphite and Rb GIC conduction

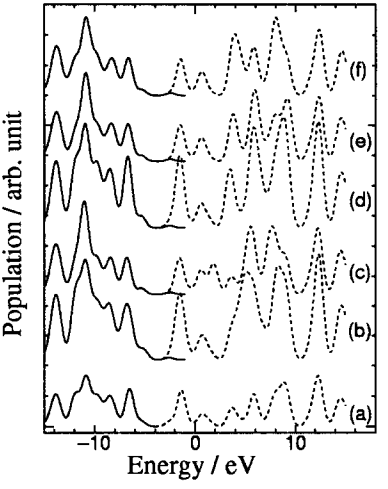

Fig. 3. Calculated DOS (solid line) and DOUS (dashed line) of graphite and alkali GIC clusters: (a) C_{24}, (b) LiC_{48}, (c) NaC_{48}, (d) KC_{48}, (e) RbC_{48} and (f) CsC_{48}.

Table II. Calculated net charges on alkali metals in GIC.

	net charge (electron)
LiC_{48}	0.870
NaC_{48}	0.998
KC_{48}	1.035
RbC_{48}	1.043
CsC_{48}	1.054

bands. They are in good agreement with the observed UPS as shown in Fig. 4. The GIC DOS profile does not change much when graphite is doped with alkali metals. However, the GIC Fermi Energies, E_F, are pushed up into the graphite conduction band.

We calculated the net charges on the alkali metals in the GIC. These are summarized in Table II. One can see that for LiC_{48} there is a charge transfer of 0.87 electrons, while the remaining alkali GIC have an almost constant value of about 1.0 electron.

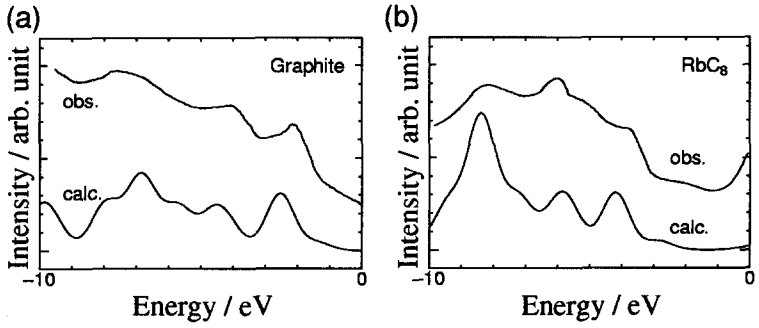

Fig. 4. Comparison between the observed UPS and the calculated DOS of (a) graphite and (b) RbC_8. The observed UPS spectra of graphite and of RbC_8 were taken from Ref. [10]. We set the energy origin at the observed Fermi Energy, E_F. We shifted the DOS energies we calculated so as to compare them with the observed spectra.

3.2. Fullerenes and Fluorinated Fullerenes

Figure 5 shows C_{60}, $C_{60}F_{36}$ and $C_{60}F_{48}$ XES spectra observed using a conventional electron probe microanalyzer. To simulate these spectra we performed DV-Xα calculations with the electronic configuration of Slater's transition state as follows. The observed XES spectra of C_{60} is represented by the C $2p$ pDOS of the carbon atom whose electronic configuration is given by $(\mathrm{CORE})^{N_0-0.5}$ $(\mathrm{UMO})^{0.5}$. Here CORE and UMO denote the core orbital and the unoccupied molecular orbital respectively and N_0 is the occupation number in the ground state. The emission energies shown in Fig. 5 (b) correspond to the energy differences between the $1s$ and $2p$ orbitals. We carried out two transition state calculations: one for the removal of 0.5 electrons from the CORE of a carbon atom connected to a fluorine atom, and the other for the removal from a bare carbon atom CORE. The simulated XES spectra are sums of the two kinds of C $2p$ pDOS, weighted by multiplying by the number of corresponding atoms of each kind. The simulated XES spectra well reproduce the observed spectra. We found that the small peak at high energy which appears on fluorination (marked with bold arrows in Fig. 5 (a)) is due to the carbon atom which is connected to a fluorine atom (Fig. 5 (b)).

Table III summarizes $C_{60}F_x$ (x = 0, 18, 36, and 48) heat of formation (HF) we calculated. The $C_{60}F_{18}$ HF is nearly equal to the average of the C_{60} and $C_{60}F_{36}$ values. Figure 6 shows the molecular structure of $C_{60}F_{18}$,

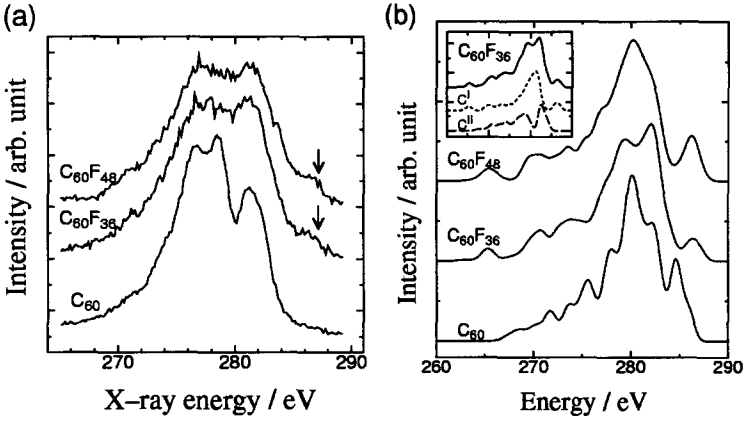

Fig. 5. (a) Observed C_{60}, $C_{60}F_{36}$ and $C_{60}F_{48}$ XES spectra. (b) Calculated C_{60}, $C_{60}F_{36}$ and $C_{60}F_{48}$ C $2p$ pDOS. The dotted (C^{I}) and dashed (C^{II}) lines in the inset indicate the C $2p$ pDOS of carbon atoms connected to fluorine atoms, and bare carbons, respectively

Table III. The calculated heat of formation of fluorinated fullerenes

	HF kcal/mol
C_{60}	812 (PM3)
$C_{60}F_{18}$	-183 (PM3)
$C_{60}F_{36}$	-952 (AM1)
$C_{60}F_{48}$	-1346 (AM1)

optimized by PM3 calculation. Since the fluorine atoms are concentrated on one side of C_{60} ball, the ball has been changed into a half sphere shape. Three C-C bonds are longer than 0.17 nm (Fig. 6) and this indicates that the bonds are weak. Therefore, we consider the $C_{60}F_{18}$ molecule to be less stable than $C_{60}F_{36}$ and $C_{60}F_{48}$. The calculated DOS of the C $1s$ (Fig. 7 (a)) and the conduction and valence bands (Fig. 7 (b)) are shown. These DOS should be compared with the XPS, UPS and XANES which, however, have not been measured so far.

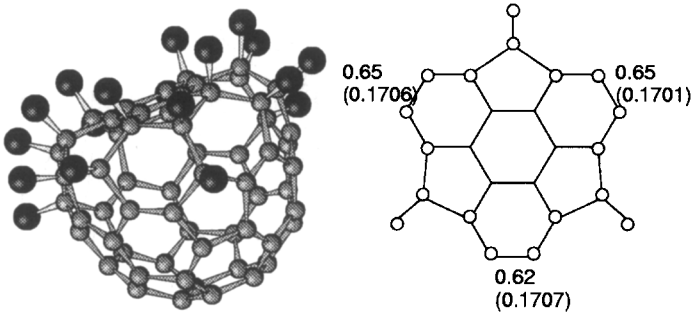

Fig. 6. Schematic picture of the $C_{60}F_{18}$ molecule (right figure). The open circle in the left figure indicates the carbon atom connected to a fluorine atom. The overlap populations (electrons) on C-C bonds are shown on the corresponding bonds. Bond lengths (nm) are shown in parentheses.

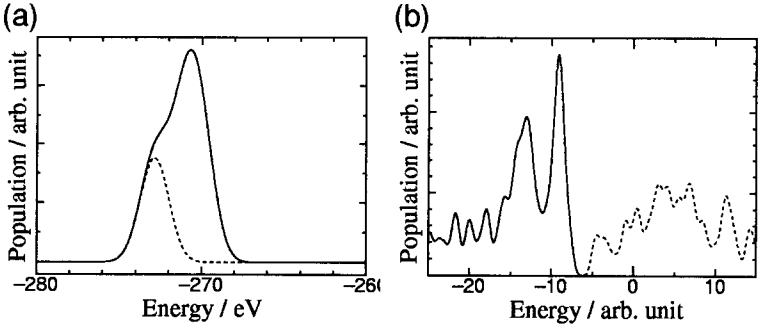

Fig. 7. (a) The calculated C 1*s* pDOS of $C_{60}F_{18}$. The dashed line indicates the pDOS of the carbon atoms connected with fluorine atoms. (b) The calculated $C_{60}F_{18}$ DOS near the Fermi Energy, E_F.

4. CONCLUSION

We have elucidated that DV-Xα calculations for model clusters of graphite, fullerene and their compounds well reproduce the appropriate XANES, UPS and XES spectra. Therefore, we consider their electronic structures as determined by the calculations to be very reliable.

REFERENCES

[1] "Advances in Quantum Chemistry", Löwdin, P., Ed.; *Academic Press*: San Diego, 1997; Vol. 29.

[2] Kawasaki, S.; Okino, F.; Touhara, H.; Sonoda, T. *Phys. Rev. B*, **1996**, *53*, 16652.

[3] Boltalina, O. V.; Borschevskii, A. Y.; Sidorov, L. N.; Street, J. M.; Taylor, R. *Chem. Commun.*, **1996**, 529.

[4] Boltalina, O. V.; Bagryantsev, V. F.; Seredenko, V. A.; Sidorov, L. N.; Zapolskii, A. S.; Taylor, R. *J. Chem. Soc., Perkin Trans. 2*, **1996**, 2275.

[5] Boltalina, O. V.; Street, J. M.; Taylor, R. *J. Chem. Soc., Perkin Trans. 2*, **1998**, 649.

[6] Boltalina, O. V.; Gol'dt, I.; Zatsepin, T.; Spiridonov, F. M.; Troyanov, S. I.; Sidorov, L. N.; Taylor, R. in *Molecular Nonostructures, Proceedings of the Intl. Winter School on Electronic Properties of Novel Materials*, World Scientific, **1998**, 114.

[7] Boltalina, O. V.; Markov, V. Y.; Taylor, R.; Waugh, M. P. *Chem. Commun.*, **1996**, 2549.

[8] Fischer, D. A.; Wentzcovitch, R. M.; Carr, R. G.; Continenza, A.; Freeman, A. J. *Phys. Rev. B*, **1991**, *44*, 1427.

[9] Loupias, G.; Rabii, S.; Tarbès, J.; Nozières, S.; Ttatr, R. C. *Phys. Rev. B.*, **1990**, *41*, 5519.

[10] Oelhafen, P.; Pfluger, P.; Hauser, E.; Güntherodt, H.-J. *Phys. Rev. Lett.*, **1980**, *44*, 197.

Atomic-number dependence of relativistic effects on chemical bonding

Jun Onoe*

The Institute of Physical and Chemical Research (RIKEN), 2-1 Hirosawa, Wako, Saitama, 351-0198 Japan.

(Received May3, 1999)

The Atomic-number dependence of the relativistic effects on chemical bonding has been studied using the difference (ΔP_B) in the bond overlap populations between the relativistic and nonrelativistic DV-Xα calculations for various XH diatomic hydrides (X=Cu, Ag, and Au) and XF_6 hexafluorides (X=S, Se, Mo, Ru, Rh, Te, W, Re, Os, Ir, Pt, U, Np, and Pu). The atomic-number dependence of ΔP_B suggests that the absolute values of ΔP_B roughly increase with order $(\alpha Z)^2$ for Z up to about 80, and the higher order term $(\alpha Z)^4$ should be taken into account for Z larger than 80, where α is the fine structure constant (=1/c, c is the velocity of light).

KEYWORDS: Relativistic effects; bond overlap population; atomic-number dependence; chemical bonding; DV-Xα

*Corresponding author: e-mail jonoe@postman.riken.go.jp

ADVANCES IN QUANTUM CHEMISTRY, VOLUME 37

0065-3276/01 $35.00

1. INTRODUCTION

Relativistic effects are significant for the understanding of the chemical properties of molecules containing heavy elements. There have been many reports concerning relativistic effects on the bond length (R_e) and the bonding energy (E_{bond}) of diatomic molecules using various kinds of molecular orbital (MO) calculations [1-3]. Pyykkö et al.[1] have systematically examined the relativistic change (ΔR_e) in R_e (the difference between relativistic and nonrelativistic results is called "relativistic change" in the present paper) for various hydride molecules using the Dirac-Fock one-centered approximation method, and shown that the ΔR_e is roughly proportional to Z^2 up to Z=80, where Z is the atomic number of the elements in the hydrides. They discussed the bond-length contraction [4-6], but did not provide the reason for the Z^2-dependence.

The relativistic changes in R_e and E_{bond} (ΔR_e and ΔE_{bond}) are often used to discuss relativistic effects on chemical bonding. ΔR_e and ΔE_{bond} are useful for examining whether or not the relativistic effects are important for molecular properties. However, these quantities are not so appropriate for describing the physical picture of the relativistic effects on chemical bonding, because it is difficult to clarify the role of the relativistic variation of each atomic orbital in connection with ΔR_e and ΔE_{bond} [7,8]. Since the chemical (covalent) bonding can be estimated by orbital overlap between atoms, the use of the relativistic changes in the overlap charge, as well as the use of ΔR_e and ΔE_{bond}, is expected to be useful in the discussion of relativistic effects on chemical bonding [9-12].

Because the bond overlap population (P_B) between valence atomic orbitals is a good indication for the strength of covalent bonding for molecules, the relativistic change (ΔP_B) in P_B corresponds to the change in bond strength that is connected with bond-length. In addition, ΔP_B is directly related to the relativistic variation of the valence atomic orbitals. Consequently, it is interesting to apply ΔP_B to the study of the atomic-number dependence of the relativistic effects on chemical bonding for various kinds of molecules.

In the previous work [13], we have examined the ΔP_B for some hexafluoride molecules XF_6 (X=S, Se, Mo, Te, W, U) using the nonrelativistic and relativistic DV-Xα methods. It was found that relativistic effects become significant in chemical bonding of molecules containing heavy elements with Z larger than 50 and ΔP_B of the XF_6 (X=S to W) shows a Z^2-dependence similar to that of ΔR_e for the hydrides [1]. On the other hand, the atomic-number dependence of ΔP_B for actinide compounds such as UF_6 was not well explained using the Z^2-dependence. However, the number of examples examined in the previous work are not satisfactory for discussing the reason for the dependence of ΔP_B.

The aim of the present work is to obtain the general trend of the atomic-number dependence of the relativistic effects on chemical bonding by examining

various kinds of XH diatomic (X=Cu, Ag, and Au) and XF_6 hexaflioride (X=S, Se, Mo, Ru, Rh, Te, W, Re, Os, Ir, Pt, U, Np, and Pu) molecules, and to discuss its reason. In section 2, the computational methods for the nonrelativistic and relativistic DV-Xα calculations are briefly described. In section 3, the results of the atomic-number dependence of the relativistic effects on chemical bonding are presented, and the reason for the atomic-number dependence is discussed. Finally, the conclusions obtained in the present work will be summarized in section 4.

2. COMPUTATIONAL METHOD

The relativistic DV-Xα calculations are based on the one-electron Hamiltonian for the Dirac-Slater MO method which is given as

$$H=c\alpha\mathbf{P} + \beta mc^2 + V(\mathbf{r}), \qquad (1)$$

where c, **P**, m, α, β, and V(**r**) denote the velocity of light, the momentum operator, the mass of an electron, the Dirac matrices, and the sum of the Coulomb and exchange potentials, respectively. The exchange potential in Eq. (1) was taken to be the same as the potential in the nonrelativistic calculation, because relativistic corrections to the exchange potential are negligibly small in the valence region which is involved in the chemical bonding [14].

The potential surrouding each atom in a molecule is not the same as that for the free atom, because electron transfer occurs between atoms in the molecule. This means that atomic orbitals in the molecule are distinct from those in the free atom. Accordingly, it is necessary to use atomic orbitals optimized for each atomic potential in the molecule, as basis functions. In the present methods, the molecular wave functions were expressed as linear combinations of atomic orbitals obtained by numerically solving the Dirac-Slater or Hartree-Fock-Slater equations in the atomic-like potential derived from the spherical average of the molecular charge density around the nuclei [15]. Thus the atomic orbitals used as basis functions were automatically optimized for the molecule and thus the minimum size of the present basis set has enough flexibility to form accurate molecular orbitals.

Matrix elements in the secular equation

$$(\mathbf{H}-\varepsilon\mathbf{S})\mathbf{C}=0 \qquad (2)$$

are evaluated as the weighted sum of integrand values at DV sample points. Here, **H**, **S**, **C**, and ε denote the Dirac Hamiltonian, overlap matrices, eigenfunctions, and eigenvalues (one-electron orbital energies), respectively.

Two-center (overlap) charge densities were partitioned into one-center (atomic) charges by means of Mulliken population analysis [16] with the self-consistent charge (SCC) method [17] which is used to approximate the self-

consistent field. According to the population analysis, the bond overlap population $P_B(k,l)$ between atoms k and l is defined by

$$P_B(k,l) = \Sigma_{(i)}\Sigma_{(r,s)}2N(i)C_{ir}{}^kC_{is}{}^l<\phi_r{}^k \mid \phi_s{}^l>. \qquad (3)$$

In eq. (3), N(i) denotes the occupation number of electrons in the i-th MO. The quantities $C_{ir}{}^k$ and $C_{is}{}^l$ represent the coefficients of the atomic orbitals $\phi_r{}^k$ and $\phi_s{}^l$ for the atoms k and l in the i-th MO, respectively. In the case of polyatomic molecules, P_B is given as a sum of all pairs of atoms by

$$P_B = \Sigma_{(k,l)}P_B(k,l). \qquad (4)$$

Since the results obtained using Mulliken population analysis depend on the choice of basis-set size, we used the same size in both nonrelativistic and relativistic calculations for each molecule. The atomic potentials for generating the basis functions were derived from the spherical average of the molecular charge density around the nuclei. The computational details of the non-relativistic and relativistic DV-Xα methods have been described elsewhere [15,18-20]. It has been confirmed that electronic structures obtained both by relativistic and non-relativistic methods agree well with each other for the molecules containing light elements, such as CF_4 and SF_6 [21], where the relativistic effects are negligibly small.

Since the relativistic DV-Xα method takes into account fully relativistic effects under Slater's exchange potential approximation, this is very useful for studying the electronic structures and chemical bonding in molecules containing heavy elements such as uranium [22-24]. Indeed, we applied the relativistic DV-Xα method to study the valence electronic structure of UF_6. The valence electronic structure obtained using the relativistic DV-Xα was in excellent agreement with the experimental valence photoelectron spectrum of UF_6 when compared with other theoretical works [25,26]. In addition, the energies corresponding to the charge transfer excitations between the F 2p and U 5f atomic orbitals obtained using this method successfully reproduced the experimental UV absorption spectrum of UF_6 and definitely explained the experimental results for the de-activation processes from the UV excited states of UF_6 [9]. Although direct relativistic effects such as mass-velocity, Darwin correction, and spin-orbit coupling are often treated with a perturbation procedure in nonrelativistic MO calculations, it is difficult to estimate the indirect relativistic effects due to the change in charge density, which is very important in the consideration of the chemical bonding in heavy molecules such as UF_6 [27].

Molecular geometries of the XH diatomic hydrides (X=Cu, Ag, Au) and XF_6 hexafluorides (X=S, Se, Mo, Ru, Rh, Te, W, Re, Os, Ir, Pt, U, Np, and Pu) molecules were assumed to be of $C_{\infty}v$ and Oh symmetry with their bond lengths taken from experiments [28-33]. As the spin function is explicitly included in eq.(1), the $C_{\infty}v$ and Oh point groups reduce to the $C_{\infty}v^*$ and Oh^* double groups, respectively, in the relativistic DV-Xα calculation. Symmetry orbitals

corresponding to irreducible representations of these double groups were constructed from the atomic orbitals using the standard projection operator method [34]. The non-relativistic and relativistic DV-Xα calculations were performed with the Slater exchange parameter α of 0.7 for all the atoms. In the numerical integration, we took 6000 DV sample points for the hexafluorides and 3000 points for the diatomic molecules. These provide a precision within an error of 0.1 eV for valence-electron energy eigenvalues. The bond lengths and basis-set sizes of the diatomic and hexafluorides molecules examined here are summarized in Table 1. Relativistic and nonrelativistic calculations were carried out self-consistently until the difference in orbital populations between the initial and final stages of the iteration was less than 0.005.

Table 1. Summary of computational conditions for diatomic molecules and hexafluorides.

Molecules	Bond length [a.u.]	Basis-set sizes			
		X		H or F	
		nonrel.	rel.	nonrel.	rel.
CuH	2.761[a]	1s-4p	$1s_{1/2}$-$4p_{1/2,3/2}$	1s-2p	$1s_{1/2}$-$2p_{1/2,3/2}$
AgH	3.056[a]	1s-5p	$1s_{1/2}$-$5p_{1/2,3/2}$	1s-2p	$1s_{1/2}$-$2p_{1/2,3/2}$
AuH	2.880[a]	1s-6p	$1s_{1/2}$-$6p_{1/2,3/2}$	1s-2p	$1s_{1/2}$-$2p_{1/2,3/2}$
SF_6	2.950[a]	1s-3d	$1s_{1/2}$-$3d_{3/2,5/2}$	1s-2p	$1s_{1/2}$-$2p_{1/2,3/2}$
SeF_6	3.194[a]	1s-4d	$1s_{1/2}$-$4d_{3/2,5/2}$	1s-2p	$1s_{1/2}$-$2p_{1/2,3/2}$
MoF_6	3.439[a]	1s-5p	$1s_{1/2}$-$5p_{1/2,3/2}$	1s-2p	$1s_{1/2}$-$2p_{1/2,3/2}$
RuF_6	3.547[c]	1s-5p	$1s_{1/2}$-$5p_{1/2,3/2}$	1s-2p	$1s_{1/2}$-$2p_{1/2,3/2}$
RhF_6	3.541[c]	1s-5p	$1s_{1/2}$-$5p_{1/2,3/2}$	1s-2p	$1s_{1/2}$-$2p_{1/2,3/2}$
TeF_6	3.430[a]	1s-5d	$1s_{1/2}$-$5d_{3/2,5/2}$	1s-2p	$1s_{1/2}$-$2p_{1/2,3/2}$
WF_6	3.462[a]	1s-6p	$1s_{1/2}$-$6p_{1/2,3/2}$	1s-2p	$1s_{1/2}$-$2p_{1/2,3/2}$
ReF_6	3.462[a]	1s-6p	$1s_{1/2}$-$6p_{1/2,3/2}$	1s-2p	$1s_{1/2}$-$2p_{1/2,3/2}$
OsF_6	3.460[a]	1s-6p	$1s_{1/2}$-$6p_{1/2,3/2}$	1s-2p	$1s_{1/2}$-$2p_{1/2,3/2}$
IrF_6	3.458[a]	1s-6p	$1s_{1/2}$-$6p_{1/2,3/2}$	1s-2p	$1s_{1/2}$-$2p_{1/2,3/2}$
PtF_6	3.439[c]	1s-6p	$1s_{1/2}$-$6p_{1/2,3/2}$	1s-2p	$1s_{1/2}$-$2p_{1/2,3/2}$
PoF_6	4.150[d]	1s-6d	$1s_{1/2}$-$6d_{3/2,5/2}$	1s-2p	$1s_{1/2}$-$2p_{1/2,3/2}$
UF_6	3.778[e]	1s-7p	$1s_{1/2}$-$7p_{1/2,3/2}$	1s-2p	$1s_{1/2}$-$2p_{1/2,3/2}$
NpF_6	3.744[f]	1s-7p	$1s_{1/2}$-$7p_{1/2,3/2}$	1s-2p	$1s_{1/2}$-$2p_{1/2,3/2}$
PuF_6	3.725[a]	1s-7p	$1s_{1/2}$-$7p_{1/2,3/2}$	1s-2p	$1s_{1/2}$-$2p_{1/2,3/2}$

a) Ref.28, b) Ref.32, c) Ref.29, d) Ref.33, e) Ref.30, f) Ref.31

3. RESULTS AND DISCUSSION

Table 2 shows the relativistic and nonrelativistic values of P_B for the diatomic and hexafluoride molecules. For the diatomic molecules, it was found that the absolute values of ΔP_B (the P_B between the relativistic and nonrelativistic calculations) increases with atomic-number Z.

Table 2. Relativistic effects on the bond overlap populations for diatomic hydride XH (X=Cu, Ag, Au) and hexafluoride molecules XF_6 (X=S, Se, Mo, Ru, Rh, Te, W, Re, Os, Ir, Pt, Po, U, Np, Pu).

	Bond overlap population (PB)		
	DV-HFS (nonrel.)	DV-DS (rel.)	ΔP_B*
29CuH	+0.646	+0.651	+0.005
47AgH	+0.57	+0.60	+0.03
79AuH	+0.53	+0.63	+0.10
$16SF_6$	+3.86	+3.85	-0.01
$34SeF_6$	+3.04	+2.95	-0.09
$42MoF_6$	+2.08	+2.23	+0.15
44RuF6	+1.49	+1.62	+0.13
45RhF6	+1.21	+1.35	+0.14
$52TeF_6$	+2.98	+2.78	-0.20
$74WF_6$	+2.13	+2.56	+0.43
75ReF6	+1.68	+2.10	+0.42
76OsF6	+1.31	+1.74	+0.43
77IrF6	+0.99	+1.44	+0.45
78PtF6	+0.69	+1.16	+0.47
84PoF6	+2.52	+2.12	-0.40
$92UF_6$	+1.21	+2.15	+0.94
93NpF6	+1.15	+2.09	+0.94
94PuF6	+1.09	+2.04	+0.95

*$\Delta P_B = P_B(\text{rel}) - P_B(\text{nonrel})$

The magnitude of ΔP_B corresponds well with that of the relativistic contraction of the bond length (ΔR_e = 1-3 pm for CuH, 4.2-10.4 pm for AgH, and 11-30.6 pm

for AuH) [1]. For the hexafluorides, the relativistic and nonrelativistic P_B values for SF_6 almost agree with each other, because the molecule has only light elements where the relativistic effects are very small. This indicates that the ΔP_B obtained using the present calculations is reliable for discussing the relativistic effects on chemical bonding. In a similar manner to the diatomic molecules, ΔP_B for the hexafluorides increases with Z. From the results of Table 2, ΔP_B becomes a good indicator for the magnitude of the relativistic effects on chemical bonding. Moreover, it is interesting to note that only the chalcogen hexafluorides such as SF_6, SeF_6, TeF_6, and PoF_6 show negative values of ΔP_B. The negative value of ΔP_B implies the relativistic weakening of chemical bonidng which results in relativistic expansion of bond length.

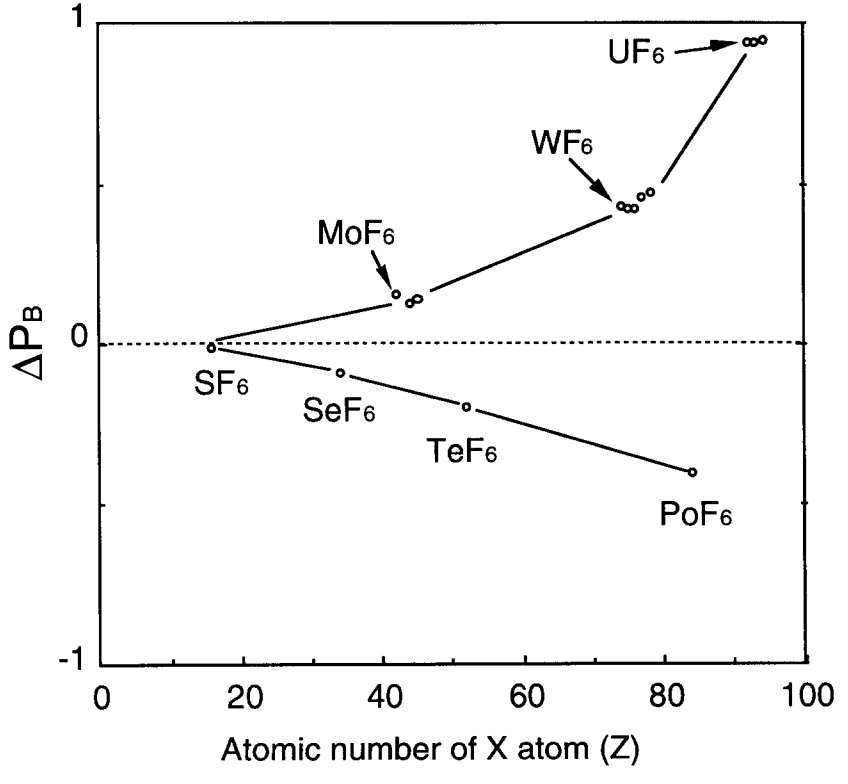

FIG. 1. The atomic-number dependence of the relativistic effects on chemical bonding for the hexafluoride molecules.

Figure 1 shows the plot of ΔP_B of the hexafluorides as a function of Z. It was found that relativistic effects on chemical bonding appear at Z larger than 10 and rapidly increase when Z goes beyond 50. As an extreme example, the P_B of the actinide hexafluorides (UF_6, NpF_6, and PuF_6) for the relativistic case are about two times greater than those for the nonrelativistic case. Figure 1 demonstrates that it is necessary to use MO calculations which fully include relativistic effects for the study of the chemical bonding in molecules containing elements with Z beyond 50.

In order to explain the atomic-number dependence of the relativistic effects on chemical bonding, the absolute value of ΔP_B, $|\Delta P_B|$, was introduced. Figure 2 shows the plot of $|\Delta P_B|$ as a function of Z^2, along with the results of the six times value of $|\Delta P_B|$ for CuH, AgH, and AuH diatomic hydrides. The reason for the multiplication of $|\Delta P_B|$ by six is to normalize the number of chemical bonds between the diatomic hydrides and hexafluorides. The solid and dashed lines shown in Fig. 2 denote functions of Z of order $(\alpha Z)^2 + (\alpha Z)^4$ and $(\alpha Z)^2$, respectively, that were fitted to the present results. B, C, and D are constants. It is interesting to note that the diatomic hydrides $|\Delta P_B|$ times six exhibits a trend similar to that for the hexafluorides with regards to Z. It is seemed that $|\Delta P_B|$ roughly increases with order Z^2 for Z up to 78 (PtF_6). This agrees well with the Z^2-dependence of ΔR_e for hydride molecules reported by Pyykkö et al. [1]. Thus ΔP_B corresponds well to ΔR_e obtained from bonding energy calculations. Let us consider the reason for the Z^2-dependence.

The physical picture on the Z^2-dependence of $|\Delta P_B|$ can be qualitatively explained as follows. As described in eq. (4), the bond overlap population P_B is obtained from the sum of all overlap populations between the X and F or H atomic orbitals. Accordingly, ΔP_B depends on the relativistic variation of the radial wavefunctions of the atomic orbitals for each molecule. Because the relativistic effects on the atomic orbitals of fluorine or hydrogen atom are negligibly small, the relativistic effects on atomic orbitals of the atom X play a dominant role in ΔP_B. It is, therefore, reasonable to investigate the atomic-number dependence of the relativistic variations of the atomic orbitals in the element X.

As described by eq.(3), ΔP_B is connected with relativistic change in atomic radial wavefunctions. It is, however, difficult to examine the atomic-number dependence of the magnitude of the ratio $|(\phi^r-\phi^{nr})/\phi^{nr}|$, where ϕ^r and ϕ^{nr} denote relativistic and nonrelativistic radial wavefunctions, respectively, for each AO. Then we investigated the atomic-number dependence of $\Delta\langle r\rangle/\langle r\rangle^{nr}$ ($\Delta\langle r\rangle=\langle r\rangle^r - \langle r\rangle^{nr}$) for each atom in the priodic table (H to Pu), where $\langle r\rangle^{nr}$ and $\langle r\rangle^r$ denote the expectation values of each atomic orbital for Hartree-Fock and Dirac-Fock atomic calculations, respectively [35]. The positive value of $\Delta\langle r\rangle/\langle r\rangle^{nr}$ shows the relativistic expansion of atomic orbitals, while the negative one shows their relativistic contraction.

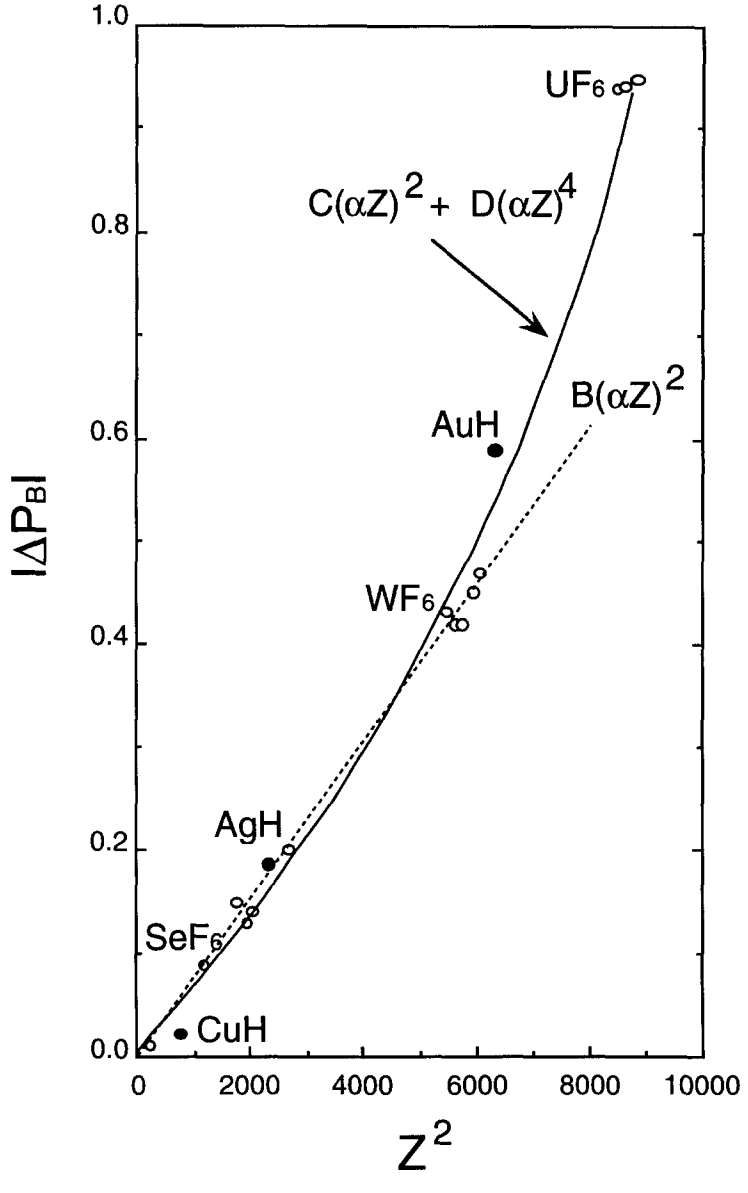

FIG. 2. The magnitudes of the relativistic effects on chemical bonding of the diatomic hydrides were plotted as a function of Z^2, together with those of the hexafluorides.

We examined the $1s_{1/2}$ radial wavefunction as a typical example. Figure 3 shows the plot of $\Delta\langle r\rangle/\langle r\rangle^{nr}$ for the $1s_{1/2}$ AO as a function of $(\alpha Z)^2$, where α is the fine structure constant (=1/137). Although the value of $\Delta\langle r\rangle$ for the $1s_{1/2}$ atomic orbital was negative for all the elements up to Z=94, we plotted its absolute value in Fig. 3, where A denotes a constant. It was found that the value of $\Delta\langle r\rangle/\langle r\rangle^{nr}$ for $1s_{1/2}$ AO changes with order $(\alpha Z)^2$ for elements with Z up to 80, while the value does not show $(\alpha Z)^2$-dependence for the actinide elements with Z beyond 80. In order to explain the entire trend of $\Delta\langle r\rangle/\langle r\rangle^{nr}$ for the $1s_{1/2}$ AO, the higher-order term $(\alpha Z)^4$ should be taken into account.

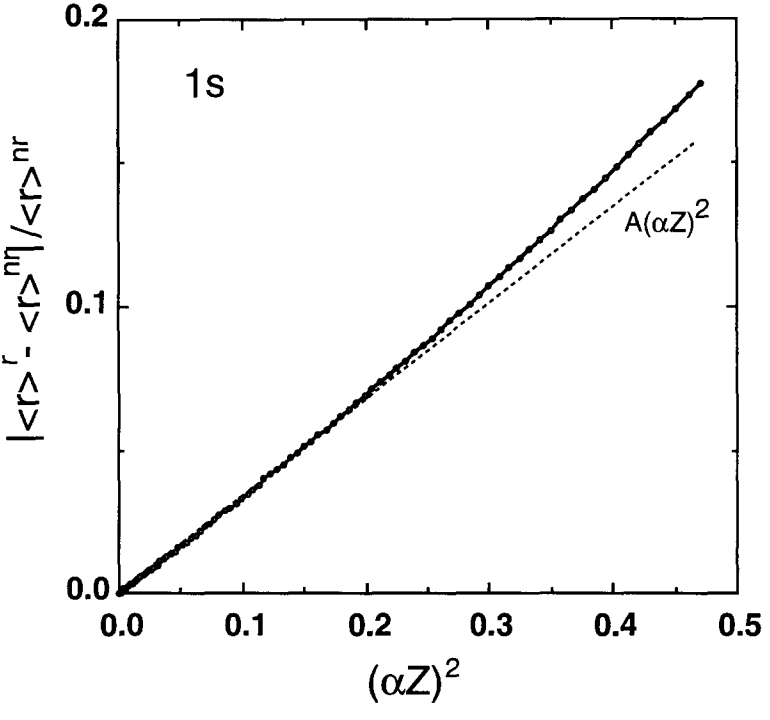

FIG. 3. Plot of $\Delta\langle r\rangle/\langle r\rangle^{nr}$ for the $1s_{1/2}$ AO as a function of $(\alpha Z)^2$

The other inner-shell orbitals with a low angular momentum (s or p orbitals) are considered to be relativistically contracted with an order similar to that of the

$1s_{1/2}$ orbital [36,37]. On the other hand, the atomic orbitals with a larger angular momentum (d or f orbitals) are relativistically expanded with the increase in the screening of the nuclear charge by the relativistic contraction of the s and p inner-shell orbitals [37]. When we focus our attention on the valence d or f atomic orbitals which can participate in the chemical bonds, we consider the magnitude of their expansion to increase with order $(\alpha Z)^2$. Hence, the difference in radial wavefunctions for atomic orbitals of the element X between the relativistic and nonrelativistic calculations varies with $(\alpha Z)^2$, which well explain the $(\alpha Z)^2$-dependence of ΔP_B for the element X with Z up to 78, as shown in Fig. 2.

It was found from Fig. 2 that the atomic-number dependence of ΔP_B for actinide hexafluorides was not well explained by the Z^2-dependence. This is because the higher-order correction $(\alpha Z)^4$ is necessary to be considered in addition to the first-order term $(\alpha Z)^2$ for Z greater than 80 [38-40]. As shown in Fig. 2, the solid line which includes both terms well explains the atomic-number dependence of $|\Delta P|$, while the dashed line including only $(\alpha Z)^2$ does not properly explain the dependence for up to the actinide compounds.

Pyykkö et al.[4] pointed out the Z^2-dependence of the relativistic bond-length contraction, but did not give its reason. Presumably, the Z^2-dependence of the bond length contraction can also be explained by the same reason. For homonuclear diatomic molecules containing heavy elements such as Pb, relativistic effects should be taken into account for both atoms when considering the atomic-number dependence of the bond overlap population.

4. SUMMARY

Relativistic molecular orbital calculations have been performed for the study of the atomic-number dependence of the relativistic effects on chemical bonding by examining the hexafluorides XF_6 (X=S, Se, Mo, Ru, Rh, Te, W, Re, Os, Ir, Pt, U, Np, Pu) and diatomic molecules (CuH, AgH, AuH), using the discrete-variational Dirac-Slater and Hartree-Fock-Slater methods. The conclusions obtained in the present work are summarized.

Examining the atomic-number dependence of the relativistic effects on the bond overlap population for the hexafluoride and diatomic molecules, it was found that the relativistic effects on chemical bonding increase with order $(\alpha Z)^2$ for Z up to 78, and the higher-order term $(\alpha Z)^4$ should be taken into account for Z beyond 78. This dependence can be roughly explained by using the scale factors for the atomic-number dependence of the relativistic effects on the $1s_{1/2}$ radial wave functions for hydrogenic atoms.

ACKNOWLEDGMENTS

The author would like to express his thanks to Prof. T. Mukoyama and Dr. H. Nakamatsu in Institute for Chemical Research at Kyoto University for helpful discussion and fruitful comments, and to Prof. R. Sekine in Department of Chemistry at Shizuoka University for a technical support.

REFERENCES

[1] P. Pyykkö, Chem. Rev. **88**, 563 (1988) and references therein.
[2] K. Balasubramanian, Chem. Rev. **89**, 1801 (1989).
[3] K. Balasubramanian, Chem. Rev. **90**, 93 (1990).
[4] P. Pyykkö, J. Chem. Soc. Faraday Trans. 2. **75**, 1256 (1979).
[5] P. Pyykkö and J.P. Desclaux, Chem. Phys. Lett. **42**, 545 (1976).
[6] P. Pyykkö and J.P. Desclaux, Chem. Phys. **34**, 261 (1978).
[7] J. Onoe et al., J. Phys. Soc. Jpn. **65**, 2459 (1996).
[8] J. Onoe, J. Phys. Soc. Jpn. **66**, 2328 (1997).
[9] J. Onoe et al., Chem. Phys. Lett. **196**, 636 (1992).
[10] J. Onoe et al., J. Chem. Phys. **99**, 6810 (1993).
[11] J. Onoe et al., J. Phys. Soc. Jpn. **63**, 3992 (1994).
[12] J. Onoe et al., Inorg. Chem. **36**, 1939 (1997).
[13] J. Onoe et al., Chem. Phys. Lett. **217**, 61 (1994).
[14] D.E. Ellis, J. Phys. B **10**, 1 (1977).
[15] H. Adachi, M. Tsukada, and C. Satoko, J. Phys. Soc. Jpn. **45**, 875 (1978).
[16] R.S. Mulliken, J. Chem. Phys. **23**, 1833, 1841, 2338, 2343 (1955).
[17] A. Rosén et al., J. Chem. Phys. **65**, 3629 (1976).
[18] F.W. Averill and D.E. Ellis, J. Chem. Phys. **59**, 6413 (1973).
[19] A. Rosén, and D.E. Ellis, J. Chem. Phys. **62**, 3039 (1975).
[20] H. Adachi, A. Rosén, and D.E. Ellis, Mol. Phys. **33**, 199 (1977).
[21] H. Nakamatsu, H. Adachi, and T. Mukoyama, Bull. Inst. Chem. Res., Kyoto Univ. **68**, 304 (1991).
[22] V. Pershina et al., J. Chem. Phys. **97**, 1123 (1992).
[23] V. Pershina et al., J. Chem. Phys. **97**, 1116 (1992).
[24] V. Pershina et al., J. Chem. Phys. **96**, 8367 (1992).
[25] J. Onoe et al., J. Electron Spectrosc. Relat. Phenom. **60**, 29 (1992).
[26] J. Onoe et al., J. Electron Spectrosc. Relat. Phenom. **70**, 89 (1994).
[27] S.J. Rose, I.P. Grant, and N.C. Pyper, J. Phys. B **11**, 1171 (1978).
[28] Jpn. Chem. Soc. ed., *Kagaku Binran* (in Japanese), Maruzen, Tokyo, II-649 (1984).
[29] G. Nagarajan and D.C. Brinkley, Z. Nature. **26a**, 1658 (1971).
[30] H.M. Seip, Act. Chem. Scand. **19**, 1955 (1965).
[31] R.A. Penneman, R.R. Ryan, and A. Rosenzweig, *Structure and Bonding*, Springer-Verlag, New York, **13**, p.1 (1973).
[32] H. Sontag and R. Weber, J. Mol. Spectrosc. **100**, 75 (1983).
[33] P. Grundevik et al., J. Mol. Srtuct. **60**, 381 (1980).
[34] J. Meyer et al., Computer Phys. Commun. **54**, 55 (1989).

[35] J.P. Desclaux, Atomic Data and Nucl. Data Tables **12**, 311 (1973).
[36] P. Pyykkö, Adv. Quantum Chem. **11**, 353 (1978) and references therein.
[37] V.M. Burke and I.P. Grant, Proc. Phys. Soc. **90**, 297 (1967).
[38] R.H. Garstang and D.F. Mayers, Proc. Camb. Phil. Soc. **62**, 777 (1966).
[39] W.H.E. Schwarz, S.Y. Chu, and F. Mark, Mol. Phys. **50**, 603 (1983).
[40] W.H.E. Schwarz et al., J. Phys. B **22**, 1515 (1989).

Relativistic Density Functional Calculations for Potential Energy Curves of Uranyl Nitrate Hydrate

Masaru Hirata*, Turgut Bastug, Shoichi Tachimori

Department of Materials Science, Japan Atomic Energy Research Institute, Tokai-mura, Naka-gun, Ibaraki 319-1195 Japan.

Rika Sekine

Department of Chemistry, Faculty of Science, Shizuoka University, Ohya 836, Shizuoka 422-8529 Japan.

Jun Onoe

The Institute of Physical and Chemical Research (RIKEN), 2-1 Hirosawa, Wako, Saitama 351-0198 Japan.

Hirohide Nakamatsu

Institute for Chemical Research, Kyoto University, Uji, Kyoto 611-0011 Japan.

(Recieved January 23, 1999)

Metal - ligand distances of U=O (uranyl oxygen) and U-OH_2 in the uranyl nitrate dihydrate have been optimized, using the all-electron fully relativistic discrete-variational Dirac - Fock - Slater (DV-DFS) MO method. The calculated bond length of U=O for a free complex is larger than the experimental value for the crystal and the U-OH_2 distance was in good agreement with the experimental results. The shape of the potential curves indicates individual strength of the U=O and U-OH_2 bonds and reveals that the U=O bond was stronger.

KEYWORDS: relativistic density functional theory, DV-DFS, uranyl nitrate, geometry optimization

*Corresponding author: e-mail hirata@popsvr.tokai.jaeri.go.jp

ADVANCES IN QUANTUM CHEMISTRY, VOLUME 37

0065-3276/01 $35.00

1. INTRODUCTION

Nuclear fuel reprocessing and partitioning allow recycling of useful fissionable materials such as uranium and plutonium, and remove harmful long-lived minor actinides (americium and curium). It is necessary also for safety storage of high-level liquid wastes(1). In order to improve efficiency of mutual separation between lanthanide and actinide elements, design of useful extractants are requisite.

For the molecular design of these extractants, knowledge of electronic and geometric structures of actinide complexes in solution are indispensable. Recently, many experimental and theoretical studies of actinide complexes have been reported by several authors (2-5). Craw and co-workers (4) studied the electronic structures of uranyl and plutonyl nitrates and their sulfates by the Hartree-Fock method with the relativistic effective core potential. In addition to the molecular orbital study, Guilbaud and Wipff (5) investigated complexation properties of uranyl nitrate and 18-crown-6 compounds by using the molecular dynamics (MD) simulation. In order to develop the suitable extractants for the actinide separation, dynamical properties of ions in solution must be clarified experimentally and theoretically. For the MD simulations, first-principles potential energy functions are necessary because of the lack of experimental data on the actinide elements. Relativistic first-principles calculations provide us important information of structural stability, potential energy functions and the electronic structure for a complex system containing heavy elements.

Since the uranyl nitrate is the most stable and fundamental species of uranium in nitric acid solutions, information on the electronic structure of this complex provides a basis of understanding stability of uranium species in solution. Information on strength of bonding between uranium and the ligands such as water and organic species is the major concern for design of novel extractants for the selective separation of the actinides.

The stability of water molecules and uranyl groups is important because the replacement of water molecules with extractants govern the extraction characteristics. In the present work, we therefore examine dependence of the total energy of the system on the interatomic distances between uranium and the ligands: the oxygen of the water molecules and the uranyl groups. In order to get the potential energy curves for the hexavalent uranyl nitrate dihydrate complex $UO_2(NO_3)_2(H_2O)_2$, we apply the all-electron fully relativistic discrete-variational Dirac-Fock-Slater(DV-DFS) method (6-9). The U 5f, 6d orbital contributions to the stabilization of these bonds are also clarified.

2. COMPUTATIONAL

The geometric structure of the uranyl nitrate dihydrate with D_{2h} symmetry is shown in Fig. 1 (10,11). Two nitrate ions and two water molecules lie in the same plane.

In all the calculations for the electronic and geometric structures of the system, the density functional method (6-9) was used. The total energy, E, in the Dirac-Fock-Slater approximation is expressed as a functional of charge density $\rho(r)$:

$$E[\rho] = \sum_i n_i \langle \phi_i | \mathbf{t} | \phi_i \rangle + \int \rho V^n \, d^3r + \frac{1}{2} \int \rho V^c d^3r$$

$$+ \frac{3}{4} \int \rho V^{ex} d^3r + \sum_{p>q} \frac{Z_p Z_q}{| R_p - R_q |} \quad , \qquad (1)$$

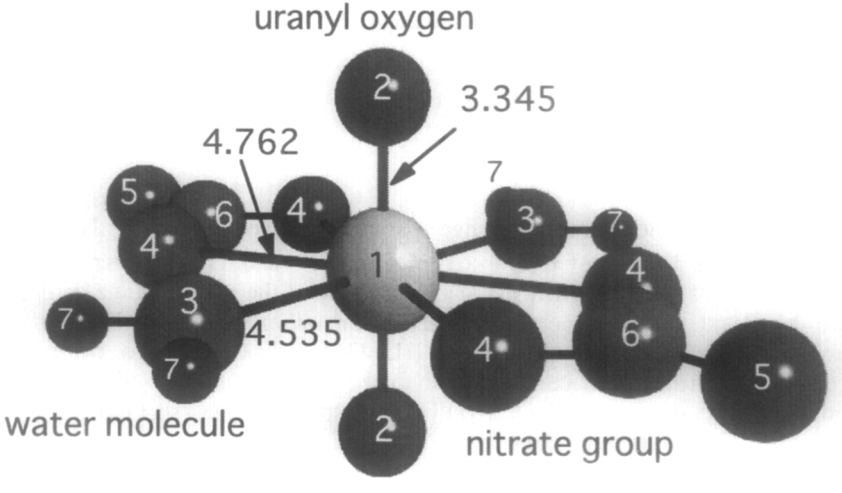

Fig 1. Model cluster of uranyl nitrate dihydrate.
Indices from 1 to 7 designate atoms U, O(O=U), O(OH_2), O(O_2NO), O(ONO_2), N and H, respectively.
Distances are shown in a.u.

where **t** is the Dirac kinetic energy operator and $\phi_i(\mathbf{r})$ is the wave functions of electron for the *i*-th molecular orbital (MO). The electronic density denoted by ρ is

$$\rho(\mathbf{r}) = \sum_i n_i \phi_i^*(\mathbf{r}) \phi_i(\mathbf{r}) \quad , \qquad (2)$$

where n_i is the occupation number of the *i*-th MO, V^n represents the potential energy of the interaction of the electrons with the nuclei, and V^c is the Coulomb-interaction potential among the electrons:

$$V^C(\mathbf{r}) = \int \frac{\rho(\mathbf{r}')}{|\mathbf{r} - \mathbf{r}'|} d^3\mathbf{r}' \quad . \qquad (3)$$

The last two terms in Eq.(1) represent the exchange-correlation energy of electrons and the nucleus-nucleus Coulomb interaction energy, respectively. The total energy functional E[ρ] in Eq. (1) has a minimum for the ground state density ρ. In the present calculations, the exchange-correlation potential was approximated by the simplest Slater potential:

$$V^{ex}(\mathbf{r}) = -3\alpha \left(\frac{3}{8\pi} \rho(\mathbf{r}) \right)^{1/3} , \qquad (4)$$

where α was the Slater exchange parameter, fixed at 0.7. Numerical wavefunctions 1s - 7p of U, 1s - 2p of O and N, and 1s of H were used as basis functions. To evaluate the stable structure of the uranyl nitrate complex, we calculated the total energies at various interatomic distances between the uranium and adjacent oxygen atoms (U=O and U-OH_2). To clarify the contribution from each atomic orbital to the chemical bonds, we examined orbital overlap populations by the Mulliken's population analysis (12).

3.RESULTS AND DISCUSSION

Figure 2 shows the valence level structure of $UO_2(NO_3)_2(H_2O)_2$. The solid and dashed lines indicate occupied and unoccupied MO levels, respectively. The energy gap between HOMO and LUMO is 1.60 eV. The main component

of HOMO is the O 2p orbitals of nitrate groups, while LUMO involves the U 5f orbitals as the main contribution.

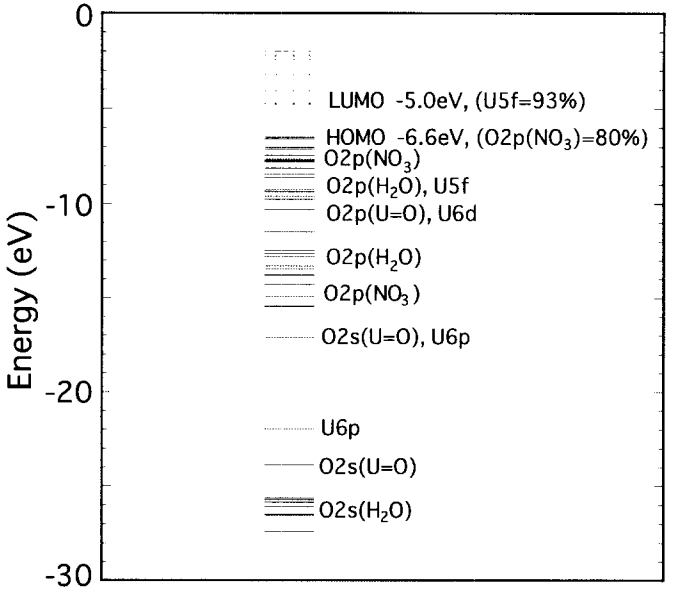

Fig 2. Energy levels of uranyl nitrate.

In order to clarify the chemical bonds between uranium and the ligands of hexavalent uranyl nitrate dihydrate, we investigate change of the total energy with the interatomic distances of U=O and U-OH_2. Figure 3 shows the obtained potential energy curves. The reference of the interatomic distance is taken from the equilibrium structure for the crystal. The change in total energy with the U-OH_2 distance is gradual around the minimum and the minimum total energy value is obtained near the experimental equilibrium distance. On the other hand, the total energy curve for U=O has different features from that for U-OH_2. The total energy increases sharply with the decreasing U=O distance. The minimum value of the total energy appears at a distance longer than the experimental value.

To confirm the minimum point of the total energy profile with respect to the U=O distance, other exchange - correlation potentials were also examined: a local density functional by Vosko-Wilk-Nusair (VWN) (14) and a nonlocal

one with the Generalized Gradient Approximation (GGA) by Becke (15). In both of the VWN and GGA calculations, relativistic extension of the exchange-correlation potentials, which was developed by Engel et al. (16,17), was used. Details of the software used is described elsewhere (18).

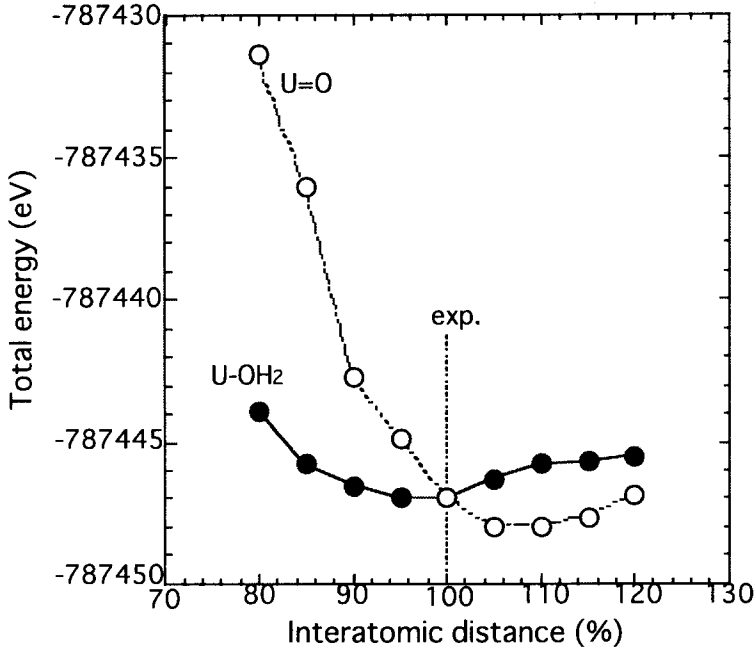

Fig 3. Total energy variations with U=O and U-OH_2 distances. Equilibrium interatomic distances for the crystal is the reference.

Table 1 shows total energies with Slater, VWN and GGA at different U=O distances. The minimum total energies are obtained at longer positions than the experimental value. The calculated results correspond to the isolated complex, but this complex in the actual crystal is surrounded by other water and nitrate species. Because the complex is placed in the network of hydrogen bonds in the crystal (10,11), the interatomic distance between U and uranyl oxygen of the free complex may be larger than the crystal data.

Table 1. Total energy variation(eV) with U=O bond distance for different exchange-correlation potentials.

Distance*	Slater	VWN	GGA
U=O 100%	-787447.830	-785325.710	-786738.038
U=O 105%	-787448.003	-785326.405	-786739.033
U=O 110%	-787448.232	-785326.328	-786739.239

*Experimental equilibrium distance for the crystal is the reference.

Table 2. Orbital overlap population for U=O and U-OH_2 bonds at the equilibrium distance.

U=O bond				U-OH_2 bond			
U6s-O2s,2p	U6p-O2s,2p	U6d-O2s,2p	U5f-O2s,2p	U6s-O2s,2p	U6p-O2s,2p	U6d-O2s,2p	U5f-O2s,2p
-0.210	-0.291	0.642	0.467	-0.021	-0.085	0.173	0.062

In the previous paper (13), we have discussed the chemical bonding nature of uranyl nitrate dihydrate and found that the bonding interaction is mainly due to the U 5f, 6d - O 2p components. In the present work, we carry out orbital overlap population analysis to understand contribution of each atomic orbital to the chemical bonding. The orbital overlap populations indicate strength of covalent bonds (19,20).

Table 2 shows orbital overlap populations between valence orbitals of U (6s, 6p, 6d and 5f) and O (sum of the 2s and 2p contributions) for the experimental equilibrium structure. The 6d-2s,2p and 5f-2s,2p orbital overlap populations of the U=O bond are 0.642 and 0.467, respectively. For the U-OH_2 bond, the orbital overlap populations are weaker, i.e., 0.173 (6d-2s,2p) and 0.062 (5f-2s,2p) for each component. Both of the U 5f and 6d covalent interactions form the U=O bonds, while the U 5f contribution to the U- OH_2 bonds is small even in comparison with the U 6d contribution. Because of the weakness of the covalent interaction in the U-OH_2 bond, the potential energy curve for the U-OH_2 bond is gradual around the minimum as shown in Fig. 3.

On the contrary to U-OH_2, the U=O potential minimum is clear due to the strong covalent interaction between U and O of the U=O group. As shown in Table 2, the U 6s - O 2s,2p and U 6p - O 2s,2p orbital overlap populations for the U=O bond are large negative values. These antibonding interactions are larger than those for the U-OH_2 bond. This means that the core-core

repulsion makes the steep rise of the total energy at the shorter distances than at the equilibrium one. Consequently, the shape of the potential curve is explained with the chemical bond nature.

The present results show that the DV-DFS method is applicable to calculations of potential energy curves for such a heavy and complicated system as uranyl nitrate dihydrate. It may also be useful to derive first-principles potential energy curves for the MD simulations. The electronic structure and MD results will be valuable for understanding dynamical properties of actinide ions in solution and for molecular design of novel extractants for selective separation of actinides.

REFERENCES

(1) K.L. Nash and G.R. Choppin eds. "Separations of f elements", Plenum press, New York, 1995.
(2) P.G. Allen, J.J. Bucher, D.K. Shuh, N.M.Edelstein and T. Reich, *Inorg. Chem.* , **1997**, *36*, 4676.
(3) T. Yaita, H. Narita, S. Suzuki, S. Tachimori, H. Shiwaku and H. Motohashi, *J. Alloys Compounds*, **1998**, *271-273* , 184 .
(4) J.S. Craw, M.A. Vincent, I.H. Hillier and A.L. Wallwork, *J. Phys. Chem.*, **1995**, *99*, 10181.
(5) P. Guilbaud and G. Wipff, *J. Phys. Chem.*, **1993**, *97*, 5685.
(6) A. Rosen and D.E. Ellis, *J. Chem. Phys.*, **1975**, *62*, 3039.
(7) H. Nakamatsu, H. Adachi and T. Mukoyama, *Bull. Inst. Chem. Res. Kyoto Univ.*, **1992**, *70*, 16.
(8) T. Bastug, D. Heinemann, W.-D. Sepp, D. Kolb and B. Fricke, *Chem. Phys. Lett.*, **1993**, *211*, 119.
(9) T. Bastug, W.-D. Sepp, D. Kolb, B. Fricke, G. Te Velde, E. J. Baerends, *J. Phys. B: At. Mol. Opt. Phys.*, **1995**, *28*, 1833.
(10) N.K. Dalley, M.H. Mueller and S.H. Simonsen, *Inorg. Chem.*, **1971**, *10* , 323.
(11) J.C. Taylor and M.H. Mueller, *Acta Crystallogr.*, **1965**, *19*, 536.
(12) R.S. Mulliken, *J. Chem. Phys.*, **1955**, *23*, 1833,1841,2338,2343 .
(13) M. Hirata, R. Sekine, J. Onoe, H. Nakamatsu, T. Mukoyama, K. Takeuchi, S. Tachimori, *J. Alloys and Compounds*, **1998**, *271-273*, 128.
(14) S.H. Vosko, L. Wilk, M.Nusair, *Can. J. Phys.*, **1980**, *58*, 1200.
(15) A.D. Becke, *Phys. Rev.*, **1988**, *A38*, 3098.
(16) E. Engel, S. Keller, R.M. Dreizler, *Phys. Rev.*, **1996**, *A53*, 1367.

(17) E. Engel, S. Keller, R.M. Dreizler, in: Electronic Density Functional Theory: Recent Progress and New Directions, eds. by J.F. Dobson, G.Vignale and M.P. Das (Plenum, New York, 1998), p.149.
(18) S. Varga, E. Engel, W.-D. Sepp, B. Fricke, *Phys. Rev. A*, submitted.
(19) J. Onoe, K.Takeuchi, H. Nakamatsu, T. Mukoyama, R. Sekine, B.-II. Kim, H. Adachi, *J. Chem. Phys.*, **1993**, *99*, 6810.
(20) J. Onoe, H. Nakamatsu, T. Mukoyama, R. Sekine, H. Adachi, K. Takeuchi, *Inorg. Chem.*, **1997**, *36*, 1934.

Electronic structures and chemical bonding of actinyl nitrates dihydrates

Masaru Hirata*, Shoichi Tachimori

Department of Materials Science, Japan Atomic Energy Research Institute, Tokai-mura, Naka-gun, Ibaraki 319-1195 Japan

Rika Sekine

Department of Chemistry, Faculty of Science, Shizuoka University, Ohya 836, Shizuoka 422-8529 Japan

Jun Onoe

The Institute of Physical and Chemical Research (RIKEN), 2-1 Hirosawa, Wako, Saitama 351-0198 Japan

Hirohide Nakamatsu

Institute for Chemical Research, Kyoto University, Uji, Kyoto 611-0011 Japan

(Recieved May 11, 1999)

The electronic structures and chemical bonding of actinyl nitrates [$AnO_2(NO_3)_2 \cdot 2H_2O$, An=U, Np and Pu] was studied using the discrete-variational Dirac-Fock-Slater MO method. The strength of both the covalent and the ionic bonds decreases with atomic number of the actinide. This change arises from variations in both the occupancy and the energy of the HOMO. Changes in the energies of the HOMO and LUMO correspond to changes in the stability of the hexavalent state in the actinyl nitrates. The characteristics of each ligand bonds were also analyzed.

KEYWORDS: Dirac-Fock-Slater, DV-DFS, uranyl nitrate, neptunyl nitrate, plutonyl nitrate, stability, bonding nature

*Corresponding author: e-mail: hirata@popsvr.tokai.jaeri.go.jp

ADVANCES IN QUANTUM CHEMISTRY, VOLUME 37

0065-3276/01 $35.00

1. INTRODUCTION

The mutual separation of actinide elements and the selective isolation of useful actinides from fission products are indispensable for the nuclear fuel cycle and have become important subjects of investigation for the development of advanced nuclear fuel reprocessing and TRU (TRans Uranium elements) waste management [1]. A variety of research concerning the separation chemistry of actinides has so far been accumulated [2]. There are, however, only a few theoretical studies on actinides in solution[3-5]. Schreckenbach et al. discussed the stability of uranyl (VI) tetrahydroxide $[UO_2(OH)_4]^{2-}$ [3] and Spencer and co-workers calculated the optimized structures of some uranyl and plutonyl hydrates $[AcO_2^{2+} \cdot nH_2O$ (Ac = U, Pu and n = 4,5,6)] [4].

From a practical point of view, results of TBP(tributyl phosphate) and other organophosphorus extraction of UO_2^{2+}, NpO_2^{2+} and PuO_2^{2+} from aqueous HNO_3 media have shown a $D(UO_2^{2+}) > D(NpO_2^{2+}) > D(PuO_2^{2+})$ tendency in the distribution coefficients[1]. In order to study the mutual separation of actinides, information concerning the electronic structure of actinide-ligand complexes is important. The interaction between the metal cation and the water molecules plays a critical role in determining the aqueous phase binding preference of the ligating species. Using the Hartree-Fock MO method with effective core potentials, Craw et al. [5] discussed the electronic structures of nitrate and sulfate complexes for uranyl and plutonyl. They calculated the binding energies for the uranyl and plutonyl nitrate and sulfate complexes. The binding energies for the uranyl and plutonyl nitrates were similar to each other.

Knowledge of the nature of the bonding between the actinide atom and the oxygen atom of the water molecule is more informative for the application of theoretical methods to the extraction separation of actinides. Since there is only a small energy difference between the An 5f and An 6d (An=U, Np, Pu) atomic orbitals, the contributions of these atomic components may change when the ligands are substituted by extractants. Therefore, information on the electronic structures of uranyl, neptunyl and plutonyl nitrate complexes is very important for understanding their stability and allows the design of ligands useful for the selective separation of actinides.

The aim of the present work is to perform a detailed theoretical study of the electronic structures of actinyl nitrates. Relativistic effects are remarkable in the electronic structure and chemical bonding of heavy atoms such as actinide elements[6]. In our previous study, we applied the relativistic discrete variational Dirac-Fock-Slater(DV-DFS) method to study of the electronic structure of uranyl nitrate dihydrate[7]. The accuracy of the DV-DFS method was demonstrated by its ability to reproduce the uranyl nitrate dihydrate experimental X-ray photoelectron spectrum.

In the present investigation we will use the DV-DFS method to compare uranyl, neptunyl and plutonyl nitrate dihydrates from the viewpoint of their partial densities of states due to the An components. We discuss the similarity and difference in the electronic structures of these actinide nitrate dihydrates in order to estimate their stabilities. We also apply population analysis to confirm how far the An electrons contribute to the chemical bonding between the actinide and donor oxygen atoms. Finally, we compare the bonding nature between the

actinides and the ligands to understand the characteristics of the water molecules which are to be replaced by extractants.

2. COMPUTATIONAL METHOD

2.1. DV-DFS molecular orbital method

The DV-DFS molecular orbital(MO) method is based on the Dirac-Fock-Slater approximation. This method provides a powerful tool for the study of the electronic structures of molecules containing heavy elements such as uranium[7,8,9,10]. The one-electron molecular Hamiltonian in the Dirac-Fock-Slater MO method is written as

$$\mathbf{H} = c\alpha\mathbf{P} + \beta mc^2 + V(r), \qquad (1)$$

where c, **P**, m, α, β and V(r) denote the velocity of light, the operator of momentum, the rest mass of electron, the Dirac matrices and the sum of Coulomb and exchange potentials, respectively. The molecular wavefunctions were obtained by taking linear combinations of atomic orbitals. The details of the DV-DFS method and the computational code used in the present work have been described elsewhere [6,11]. The basis functions, which were numerical solutions of the atomic Dirac-Fock-Slater equations for an atomic-like potential, were obtained at the initial stage of each iteration of the self-consistent procedures[12]. The atomic-like potentials for generating the basis functions were derived from the spherical average of the molecular charge density around the nuclei. One-center(atomic) charges were estimated in terms of the Mulliken populations [13] by the self-consistent charge(SCC) method[14] which was used to approximate the self-consistent field.

All the DV-DFS calculations were performed with the Slater exchange parameter α of 0.7 and with 20000 DV sample points. The basis functions for the actinide atoms were used up to the 7p orbital, while those for the oxygen and nitrogen atoms up to the 2p orbital and 1s for the hydrogen atom. The calculations were carried out self-consistently until the difference in orbital populations between the initial and final stages of the iteration was less than 0.01.

2.2. Cluster model

For the present work, we took neutral $AnO_2(NO_3)_2 \cdot 2H_2O$ (where An=U, Np and Pu) complexes with D_{2h} symmetry. Since the spin function is included in

eqn.(1), the D_{2h} symmetry reduces to the D_{2h}^{*} double group. Symmetry orbitals corresponding to irreducible representations of the D_{2h}^{*} symmetry were constructed from the atomic orbitals using the projection operator method [15].

The geometry of $UO_2(NO_3)_2 \cdot 2H_2O$ shown in Fig. 1 was taken from the X-ray and neutron diffraction data reported by Taylor et al. [16,17]. Bond lengths and angles for $NpO_2(NO_3)_2 \cdot 2H_2O$ and $PuO_2(NO_3)_2 \cdot 2H_2O$ were estimated using the ionic radius ratios between uranium and the respective hexavalent actinide ions as a basis [18]. The An ionic radii used were 0.73 Å for UO_2^{2+}, 0.72 Å for NpO_2^{2+} and 0.71 Å for PuO_2^{2+}[19].

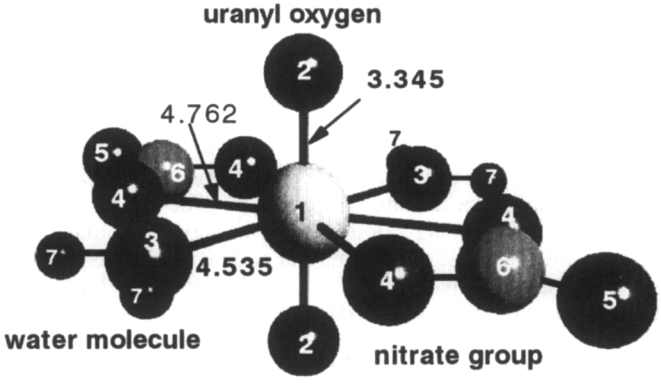

Fig 1. Geometry of $UO_2(NO_3)_2 \cdot 2H_2O$.
The bond lengths are in the atomic units.
The atoms are numbered for later reference.

3. RESULTS AND DISCUSSION

3.1. Electronic structure of valence levels

Figure 2 shows the valence energy level structures for the actinyl nitrate dihydrates obtained from the relativistic DV-DFS method. The highest occupied molecular orbitals (HOMO) are shown connected with broken lines as are the lowest unoccupied molecular orbitals (LUMO). These energy level

structures are basically similar to each other. The HOMO for uranyl nitrate ($48g_{5u}$) is full with two electrons in it. Surplus electrons occupy the next level, $49g_{5u}$, in the other actinides. The HOMO of neptunyl nitrate is occupied by a single electron while that for plutonyl nitrate is doubly occupied.

Table 1 shows atomic orbital components for the valence MOs. The notation O, in (O=U) for example, refers to the oxygen atom of the uranyl group. The occupied energy levels are divided into two parts, i.e., an upper part (> -16 eV) and a lower part (< -17 eV). The lower part is constructed mainly of O 2s and An 6p components.

In the upper part, the O 2p components of the ligands are dominant. Above $49g_{5u}$ which is occupied in the neptunyl and plutonyl nitrates, An 5f is the major component. The components and energies of each orbital are similar in all of the complexes. The electronic structures are also almost equivalent, with the exception of the number of electrons in $49g_{5u}$.

Next, we studied the distributions of the An orbital components and of the ligand oxygen components. As shown in Table 1(a), the O 2p component arises from the donors of O_2NO, U=O, OH_2 and O_2NO, in order from high energy down. The O 2p component of O(U-O_2NO) mainly contributes to the MOs from $48g_{5u}$ to $43g_{5u}$. The O 2p component of O(O=U) group distribute from $44g_{5u}$ to $39g_{5g}$ (-7.9 ~ -10.4 eV) and O 2p of O(U-OH_2) is located from $44g_{5u}$ to $34g_{5u}$ (-7.9 ~ -15.5 eV). That of O(U-O_2NO) appears again in the levels from $38g_{5g}$ to $33g_{5g}$ (-12.5 ~ -15.5 eV). The U 5f and 6d components, which contribute to the covalent bonding interact with the O 2p major components in the upper part of the valence region. The U 6d component appears lower than U 5f in the O 2p band. This means that U 6d interacts more strongly with the ligands than does U 5f. The An 6p levels appear in the lower part of Table 1. They are split into two groups, the $33g_{5u}$, $32g_{5u}$ group and the $28g_{5u}$, $26g_{5u}$ group, due to the spin - orbit interaction. The An 6p orbitals strongly interact with O 2s of O(O=An).

The An 5f and the An 6d orbitals in the actinides have similar energies. Therefore, both the An 5f and 6d components of the valence levels play an important role in the chemical bonding between the actinide atoms and the ligands. Figure 3 illustrates how the An 5f and An 6d components are distributed in the levels, for uranyl, neptunyl and plutonyl nitrates dihydrates. The components of An 5f and An 6d in each level are convoluted with a Gaussian function for convenience of comparison. The perpendicular lines indicate the HOMO. The energy of the $49g_{5u}$ level containing the main An 5f component, gradually decreases as the atomic number increases. On the other hand, the $53g_{5g}$ level, which is mainly made up of An 6d, remains unchanged. Therefore, the An 5f contribution to the O 2p valence levels increases with atomic number and the area occupied by An 5f in the O 2p region is extended.

As we have shown, a distinct difference which occurs in the electronic structures of these complexes is that the number of electrons and location of the An 5f levels is not fixed. This difference leads to some trends in the stability of the complexes, which will be discussed in the next section.

Table 1(a). Atomic orbital components for valence levels of $UO_2(NO_3)_2 \cdot 2H_2O$.

Orbital	Eergy	*(1)U			(2)O (O=U)		(3)O (-OH2)		(4)O (-O2NO)		(5)O (-O2NO)		(6)N		(7)H
	(eV)	5f	6p	6d	2s	2p	2s	2p	2s	2p	2s	2p	2s	2p	1s
49 γ 5u	-4.8	0.94													
	(HOMO)														
48 γ 5u	-6.6	0.09								0.29		0.60			
	(LUMO)														
47 γ 5g	-6.7			0.06						0.25		0.69			
47 γ 5u	-7.1	0.07				0.07				0.32		0.51			
46 γ 5g	-7.1					0.06				0.36		0.58			
45 γ 5g	-7.5									0.97					
46 γ 5u	-7.7	0.05								0.95					
45 γ 5u	-7.7									0.67		0.26			
44 γ 5g	-7.8									0.77		0.21			
44 γ 5u	-7.9	0.13				0.12		0.07		0.5		0.12			
43 γ 5u	-8.2	0.21				0.21		0.18		0.28		0.06			
43 γ 5g	-8.5					0.29		0.59							
42 γ 5g	-8.7					0.60				0.29					
42 γ 5u	-9.3	0.20				0.45		0.26		0.05					
41 γ 5u	-9.4	0.21				0.27		0.42		0.05					
41 γ 5g	-9.4			0.09		0.29				0.43		0.09			
40 γ 5u	-9.7	0.31				0.59		0.06							
40 γ 5g	-9.8			0.24		0.69									
39 γ 5g	-10.4			0.24		0.47		0.26							
39 γ 5u	-11.5	0.09					0.08	0.62							0.12
38 γ 5g	-12.5			0.06			0.05	0.48	0.05	0.10		0.06			0.09
38 γ 5u	-12.6								0.05	0.18	0.25	0.33		0.16	
37 γ 5g	-12.8							0.17		0.12	0.22	0.27		0.11	
36 γ 5g	-13.3							0.16	0.16	0.33				0.16	0.10
37 γ 5u	-13.5								0.22	0.47		0.05		0.21	
36 γ 5g	-13.8									0.28		0.11		0.61	
35 γ 5g	-13.8									0.28		0.11		0.61	
35 γ 5u	-14.3							0.48	0.08		0.05				0.28
34 γ 5g	-14.9							0.48		0.14				0.05	0.27
34 γ 5u	-15.5							0.14	0.28	0.23	0.07		0.09		0.08
33 γ 5g	-15.5								0.33	0.28	0.12		0.13		
33 γ 5u	-17.2		0.31		0.50	0.08									
32 γ 5u	-22.1		0.85												
32 γ 5g	-23.9			0.13	0.82										
31 γ 5u	-25.7		0.06						0.55		0.05			0.28	
31 γ 5g	-25.8								0.66					0.29	
30 γ 5u	-25.9		0.12		0.05		0.20		0.19		0.17			0.19	0.05
30 γ 5g	-26.1								0.19		0.39			0.33	
29 γ 5u	-26.5		0.12				0.34		0.08		0.17			0.14	0.09
29 γ 5g	-26.5						0.76								0.17
28 γ 5u	-27.5		0.44		0.17		0.24								0.06
28 γ 5g	-31.5								0.30	0.09	0.12		0.47		
27 γ 5u	-31.6								0.30	0.08	0.11		0.47		
26 γ 5u	-33.4		0.77		0.15	0.05									

* Numbers correspond to those in Fig. 1.

Table 1(b). Atomic orbital components for valence levels of $NpO_2(NO_3)_2 \cdot 2H_2O$.

Orbital	Energy	*(1)Np			(2)O (O=Np)		(3)O (-OH2)		(4)O (-O2NO)		(5)O (-O2NO)		(6)N		(7)H
	(eV)	5f	6p	6d	2s	2p	2s	2p	2s	2p	2s	2p	2s	2p	1s
50 γ 5u	-5.3	0.92													
	(LUMO)														
49 γ 5u	-5.4	0.91													
	(HOMO)														
48 γ 5u	-6.6	0.13								0.25		0.60			
47 γ 5g	-6.7									0.26		0.67			
47 γ 5u	-7.2	0.09								0.30		0.48			
46 γ 5g	-7.2					0.09				0.34		0.57			
45 γ 5g	-7.6									0.95					
46 γ 5u	-7.8									0.92					
45 γ 5u	-7.8									0.65		0.23			
44 γ 5g	-7.9									0.76		0.22			
44 γ 5u	-7.9	0.20				0.16		0.10		0.34		0.15			
43 γ 5u	-8.2	0.16				0.19		0.10		0.43					
43 γ 5g	-8.3					0.37		0.59							
42 γ 5g	-8.7					0.75				0.16					
42 γ 5u	-9.1	0.26				0.52				0.11					
41 γ 5u	-9.3	0.23				0.40		0.30							
41 γ 5g	-9.3			0.14		0.35				0.37		0.09			
40 γ 5u	-9.4	0.25				0.30		0.39							
40 γ 5g	-9.4			0.18		0.43				0.23					
39 γ 5g	-10.1			0.22		0.38		0.37							
39 γ 5u	-11.5	0.09					0.09	0.63							0.11
38 γ 5g	-12.6			0.07				0.51		0.09					0.09
38 γ 5u	-12.7									0.18	0.27	0.33		0.15	
37 γ 5g	-12.9							0.14		0.12	0.24	0.28		0.11	
36 γ 5g	-13.5							0.18	0.17	0.32				0.14	0.11
37 γ 5u	-13.7								0.23	0.47				0.19	
36 γ 5u	-14.1									0.28		0.11		0.61	
35 γ 5g	-14.1									0.28		0.11		0.61	
35 γ 5u	-14.4							0.44	0.10						0.26
34 γ 5g	-15.1							0.46		0.15					0.26
33 γ 5g	-15.5								0.34	0.30	0.11		0.12		
34 γ 5u	-15.5							0.18	0.26	0.23					0.10
33 γ 5u	-17.6		0.32		0.52										
32 γ 5u	-22.3		0.86												
32 γ 5g	-23.6				0.84										
31 γ 5u	-26		0.13						0.42					0.25	
31 γ 5g	-26.1								0.65					0.31	
30 γ 5u	-26.1		0.11				0.24		0.26					0.17	
30 γ 5g	-26.5						0.15		0.15					0.29	
29 γ 5g	-26.7						0.64								0.15
29 γ 5u	-26.8						0.23		0.12		0.24			0.21	
28 γ 5u	-27.5		0.36		0.17		0.29								
28 γ 5g	-32								0.30				0.47		
27 γ 5u	-32.1								0.29		0.11		0.46		
26 γ 5u	-33.6		0.83												

* Numbers correspond to those in Fig. 1.

Table 1(c). Atomic orbital components for valence levels of $PuO_2(NO_3)_2 \cdot 2H_2O$.

Orbital	Energy	(1)Pu			(2)O (O=Pu)		(3)O (-OH2)		(4)O (-O2NO)		(5)O (-O2NO)		(6)N		(7) H
	(eV)	5f	6p	6d	2s	2p	2s	2p	2s	2p	2s	2p	2s	2p	1s
50 γ 5u	-5.7	0.88													
	(LUMO)														
49 γ 5u	-5.8	0.88													
	(HOMO)														
47 γ 5g	-6.7									0.28		0.66			
48 γ 5u	-6.6	0.18								0.22		0.57			
46 γ 5g	-7.3					0.14				0.32		0.54			
47 γ 5u	-7.3	0.11				0.11				0.28		0.46			
45 γ 5g	-7.6					0.11				0.89					
46 γ 5u	-7.9	0.07				0.12				0.64		0.13			
45 γ 5u	-7.9	0.08								0.79					
44 γ 5u	-8.0	0.19				0.15				0.34		0.20			
44 γ 5g	-8.0									0.75		0.23			
43 γ 5g	-8.1					0.40		0.51							
43 γ 5u	-8.3	0.15				0.21				0.47		0.08			
42 γ 5g	-8.6					0.85									
42 γ 5u	-8.9	0.25				0.47				0.19					
41 γ 5u	-9.1	0.31				0.50		0.09							
41 γ 5g	-9.1			0.22		0.64									
40 γ 5u	-9.4	0.19				0.11		0.65							
40 γ 5g	-9.5			0.09						0.65		0.13			
39 γ 5g	-10.0			0.20		0.30		0.46							
39 γ 5u	-11.5	0.09					0.09	0.63							0.11
38 γ 5g	-12.6			0.08				0.55							0.10
38 γ 5u	-12.9									0.17	0.29	0.33		0.13	
37 γ 5g	-13.0							0.09		0.14	0.27	0.30		0.11	
36 γ 5g	-13.6							0.19	0.17	0.21				0.23	0.12
37 γ 5u	-13.8								0.24	0.46				0.18	
36 γ 5u	-14.4							0.39	0.13	0.08					0.23
35 γ 5g	-14.5									0.27		0.11		0.61	
35 γ 5u	-14.5									0.27		0.11		0.60	
34 γ 5g	-15.3							0.45		0.16					0.25
33 γ 5g	-15.5								0.34	0.31	0.10		0.11		
34 γ 5u	-15.6							0.23	0.24	0.22					0.13
33 γ 5u	-18.0		0.33		0.54										
32 γ 5u	-22.5		0.86												
32 γ 5g	-23.4			0.11	0.85										
31 γ 5u	-26.1		0.33		0.19		0.15		0.08					0.09	
30 γ 5u	-26.4						0.13		0.52					0.27	
31 γ 5g	-26.5								0.63					0.32	
30 γ 5g	-26.8						0.62				0.08			0.08	0.14
29 γ 5g	-27.0						0.16		0.15		0.31			0.29	
29 γ 5u	-27.1		0.06				0.15		0.14		0.28			0.27	
28 γ 5u	-27.5		0.28		0.14		0.34								0.08
28 γ 5g	-32.6								0.30				0.47		
27 γ 5u	-32.6								0.29				0.46		
26 γ 5u	-34.1		0.86												

*Numbers correspond to those in Fig. 1.

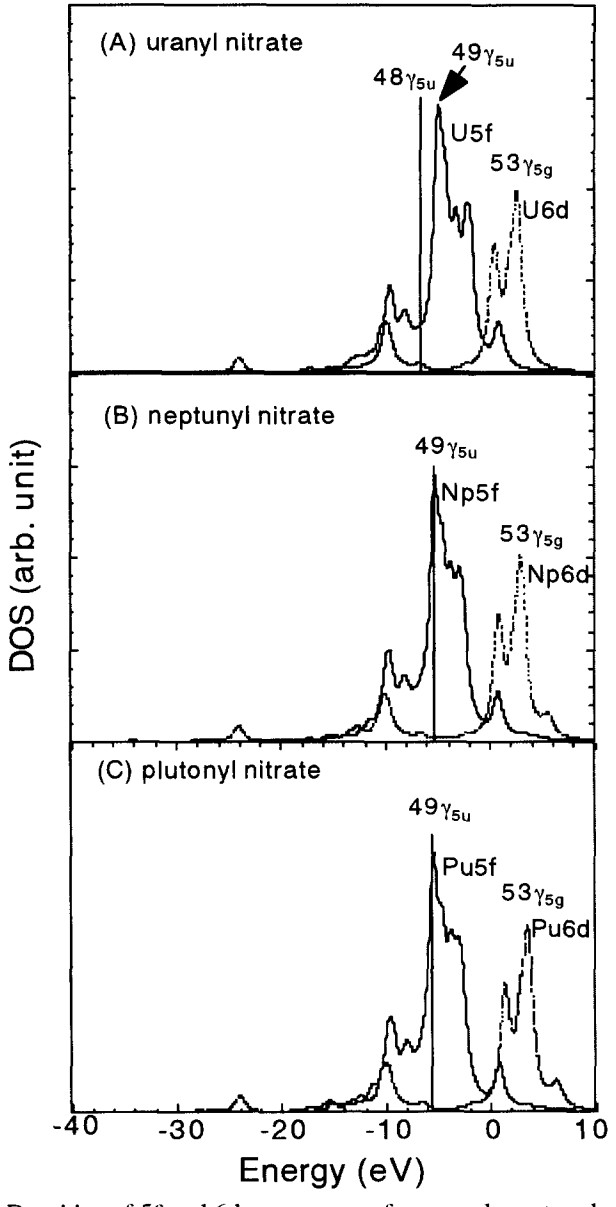

Fig 3. Densities of 5f and 6d components for uranyl, neptunyl and plutonyl nitrates dihydrates.

This increase in the An 5f contribution, discussed above, changes the effective charge of the An which affects the strength of the ionic bond with the ligands. The change in the An 5f contribution also has an effect on the covalent bond, this, however, is negligible compared with another change which occurs in the covalent bond. This is described in the next section. A complex's resistivity to oxidation and reduction also depends on the level position.

3.2. Chemical bonding

Table 2 summarizes orbital populations for both the actinide atoms and the donor oxygen atoms. The electron configurations for the ideal perfect ions which are defined for formal charges in these actinyl nitrates are [Rn] $5f^0 6d^0$ for U(VI), [Rn] $5f^1 6d^0$ for Np(VI) and [Rn] $5f^2 6d^0$ for Pu(VI). Any variation in the orbital populations from those of the formal configurations means that to some extent there is some covalent bond formation. A significant changes in the orbital population is an increase in the number of An 5f, 6d electrons.

Table 2. Valence orbital population and effective charges of actinides and oxygen atoms

		$UO_2(NO_3)_2 \cdot 2H_2O$	$NpO_2(NO_3)_2 \cdot 2H_2O$	$PuO_2(NO_3)_2 \cdot 2H_2O$
An	An5f	2.94	4.07	5.14
	An6s	1.99	1.99	1.99
	An6p	5.75	5.77	5.80
	An6d	1.99	1.95	1.90
	An7s	0.19	0.18	0.18
	An7p	0.26	0.25	0.24
effective charge		+0.84	+0.76	+0.69
An=O	O2s	1.85	1.87	1.88
	O2p	4.46	4.43	4.42
effective charge		-0.30	-0.27	-0.25
OH_2	O2s	1.75	1.74	1.73
	O2p	3.64	4.65	4.66
effective charge		-0.39	-0.39	-0.40
O_2NO	O2s	1.80	1.79	1.78
	O2p	4.50	4.50	4.50
effective charge		-0.29	-0.29	-0.29

To clarify how far An 5f and An 6d components contribute to the covalent bonds with the ligands, the bond overlap population, which is a good indicator of the strength of a covalent bond, is used. When this value is positive, the An-O interaction is bonding one. Negative values, however, imply an antibonding interaction. An analysis of the bond overlap populations for each atomic orbital is useful for the understanding of the nature of the chemical bond [6, 20]. Table 3 shows the bond overlap populations between the actinide atoms and the oxygen atoms of the ligands. The An 6s - O 2s, 2p and An 6p - O 2s, 2p interactions are found to be antibonding. The bonding interaction is mainly due to the An 5f - O 2p and An 6d - O 2s, 2p overlaps.

The An 5f and An 6d electrons mainly contribute to the covalent bonding between the actinide and actinyl oxygen atoms, as shown in Table 3(a). The orbital overlap populations for both the water molecules and the nitrate groups are found to be smaller. As shown in Table 2, as atomic number changes, the positive effective charge on An slightly decreases and the orbital population of the An 5f electrons increases from 2.94 to 5.14. The increased An 5f electrons in Np and Pu, compared to U, occupy the antibonding state $49\gamma_{5u}$ and so decrease the bond overlap population. Actually, for all the ligands the orbital overlap populations between the An 5f and the O 2s and O 2p orbitals, for U, Np and Pu complexes, decrease in the order of the U > Np > Pu as shown in Table 3.

Ionic contribution to the chemical bonding are also important for the stability of these actinyl nitrate complexes. As shown in Table 2, the magnitude of the effective charge on An, on O(O=An) and on O(An-O_2NO) decreases with increase in atomic number. On the other hand, the magnitude of effective charges on O(An-OH_2) for U, Np and Pu complexes increases in the order U < Np < Pu.

To estimate the ionic bonding strength between the actinide atoms and the water molecules, we estimate the Coulomb energy V which exists between the effective charges on the ions.

$$V = Z_{eff}(\text{cation}) \cdot Z_{eff}(\text{anion}) / R(\text{c-a}), \qquad (2)$$

where Z_{eff}(cation), Z_{eff}(anion) are the effective charges on the cation and anion respectively. R(c-a) is the interatomic distance between the cation and anion in atomic units (a.u.). Here, the cations are the actinide atoms and the anions are the water molecule oxygen atoms. As shown in Table 4, the Coulomb energies thus calculated are -1.93 , -1.79 and -1.69 eV for the uranyl, neptunyl and plutonyl nitrates respectively. Therefore, the Coulomb interaction between the actinides and the water molecule oxygen atoms, for U, Np and Pu complexes, decreases in the order U > Np > Pu.

Table 3. Orbital overlap and bond overlap population between actinide atoms and adjacent oxygen atoms (b.o.p.:bond overlap population)

(a) An=O

	U			Np			Pu	
	O2s	O2p		O2s	O2p		O2s	O2p
5f	0.04	0.42	5f	0.04	0.41	5f	0.04	0.40
6s	-0.03	-0.18	6s	-0.03	-0.19	6s	-0.03	-0.19
6p	-0.17	-0.12	6p	-0.17	-0.11	6p	-0.17	-0.10
6d	0.10	0.54	6d	0.10	0.53	6d	0.10	0.53
7s	0.04	-0.02	7s	0.04	-0.02	7s	0.03	-0.03
7p	0.06	0.05	7p	0.05	0.04	7p	0.05	0.04
b.o.p.		1.35			1.30			1.27

(b) An-OH_2

	U			Np			Pu	
	O2s	O2p		O2s	O2p		O2s	O2p
5f	0.02	0.04	5f	0.02	0.03	5f	0.02	0.02
6s	-0.01	-0.02	6s	-0.01	-0.02	6s	-0.01	-0.02
6p	-0.04	-0.06	6p	-0.04	-0.06	6p	-0.04	-0.06
6d	0.08	0.09	6d	0.08	0.09	6d	0.09	0.09
7s	0.01	0.04	7s	0.01	0.04	7s	0.01	0.04
7p	0.03	0.01	7p	0.03	0.01	7p	0.03	0.01
b.o.p.		0.40			0.40			0.38

(c) An-O_2NO (per bond)

	U			Np			Pu	
	O2s	O2p		O2s	O2p		O2s	O2p
5f	0.00	0.05	5f	0.00	0.05	5f	0.00	0.04
6s	-0.00	-0.02	6s	-0.00	0.02	6s	-0.00	-0.02
6p	-0.01	-0.06	6p	-0.01	0.06	6p	-0.01	-0.06
6d	0.03	0.09	6d	0.03	0.09	6d	0.03	0.09
7s	0.01	0.03	7s	0.01	0.03	7s	0.01	0.03
7p	0.05	0.01	7p	0.06	0.01	7p	0.06	0.01
b.o.p.		0.40			0.38			0.37

Table 4. Coulomb interactions between actinides and the oxygens of the water molecules.

	$UO_2(NO_3)_2 \cdot 2H_2O$	$NpO_2(NO_3)_2 \cdot 2H_2O$	$PuO_2(NO_3)_2 \cdot 2H_2O$
Z_{eff}(cation)	+0.84	+0.76	+0.69
Z_{eff}(anion)	-0.39	-0.39	-0.40
R(An-O) (a.u.)	4.535	4.478	4.403
V* (eV)	-1.93	-1.79	-1.69

* Coulomb energy between effective charges (see the text)

The extraction proceeds through replacement of the water molecules of the complex by extractants at the organic solvent - water interface. Consequently, the bonding nature between the actinide atoms and the water molecules is important in estimating the stability of the extractant complexes. The stability of the water ligand in actinyl nitrates decreases in the order of U > Np > Pu in both the ionic and covalent interactions as discussed above. In Fig. 2, the HOMO of the uranyl nitrate is lower in energy than that of the other actinyl nitrates. The LUMO of plutonyl nitrate is the lowest and that of uranyl nitrate is the highest of these nitrates. The energy levels for the HOMO and LUMO correspond to the oxidation and reduction reactions, respectively, and to the stability of the An oxidation states. It is well known that the hexavalent uranyl nitrate is the most stable of these actinyl nitrates and is difficult to reduce, while plutonyl nitrate is less stable and fairly easy to reduce [21]. Because of the HOMO and LUMO energies, the hexavalent uranyl nitrate is more stable than neptunyl and plutonyl nitrates.

To elucidate individual covalent interaction between U and each ligand, we investigate the energy dependence of the bond overlap populations between U and the oxygen atoms of the ligands as shown in Fig. 4. In this figure as well as Fig. 3, each level is convoluted with a Gaussian function for convenience of comparison. The positive bond overlap population indicates covalent bonding. In the bond overlap population profile of the U=O bond, a large bond overlap population appears around -33 eV and it is attributed to the U 6p - O 2s overlap. As the counter part of this, a large antibonding part lies around -17 eV. There is bonding interaction between -33 to -17 eV, which is ascribed to the O 2s, 2p - U 6d overlap. Because of the shorter distance of U=O, the orbital interaction between U and O(O=U) is considerably large while those for the other ligands is small in this energy region.

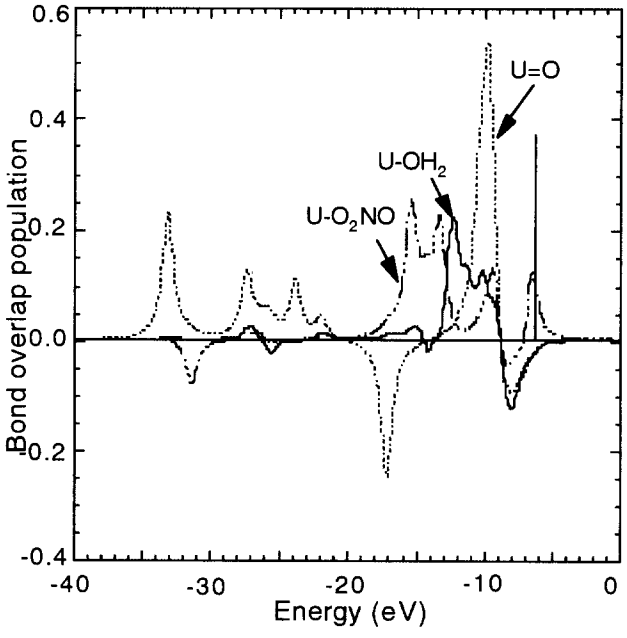

Fig 4. Bond overlap population plots for U=O, U-O_2NO and U-OH_2 of uranyl nitrate dihydrate.

The bonding interactions between the uranium and the oxygen which occur for each ligand are attributable to the positive overlap populations from -9 to -17 eV. These are mainly due to the bonding interactions which exist between the U 5f, 6d and the ligand O 2p. The peaks are located sequentially from the low energy side in the order U-O_2NO, U-OH_2 and U=O. The negative effective charge of the O(OH_2) is larger than that of O(O_2NO). We therefore make the interpretation that the peaks for each ligand arise mainly from the interaction with the An 5f, 6d and are located in the same order as the respective ligand O 2p orbital energies. For U=O, the situation is not so simple because of the participation of U 6p. The U-O bonds show notable antibonding interaction near the HOMO level. In this region, the U 6s, 6p - O 2p antibonding interactions are found to be predominant. The antibonding due to occupied U 6s and 6p means that the sphere of the U ion produces a repulsive interaction with the oxygen ion. The first stage of the extraction reaction is governed by replacement of the water molecules with extractants. Thus, the nature of the bonding which occurs between the actinide atoms and the water molecules is much more important than that which occurs between the actinide atoms and the other ligands.

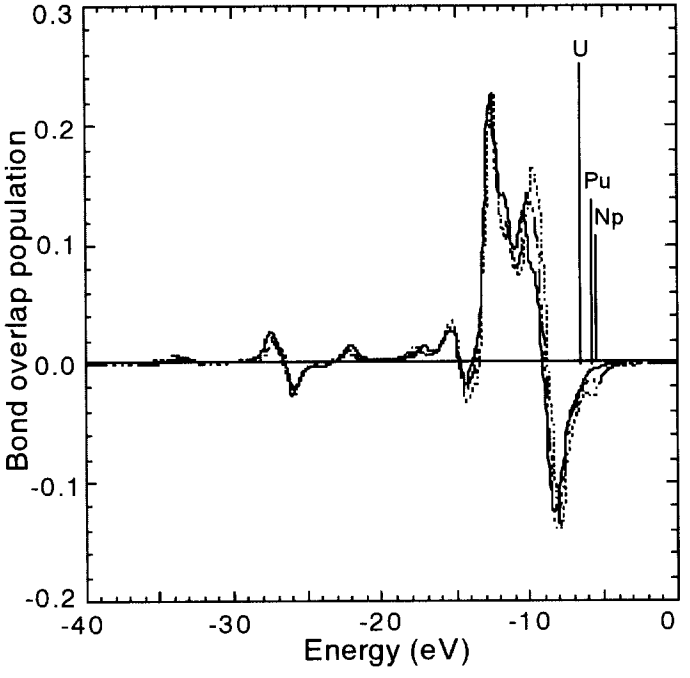

Fig 5. Bond overlap population plots for U-OH_2, Np-OH_2 and Pu-OH_2 of actinyl nitrate dihydrate, rigid curve: U, broken curve: Np and dotted curve: Pu.

It is remarkable that the strength of the covalent bond with the water ligand is not small, as shown in Fig. 4 and Table 3. Figure 5 shows how the overlap populations between the actinide atoms and the oxygen atom of the water molecule depend on the energy. The bonding interaction between the water molecules and actinyl exists in the energy range -10 eV to -15 eV, and the energy levels near the HOMO are antibonding.

Around -10 eV, the overlap population increases with actinide atom in the order U < Np < Pu. This corresponds to the increase of the An 5f population which is shown in Fig. 3. That is, the lowering of the An 5f level enhances the covalency in this energy region. The next prominent change is found at the HOMO where the electrons in the An 5f MO level produce an antibonding character. In Table 3, the decrease in the overlap population of An-OH_2 is attributed to the decrease in the orbital overlap population of An 5f - O 2p. This arises from the An 5f HOMO level though it is not obvious in Fig. 5 that the

increase of the An 5f population around -10 eV is actually canceled by the sum of the small negative changes of the population.

4. CONCLUSION

We have performed relativistic calculations on hexavalent uranyl, neptunyl and plutonyl nitrate dihydrates using the DV-DFS method. The valence energy level structures were similar to each other except for the HOMO level. The An 5f electrons of Np and Pu occupy the antibonding states and they contribute to the decrease in the bonding interaction between the actinide atoms and the oxygen atom of the water molecules.

The HOMO and LUMO energies correspond to the oxidation and reduction stabilities of hexavalent actinide nitrates in solution. The strength of both the covalent and the ionic bonds decreases with the atomic number of the actinides. This change arises from variation in both the occupancy and the energy of the HOMO. The characteristics of each of the ligand bonds were also analyzed. These bases for understanding the chemical nature will be useful for stability estimation of actinide-extractant complexes and the following molecular design of new extractants for selective separation of actinides.

ACKNOWLEDGMENTS

We are grateful to Professors T. Mukoyama and H. Adachi at Kyoto university for valuable discussions and encouragement.

REFERENCES

(1) Z. Kolarik, "Behavior of transuranium elements in the PUREX process" in A.J. Freeman and C. Keller eds. " Handbook on the physics and chemistry of the actinides" , Elsevier Science Publishers B.V., (1991).
(2) K.L. Nash and G.R. Choppin eds. "Separation of f elements" Plenum Press, New York (1995).
(3) G. Schreckenbach, P.J. Hay and R.L. Martin, *Inorg. Chem.*, **1998**, *37*, 444.
(4) S. Spencer, L. Gagliardi, N.C. Handy, A.G. Ioannou, C-K. Skylaris, A. Willetts and A.M. Simper, *J. Phys. Chem. A*, **1999**, *103*, 1831.
(5) J. S. Craw, M.A. Vincent, I.H. Hillier and A.L. Wallwork *J. Phys. Chem.*, **1995**, *99* , 10181.
(6) J. Onoe, K. Takeuchi, H. Nakamatsu, T. Mukoyama, R. Sekine, B. Kim and H. Adachi, *J. Chem. Phys.*, **1993**, *99* , 6810.
(7) M. Hirata, H. Monjyushiro, R. Sekine, J. Onoe, H. Nakamatsu, T. Mukoyama, H. Adachi and K. Takeuchi. *J. Electron Spectrosc. Relat. Phenom.*, **1997**, *83*, 59.

(8) J.Onoe, K. Takeuchi, H. Nakamatsu, T. Mukoyama, R. Sekine and H. Adachi, *J. Electron Spectrosc. Relat. Phenom.*, **1992**, *60*, 29.
(9) J.Onoe, K. Takeuchi, H. Nakamatsu, T. Mukoyama, R. Sekine and H. Adachi, *J. Electron Spectrosc. Relat. Phenom.*, **1994**, *70* , 89.
(10) T. Mukoyama, H. Nakamatsu and H. Adachi, *J. Electron Spectrosc. Relat. Phenom.*, **1993**, *63* , 409 .
(11) A. Rosen and D.E. Ellis, *J. Chem. Phys.*, **1975**, *62* , 3039.
(12) H. Adachi, M. Tsukada and C. Satoko, *J. Phys. Soc. Jpn. 1978*, *45* , 875 .
(13) R. S. Mulliken, *J. Chem. Phys.*, **1955**, *23* , 1833; **1955**, *23* , 1841; **1955**, *23* , 2338 ; **1955**, *23* , 2343.
(14) A. Rosen, D.E. Ellis, H. Adachi and F.W. Averill, *J. Chem. Phys.*, **1976**, *65* , 3629 .
(15) J. Meyer, W.D. Sepp, B. Fricke and A. Rosen, *Computer Phys. Commun.*, **1989**, *54* , 55.
(16) J.C. Taylor and M.H. Mueller, *Acta Cryst.*, **1965**, *19* , 536.
(17) N.K. Dalley, M.H. Mueller and S.H. Simonsen, *Inorg. Chem.*, **1971**, *10* , 323 .
(18) Yu. F. Volkov, I.I. Kapshukov, *Radiokhimiya*, **1976**, *18*, 284.
(19) R.D. Shannon, *Acta Cryst.*, **1976**, *A32* , 751.
(20) J.Onoe, *J. Phys. Soc. Jpn.*, **1997**, *66* , 2328.
(21) J.C. Bailar, H.J. Emeleus, R. Nyholm, A.F. Trotman-Dickenson eds., "Comprehensive inorganic chemistry, Vol. 5, Actinides", Pergamon press, New York (1973).

Molecular-dynamics simulations of gold clusters

Turgut Baştuğ[1] Masaru Hirata, Sven Varga[2], Burkhard Fricke[2]

Department of Materials Science, Japan Atomic Energy Research Institute, Tokai-mura, Naka-gun, Ibaraki 319-1195, Japan.

Şakir Erkoç

Department of Physics, Middle East Technical University, 06531 Ankara , Turkey.

Takeshi Mukoyama

Institute for Chemical Research, Kyoto University, 611-0011 Kyoto, Japan.

(Received May1, 1999)

Structural stability and energetics of gold microclusters Au_n (n=3-13,19-555) have been investigated by molecular-dynamics simulations. A model potential energy function has been parametrized for the gold element by using the dimer interaction potential energy profile of the Au_2, which is calculated by relativistic density functional method. Stable structures of the microclusters for (n=3-13) have been determined by a molecular-dynamics simulation. It has been found that gold microclusters prefer to form three-dimensional compact structures. Molecular-dynamics simulations have also been performed for spherical gold clusters generated from *fcc* crystal structure with sizes (n=19-555).

KEYWORDS: gold clusters, molecular dynamics, density functional
e-mail address: bastug@matres.tokai.jaeri.go.jp

[1]Author to whom correspondence should be addressed
[2]Permanent address: Fachbereich Physik, Universität Kassel, 34109-Kassel, Germany

ADVANCES IN QUANTUM CHEMISTRY, VOLUME 37

0065-3276/01 $35.00

1. INTRODUCTION

Clusters play an important role in understanding the transition from the microscopic to the macroscopic structure of matter. The research field of clusters, particularly microclusters, has shown rapid development in both experimental and theoretical investigations in the last two decades [1–3]. Although there has been considerable improvement in the experimental techniques [4], there are still difficulties in the production and/or investigation of isolated microclusters of some elements. Accurate quantum-chemical [2, 5] or molecular dynamics [6] methods are very useful in explaining many finer experimental details of microclusters with some 20 or fewer atoms. Although the capacity of computers has strongly been increased during recent years, these kind of calculations are still limited to either rather small numbers of atoms or to high symmetric cluster models. On the other side classical molecular-dynamics computer simulations provide both a deeper understanding of the experimental observations and they can also be applied for large systems which are practically difficult to calculate with *ab-initio* or quantum molecular-dynamics methods. Molecular dynamics simulations using empirical model potentials have been used successfully to investigate bulk, surface, and cluster properties of elements. Several empirical potential energy functions have been proposed and applied to various systems in the last decade [7-9].

Gold clusters are the most studied metal species that ranges from compounds with typical molecular properties to colloids [10, 11]. There exist many experimental and theoretical works on gold compounds like $Au_{55}(PPh_3)_{12}Cl_6$ [12]. The structures and the properties of this clusters have been well characterised by different spectroscopic techniques. Recently in an density functional *ab-initio* study Häberlen et. al [13] have studied the properties of naked high symmetric gold clusters.

Although there exist accurate *ab-initio* calculations on gold cluster, these calculations are quite expensive and time consuming. On the other hand molecular-dynamics (MD) simulations provide an easy tool to obtain the structural stability of clusters. One of the authors (S.E.) has performed molecular dynamics simulations for gold clusters [14] using empirical potentials based on purely experimental data.

In this study we have parameterised a semi-empirical potential energy function (PEF) for the gold element which is discussed in part two and three. Using the semi-empirical PEF we performed molecular-dynamics (MD) simulations to predict the optimum geometries of gold microclusters. Results and discussions are given in part four.

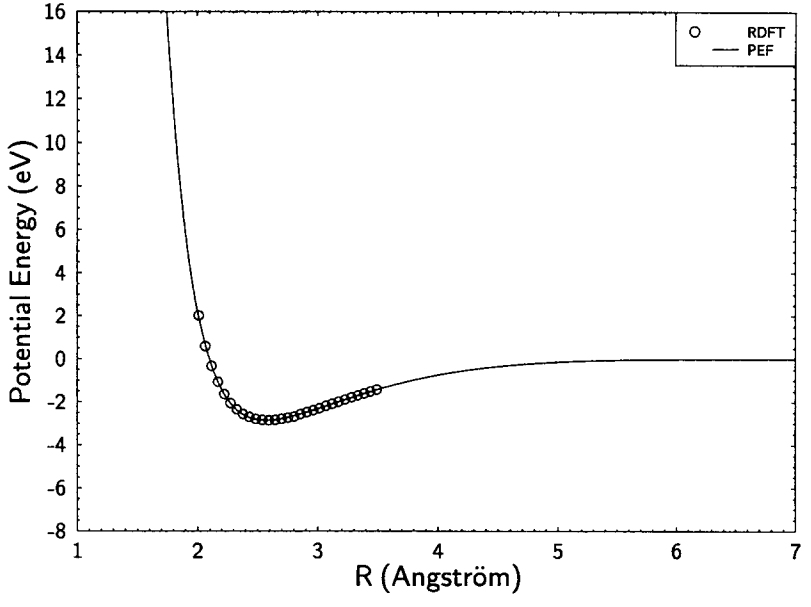

Fig 1. Potential energy curve of the Au_2. Circles represent the relativistic density functional theory (RDFT) results, full line represents the fitted empirical pair potential energy function (PEF).

These atomic orbitals are four-component Dirac spinors. The symmetrization coefficients are obtained by the use of group theoretical projection operators [21]

$$\phi_i(r) = \sum_j \chi_j c_{ji} = \sum_j \xi_{n_v}(r) d_{n_v j} c_{ji}, \tag{4}$$

where $n_v = (\nu, n, \kappa, m)$. Here v indicates atomic site and m and κ are magnetic and Dirac quantum numbers. The variational coefficients are determined by using standard procedure for solving the secular equation

$$\mathbf{HC} = \varepsilon \mathbf{SC} \tag{5}$$

where **H** and **S** are the Hamiltonian and overlap matrices, respectively. The matrix elements are evaluated numerically by using the modified version for relativistic numerical wave functions [22] of the integration scheme of Boerrigter, Velde and Baerends [23]. The direct Coulomb potential V^c has been calculated via an additional variational procedure, which reduces the numerical errors and yields a variationally consistent total energy [16].

The numerical (1s-6p) Kohn-Sham orbitals of the neutral Au atom are chosen together with 6d orbitals of the $Au^{2.5+}$ion as the basis set. The binding energy of the Au_2 is calculated as a difference of total energies of the Au_2 molecule and two Au atoms in their ground states. The atomic total energies are calculated by the molecular code in order to increase the numerical accuracy.

The calculated potential energy curve of the Au_2 molecule is presented in Fig. 1 together with the fitted PEF. Using different basis set and exchange correlation potentials we have calculated $r_e = 2.534$ Å, $D_e = 3.11$ eV, and $\omega_e = 187$ cm^{-1} [24]. Comparing to experimental results [25] of bond distance, $r_e = 2.470$ Å, binding energy $D_e = 2.30$ eV, and vibration frequency $\omega_e = 191$ cm^{-1} we estimate slightly deeper binding energy and larger bond distances. Reasons of this has been discussed in [24].

3. PARAMETRIZATION OF THE PEF

We have expressed the pair potential energy function (PEF) of the dimer with in the form of the recently developed empirical function, which works well for transition metals [14]. It's form is

$$U(r) = \frac{A_1}{r^{\lambda_1}} e^{-\alpha_1 r^2} + \frac{A_2}{r^{\lambda_2}} e^{-\alpha_2 r^2} = U_{21}(r) + U_{22}(r). \tag{6}$$

The first term represents the repulsive branch and the second term represents the attractive branch of the interaction potential between two atoms. By performing a non linear least square fit procedure the parameters $(A_1, \alpha_1, \lambda_1; A_2, \alpha_2, \lambda_2)$ of the empirical pair potential are determined. In the fit procedure we have used the binding energy values of Au-dimer calculated at various interatomic distances by RDFT. The estimated points by RDFT and the fitted function are shown in Fig. 1. The potential parameters for the gold dimer interaction are determined as: $A_1 = 1222.86345$, $A_2 = -3.93623329$, $\lambda_1 = 2.94056151$, $\lambda_2 = -1.30223862$, $\alpha_1 = 0.806351693$, $\alpha_2 = 0.216139972$. In these parameters energy is in eV, and distance is in Å.

The total interaction energy Φ of an N particle system may be calculated from the sum of pair interactions

$$\Phi = \sum_{i<j}^{N} U(r_{ij}). \tag{7}$$

Due to the lack of many-body interactions in the potential energy function, the calculated cohesive energy by using Eq. (7) might be much lower than

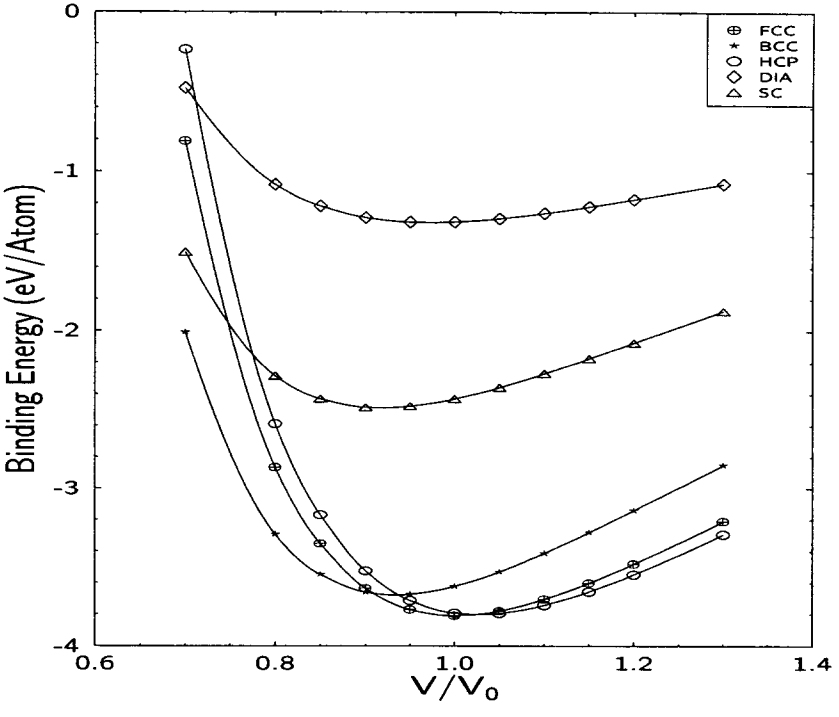

Fig 2. Variation of cohesive energy with respect to atomic volume for various crystal structures. Atomic volume (V) is presented in ratio to atomic volume in equilibrium (V_0). Abbreviations on the picture are: FCC: face centred cubic, BCC: body centred cubic, HCP: hexagonal close-packed, DIA: diamond, SC: single cubic structures.

the experimental value. In order to overcome this deficiency one may scale the total interaction energy to the experimental bulk value by separating the pair energy into two parts a repulsive $U_{21}(r)$ and an attractive $U_{22}(r)$ term [14]. The final form of the potential energy function containing the many-body contributions may be expressed as

$$\Phi = D_{21} \sum_{i<j}^{N} U_{21}(r_{ij}) + D_{22} \sum_{i<j}^{N} U_{22}(r_{ij}). \tag{8}$$

The additional parameters (D_{21},D_{22}) may be determined analytically from

2. RELETIVISTIC DENSITY FUNCTIONAL CALCULATION OF Au_2

Relativistic effects remarkably influence the electronic structure and the chemical bonding of heavy atoms [15]. In order to calculate the relativistic effects a four-component relativistic formulation by solving the Dirac equation is essential [16].

In this work, we first calculate the geometric structure of the Au-dimer with an *ab-initio* all-electron fully relativistic density functional method [17]. The total energy is expressed as a functional of the charge density $\rho(r)$,

$$E[\rho] = \sum_i n_i \langle \phi_i | \, t \, | \phi_i \rangle - \int \rho V^n d\vec{r} + \frac{1}{2} \int \rho V^c d\vec{r} - E^{xc} + \sum_{p>q} \frac{Z_p Z_q}{|R_p - R_q|}, \quad (1)$$

where t is the Dirac kinetic energy operator, a 4×4 matrix in spinor space, V^n rep resents the potential energy of the interaction of the electrons with the nuclei, and V^c is the direct Coulomb-interaction potential among the electrons. The last two terms represent the exchange-correlation energy and the nucleus-nucleus Coulomb interaction energy, respectively. The total energy functional $E[\rho]$, Eq. (1), has a minimum with the ground state density ρ of the system. Application of the variational principle with the constraint of conservation of the number of electrons leads to the single particle Kohn-Sham equations

$$[t + V^n + V^c + V^{xc}] \, |\phi_i\rangle = \varepsilon_i \, |\phi_i\rangle \, . \qquad i = 1...N \quad (2)$$

The exchange-correlation potential V^{xc} is a functional derivative of the exchange-correlation energy E^{xc} with respect to the density, that is,

$$\rho(r) = \sum_i n_i \phi_i^\dagger(r) \phi_i(r), \quad (3)$$

where n_i are the occupation numbers. The parametrized exchange-correlation potential of Vosko, Wilk, Nusair [18] is used for the local density approximation. The generalised gradient approximation (GGA)of Becke [19] is included perturbatively in order to consider nonlocal contributions. In both LDA and GGA level calculations the relativistic form of the exchange-correlation potentials, which was developed by Engel et al. [20] has been used.

In order to solve the Kohn-Sham equations (Eqn. (2)) we used the molecular orbital-linear combination of atomic orbitals (MO-LCAO) approach. The molecular wave functions ϕ_i are expanded the symmetry adapted orbitals χ_j, which are also expanded in terms of the atomic orbitals $\xi_{n_\nu}(r)$.

the total interaction energy expression, Eq. (8), and the bulk stability condition, $\delta\Phi/\delta V = 0$ at $T = 0K$. The combination $D_{21}U_{21}(r) + D_{22}U_{22}(r)$ represents the effective pair interaction [14]. The lattice sums have been calculated using the fcc crystal structure for gold with the lattice constants $a = 4.08$ Å[26]. We have used the value of -3.81eV for bulk cohesive energy [26]. A nine digit accuracy is obtained in the lattice sums. The additional parameters calculated for the gold PEF are: $D_{21} = 0.66756671$, $D_{22} = 0.655442692$, they are unitless. Therefore, the present semi-empirical potential energy function for the gold element satisfies the dimer potential, the bulk cohesive energy, and the bulk stability condition exactly. The present PEF also satisfies the crystal stability. The variation of cohesive energy with respect to the atomic volume for various crystal structures are shown in Fig. 2, fcc is the most stable structure. Using this PEF we have performed molecular-dynamics simulations to obtain the most stable structures of gold microclusters with the number of atoms from 3 to 555. The similar PEF with different parameter sets, obtained from experimental data was successful to simulate bulk and cluster properties of Cu, Ag, and Au elements [14], and nanowire properties of Cu [27]. The aim of the present work is to obtain similar results using a semi-empirical PEF which is based from a *ab-initio* density functional calculation.

4. RESULTS AND DISCUSSIONS

Gold microclusters having 3 to 555 atoms have been investigated by performing a molecular dynamics simulation at constant temperature to obtain the most stable structure of each cluster. In the MD simulations the parametrized semi-empirical PEF was used. The simulations are carried out by starting at 600 K, then the temperature was reduced gradually to 1 K. We have performed this procedure to be able to increase the probability of catching the global minimum of the potential energy surface of the cluster simulated. The time step we used was 1.65×10^{-15} seconds. In the simulations we have taken the number of MD steps at least 80 000 or more. This number of steps was enough to reach the equilibrium in total energy and to get the thermal equilibrium of the systems studied.

Like conventional molecules, most clusters, in general, have a well-defined geometry corresponding to the absolute minimum energy of their potential surfaces. There might be many local minima on the potential energy surface of a many-particle system. In the present study we have generated the microclusters starting from three particles. After obtaining the most stable structure by quenching procedure we added one atom to

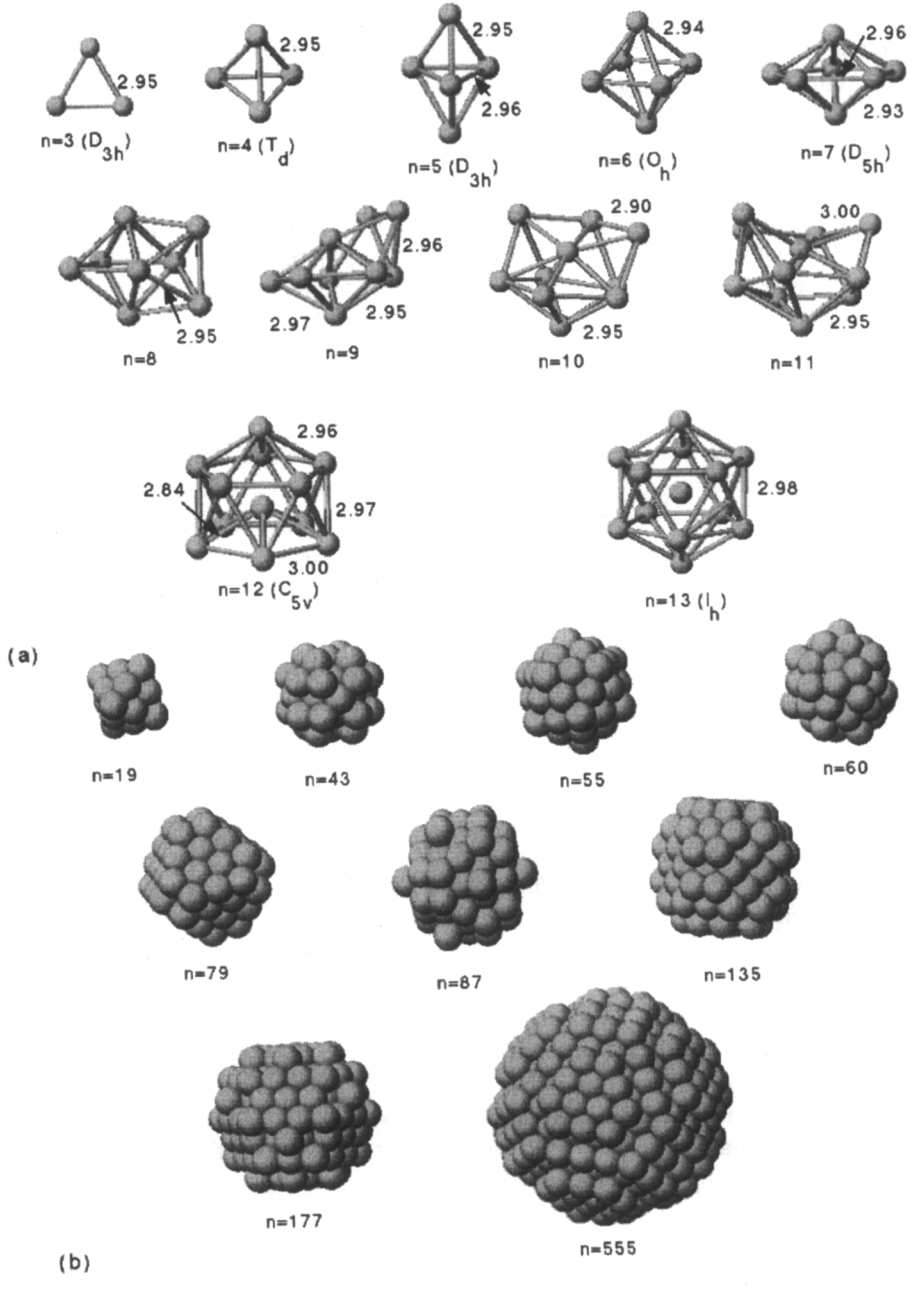

Fig 3. (a) Equilibrium structures of gold microclusters for n=3-13, (b) equilibrated spherical clusters generated from *fcc* structure.

obtain the next cluster, and repeated the quenching procedure. We applied this method for the microclusters with sizes $n = 3 - 13$. For each cluster model we obtained a unique structure. The most stable structures of gold microclusters with sizes $n = 3 - 13$ obtained by the MD simulations are shown in Fig. 3(a). These structures represent the configuration of the system studied at the last MD step. We have also simulated spherical clusters of gold. In this case we generated the clusters from fcc crystalline structure by taking the first, second and so on up to 20th neighbours, and we have selected nine cluster models with the number of atoms $n = 19, 43, 55, 79, 87, 135, 177, 321$, and 555. For these spherical clusters we have performed also the quenching procedure. The three dimensional structures of these clusters are presented in Fig. 3(b). Present results are in agreement with previous MD calculations [14]. Häberlen et. al [13] have studied the structures of spherical Au clusters by the density functional *ab-initio* method. They reported a bond lengths of 2.70 Åfor Au_6, and we estimated it as 2.94 Å. Comparing to their density functional *ab-initio* calculations the average internuclear distances in our study is slightly larger. The binding energy, namely, the average interaction energy per atom in the cluster, versus the cluster size, i.e., the number of atoms in the cluster, is plotted for the most stable structures in Fig. 4 (a). The average binding energy per atom decreases as the cluster size increases, it shows an exponential like decay, as expected. The change is fast for the sizes $n = 3 - 19$. However, the variation of binding energy with respect to the cluster size for the sizes $n = 19 - 147$ changes relatively slow. The general exponential behaviour in the average interaction energy with respect to the cluster size is common for almost all microclusters. Since we scaled the PEF during parametrization to the bulk cohesive energy, as $n \to \infty$ this curve should go asymptoticly to the bulk cohesive energy value of -3.81 eV. For isolated clusters the average binding energy per atom in the cluster, $E_b = \Phi/N$, may be expressed as a function of cluster size N [3],

$$E_b = E_v + E_s N^{-1/3} + E_c N^{-2/3},$$

where the coefficients E_v, E_s, and E_c correspond to the volume, surface, and curvature energies of the particles forming the cluster, respectively. The corresponding plot for this expression is given in Fig. 4 (b). The linear fit to this equation leads to $E_v = -1.807$ and $E_s = 2.259$ and the quadratic fit leads to $E_v = -1.865$, $E_s = 2.626$, and $E_c = -0.474$. The volume energy term should be equal to the bulk cohesive energy value of -3.810. The reason for the difference between the calculated value from the fit and the experimental value is that the clusters considered in the present study are not large enough. As the cluster size increases the calculated volume energy approaches the bulk cohesive energy.

The most stable structures of the microclusters with sizes $n = 3-7$ have a regular symmetry. The corresponding point groups of these clusters are

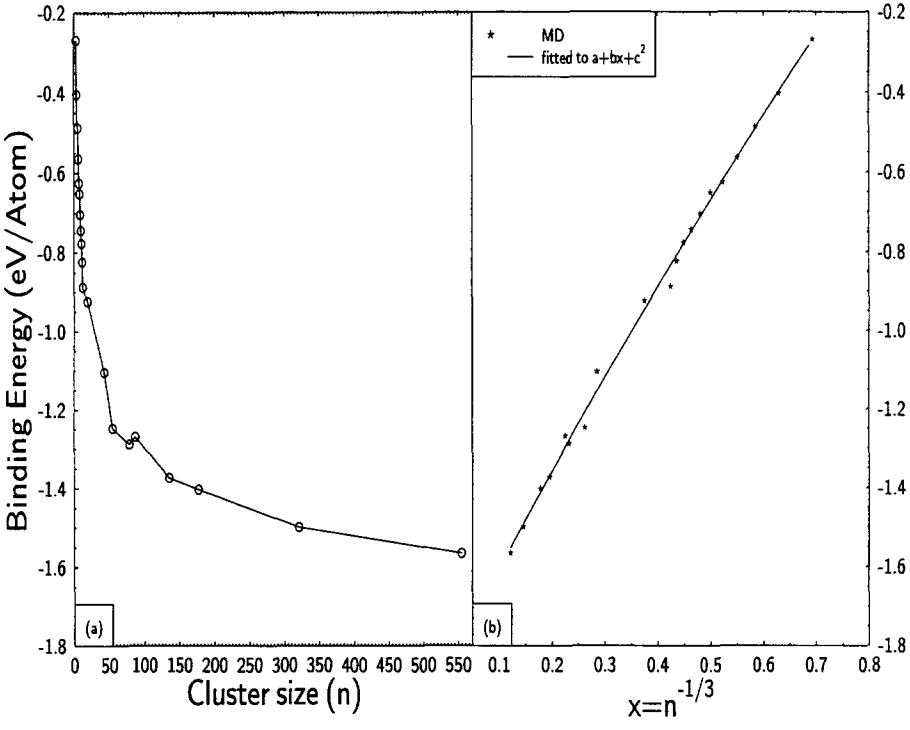

Fig 4. (a) Average interaction energy per atom (binding energy, E_b) versus cluster size (n), (b) Average interaction energy per atom (binding energy, E_b) versus gold cluster size ($n^{-1/3}$).

shown in Fig. 3(a). On the other hand, the clusters for the sizes $n = 8-11$, have no regular symmetry. The Au_{13} has the highest symmetry, I_h. The bond lengths shown on in Fig. 3(a) correspond to the average nearest-neighbor distance values at the last MD step. The spherical clusters kept their spherical form after the simulation, but atoms on the surface region reconstructed slightly with respect to the original positions. The estimated interatomic distances in the microclusters obey the general relation ($r_e < r < d_{nn}$), where r_e is the dimer distance, d_{nn} is the nearest-neighbor distance in the crystal and r is the average nearest-neighbor distance in the cluster. Since we determine the effective pair potential parameters using crystal structure information, the estimated average interatomic distances

in the clusters might be slightly larger than the actual values.

We have investigated the structural stability and energetics of isolated gold microclusters containing 3 to 555 atoms. As a conclusion we may say that gold microclusters prefer to form three-dimensional compact structures. We should say that the MD results obtained in this work are qualitative and we belive that they represent the correct trend. The electronic and geometric structure calculations by direct RDFT for gold microclusters for $n = 3 - 7$ are in progress.

ACKNOWLEDGEMENTS

S.V. and B.F. would like to thank Deutsche Forschungsgemeinschaft (DFG) and JAERI for financial support. We also thank the members of JAERI for their hospitality during the course of this work at Tokai.

REFERENCES

[1] *Microclusters*, edited by Sugano, Y. Nishina, and S. Ohnishi: Springer-Verlag, Berlin, 1987.

[2] *Clusters of Atoms and Molecules,* edited by H. Haberland: Springer-Verlag, Berlin, 1987).

[3] *The Chemical Physics of Atomic and Molecular Clusters,* edited by G. Scoles: North Holland, Amsterdam, 1990.

[4] Walt A. de Heer, *Rev. Mod. Phys.* **1993**, *65*, 611.

[5] J. Koutecky and P. Fantucci, *Chem. Rev.* **1986**, *86*, 539.

[6] G. Galli, and M. Parinello, 1991, in *Computer Simulations in Material Science*, NATO ASI Series E: edited by M. Meyer and V. Pontikis: Kluver Academic, Dordrecht, Applied Science Vol. 205, p. 283.

[7] Ş. Erkoç, *Phys. Rep.* **1997**, *278*, 79.

[8] Ş. Erkoç, T. Baştuğ, M. Hirata, and S. Tachimori, J. Phys. Soc. Jap., **1999**, *68*, 440.

[9] T. Baştuğ, Ş. Erkoç,M. Hirata, and S. Tachimori, *Phys. Rev. A* **1999**, *59*, 3690.

[10] R. J. Puddephatt, *The Chemistry of Gold*: Elsevier, Amsterdam, 1978.

[11] J. S. Bradley, in *Clusters and Colloids:from Theory to Application*, edited by G. Schmid: VCH, Weinheim, 1994.

[12] K. Fauth, U. Keibig, and G. Schmid, *Z. Phys. D* **1994**, *12*, 515.

[13] O. D. Häberlen, S.-C. Chung, M. Stener, and N. Rösch *J. Chem. Phys.* **1997**, *106*, 5189.

[14] Ş. Erkoç, *Z. Phys. D* **1994**, *32*, 257.

[15] P. Pyykkö, *Chem. Rev.* **1997**, *97*, 597.

[16] T. Baştuğ, D. Heinemann, W.-D. Sepp, D. Kolb, and B. Fricke, *Chem. Phys. Lett.* **1993**, *211*, 119.

[17] B. Fricke, W.-D. Sepp, T. Baştuğ, S. Varga, K. Schulze, J. Anton, V. Pershina, *Adv. in Quan. Chem.* **1997**, *29*, 109.

[18] S.H. Vosko, L. Wilk, and M. Nusair, *Can. J. Phys.* **1980**, *58*, 1200.

[19] A. D. Becke, *Phys. Rev. A* **1988**, *38*, 3098.

[20] E.Engel, S.Keller, R.M.Dreizler, **Phys. Rev. A 1996**, *53*, 1367.

[21] J. Meyer, W.-D. Sepp, B. Fricke, and A. Rosén, *Comp. Phys. Comm.* **1996**, *96*, 263.

[22] T. Baştuğ, W.-D. Sepp, D. Kolb, B. Fricke, G. Te Velde, E. J. Baerends, *J. Phys. B:At. Mol. Opt. Phys.* **1995**, *28*, 2325.

[23] P. M. Boerrigter, G. Te Velde, E.J. Baerends, *Int. J.Quant. Chem.* **1988**, *33*, 87; G. Te Velde, and E. J. Bearends, *J. Comp. Phys.*, **1992**, *99*, 84.

[24] S. Varga, E. Engel, W.-D. Sepp, and B. Fricke, *Phys. Rev. A* **1999**, *59*, 4288.

[25] K. P. Huber and G. Herzberg, *Molecular spectra and molecular structure* I: Van Nostrand Reinhold, New York, 1950.

[26] C. Kittel, *Introduction to Solid State Physics*, 4th ed.: Wiley, 1971.

[27] H. Mehrez, S. Ciraci, C.Y. Fong, and Ş. Erkoç, *J. Phys.: Condens. Matter* **1997**, *9*, 10843.

Bond index and Energy partition method for DV-Xα

Katsumi Nakagawa

Canon Ecology R & D Center,
4-1-1 Kizugawadai Kizu-cho Souraku-gun Kyoto Japan.

(Received October 29, 1998)

The bond index and the valency proposed by Armstrong, Perkins and Stewart coincides very well with chemist's intuition and is used in MOPAC. Their method is extended for general molecular orbital methods including DV-Xα. Furthermore, the energy partition method using the Fock matrix is adopted to indicate bond strengths. Bond indices and partitioned energies can be calculated using the standard DV-Xα output file and draw more quantitative and vivid image of chemical bonds than Mulliken's population analysis. The procedures of new method and some interesting results are described.

KEYWORDS: bond index, valency, energy partition, population analysis

1. INTRODUCTION

Mulliken's population analysis(1) is helpful to interpret results of MO (molecular orbital) calculation and has been used by many researchers. But it sometimes gives embarrassing results for the molecules including non-typical covalent bonds. The bond index proposed by Armstrong, Perkins and Stewart(2) gives figures reasonable even for such cases, as well as intuitively understandable. But their method is defined only for MO calculations with orthonormalized basis functions. The author extends their method for general MO calculations including DV-Xα by the way of basis function ortho-normalization. The extended bond index is always non-negative and can be interpreted as an electron density. But it can't distinguish antibonds from normal bonds. To complement the bond index, he also adopted the energy partition method using the Fock matrix and MO coefficients. Bond indices and partitioned energies, both of which can be calculated using the standard output file of DV-Xα, show vivid and complete features of chemical bonds.

e-mail: nakagawa@cer.canon.co.jp

ADVANCES IN QUANTUM CHEMISTRY, VOLUME 37

0065-3276/01 $35.00

2. COMPUTATIONAL METHOD

2.1. Restriction for effectiveness of Mulliken's population analysis

Suppose that molecular orbitals φ_i $(i = 1,2,\cdots,n)$ are expressed like $\varphi_i = \sum_{r=1}^{n} C_{ir}\chi_r$, where $\chi_r (r = 1,2,\cdots,n)$ are basis functions (atomic orbitals) and φ_i are orthonormalized. $(\int \varphi_i \varphi_j d\upsilon = \delta_{ij})$ The atomic orbital bond population (overlap population) between χ_r and χ_s (N_{rs}) and the atomic orbital population on χ_r (N_r) are defined as

$$N_{rs} = 4\sum_{i=1}^{m} C_{ir}C_{is}S_{rs} \quad (r \neq s) \quad \cdots (1) \quad \text{and}$$

$$N_r = 2\sum_{i=1}^{m} C_{ir}C_{ir}S_{rr}, \quad \cdots (2)$$

where $S_{rs} = \int \chi_r \chi_s d\upsilon$ (overlap integral) and m is the number of occupied orbitals. The atomic orbital bond population between atom A and atom B (N_{AB}) and the atomic orbital population on atom A (N_{AA}) are defined like

$$N_{AB} = \sum_{r\in A}\sum_{s\in B} N_{rs} \quad (A \neq B) \quad \cdots (3) \quad \text{and}$$

$$N_{AA} = \sum_{s\leq r} N_{rs} \quad (r,s \in A). \quad \cdots (4)$$

N_{rs} and N_{AB} may seem to be electron densities, because

$$\sum_{s\leq r} N_{rs} = \sum_{B\leq A} N_{AB} = 2m. \quad \cdots (5)$$

But N_{rs} or N_{AB} can be negative, which is strange as an electron density and is usually interpreted to indicate antibonding characteristics. It can be justified partly as follows(3).

Based on the extended Huckel theory, the total electronic energy of a singlet state molecule (E_{el}) is expressed like

$$E_{el} = 2\sum_{i=1}^{m}\sum_{r=1}^{n} C_{ir}{}^2 H_{rr} + 4\sum_{i=1}^{m}\sum_{s<r} C_{ir}C_{is}H_{rs}, \quad \cdots (6)$$

where H_{rs} is the extended Huckel Hamiltonian. If the Hoffmann's approximation

$$H_{rs} = \frac{K}{2} S_{rs}(H_{rr} + H_{ss}) \quad \cdots (7)$$

is adopted, the second term of Eq. (6) becomes

$$\frac{K}{2}\sum_{s<r} N_{rs}(H_{rr}+H_{ss}). \quad (K = \text{a positive constant}) \quad \cdots \quad (8)$$

Because $(H_{rr}+H_{ss})$ is negative, positive N_{rs} decreases E_{el} and negative N_{rs} increases E_{el}, which is agrees well with the interpretation of negative N_{rs}. But if N_{AB} includes both of positive N_{rs} and negative N_{rs} and the absolute value of $(H_{rr}+H_{ss})$ corresponding to positive N_{rs} is far larger than others, $\sum_{r\in A}\sum_{s\in B} N_{rs}(H_{rr}+H_{ss})$ can be negative and decreases E_{el} in spite that N_{AB} is negative. Indeed we sometimes experience the cases that N_{AB} is negative for a stable bond as demonstrated later.

To improve this situation, the author proposes to adopt a pair of parameters. One of them has the electron density characteristics and the other has the characteristics of the energy partitioned to each atom pair.

2.2. Bond index and valency

Let's assume the basis functions to be orthonormalized. Then

$$\sum_{s=1}^{n}(\sum_{i=1}^{m} C_{ir}C_{is})^2 = \sum_{s=1}^{n}\sum_{i=1}^{m}\sum_{j=1}^{m} C_{ir}C_{is}C_{jr}C_{js} = \sum_{i=1}^{m}\sum_{j=1}^{m} C_{ir}C_{jr}\sum_{s=1}^{n} C_{is}C_{js}$$

$$= \sum_{i=1}^{m}\sum_{j=1}^{m} C_{ir}C_{jr}\delta_{ij} = \sum_{i=1}^{m} C_{ir}^{\,2} = \sum_{i=1}^{m} C_{ir}^{\,2} \quad \cdots \quad (9) \quad \text{and}$$

$$\sum_{r=1}^{n}(\sum_{i=1}^{m} C_{ir}^{\,2}) = \sum_{i=1}^{m}\sum_{r=1}^{n} C_{ir}^{\,2} = \sum_{i=1}^{m} 1 = m. \quad \cdots \quad (10)$$

The equation (10) allows the interpretation that α-spin (or β-spin) electrons of the system are divided into χ_r via $\sum_{i=1}^{m} C_{ir}^{\,2}$, each of which is divided further into the bond between χ_r and χ_s via $(\sum_{i=1}^{m} C_{ir}C_{is})^2$ as suggested by the Eq. (9). If we denote $B_{rs}' = 2(\sum_{i=1}^{m} C_{ir}C_{is})^2 \quad (r \neq s)$ and $B_{rr}' = (\sum_{i=1}^{m} C_{ir}^{\,2})^2$, Eq. (9) and Eq. (10) lead

$$\sum_{s\leq r} B_{rs}' = m. \quad \cdots \quad (11)$$

Further, if we denote $B_{AB}' = \sum_{r\in A}\sum_{s\in B} B_{rs}' \quad (A \neq B)$ and $B_{AA}' = \sum_{s\leq r} B_{rs}', \quad (r,s \in A)$

$$\sum_{A\leq B} B_{AB}' = \sum_{s\leq r} B_{rs}' = m. \quad \cdots \quad (12)$$

As the bond index B_{AB} should be the sum of α-spin and β-spin contributions between atom A and atom B or on atom A itself,

$$B_{AB} = 2\sum_{r\in A}\sum_{s\in B}\left(\sum_{i=1}^{m(\alpha)} C^{\alpha}_{ir}C^{\alpha}_{is}\right)^2 + 2\sum_{r\in A}\sum_{s\in B}\left(\sum_{i=1}^{m(\beta)} C^{\beta}_{ir}C^{\beta}_{is}\right)^2 \quad (A \neq B) \quad \cdots (13)$$

and

$$B_{AA} = \sum_{r\in A}\sum_{s\in A}\left(\sum_{i=1}^{m(\alpha)} C^{\alpha}_{ir}C^{\alpha}_{is}\right)^2 + \sum_{r\in A}\sum_{s\in A}\left(\sum_{i=1}^{m(\beta)} C^{\beta}_{ir}C^{\beta}_{is}\right)^2, \quad \cdots (14)$$

where $m(\alpha)$ is the number of α-electrons and $m(\beta)$ is that of β-electrons.

The equation(12) is generalized to the conservation law like

$$\sum_{B\leq A} B_{AB} = m(\alpha) + m(\beta). \quad \cdots (15)$$

B_{AB} and B_{AA} are non-negative as clearly seen from Eq. (13) and Eq. (14), and B_{AB} for typical single-, double- or triple-bond (like C-C of C_2H_6, C_2H_4 or C_2H_2) is 1, 2 or 3 respectively as demonstrated later. These characters are very helpful to interpret the various chemical bonds in molecules.

Okada proposed the bond order(4,5). For singlet state, his bond order between χ_r and χ_s (B^{Okada}_{rs}) is defined as

$$B^{Okada}_{rs} = \left(\sum_{t=1}^{n}\left(\sum_{i=1}^{m} 2C_{ir}C_{it}\right)S_{ts}\right)\left(\sum_{t=1}^{n}\left(\sum_{i=1}^{m} 2C_{is}C_{it}\right)S_{tr}\right). \quad \cdots (16)$$

The definition (16) doesn't require orthonormalized basis functions, but becomes strictly the same as Armstrong, Perkins and Stewart's bond index, when orthonormalized basis functions are used. ($S_{rs} = \delta_{rs}$) His bond order is interpreted as the expectation value of the spin coupling of a electron pair in the bond and integer bond order means the complete spin coupling.

Furthermore, the valency of atom A is defined as

$$V_A = \sum_{B\neq A} B_{AB}. \quad \cdots (17)$$

For typical covalent molecule, V_A also becomes integer because all B_{AB} are integers. These features coincide very well with chemist's intuition.

2.3. Orthonormalization of basis functions

As explained in the preceding section, the bond index and the valency have definite physical meanings only when basis functions are orthonormalized. MOPAC satisfies this assumption(6), but general MO methods, including DV-Xα, don't satisfy it. Fortunately basis functions can be orthonormalized after MO calculation without any loss of accuracy, provided that all overlap integrals are known.

Besides the orthonormalizatin of basis functions seems to be of essential

importance even for the bond parameter which doesn't require orthonormalized basis functions. For example, Okada's bond order(4,5) based on the orthonormalized basis functions is often larger and indicates bond characteristics more clearly than the counterpart based on the non-orthonormalized basis functions.

The procedure to orthonormalize basis functions isn't unique. But the degrees of mixture between basis functions accompanied with the orthonormalization should be equalized for all basis functions to preserve characteristics of original ones. From this viewpoint, well-known Schmidt's method is unsuitable here. Lowdin developed the systematic way to orthogonalize basis functions and emphasized its usefulness for the bond analysis(7). He orthogonalized χ_r into χ_r', using the infinite series

$$\chi_r' = \chi_r - \frac{1}{2}\sum_{s\neq r} S_{rs}\chi_s + \frac{3}{8}\sum_{s\neq r} S_{rs}\sum_{t\neq s} S_{st}\chi_t - \cdots, \quad \cdots (18)$$

where χ_r are assumed to be already normalized. ($S_{rr} = 1 \quad r = 1,2,3,\cdots,n$)

The author adopts the following way. Firstly the tentative functions χ_r' are defined as

$$\chi_r' = \chi_r - \sum_{s\neq r} \frac{S_{rs}}{S_{rr} + S_{ss}}\chi_s, \quad \cdots (19)$$

where $S_{rs} = \int \chi_r \chi_s d\upsilon$. As the right hand of Eq. (19) is equivalent to the first two terms of Eq. (18) for normalized χ_r, χ_r' are roughly orthonormalized. To make the ortho-noramalization complete, the procedure Eq. (19) should be repeated several times, after substituting S_{rs}' into S_{rs} in Eq. (19), where

$$S_{rs}' = \int \chi_r' \chi_s' d\upsilon = S_{rs} - \sum_{t\neq r}^{n} \frac{S_{rt}S_{ts}}{S_{rr} + S_{tt}} - \sum_{u\neq s}^{n} \frac{S_{ru}S_{us}}{S_{uu} + S_{ss}}$$

$$+ \sum_{t\neq r}^{n}\sum_{u\neq s}^{n} \frac{S_{rt}S_{tu}S_{us}}{[S_{rr} + S_{tt}][S_{uu} + S_{ss}]}. \quad \cdots (20)$$

Once basis functions get orthonormalized, MO coefficients should be recalculated before evaluating bond indices and valencies.

2.4. Energy partition method

Usually larger bond index suggests more electrons in the bond and larger bond strength. But even if the bond 1 and the bond 2 have the same bond indices, electrons in the bond 1 and electrons in the bond 2 may feel different potentials, which cause different bond strengths. As an extreme case, an antibond of an excited molecule has positive bond index as demonstrated later. To avoid confusion, the analysis of energies partitioned among bonds is helpful. The equation (6) can be utilized as a simple definition of the energy

partition by replacing the Hamiltonian with the Fock matrix.

For α-(or β-) electrons,

$$\sum_{i=1}^{m}\sum_{r=1}^{n} C_{ir}{}^2 F_{rr} + 2\sum_{i=1}^{m}\sum_{s<r} C_{ir}C_{is}F_{rs} = \sum_{i=1}^{m}\sum_{r=1}^{n}\sum_{s=1}^{n} C_{ir}C_{is}F_{rs}$$

$$= \sum_{i=1}^{m}\int (\sum_{r=1}^{n} C_{ir}\chi_r) F (\sum_{s=1}^{n} C_{is}\chi_s) d\upsilon = \sum_{i=1}^{m}\int \varphi_i F \varphi_i d\upsilon = \sum_{i=1}^{m}\int \varphi_i \varepsilon_i \varphi_i d\upsilon = \sum_{i=1}^{m} \varepsilon_i \,, \quad \cdots (21)$$

where F_{rs} is a Fock matrix and the suffix α (or β) is omitted.

If we define the partitioned energy between orbitals PE_{rs} as

$$PE_{rs} = 2\sum_{i=1}^{m(\alpha)} C_{ir}{}^{\alpha} C_{is}{}^{\alpha} F_{rs}{}^{\alpha} + 2\sum_{i=1}^{m(\beta)} C_{ir}{}^{\beta} C_{is}{}^{\beta} F_{rs}{}^{\beta} \quad (r \neq s) \quad \cdots (22) \quad \text{and}$$

$$PE_{rr} = \sum_{i=1}^{m(\alpha)} (C_{ir}{}^{\alpha})^2 F_{rr}{}^{\alpha} + \sum_{i=1}^{m(\beta)} (C_{ir}{}^{\beta})^2 F_{rr}{}^{\beta} \,, \quad \cdots (23)$$

Eq. (21) is generalized like

$$\sum_{s\leq r} PE_{rs} = \sum_{i=1}^{m(\alpha)} \varepsilon_i{}^{\alpha} + \sum_{i=1}^{m(\beta)} \varepsilon_i{}^{\beta} \,. \quad \cdots (24)$$

If the partitioned energy between atoms (PE_{AB}) is defined as

$$PE_{AB} = \sum_{r\in A}\sum_{s\in B} PE_{rs} \quad (A \neq B) \quad \cdots (25) \quad \text{and}$$

$$PE_{AA} = \sum_{s\leq r} PE_{rs} \quad (r, s \in A) \,, \quad \cdots (26)$$

(24) can be written like

$$\sum_{B\leq A} PE_{AB} = \sum_{i=1}^{m(\alpha)} \varepsilon_i{}^{\alpha} + \sum_{i=1}^{m(\beta)} \varepsilon_i{}^{\beta} \,. \quad \cdots (27)$$

As PE_{AB} consists of energy fragments PE_{rs}, it has always a definite meaning as energy unlike N_{AB}. Besides PE_{AB} can be calculated easily like N_{AB}, using the MO calculation results.

The sum of eigenvalues($\sum_{i=1}^{m(\alpha)} \varepsilon_i{}^{\alpha} + \sum_{i=1}^{m(\beta)} \varepsilon_i{}^{\beta}$) in Eq. (27) isn't the exact total electronic energy in general(8). But Ruedenberg(9) or March(10) proved that the following correlation approximately holds around the equilibrium structure of the molecule.

$$E_{tot} = 1.55\sum_{i=1}^{m} 2\varepsilon_i \,, \quad \cdots (28)$$

where E_{tot} is the total energy of the molecule including nuclear-nuclear Culomb interactions. The correlation (28) rationalizes that the energy partition method is a good indicator of the bond stabilities, as well as that the Walsh diagram method(11) is a good indicator of the equilibrium structure of

molecules.

The energy partition method described here is essentially the same as Pettifor's bond order potential(12,13). He and his coauthors utilize it to analyze chemical bonds of variety of materials quantitatively(14).

The definitions (22) and (23) don't require ortho-normalized basis functions. But calculated results fairly depends on basis functions. The absolute value of partitioned energy with orthonormalized basis functions is usually larger and seems more reasonable than the counterpart with non-orthonormalized basis functions, like the case of Okada's bond order. The basis functions orthonormalized by Eq. (19) and Eq. (20) are used for the energy partition calculations in the following sections. But systematic and theoretical studies are necessary to clarify the dependence of bond parameters on the basis functions and the optimization of them.

The DV-Xα program outputs the overlap integrals, the Fock matrix and MO coefficients into the f08 file. The author developed the postprocessor program which reads data listed above from the f08 file and orthonormalizes basis functions and calculates bond indices, valencies and partitioned energies. DV-Xα calculation should be done with actual atomic orbitals instead of the symmetry adapted basis funtiones to get all overlap inegrals.

3. EXAMPLES

3.1. Ground state molecules

As a simple example, bond indices, valencies, partitioned energies and atomic orbital bond populations for a formaldehyde(H_2CO) molecule are listed

Table I. bond parameters of H_2CO

bond index

	H_A	H_B	C	O
H_A	0.420			
H_B	0.005	0.425		
C	0.922	0.922	4.058	
O	0.066	0.067	2.071	7.045

partitioned energy(eV)

	H_A	H_B	C	O
H_A	-1.59			
H_B	0.15	-1.65		
C	-9.96	-9.95	-281.02	
O	-0.31	-0.30	-23.36	-536.66

atomic orbital bond energy

	H_A	H_B	C	O
H_A	0.636			
H_B	-0.185	0.641		
C	0.768	0.758	4.794	
O	-0.151	-0.144	1.033	7.849

valency

0.993	0.994	3.915	2.204

in Table Ⅰ. The bond index(H-C) is roughly 1 which indicates a single bond formation and the bond index(C-O) is roughly 2 which indicates a double bond formation. And the partitioned energies of these bonds are negative and suggest they are stable.

Table Ⅱ shows bond parameters of various molecules, which are averaged if equivalent bonds exist. Well potentials are not adopted in DV-Xα calculatins here. The bond index(C-C) of C_2H_6, C_2H_4 or C_2H_2 is 1, 2 or 3 respectively. The bond index (C-C) of C_6H_6 is 1.4 and the bond index (B-F) of BF_3 is 1.2, both of which are sums of a σ-bond and smaller π-bond contributions. The bond index(C-O) of CO near to 3 and its partitioned energy as large as that of C-C of C_2H_2 suggest a triple bond formation. The bond indices (S-F) of SF_6, (B-B) of B_2H_6 and (Fe-C) of $Fe(C_5H_5)_2$ (Fig.2) are smaller than 1. But the partitioned energies for those bonds are negative and explain their stabilities. On the other hand, the atomic orbital bond population for (Fe-C) of $Fe(C_5H_5)_2$ is negative and can't explain its stability.

molecule	bond	bond index	partitioned Energy (eV)	atomic orbital bond population
C_2H_6	C-C	1.074	-11.949	0.747
	C-H	0.929	-8.973	0.813
C_6H_6	C-C	1.405	-19.780	1.061
	C-H	0.911	-10.028	0.895
C_2H_4	C-C	2.036	-19.934	1.167
	C-H	0.956	-10.621	0.859
C_2H_2	C-C	2.996	-30.722	1.890
	C-H	0.956	-11.274	0.867
CH_3Br	C-Br	1.011	-7.064	0.481
CO	C-O	2.710	-30.250	1.159
H_2CO	C-O	2.071	-23.359	1.033
	C-H	0.922	-9.957	0.763
BF_3	B-F	1.172	-17.650	0.644
NF_3	N-F	0.983	-8.985	0.268
SF_6	S-F	0.657	-9.520	0.237
B_2H_6	B-B	0.717	-4.654	0.413
	B-H(BHB)	0.473	-4.775	0.419
	B-H(HBH)	0.961	-9.089	0.876
$(C_5H_5)_2Fe$	Fe-C	0.571	-5.600	-0.049
	C-C	1.083	-12.700	1.029
	C-H	0.804	-9.928	0.625

Table Ⅱ. Bond parameters of various ground state molecules. The DV-Xα calculations were done based on the strutural parameters linted in (15).

Fig.1. The structure of a ferrocene ($(C_5H_5)_2Fe$) molecule.

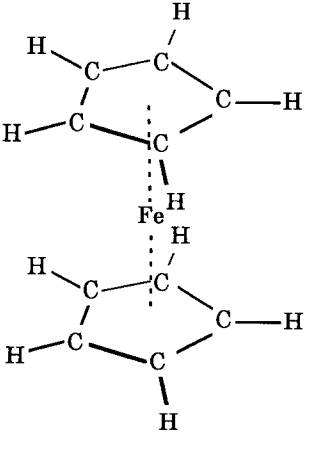

3.2. Antibond of excited molecule

An excited molecule of CH_3Br demonstrates a typical example of the complementary role of the energy partition method for the bond index. Each set of coefficients are calculated by obtaining SCF for the ground state and the exited state but the molecular structure is fixed to that for the ground state(15). They are listed in Table Ⅲ. It may be a little embarrassing that the bond between C and Br of the excited state, which is considered to be an antibond, has positive bond index. This is because that the bond index is an electron density and electrons in an antibonding orbital make their bond index positive as well as those in a bonding orbital. But the partitioned energy (C-Br) for the ground state is negative and that for the excited state is positive in accordance with bonding or antibonding characteristics of the bond. Threfore we will not overlook antibonds, even if non-optimized structres are used in DV-Xα calculation.

		ground state	excited state
bond index	C-Br	1.011	0.743
	C-H	0.977	0.950
partitioned energy(eV)	C-Br	-7.064	2.773
	C-H	-10.341	-10.072

Table Ⅲ. The bond indices and partitioned energies of a CH_3Br molecule in the ground state and the excited state.

4. SUMMARY

1) The reason why Mulliken's atomic orbital bond population between atoms sometimes becomes negative for bonds in stable molecules was suggested.
2) Armstrong, Perkins and Stewart's bond index and valency, which have been used in MOPAC, were extended to general MO methods including DV-Xα, by the way of basis function orthonormalization.
3) The energy partition method, using the Fock matrix and MO coefficients based on orhonormalized basis functions, was adopted to indicate bond strength.
4) Systematic and theoretical studies of the dependence of bond parameters on basis functions and the optimization of the basis functions are neccessary.
5) Bond indices and partitioned energies of various molecules were calculated, using the standard outputs of the DV-Xα calculation.
6) The bond index and the partitioned energy complement each other. They can explain the stabilities of complex structured molecules like a ferrocene and indicate the antibonding characteristics of excited molecule.

ACKNOWLEDGMENT

The author would like to thank Dr. Jun Yasui of Toyobo co., ltd. for his helpful discussion especially on Mulliken's population analysis. He is grateful to Mr. Fumihito Mohri of Institute for Fundamental Chemistry (now of Kaneka corporation) for his kind introduction of Okada's works(4,5) and Lowdin's work(7). He is also grateful to Dr. Shigeto Nishitani of Kyoto Univ. for his kind introduction of works of Pettifor and his coauthors(12-14).

REFERENCES (" * " indicates Japanese documents.)

(1) Mulliken, R.S. *J. Chem. Phys.* **1955,** *23* , 1841
(2) Armstrong,D.R.; Perkins,P.G.; Stewart,J.J.P. *J . Chem . Soc. Dalton.* **1973,** 838
(3)* Yonezawa; Nagata; Kato; Imamura; Morokuma In "Ryosi Kagaku Nyumon(3rd ed.)," , Kagaku-Dojin: Kyoto, **1983**; 83-85
(4) Okada, T.; Fueno, T.; *Bull. Chem. Soc. Jpn.* **1975,** 48, 2025
(5)* Okada, T.; *Kagaku no ryouiki* **1997,** 31, 1007
(6) Stewart, J.J.P.; *J. Computer-Aided Molecular Design*, **1990,** 4, No.1
(7) Löwdin,P.O. *J. Chem. Phys.* **1950,** 18, 365
(8)* Adachi, T. In "Ryosi Zairyo Kagaku Nyumon", Sankyo Syuppan: Tokyo, **1991**; 15-18
(9) Rudenberg, K. *J. Chem. Phys.* **1977,** 66, 375
(10) March, N.H. *J. Chem. Phys.* **1977,** 67, 4618
(11) Walsh, A.D. *J. Chem. Soc.* **1953,** 2260
(12) Pettifor,D.G. *Phys. Rev. Lett.* **1989,** 63, 2480
(13)* Pettifor,D.G. In "Bunshi・Kotai no ketsugou to kouzou(translation)", Gihoudou shuppan: Tokyo, **1997**; 104-105
(14) Alinaghian,P.; Nishitani,S.; Pettifor,D.G. *Phil. Mag. B* **1994,** 69, 889
(15)* In "Kagaku binran kiso-hen (4th ed.)", Jpn. Chem. Soc. Eds.; Maruzen: Tokyo, **1993**; Vol. II , 656-687

On Role of the 3d Atomic Orbital in the Chemical Bonding of Sulfur Fluorides

Kumiko TANAKA, Rika SEKINE*

Department of Chemistry, Faculty of Science, Shizuoka University, 836 Ohya, Shizuoka 422-8529, Japan

Jun ONOE

The Institute of Physical and Chemical Research (RIKEN), Hirosawa, Wako, 351-0198, Japan

Hirohide NAKAMATSU

Institute for Chemical Research, Kyoto University, Uji, Kyoto 611-0011, Japan

(Received May 7, 1999)

The electronic structure of SF_2, SF_4, SF_6 and S_2F_2 was studied, using the DV-Xα molecular orbital method. The chemical bonding of these sulfur fluorides was characterized using the Mulliken population analysis. We determined the *1s*∼*3d* as an appropriate basis set for sulfur atom. Near-linear correlations were found between the valence of sulfur and the *3d* orbital population and between the valence of the sulfur atom and the effective charge. We confirm that the *3d* orbital of sulfur should be taken as a valence orbital.

KEYWORDS: chemical bond, 3d-orbital, sulfur fluoride

*Corresponding author: e-mail scrseki@ipc.shizuoka.ac.jp

ADVANCES IN QUANTUM CHEMISTRY, VOLUME 37

0065-3276/01 $35.00

1. INTRODUCTION

It is well known that the octet rule explains most of the chemical bonding of typical elements. Sulfur has, however, a variety of valences, as in such molecules as SF_2, SF_4 and SF_6. As the SF_2 molecule has two electron-lone-pairs and two covalent bonds, it satisfies the octet rule. While the valence shell of the SF_4 molecule consists of decet electrons; the sulfur atom of the SF_6 molecule is surrounded by dodecet electrons. Therefore sulfur compounds do not always follow the octet rule. It has been said that the sulfur *3d* orbital plays an important role in chemical bonding, and many researches have tried to clarify the nature of sulfur chemical bonding.

Reed and Weinhold studied the role of the *3d* orbitals in the bonding of sulfur (1). They discussed the effect of the *d* orbital by comparing the energy difference between the case where the basis set has *3d* orbitals and the case where it does not. However, their study was limited to SF_6. Takano et al. have obtained the relationship between the classical oxidation numbers and the charge density of sulfur for various SF_X molecules (2). However, the role of the *3d* orbital in the chemical bonding was not mentioned. Thus, the contribution of the sulfur *3d* orbitals, for the series of SF_X compounds, has not yet been clarified.

In the present study, we directly estimate how each sulfur atomic orbital contributes to the chemical bonding in various fluorides. We have already found many cases where, through the DV-Xα method framework, Mulliken population analysis can be successfully applied to the explanation of chemical bonding (3-6). Thus, in order to understand the electronic structures of SF_2, SF_4, SF_6 and S_2F_2, we adopt the DV-Xα method.

2. CALCULATION

We carried out non-spin-polarized molecular orbital calculations using a DV-Xα code called SCAT (7). In the DV-Xα method, matrix elements in the secular equation are derived from the weighted sum of integrand values at sampling points. Hence numerical atomic orbitals can be used as basis sets. These atomic orbitals were generated on each iteration in atomic-like potentials derived from spherically averaging the molecular potential around each nucleus (7). The numerical wave functions thus obtained can be used efficiently for the molecular orbitals and have a practical character making them suitable for population analysis. The Xα method makes use of the local density approximation, where the exchange potential, introduced by Slater, is given by

$$V_X(\boldsymbol{r}) = -3\alpha[(3/8\pi)\rho(\boldsymbol{r})^{1/3}]. \qquad (1)$$

In the present calculation, the parameter α was fixed at 0.7. The one-electron equation for $\varphi_i(\boldsymbol{r})$, a wave function with orbital energy ε_i, is

$$H(\boldsymbol{r})\varphi_i(\boldsymbol{r}) = \varepsilon_i\varphi_i(\boldsymbol{r}). \quad (2)$$

Here the Hamiltonian is represented as

$$H(\boldsymbol{r}) = -1/2\nabla^2 + V_n(\boldsymbol{r}) + V_c(\boldsymbol{r}) + V_x(\boldsymbol{r}), \quad (3)$$

where $V_n(\boldsymbol{r})$ and $V_c(\boldsymbol{r})$ are the electron-nucleus and electron-electron Coulomb potentials of electron-nucleus and electron-electron, respectively.

In order to obtain information concerning the bonding nature, we used the Mulliken population analysis (8). The number of electrons are partitioned into gross populations for the ith atomic orbital, n_i

$$n_i = 2\Sigma_{(l,j)} f_l C_{il} C_{jl} S_{ij}, \quad (4)$$

where f_l is the occupancy of the lth molecular orbital, C_{il} (C_{jl}) is the coefficient of the linear combination of atomic orbitals (LCAO), and S_{ij} is the overlap integral between the ith and the jth atomic orbitals. Two-center charges were estimated with overlap populations:

$$n_{ij} = \Sigma_{(l)} f_l C_{il} C_{jl} S_{ij}, \ (i \text{ on atom A and } j \text{ on atom B}). \quad (5)$$

The bond overlap population, or bond order, for a pair of atoms is defined as the sum of the overlap populations for all the atomic orbitals which belong to the atoms under study.

In order to figure out the nature of their bonding, we performed the calculation for the sulfur fluorides, SF_2, SF_4, SF_6 and S_2F_2. The molecular structures which were taken from Ref. 9 are shown in Fig 1. We took the symmetry of these molecules as C_{2v} for SF_2 and SF_4, O_h for SF_6 and C_s for S_2F_2. The number of sample points used in the numerical integration was taken up to 500 per atoms for each calculation. Self-consistency within 0.0005 electrons was obtained for the final orbital populations. A well potential with width of 7.0 and depth of 0.5 was added.

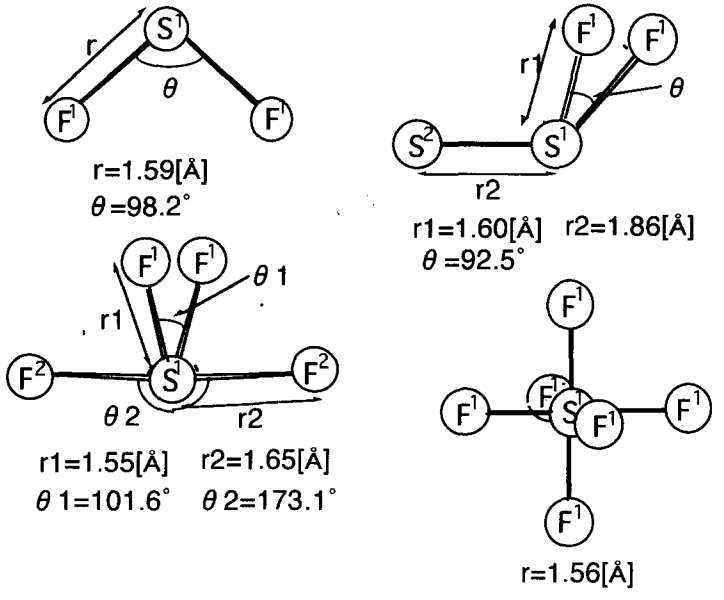

Fig 1. Molecular structure of S_nF_n. Superscripts indicate different type of atoms.

3. RESULTS AND DISCUSSION

First, we examine three kinds of basis sets to clarify the role of the sulfur *3d* orbital. The basis sets we test here are *1s*~*3p*, *1s*~*3d* and *1s*~*4s* for S, and we fix F basis set to *1s*~*2p*. Table I shows the overlap populations obtained by the Mulliken population analysis for SF_2, they clearly indicate the *3d* orbital contribution through the change in the sulfur basis set. The total overlap population for the *1s*~*3p* basis set is particularly small, while the change in the total overlap population from the *1s*~*3d* basis set to the *1s*~*4s* basis set is not so large. This result indicates that a *1s*~*3p* basis set is not suitable for sulfur. In addition, the overlap populations for each atomic orbital pair for the *1s*~*3d* and *1s*~*4s* basis sets are almost the same, and those involving *4s* are very small. We have confirmed that the sulfur *3d* orbital is essential for the understanding of its chemical bonding.

We calculated the overlap populations for each SF_X molecule as well. Table II shows the overlap populations between the sulfur and fluorine atomic orbitals. The values are per bond averages. For all the molecules the overlap populations of the S*3p*-F*2p* and S*3d*-F*2p* pairs are larger than the others. The

overlap populations of S*3p*-F2*p* are 0.29, 0.35 and 0.31 and those of S*3d*-F2*p* are 0.18, 0.24 and 0.26 for SF_2, SF_4 and SF_6, respectively. These results indicate that contribution of the sulfur *3d* orbital to the chemical bonding is comparable with that of the *3p* orbital. As the valence of sulfur increases, the overlap population of the S*3d*-F2*p* pairs becomes larger. Since S_2F_2 behaves differently from the other sulfur fluorides, we will discuss this molecule later. We confirm that the sulfur *3d* orbital participates in the chemical bonding of the sulfur fluorides. It is remarkable that even for SF_2 where the octet rule is satisfied, the contribution of the S*3d* orbital to the chemical bonding is not small. The fact that the *3d* contribution is comparable to the *3p* one for the SF_n compounds is ascribed to the fact that the energy level of the *3d* orbital in S is close to that of *3p*. The *3d* orbital of sulfur should therefore be taken as a valence orbital.

Table I. Overlap populations for SF_2 with different basis sets of sulfur.

Basis set		*1s*~*3p*	*1s*~*3d*	*1s*~*4s*
Total overlap population		0.13	0.39	0.42
Overlap population	S*3s*-F2*s*	-0.08	-0.08	-0.07
	S*3s*-F2*p*	-0.01	-0.01	-0.02
	S*3p*-F2*s*	-0.04	-0.03	-0.02
	S*3p*-F2*p*	0.27	0.29	0.29
	S*3d*-F2*s*		0.04	0.04
	S*3d*-F2*p*		0.18	0.19
	S*4s*-F2*s*			0.01
	S*4s*-F2*p*			0.01

Table II. Overlap populations for sulfur fluorides.

		SF_2	SF_4	SF_6	S_2F_2
Valence		2	4	6	2 to 4
Overlap population	S*3s*-F2*s*	-0.08	-0.09	-0.08	-0.08
	S*3s*-F2*p*	-0.01	-0.04	0.13	0.01
	S*3p*-F2*s*	-0.03	-0.06	-0.06	-0.06
	S*3p*-F2*p*	0.29	0.35	0.31	0.34
	S*3d*-F2*s*	0.04	0.05	0.07	0.08
	S*3d*-F2*p*	0.18	0.24	0.26	0.24

In order to characterize the chemical bonding of sulfur, we analyze effective charges, orbital populations and overlap populations. Table III shows the effective charge of the sulfur atom together with the valence state of sulfur in SF_2, SF_4 and SF_6. The values are 0.30, 0.51, and 0.67 for SF_2, SF_4 and SF_6, respectively. Here we used the *1s*~*3d* orbitals as basis functions for S. When we adopted the *1s*~*4s* basis functions the values were 0.28, 0.49, and 0.60, which are not largely different from the values for the *1s*~*3d* set. The S*4s* orbital is therefore not essential for the discussion of the chemical bonding of S.

We found that the effective charge of fluorine takes an almost constant value even though the sulfur valence changes. On the other hand, as the valence of sulfur increases, its effective charge becomes larger. Figure 2 shows the relation between the effective charge and the valence for SF_2, SF_4 and SF_6. The relation can be fitted by a second order polynomial function, which is almost linear. This correlation originates from the fact that the effective charge of fluorine takes an almost constant value -0.11~-0.15 (S_2F_2 will be discussed later due to its distinct S-S bonds), while the sulfur electron can transfer flexibly.

Table III. Effective charges and orbital populations for S_nF_n. Orbital population of S^1 (center) is indicated for S_2F_2.

		SF_2	SF_4	SF_6	S_2F_2
Valence		2	4	6	2 or 4
Effective charge	S^1	+0.30	+0.51	+0.67	+0.19
	S^2	------	------	------	+0.04
	F^1	-0.15	-0.19	-0.11	-0.11
	F^2	------	-0.07	------	------
Orbital population	*3s*	1.79	1.70	1.26	1.73
	3p	3.59	2.79	2.50	3.25
	3d	0.31	1.00	1.57	0.83

Table III shows the orbital population for the sulfur atoms as well. We found that as the valence of sulfur increases, the *3d* orbital population becomes larger. That is, the values are 0.31, 1.00, and 1.57 for SF_2, SF_4 and SF_6, respectively. These values are also almost the same as in the case where we used the *1s*~*4s* basis set for S. These results for the populations show that the

sulfur *3d* orbital is strongly connected with the valence state of sulfur. Figure 3 shows the correlation between the valence and the *3d* orbital populations for SF_2, SF_4 and SF_6. They also show a relationship which can be fitted by an almost linear second-order polynomial function.

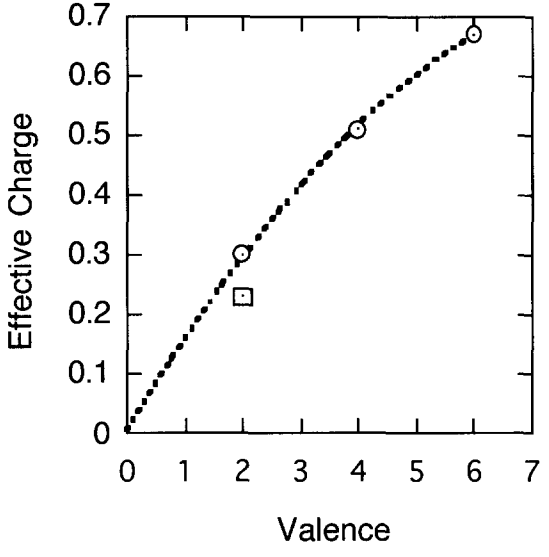

Fig 2. Correlation between valence and effective charges of S.
○: SF_2, SF_4, SF_6; □: S_2F_2.

Two kinds of sulfur atom occur in S_2F_2. One sulfur atom (S^1) is at the center and is coordinated by two fluorine atoms and one sulfur (S^2) atom, while the other (S^2) is situated at the end. Thus these sulfur atoms behave rather differently from ones in the other sulfur fluorides. An effective charge of 0.19 was obtained for the central sulfur atom, as shown is Table III. This value is very small when compared with the other S in SF_x. We interpret this as follows. Fluorine has large electron negativity which draws electrons from sulfur. As we have shown for the other sulfur fluorides, the effective charge for fluorine is -0.11～-0.15. The fluorine in S_2F_2 has a similar effective charge. However, for S_2F_2, electrons are drawn from both the central and the terminal sulfur atoms. Both the terminal sulfur atom and the central sulfur atom bear charge induced by

F_2. If we take this +0.04 charge into consideration, then sulfur has a total effective charge of +0.23. This value is comparable to that for SF_2 which also has two fluorine atoms. The value thus calibrated for S_2F_2 is plotted in Fig 2 as a square.

On the other hand, the *3d* orbital population is 0.83 for the S^1 (center) sulfur of S_2F_2. This value is close to that for SF_4. The S_2F_2 *3d* orbital population value is plotted as a square in Fig 3. This point is fairly close to the $SF_2 \sim SF_6$ line. We interpret this as follows. The central sulfur in S_2F_2 donates a lone pair of electrons to the terminal sulfur atom. Therefore, we take the valence of the central sulfur atom to be four. As shown in Table II, the value of overlap population is also almost the same for SF_4. As a result, we take the valence of S_2F_2 to be two from the effective charge, which is proportional to the number of electronegative atoms, and four from the number of electrons which the central atoms donate to the covalent bonds.

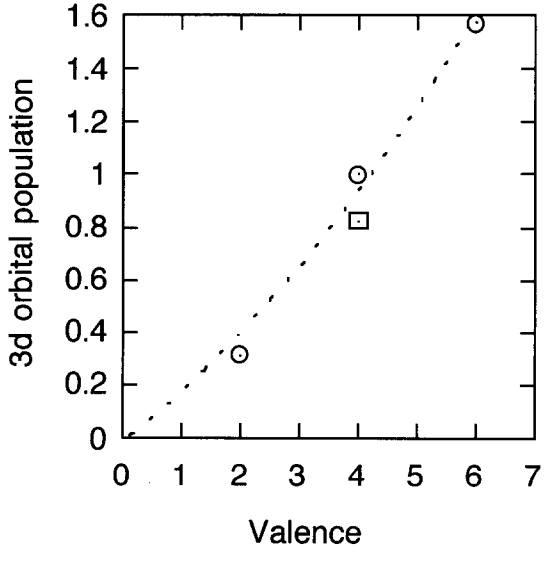

Fig 3. Correlation between valence and *3d* orbital population.
○: SF_2, SF_4, SF_6; □: S_2F_2.

4. CONCLUSION

We have studied the electronic structure of sulfur compounds like SF_2, S_2F_2, SF_4 and SF_6 using the DV-Xα molecular orbital method and Mulliken population analysis. We determined that *1s*~*3d* is an appropriate basis set for sulfur, and is sufficient to express the nature of the chemical bonding. Near-linear correlations are found between the valence of the sulfur atom and the *3d* orbital populations and between the valence of the sulfur atom and the effective charge. Population analysis has clarified that the contribution of the *3d* orbital to the chemical bonding is comparable to that of *3p* orbital. Through the present study, we have obtained the direct evidence indicating how important the *3d*-orbital is in the chemical bonding.

ACKNOWLEDGMENT

The authors would like to thank to Professor K. Tamao of Kyoto University for inspiring this study.

REFERENCE

(1) Reed, A. E.; Weinhold F. *J. Am. Chem. Soc.* **1986**, *108*, 3586.
(2) Takano, K; Hosoya, H.; Iwata, S. *J. Am. Chem. Soc.* **1982**, *104*, 3998.
(3) Onoe, J.; Nakamatsu, H.; Mukoyama, T.; Sekine, R.; Adachi, H.; Takeuchi, K. *Inorg. Chem.* **1997**, *36*, 1934.
(4) Onoe, J. *J. Phys. Soc. Jpn.* **1997**, *66*, 2328.
(5) Onoe, J.; Takeuchi, K.; Nakamatsu, H.; Mukoyama, T.; Sekine, R.; Kim, B. –I.; Adachi, H.; *J. Chem. Phys.* **1993**, *99*, 6810.
(6) Hirata, M.; Sekine, R.; Onoe, J.; Nakamatsu, H.; Mukoyama, T.; Takeuchi, K.; Tachimori, S. *J. Alloys Compounds* **1998**, *271-273*, 128.
(7) Adachi, H.; Tsukada, M.; Satoko, C. *J. Phys. Soc. Jpn.*, **1978**, *45*, 875.
(8) Mulliken, R. S. *J. Chem. Phys.* **1955**, *23*, 1833, 1841, 2338, 2343.
(9) Hellwege, K. –H.; Hellwege, A. M., Eds. "*Landolt-Börnstein*"; Springer-Verlag: Berlin, 1976; Vol. 7, 75.

Index

E

F

G

H

I

L

M

N

O

P

R

S

Z